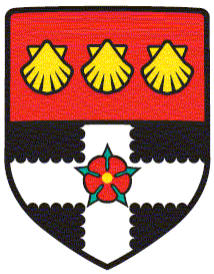

University of Reading

School of Chemistry, Food Biosciences and Pharmacy

Mechanistic Spectro-electrochemistry of Group-6 and -7 Metal Carbonyl Electrocatalysts of CO_2 Reduction

by

James Taylor

A thesis submitted in partial fulfilment of the requirements for the degree of Doctor of Philosophy in Chemistry

Department of Chemistry

March 2020

University of Reading

In the beginning the Universe was created. This has made a lot of people very angry and been widely regarded as a bad move.

- Douglas Adams

Declaration

I, James Taylor, declare that this is my own work and the use of all material from other sources has been properly and fully acknowledged.

J. Taylor	03/04/2020
Signature	*Date*

Acknowledgements

In many ways this thesis represents the pinnacle of my career in full-time education. It is only appropriate then, that upon reaching this milestone, I briefly take some time now to reflect on this formative period but also thank a few of those that have supported me along the way.

Three years ago, I made the decision, with a certain amount of apprehension, to stay at the University of Reading as I watched friends move on, and take up a PhD position in Franti's group. Thankfully this has proven to be one of best decisions I could have made. As a supervisor, Franti is everything you could want. For the last three years his infectious passion for science, seemingly endless knowledge on electrochemistry, trilobites and global politics, not to mention the unbelievable dedication he has to the work and his students, has both inspired and terrified me in equal measure. Without his support and guidance the work in this Thesis just wouldn't have been possible. I feel very fortunate to know that whatever the next step (still unknown at time of writing!), that with Franti's help, I've been able to make a (hopefully) lasting contribution to the scientific literature and maybe even push against the boundaries of our collective knowledge a little.

I have also been lucky to work with several wonderful collaborators and who's expertise in their respective fields continues to inspire. I would like to thank Professor Maria José Calhorda, who has provided invaluable theoretical support over the years in our efforts to characterise our Group-6 carbonyl compounds and Professor Ann Chippindale, for her expertise in X-ray crystallography. As for Martin Pižl and Professor Tony Vlček Jr, it was an absolute pleasure to get to know them both during our experimental visits to RAL, and

I look forward to producing several collaborative manuscripts with them in the near future.

I will always be grateful to Franti for the generous trust he so freely gives to his PhD students, and for the responsibilities and opportunities that come with it. One of the more pleasurable of these is the opportunity I was given to co-supervise the undergraduate and MSc students in our lab. So thank you also to Sophie, Florentine, Ryan, Roisin, Dan, Freddie, Briagha and Ioanna. They definitely made my time at Reading more interesting.

I am lucky to have several great friends in my life. Abbie, my fellow PhD comrade, I'd like to thank you for always listening to my concerns and deftly putting them in perspective; you have a wonderful way of keeping calm when faced with even the most bizarre of challenges. Dan, thank you for always being there, supporting me, and working tirelessly to raise my confidence. Elliott, for being the perfect housemate and for always being willing to listen to my complaints after a long day. Alp, who I shared many lunchtimes with and who provided me with many interesting discussions, about anything other than chemistry. And thank you to all the others who have supported me throughout my time at university, Chris, Justine, Adam, Ankit, Evita. Also to the postgraduate students I've shared an office space with for the past few years, thank you for providing an amusing, friendly atmosphere in the office.

For Alex, thank you for continuing to believe in me during the times when I lost faith, for all your support over the years and all the experiences we've shared. I look forward to sharing many more in the future. Also thank you to Ann and Dave, for welcoming me into their family.

Ultimately though, I would never had made it this far without the support of my mad family. I am very fortunate that my parents were able to give me a wonderful beginning in life and have always been there to encourage, support and give advice when needed. I am as much a product of their upbringing, as I am of my time in Reading. I also want to wish every success and happiness to my sisters, Jenny and Charlotte, as they start to build their own lives outside of a tiny village called West Coker.

Abstract

Bio-inspired transition metal complexes have recently revealed their potential to catalytically convert waste CO_2 from industry into a sustainable source of carbonaceous fuel and chemical feedstock. Ultimately working to close the carbon cycle and helping to alleviate some of the most concerning impacts of anthropogenic climate warming. Significant research efforts have been expended thus far in the race to understand the underlying mechanisms, the trends in reactivity, and the factors which can aid rational design of improved catalysts. There are now hundreds of reported transition metal catalysts for the most facile $2e^-$ reduction of CO_2 to CO or formate, many of which have high activity and tunable selectivity. The majority of catalysts feature a diverse ligand framework, which works cooperatively with the metal centre(s) to reduce CO_2, and much of the work that goes into optimizing the electrocatalytic behaviour actually involves systematic alteration of the non-innocent coordination sphere. A lot of attention has been paid in the recent decade to the Earth-abundant materials such as Mn, Fe, Co, Ni and Cu. Much less attention however has been paid to the Group-6 triad (Cr, Mo, W), leading to the primary aim of this thesis, which is to explore the rich reduction-induced chemistry of these metals and their coordinated ligands.

In Chapter 1, a concise overview of the major milestones concerning the most promising catalysts, as well as an outlook on the field as a whole is presented, while in Chapter 2, an introduction to the major experimental techniques utilized in the thesis is given. The novel research presented in this thesis begins initially with Chapter 3, which reports an in-depth study using mainly cyclic voltammetry and spectroelectrochemistry on the [Mo(x,x′-dmbipy)$(CO)_4$] (x = 4-6, dmbipy = dimethyl-2,2′-bipyridine) series of complexes. A low-

energy pathway to the active catalyst is probed by systematic changes to the ligand, electrode and solvent. The most promising results are obtained with [Mo(6,6′-dmbipy)$(CO)_4$] on an Au cathode in conjunction with the solvent, NMP (*N*-methyl-pyrrolidone), revealing an important synergy between ligand, electrode and solvent effects. This initial research chapter serves to highlight that with careful, rational control, the Group-6 metals are far more promising than previously imagined.

In Chapter 4, a new cooperative approach between photo and electrochemistry toward reducing the catalytic overpotential is trialled with [Mn(bipy)$(CO)_3$Br] (bipy = 2,2′-bipyridine) and [Mo(6,6′-dmbipy)$(CO)_4$]. In the $1e^-$ reduced state, both catalyst precursors have photochemistry which may be exploited to produce the active catalyst already at the $1e^-$ reduced state, without shifting the electrochemical potential more negatively. In both cases, this represents a significant saving of energy, as there is an appreciable separation between the initial reduction and the follow-up reduction which produces the active catalyst. In the future, the novel approach may aid the design of functional devices for CO_2 reduction.

Chapter 5 covers the characterization of a new series of complexes with the structure [Mo(η^3-allyl)(x,x′-dmbipy)$(CO)_2$(NCS)] (x = 4-6) and an in-depth study of their varied cathodic paths under Ar and CO_2 using a combination of cyclic voltammetry, IR/UV-Vis spectroelectrochemistry and supporting DFT calculations. It is revealed that the cathodic path of [Mo(η^3-allyl)(x,x′-dmbipy)$(CO)_2$(NCS)] bears striking similarity to the well-studied and highly promising catalyst, [Mn(bipy)$(CO)_3$Br]. Seemingly small, but systematic changes in the ligand sphere induces significant change in cathodic path, particularly in the stability of the $1e^-$ reduced state and the proclivity for the formation of an inactive dimer (x = 4), vs formation of the active catalyst (x = 6). Under CO_2, catalytic conversion to CO and formate is observed by IR spectroelectrochemistry.

Chapter 6 follows directly from the work presented in Chapter 5, beginning with the characterization of several new complexes, with the structures [Mo(η^3-allyl)(6,6′-

dmbipy)$(CO)_2Cl$] (dmbipy = dimethyl-2,2′-bipyridine, allyl = allyl or 2-methyl-allyl) and [Mo(η^3-2-methyl-allyl)(pTol-bian)$(CO)_2Cl$] (pTol-bian = bis(p-tolylimino)acenaphthene). These complexes were specifically designed in order to systematically probe the innocence of the allyl and halide/pseudo-halide ligands. The results reveal that both types of ligands also have a strong impact on the cathodic path, revealing previously unknown complexity and questions about the non-innocence of the allyl ligand.

Finally, Chapter 7 describes the unusual cathodic path of the Group-7 complexes, [Re(3,3′-dhbipy)$(CO)_3X]^n$ (X = Cl, n = 0; X = PrCN, n = +1; dhbipy = dihydroxy-2,2′-bipyridine) which bear local proton sources, namely two hydroxyl groups in close proximity. Upon reaching the initial reduction, reductive deprotonation occurs, allowing a strong hydrogen bond to form, which radically alters the subsequent cathodic path. The complexes display markedly different behaviour even when compared to their close relative, [Re(4,4′-dhbipy)$(CO)_3Cl$] and the progenitor [Re(bipy)$(CO)_3Cl$] complex. Following a second concerted reduction involving multiple electrons, [Re(3,3′-dhbipy-$2H^+$)$(CO)_3]^{3-}$ forms, which under CO_2 is revealed, by cyclic voltammetry and bulk electrolysis, to be catalytically active toward the reductive disproportionation of CO_2 producing CO and CO_3^{2-}. With careful potentiostatic control, evidence of an electrode catalysed reaction is also revealed. This reaction ultimately allows the radical anion of the parent complex to form in a limited potential range. That is to say, following the initial reductive deprotonation but prior to its close-lying reduction to the active CO_2 reduction catalyst.

Contributions to Chapters

Chapters 1 and 2: All text and images by **James Taylor**.

Chapter 3: All text and images by **James Taylor**. Almost all reported syntheses and CV/SEC experiments by **JT**. Preliminary experiments by **Roisin Leavey** (BSC, supervised by **JT**). Supervision of **JT**, final edit and advice by **Franti Hartl**.

Chapter 4: All text and images by **James Taylor**. All reported syntheses and CV/SEC experiments by **JT**. Preliminary experiments on novel Cu Electrode by **Yibo Wang** (NUIST, supervised by **JT**). Supervision of **JT**, final edit and advice by **Franti Hartl**.

Chapter 5: Majority of text and images by **James Taylor**. Majority of CV/SEC experiments by **JT**. Preliminary experiments and reported syntheses by **Florentine Veenstra** (MSc Amsterdam, supervised by **JT**). DFT section by **Maria José Calhorda** (Lisbon). X-ray crystallography by **Ann Chippindale**. Supervision of **JT**, final edit and advice by **Franti Hartl**.

Chapter 6: All text and images by **James Taylor**. All reported syntheses and CV/SEC experiments by **JT**. Preliminary experiments by **Ryan Culpeck** (MChem, supervised by **JT**). X-ray crystallography by **Ann Chippindale**. DFT experiments by **Maria José Calhorda** (Lisbon). Supervision of **JT**, final edit and advice by **Franti Hartl**.

Chapter 7: All text and images by **James Taylor**. All reported synthesis and CV/SEC experiments by **JT**. Supervision of **JT**, final edit and advice by **Franti Hartl**. Experimental assistance with CPE measurements by **Gaia Neri** (Liverpool) and co-workers.

Publication List

Chapter 3

J. O. Taylor, R. D. Leavey, F. Hartl, *ChemElectroChem*, 2018, **5**, 3155–3161.

Chapter 4

J. O. Taylor, Y. Wang, F. Hartl, *ChemCatChem*, 2020, **12**, 386–393.

Chapter 5

J. O. Taylor, F. L. P. Veenstra, A. M. Chippindale, M. J. Calhorda, F. Hartl, *Organometallics*, 2019, **38**, 1372-1390.

Chapter 6

J. O. Taylor, R. Culpeck, A. M. Chippindale, M. J. Calhorda, F. Hartl, *Organometallics*, Manuscript Submitted.

Chapter 7

J. O. Taylor, G. Neri, L. Banerji, A. Cowan, F. Hartl, *Inorganic Chemistry*, Manuscript In Press, DOI: 10.1021/acs.inorgchem.0c00263.

Other Publications

L. Chen, K. J. C. Lim, T. S. Babra, **J. O. Taylor**, M. Pižl, R. Evans, A. M. Chippindale, F. Hartl, H. M. Colquhoun, B. W. Greenland, A macrocyclic receptor containing two viologen species connected by conjugated terphenyl groups, *Org. Biomol. Chem.* 2018, **16**, 5006–5015.

J. O. Taylor, D. Skelson, A. M. Chippindale, M. J. Calhorda, F. Hartl, *Topic*: (Spectro)-electrochemical Study of a Series of [Mo(η^3-allyl)(R_2-(Me)-dab)$(CO)_2$(X)] (X = Br^-, NCS^-, MeCN; R = phenyl or 2,6-dimethylphenyl; (Me)-dab = (2,3-dimethyl)-1,4-diazobuta-1,3-diene), Manuscript in preparation.

M. Pižl, **J. O. Taylor**, P. Donaldson, M. Fuse, V. Barone, M. Towrie, S. Záliš, A. Vlček, F. Hartl, *Topic*: 2D-IR Spectroelectrochemistry of [Ru(R-bipy)$_2$(NCS)$_2$] (R = OMe, COOEt; bipy = 2,2′-bipyridine), Manuscript in preparation.

M. Pižl, **J. O. Taylor**, A. Vlček, F. Hartl, *Topic*: IR/UV-Vis-NIR and TR-NIR Spectroelectrochemistry of [Ru(bipy)$_n$(CN-bipy)$_{3-n}$](PF$_6$)$_2$ (n = 0, 1, 2; bipy = 2,2′-bipyridine; CN-bipy = 4,4′-dicyano-5,5′-dimethyl-bipyridine), Manuscript in preparation.

S. D. Midgley, **J. O. Taylor**, S. Black, D. Fleitmann, R. Grau-Grespo, *Topic*: Trace Element Impurities as Records of Volcanic Activity: A Computational Investigation, Manuscript in preparation.

Contents

Chapter 1

Introduction

1.1 Solar Fuels

1.1.1 Perspectives on Carbon Dioxide and Global Warming

There is increasing concern over the rising levels of anthropogenic emission of CO_2, its impact on global warming and the implications of the latter on society at large - for example a warming of just 1.5 °C from pre-industrial times is expected to have a significant impact on the global economy, as well as displace potentially millions of people as climate refugees.[1–3] This crisis has, of course, driven cutting-edge research and also the marshalling of considerable resources directed toward developing a number of possible solutions. Despite this, the world still almost completely relies upon carbon-rich fossil fuels to generate power and produce key industrial products. So much so that fossil fuels made up almost 80% of global energy consumption in 2017 (ref.[4]), and with the modernization of economies such as India and China the demand for energy is predicted to increase over the coming years at a rapid pace. Despite its poor reputation, nuclear energy derived from fissionable material is still an attractive alternative to carbon-rich fossil fuels and has a key role to play in efforts to phase out fossil fuels. Of course, nuclear energy produced in this manner has several safety concerns associated with the long-term storage of waste material, and thankfully there is rapid growth in 'true' renewable clean energy sources such as solar and wind power. However, by their nature these are irregular in their output, experiencing periods of high output but low demand and vice versa. Effective storage of renewable energy remains a key obstacle. Processes by which solar energy may be converted to chemical energy, which is much easier to store and transport, are an attractive route to overcoming these longer-term storage concerns. Especially as these renewable energy sources by themselves do not provide the combustible fuels needed for short-term applications, such as in the transport industry, nor the feedstock chemicals required for key industrial processes. In this regard, CO_2 itself has been identified as a potential target.[5]

Inspiration may be taken from nature, where photosynthesis converts roughly 100-120 gigatons of CO_2 per annum[6] into a biological fuel by way of electrochemical reduction

using solar energy.[7–9] Thus, efforts to mimic these efficient biological pathways has spawned sub-fields of renewable technology, known collectively as artificial photosynthesis[10], the products of which are termed solar fuels. A solar fuel 'describes any concentrated chemical energy carrier with long-term storage capacity that contains chemical bonds in which solar energy has been stored'.[11] A solar fuel may be produced directly from solar energy (e.g., photocatalysis) or indirectly (e.g., electro- or photo-electrocatalysis).

1.1.2 Carbon Dioxide Reduction

CO_2 is a thermodyanamically stable linear molecule, the end point of many chemical reactions and also represents carbon in its most oxidised state. To go in the opposite direction (i.e., to reduce CO_2) therefore has a high activation barrier and is associated with significant energy cost. For instance, the $1e^-$ reduction producing the radical anion $CO_2^{\bullet -}$ has an appreciably high reduction potential of -1.9 V vs standard hydrogen electrode (SHE). In nature, this problem is overcome by metalloenzymes, such as the carbon monoxide or formate dehydrogenases [NiFe]-CODH and [Mo^{IV}]-FdsABG, which can catalyse the reversible reduction of CO_2 to CO (or formate) with high activity and selectivity but are sensitive to temperature and pH.[12–14] Unfortunately, they are also expensive and difficult to isolate; making it a practical impossibility to use them directly as catalysts of CO_2 reduction on an industrial scale. However, understanding how they work is essential to developing viable industrial catalysts. Nearly all metalloenzymes have at least one $3d$ transition metal within the active site, with switchable oxidation states, they are capable of reversibly storing electrons and protons. Thus, nature has pointed the way and transition metal catalysts have become the main focus of this research field.

The reduction of CO_2 may actually proceed via several diverse routes, involving reduction by one-, two-, four- and eight-electrons, these are summarized in Table 1.1.[15] The most frequently encountered reduction products are those resulting from the $2e^-$ reduction of CO_2: i.e., CO and formate or formic acid. Beyond this, oxalate ($1e^-$), formaldehyde ($4e^-$) and methanol ($6e^-$) are seen less frequently. Comparatively, methane ($8e^-$) and ethanol ($12e^-$)

are only rarely observed. As can be seen from Table 1.1, a proton-coupled electron-transfer (PCET) reaction is a much more attractive route than direct electrochemical reduction, as it has a generally lower energy requirement for the transformation of CO_2, although the need to handle both electrons and protons obviously adds mechanistic complexity.

Table 1.1: Several proton-coupled pathways, the products, and the thermodynamic potential ($E^{\circ\prime}$) in V vs the standard hydrogen electrode (SHE) required to trigger the reaction. Reproduced from ref. [15]

Redox Reaction	$E^{\circ\prime}$ / V vs SHE
$CO_2 + e^- \longrightarrow CO_2^{\bullet -}$	-1.90
$CO_2 + 2\,H^+ + 2\,e^- \longrightarrow HCO_2H$	-0.61
$CO_2 + 2\,H^+ + 2\,e^- \longrightarrow CO + H_2O$	-0.53
$2\,CO_2 + 2\,H^+ + 2\,e^- \longrightarrow H_2C_2O_4$	-0.49
$CO_2 + 4\,H^+ + 4\,e^- \longrightarrow HCHO + H_2O$	-0.48
$CO_2 + 6\,H^+ + 6\,e^- \longrightarrow CH_3OH + H_2O$	-0.38
$CO_2 + 8\,H^+ + 8\,e^- \longrightarrow CH_4 + H_2O$	-0.24

The most realistic and attractive of these products for the purposes of sustainable chemistry are CO, formate and methanol. CO is a C1-building block for Fischer-Tropsch chemistry, from which it may be converted to short chain alkanes and alcohols; molecules which underpin the petrochemical industry.[16,17] Methanol derived from CO_2 has recently be championed in the methanol economy paradigm[18–20], where it functions as a sustainably sourced carbon-based fuel. Indeed, methanol-based fuel cells can be considered as a highly active area of research.[21,22] In addition, formic acid is a promising material for the reversible storage of hydrogen; a key component in the proposed, and complementary, hydrogen economy.[23]

1.1.3 A Comparison of Homogeneous and Heterogeneous Catalysts

The fields of heterogeneous and homogeneous transition metal catalysts of the electrochemical reduction of CO_2 have developed more or less in parallel.[24] The different approaches are depicted in Scheme 1.1. In heterogeneous catalysis, CO_2 is adsorbed onto the electrode surface and reduced directly while in homogeneous catalysis, the catalyst acts as an intermediate electron shuttle between the electrode surface and CO_2.

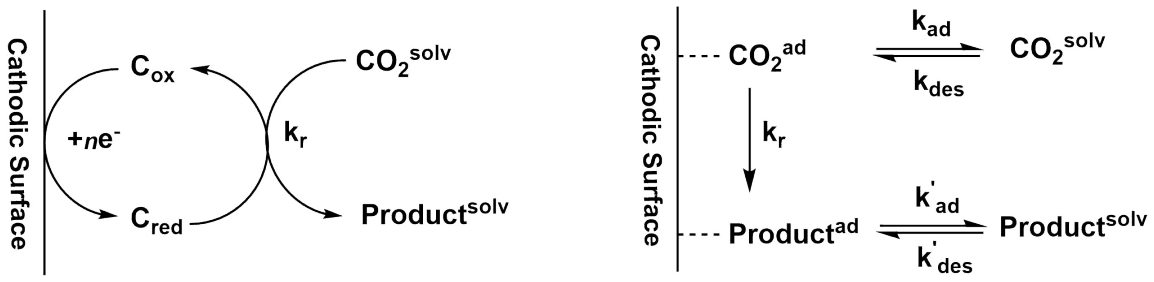

Scheme 1.1: Electrochemical CO_2 reduction via homogeneous (left) or heterogeneous (right) catalysis. Adapted from ref.[25]

Typical electrode materials studied as heterogeneous catalysts include Pd, Pt, Ag and Cu. Materials derived from Pt and Ag are known to favour the production of CO while those containing Pd are known to favour more the conversion to formate[26]. Cu seems particularly unique among the heterogeneous catalysts in its ability to produce highly reduced, and valuable, reduction products - such as methanol, methane and even ethanol.[27,28] Although heterogeneous catalysts are generally more suitable for scale up via flow-chemistry and the reduction products are of course easier to separate, they tend to be less selective for a single product, as there are potentially several different types of reactive sites on the surface of the metal; ultimately producing a multitude of different products but with a low yield for each. On the other hand, homogeneous catalysts are superior in this regard, and high ($> 90\%$) faradaic efficiencies (FE) for a single product are not uncommon.[25] The electronic properties and in particular the reduction potentials of homogeneous catalysts are also more easily tailored, by altering the structures of the coordinated ligands. They are also much more amenable to in-depth mechanistic studies by in-situ spectroscopic methods (see Chapter 2). However, in both cases, degradation of the catalyst is a major concern, as currently most are not stable for long periods (ca. $>$ 100 hrs). In any case, the ultimate goal for homogeneous catalysts is that they be bound to the electrode, in order to get the 'best of both worlds', combining the properties of a heterogeneous catalyst that make it amenable to scale up, with the selectivity of a homogeneous catalyst. Strategies for immobilization have been reviewed extensively elsewhere.[10] Briefly though, immobilization of the catalyst most often requires modification of the appended ligands with functional groups featuring both an

anchor and linker moiety. The anchor moiety is able to bind at the electrode surface, while the linker must facilitate efficient electronic communication between the electrode surface and molecular catalyst.

1.1.4 Fundamentals of Catalytic Carbon Dioxide Reduction by Molecular Catalyst

In general, molecular catalysis proceeds via three steps: (i) electron transfer from the electrode to the catalytic intermediate, (ii) interaction of the active catalyst with CO_2 - via coordination or hydride insertion and (iii) protonation of the catalytic intermediates.[25]

Catalytic CO_2 reduction is induced by reduction of the catalyst, forming the active species which enters the catalytic cycle. The reduction potential of the catalyst must not exceed the onset potential of direct CO_2 reduction at the electrode. On the other hand, the reduction potential of the catalyst should be at least 100-200 mV more negative than the thermodynamic potential of the corresponding reaction couple, in order to ensure there is sufficient driving force for the reaction to occur at a reasonable rate.

Prior to its reduction, the CO_2 molecule must first be activated either by binding to the metal center or in some selected cases insertion into a metal-hydride bond.[29] There are three common modes of binding to a center which are depicted in Scheme 1.2, these include (i) η^1-C, which is preferred for electron-rich metals, since there is the potential for strong overlap between the metal orbitals and the π^*-orbital of CO_2, (ii) η^2-(C,O) where the CO_2 is bent and binds in a side-on fashion through both the C and O atoms and (iii) η^1-O, a rare end-on case in which it may bind as a Lewis base through one of the oxygen atoms. Other cases can involve CO_2 binding in a bridging fashion, either between two metal centers or between the metal and the ligand itself.

Initially, most catalysts are studied in dry organic solvents such as dimethylformamide (DMF), acetonitrile (MeCN) or tetrahydrofuran (THF). This is for a number of reasons, first of all CO_2 has a higher solubility in these solvents compared to H_2O. Secondly, the catalyst

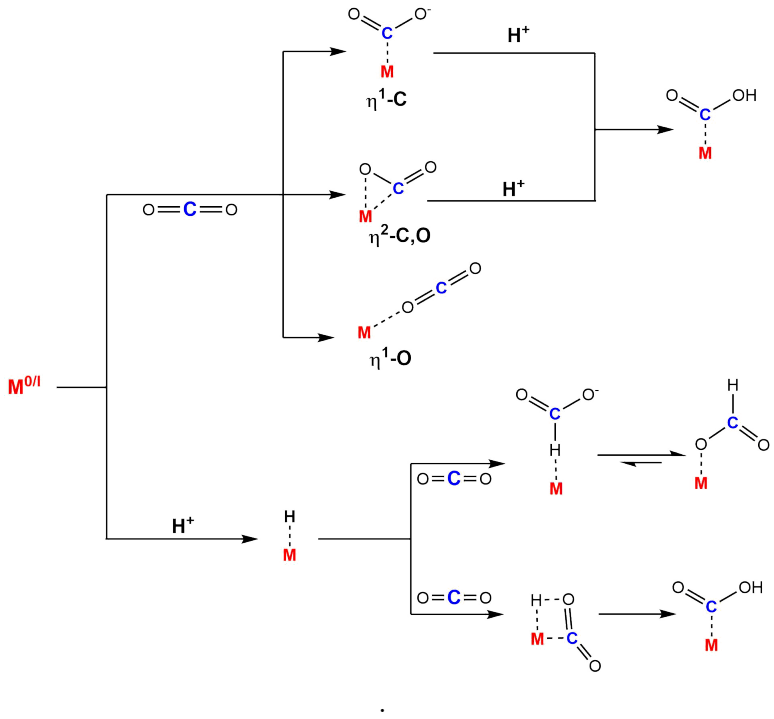

Scheme 1.2: CO_2 activation pathways by reduced transition metal complexes and the role of protons in the catalytic cycle. Adapted from ref.[30]

itself may not be soluble in aqueous solution. Finally, proton reduction is a serious competing side reaction, which is significantly suppressed in the dry organic solvent. This also has the effect of expanding the available potential window for the electrocatalytic experiment. That being said, it is PCET (proton-coupled electron transfer) which is truly desired and therefore protons are actually considered essential for the catalysis. Thus, catalytic studies are often conducted in the presence of small concentrations of a proton donor (e.g., trifluoroethanol (TFE), phenol (PhOH) or H_2O) to augment the catalytic efficiency, the possible roles of protons in the catalytic cycle may be seen in Scheme 1.2. As is shown, they may react in two ways: either further activating the M−CO_2 intermediate (top) or by forming a metal-hydride (M−H), which then reacts with CO_2 (bottom).

The hydroxycarbonyl intermediate (η^1-COOH) shown in Scheme 1.2 has been identified, via application of theoretical techniques, as a key intermediate in the electrocatalytic reduction of CO_2. In reality, the intermediate is short-lived and only observed ex-

perimentally in rare instances, one of these is the work of Tanaka and co-workers, with $[Ru(bpy)_2(CO)_2]^{2+}$, who observed the η^1-COOH intermediate as a member of pH-dependent equilibria between three species: the η^1-CO_2, η^1-COOH and a CO adduct.[31] More recently Cowan and co-workers have provided, using sum frequency generation (SFG) spectroscopy, the first experimental evidence with the popular $[Mn(bipy)(CO)_3Br]$ catalyst (see following section) for formation of the η^1-COOH intermediate during the catalytic cycle in MeCN.[32]

1.2 Selected Metal Complexes for the Electrochemical Reduction of CO_2

There is now a vast amount of literature which has demonstrated efficient CO_2 reduction by transition metal complexes, consisting of metals ranging from Groups 6-10 and including many diverse subsets of ligand frameworks. The literature on this topic has been the subject of many extensive review articles from several perspectives in recent years.[10,15,25,30,33–35] The field has matured over several decades now, with the very first reports dating back to the 1980s. These focused largely on complexes derived from precious (Re, Ru, Pd, Ir) metals. One of the main trends to notice is that more attention is now payed to the Earth-abundant $3d$ metals (Mn, Fe, Co and Ni), which have equivalent or even higher activity. Since the enormous cost and limited supply of noble metals precluded the possibilities of industrial scale applications it is very encouraging to see the impressive results coming from a range of complexes derived from these Earth-abundant metals.

The redox non-innocent ligands, particularly the various roles in the cathodic path that they may play, has proven to be a critical point in the design of molecular catalysts. Efficient cooperation between the metal and its appended ligands is now regarded as being essential for effective catalysis. Across the periodic table, the general trend is that in order to be active toward CO_2 the mid-transition metals (Groups 6 and 7) require strongly π-accepting ligands such as CO, while the later transition metals (Groups 8 to 10) tend to require strong σ-donor ligands such as porphyrins or other macrocyclic amines.[30] This may

be rationalized in terms of the relative energies of the *d*-orbitals. For the earlier transition metals, especially in their reduced states, the energy of the *d*-orbitals is quite high. The π-accepting ligands thus play the role of stabilizing the *d*-orbital energy through π-back donation. For the later transition metals the opposite is true; the *d*-orbital energy is low, and the σ-donor ligands work to increase the orbital energy and also the nucleophilicity of the metal center. The following section presents highlights from the electrocatalytic CO_2 reduction by transition metal complexes with some selected examples.

1.2.1 Mid Transition Metal Complexes with Polypyridine Ligands

In order to mediate multi-electron/multi-proton transformations, molecular catalysts must have the ability to store electrons/protons and transfer them to CO_2 at the appropriate time. This necessitates either reduction at the metal center or reduction of the ligand scaffold with the metal acting as a relay. Polypyridine ligands have thus found extensive use in the catalysis of small molecules.[33] They are well suited to this task, as most consist of (extended) ligand π-systems, which may serve a dual function: storage of the electrons prior to delivery to CO_2 and stabilizing the reduced metal center. They easily represent the most diverse family of catalyst and it is simple to find examples of catalysts with these ligands at either end of the *d*-block in the periodic table.

No discussion of this topic would be complete without first mention of the pioneering work by Lehn and co-workers, who first reported the catalytic ability of $[Re(bipy)(CO)_3Cl]$ (Re-1, Chart 1.1) and whose work continues to inspire new developments in the sub-field of Group-7 polypyridine electrocatalysts.[33,36] The first mechanistic studies[37] revealed that $[Re(bipy)(CO)_3Cl]$ is reduced in two steps, the first is a reversible ligand-based reduction at -1.68 V vs Fc/Fc^+ which produces the radical anion, $[Re(bipy)(CO)_3Cl]^{\bullet -}$ as the dominant species. IR spectroelectrochemistry revealed that reduction at the initial wave is also accompanied by formation of the dimer, $[Re(bipy)(CO)_3]_2$, predicted to be inactive toward CO_2, although this is only minor species.[38] The second reduction step occurs at -1.98 V vs Fc/Fc^+, and corresponds to a metal-centered (Re^I/Re^0) reduction, which triggers con-

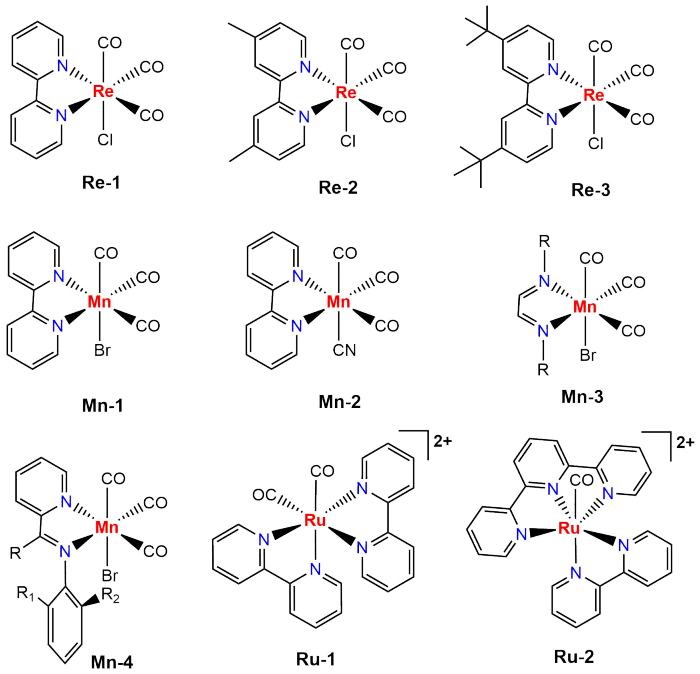

Chart 1.1: Selected transition metal complexes with polypyridine ligands studied in the context of electrocatalytic CO_2 reduction.

taminant loss of the Cl^- ligand. Under CO_2 there is a one-electron and a two-electron pathway by which the catalyst may reduce CO_2 to CO and CO_3^{2-} (Scheme 1.3).[37,38] The two-electron pathway, which is preferred in coordinating solvents, probably occurs via transient formation of two-electron reduced $[Re(bipy)(CO)_3Cl]^{2-}$, which is accompanied by rapid Cl^- loss producing the 5-coordinate anion, $[Re^0(bipy)(CO)_3]^-$. Later, from IR SEC experiments, which revealed formation of the 5-coordinate anion at potentials less negative than those coinciding with the second wave, it became conceivable that the two-electron pathway may actually proceed via reduction of the solvated radical, $[Re(bipy)(CO)_3(CH_3CN)]^{\bullet}$. On the basis that it is reducible at less negative potentials than $[Re(bipy)(CO)_3Cl]^{\bullet-}$.[38] On the other hand, the one-electron pathway is characterized by slow intramolecular electron transfer from $[Re(bipy^{\bullet-})(CO)_3Cl]^-$ producing $[Re^0(bipy)(CO)_3Cl]^-$, loss of Cl^- ligand from this species results in neutral $[Re^0(bipy)(CO)_3]$. Thus, the active catalyst may either be two-electron reduced $[Re^0(bipy)(CO)_3]^-$ or one-electron reduced $[Re^0(bipy)(CO)_3]$. These pathways are summarized in Scheme 1.3.

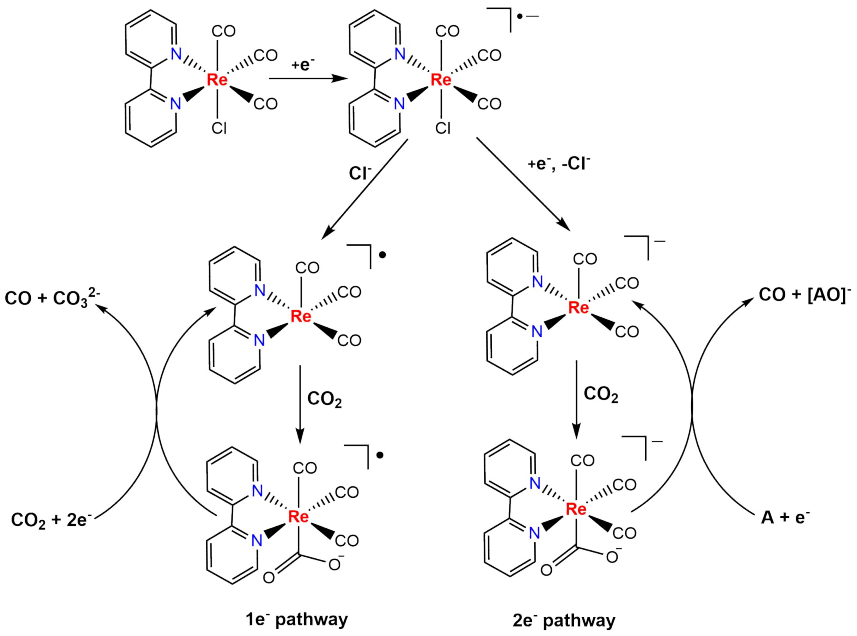

Scheme 1.3: The $1e^-$ and $2e^-$ cathodic pathways of $[Re(bipy)(CO)_3Cl]$. AO corresponds to an oxide ion acceptor. Adapted from ref.[37]

The pathway may be modulated by changes in the applied potential and solvent - less coordinating solvents, like THF, favour the one-electron pathway. Further, the nature of the redox non-innocent bipy ligand, for example, $[Re(4,4'\text{-dmbipy})(CO)_3Cl]$ (4,4′-dmbipy = 4,4′-dimethyl-2,2′-bipyridine) (Re-2, Chart 1.1) follows the one-electron pathway even in coordinating solvents such as MeCN.[38] The mechanisms surrounding CO_2 reduction by these complexes have since been probed by making systematic changes in the ligand sphere.

One such of example of this is the work of Kubiak and co-workers, who showed in 2010, that the reduction potential of the catalyst can be adjusted in the region of -1.7 to -2 V vs saturated calomel electrode (SCE); by decorating the bipy ligand in the 4,4′-position with various substituents (Me, OMe, *tert*-butyl (*t*Bu), COOH).[39] The potential shifts may be rationalized in terms of the electron donating/withdrawing character of the appended functional groups, with the COOH-appended complex exhibiting the most positive reduction potential, due to the stabilization of the LUMO. For CO_2 reduction, however, an increasing catalytic current was observed for the more electron donating substituents,

with peak catalytic current observed for the *t*Bu-appended complex (Re-3, Chart 1.1). The bulky *t*Bu group is thought to have a double impact; in the first instance, it directs electron density toward the Re-NN metallocycle, increasing its nucleophilicity and reactivity toward CO_2 (its electronic impact). While its other impact is to suppress the formation of the inactive dimer mentioned above through unfavourable steric interactions. This case nicely illustrates tuning of a catalyst's behavior via electronic and steric effects. During controlled-potential electrolysis (CPE), a FE_{CO} of 99±2% was recorded, highlighting the extremely high selectivity of this catalyst toward CO_2-to-CO reduction over competing H^+ reduction. This study was later followed by another, published in 2018, where the list of bipy substituents was expanded to include CF_3 and CN, while the effects of alternative axial ligands (Cl, Br, CH_3CN, Py), as well as external proton donors were also considered.[40]

In these cases the presence of an external proton donor enhances the catalysis by promoting the PCET reactions described in the preceding sections.[41–43] The experimental efforts were also supported by rigorous theoretical calculations, which are able to explain the exceptional selectivity of the active catalyst, $[Re(bipy)(CO)_3]^-$, towards CO_2 over competing proton reduction. A weak overlap of the bipy π^*-orbital with Re $5d$ orbitals and also the HOMO results in an essentially barrier-less interaction with CO_2 compared to a ca. 21 kcal mol^{-1} barrier for the interaction with H^+.[41,43,44] Most often CO_2 reduction with these catalysts appears to result in the formation of CO and CO_3^{2-} through the disproportionation of two equivalents of the one-electron reduced form of CO_2. Since it is not possible that this results from the generation of $[CO_2]^{\bullet-}$ the process is thought to actually involve disproportionation of a bimetallic CO_2 bridged dimer, although the mechanism will not be discussed in detail here.[45]

Manganese is an Earth-abundant $3d$ transition metal in the same periodic group as rhenium, which since the report revealing the Mn-analogue of $[Re(bipy)(CO)_3Cl]$ as a functional electrocatalyst[46], has exploded in popularity in the context of CO_2 reduction.[10,30,33,34,47,48] This exciting discovery has come relatively late in the development of the field because, in contrast to rhenium, the manganese systems only show activity toward CO_2 in the presence

of a proton donor[46,49] such as trifluroethanol (TFE) and the initial negative reports were conducted only in dry organic solvent.[38] Many Mn-based molecular catalysts of CO_2 reduction have been studied by varying both the substituent (R) group and the ligand itself, giving insights into the role sterics and electronics play in the catalysis. In addition, varying the α-diimine ligand itself has also proven quite informative.[50,51] In contrast to rhenium, the initial reduction of [Mn(bipy)$(CO)_3$Br] (Mn-1, Chart 1.1) is irreversible, producing the neutral radical [Mn(bipy)$(CO)_3$] via loss of the labile Br^- ligand. The radical is reducible with one electron already at the parent wave, resulting in $[Mn(bipy)(CO)_3]^-$. In the absence of steric control, the 5-coordinate anion is able to react at this potential with as-yet unreduced parent diffusing from the bulk solution, producing a dimer $[Mn(bipy)(CO)_3]_2$ (an ECEC mechanism) while further reduction of the dimer at more negative potentials leads to recovery of $[Mn(bipy)(CO)_3]^-$ (see also Chapter 4). Under CO_2 and only in the presence of a proton donor, the observed catalytic current is largely associated with potentials coinciding with dimer reduction. However, there is evidence from pulsed electron paramagnetic resonance (EPR) and SFG spectroscopy that the dimer itself may also be capable of catalysing CO_2 reduction in selected cases.[52,53] The strict requirement for a proton donor is thought to arise from both the need for a proton to stabilize a key metallo-carboxylate intermediate during the catalytic cycle and the lower binding affinity between CO_2 and $[Mn(bipy)(CO)_3]^-$, which in the absence of the added proton donor prevents accumulation of the Mn-η^1-CO_2 adduct.[10,30,49] Compared to Re, the catalyst operates already at a lower overpotential, this difference is the result of an alternative protonation-first pathway (see Scheme 1.4) that is only available to the Mn catalysts.

The dimer formation shifts the catalytic onset to more negative potentials, so an initial strategy for optimizing the behavior of these catalysts was to suppress the dimer formation, this was achieved in two cases. The first is when Br was replaced with CN (Mn-2, Chart 1.1) and the second, when the bipy ligand was modified with bulky mesityl groups in the 6,6′ positions.[55,56] In both cases this also resulted in a change in the catalytic mechanism, proving that seemingly trivial changes can have a strong impact on the cathodic path of

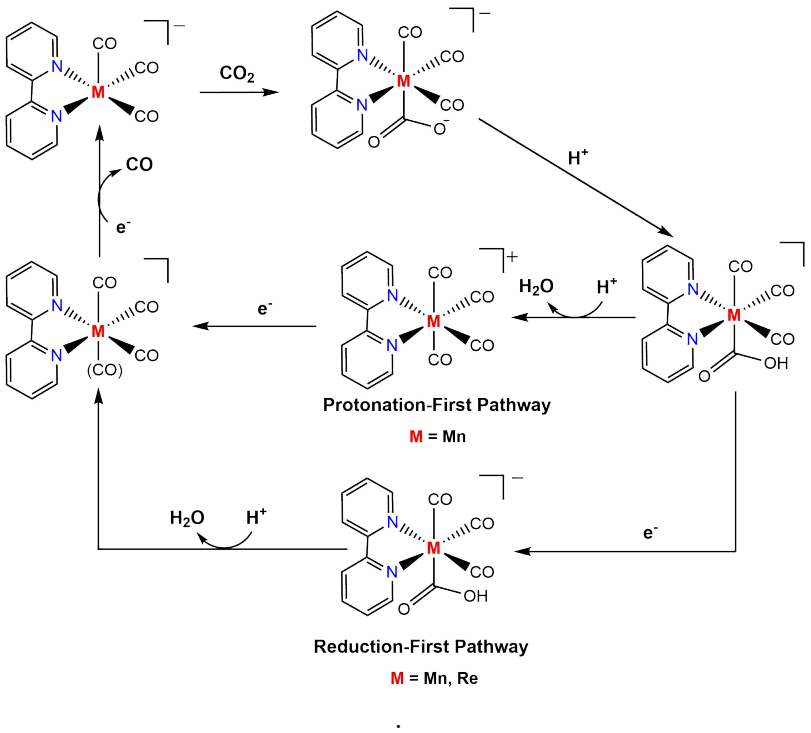

Scheme 1.4: The protonation-first and reduction-first pathways of $[M(bipy)(CO)_3]^-$ (M = Mn, Re). Adapted from ref.[54]

these complexes. In the first case, the initial potential was shifted more negatively relative to the original complex but catalytic CO_2 reduction was observed already at the first wave, due to a different mechanism involving disproportionation between two equivalents of the singly reduced species, which recovers the parent complex and also produces one equivalent of the catalytically active 5-coordinate anion. In the second complex, only a single two-electron cathodic wave was seen by cyclic voltammetry (CV) which was assigned to the conversion of the parent complex to the 5-coordinate anion. However, the majority of the catalytic current is not seen until the potential is shifted 400 mV more negatively, which according to IR SEC corresponded to the reduction of the metallocarboxylic acid intermediate, in this case it needed to be reduced with an extra electron in order to initiate catalytic turnover. A later report showed that in the presence of a Lewis acid such as Mg^{2+}, the catalytic rate can be improved already at the parent reduction.[57] However in this case the catalysis proceeds via reductive disproportionation of CO_2 ($2\,CO_2 + 2\,e^- \longrightarrow CO + CO_3^{2-}$) differently from the Brønsted acid route ($CO_2 + 2\,H^+ + 2\,e^- \longrightarrow CO + H_2O$).

Other α-diimine complexes of manganese have been studied in this context, including those with the non-aromatic 1,4-diazabuta-1,3-diene (dab) ligand and those with mixed aromaticity such as the iminopyridine ligands. In those complexes which feature a 1,4-diazabuta-1,3-diene ligand (Mn-3, Chart 1.1), a similar situation to [Mn(mes-bipy)$(CO)_3$Br] (mes-bipy = 6,6′-dimesityl-2,2′-bipyridine) is observed.[58–60] In the case of [Mn(R-dab)$(CO)_3$Br] the dimer is formed readily at the parent wave, but differently from the bipy derived dimers, the reduction potential of [Mn(R-dab)$(CO)_3$Br]$_2$ coincides with that of the parent complex, meaning that the 5-coordinate anion is produced directly at the initial wave. However, under CO_2, at this potential the 5-coordinate anion reacts with CO_2 non-catalytically to produce a stable bicarbonate complex which must be reduce more negatively to trigger any catalytic turnover.

The first attempt with these complexes to decouple steric and electronic effects was made with a series of asymmetric iminopyridine ligands (Mn-4, Chart 1.1), which combined the features of the dab and bipy ligands.[61] The distribution of cathodic products may be effectively tuned by altering the steric bulk of the pendant, out-of-plane, pyridine moiety, with only a limited corresponding impact on the reduction potential and as a result, the catalytic onset. For the more bulky ligands, direct electrochemical-chemical-electrochemical (ECE) formation of the 5-coordinate anion was observed, while for smaller ligands, the cathodic path proceeds via the intermediate dimer, as in the case of the bipy cogener. Catalytic conversion of CO_2 to CO was observed in all cases, following reduction of the stable bicarbonate complex at ca. -2.2 V vs Fc/Fc^+.

Besides the Group-7 metals, the complexes of Group-8 metals (and in particular of ruthenium) have been featured heavily in the earliest reports of electrocatalytic CO_2 reduction.[25,33] An expansive area of the literature is devoted to the subject and it even continues to evolve in the modern day. In general, ruthenium catalysts exhibit high activity toward CO_2 reduction to formate and CO, as well as good stability and tunability.[25] However, the work of Tanaka and co-workers, stands out from the field as one of the rare examples of the reduction of CO_2 beyond two electrons with a molecular catalyst.[31,62–65] This work

mostly regards the electrochemical reduction of CO_2 by derivatives of $[Ru(bipy)_2(CO)_2]^{2+}$ (Ru-1, Chart 1.1). In aqueous solution, the title complex exists as a three-part equilibrium between $[Ru(bipy)_2(CO)(COOH)]^+$, $[Ru(bipy)_2(CO)_2]^{2+}$ and $[Ru(bipy)_2(CO)(CO_2)]$. The complex $[Ru(bipy)_2(CO)_2]^{2+}$ may be reduced in a single $2e^-$ step at the bipy ligand scaffold, evolving CO and generating $[Ru(bipy)_2(CO)]$, which may react with CO_2 regenerating $[Ru(bipy)_2(CO)(CO_2)]$ and closing the catalytic cycle.[31,63,64] The product distribution is pH-dependent, with alkaline pH favouring the production of formate, while acidic pH result in more selective formation of CO. Moving beyond the $2e^-$ reduction of CO_2 required suppression of the CO evolution reaction. This was achieved in EtOH-H_2O with the derivative $[Ru(bipy)(trpy)(CO)]^{2+}$ (trpy = 2,2′:6′,2″-terpyridine) (Ru-2, Chart 1.1) which at 253 K is reversibly reduced in two steps producing at the second wave, $[Ru(bipy)(trpy)(CO)]^+$. Reaction with a proton produces the reactive $[Ru(bipy)(trpy)(CHO)]^+$.[62] Under CO_2 a mixture of products, including CO and HCOOH, but also HCHO, CH_3OH, HOOCCHO and $HOOCCH_2OH$ are able to form via $[Ru(bipy)(trpy)(CHO)]^+$ but only at 253 K (-20 °C). At temperatures above 253 K, the formyl complex reacts with CO_2 to produce only formate and regenerate $[Ru(bipy)(trpy)(CO)]^{2+}$.

Further, the complex $[Ru(bipy)_2(CO)_2]^{2+}$ has also been shown in the presence of Me_2NH to catalyse the production of DMF from CO_2, while treatment with BF_4^- produces CH_3OH.[65] One of the first reports of the electrocatalytic production of acetone from CO_2 also came from the related complex $[Ru(bipy)(napy)_2(CO)_2]^{2+}$ (napy = 1,8-naphthyridine) in the presence of the $(CH_3)_4NBF_4$, which worked as both the electrolyte and the methylation reagent.[31]

1.2.2 Mid to Late Transition Metal Complexes with Porphyrin Ligands

Alongside the polypyridine complexes, Fe-porphyrin complexes derived from TPP (tetraphenylporphyrin) as shown in Chart 1.2, are extremely prevalent in the literature, and to date have received extensive attention as both electrocatalysts and photocatalysts of CO_2-to-CO reduction.[66–77] TPP has proven to be an adaptable platform to add functionality which affects the catalytic performance, electronic properties, solubility and substrate binding. The

progenitor complex, [Fe(TPP)], has Fe in the +2 oxidation state and cyclic voltammetry revealed it may undergo two reversible $1e^-$ reductions yielding Fe(I) in $[Fe(TPP)]^-$ and finally Fe(0) in $[Fe(TPP)]^{2-}$ (-1.67 V vs SCE). Under CO_2, catalytic current is associated with the final cathodic wave. In the absence of any Brønsted or Lewis acid, the original reports showed only modest catalytic current, which was consistent with the rapid degradation of the catalyst seen under preparative-scale conditions. Addition of a proton donor improves the catalysis remarkably. Internal proton donors (see also Chapter 7), in the form of resorcinol groups, had a remarkable enhancement on the catalytic efficiency, with a turnover number (TON_{CO}) reaching 5 x 10^7 within 4 h at a FE of 94%, following CPE at -1.16 V vs NHE.[67,69]

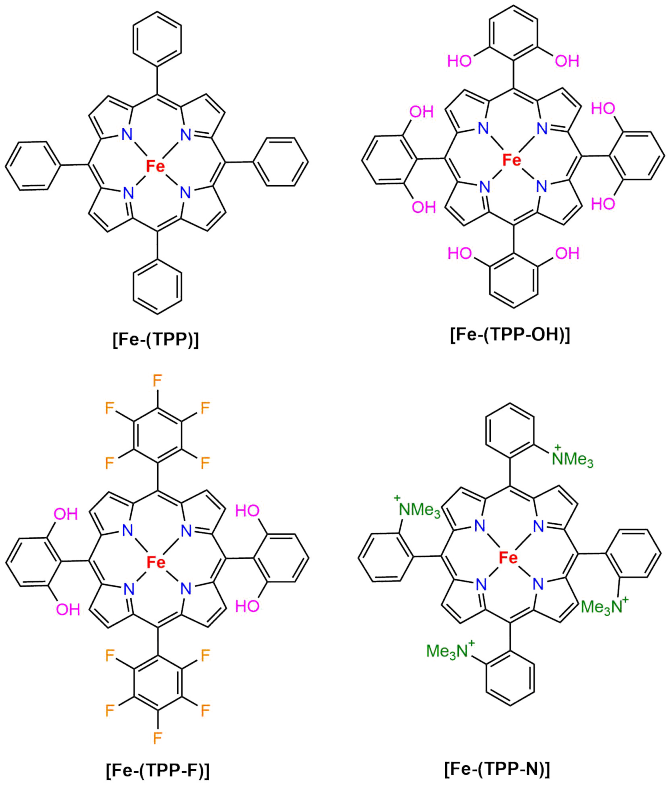

Chart 1.2: Selected Fe-porphyin complexes studied in the context of electrocatalytic CO_2 reduction.[71,72,76]

Electrochemical analysis indicated that the effect of the internal proton donors is twofold, stabilizing the initial reactive $Fe^+-CO_2^{\bullet-}$ intermediate and allowing for the formation of a metallocarboxylic acid intermediate, which according to CV (pre-wave observed) re-

quires reduction prior to the catalytic onset. The addition of electron-withdrawing groups is also another route toward improving catalytic efficiency; the inductive effect may shift the catalytic wave toward less negative potentials. This results in higher or equivalent TON at lower overpotential. In this context, [Fe(TTP-F)] showed equivalent current enhancement, at 60 mV lower overpotential than [Fe(TTP-OH].[71] Further, the inclusion of ortho-trimethylammonium groups produced a complex with the most positive reduction potential recorded for the Fe^{+}/Fe^{0} redox couple (-1.19 V vs SCE) as well as significantly enhanced catalytic currrent due to coulombic charge stabilization of the CO_2 adduct. In DMF/PhOH, this catalyst exhibited a FE_{CO} of 100% and no degradation after 84 h, making it one of the most promising catalysts of CO_2 to CO reduction to date.[72,76]

Besides this, bio-inspired covalently bound Fe(III)-porphyrin dimers were also prepared.[73,74] They feature three quasi-reversible waves corresponding to the overlapping, successive reduction of the two Fe centers, finally producing the catalytically active [Fe^{0}-Fe^{0}]. Under CO_2, catalytic current at this wave is in 6-fold excess compared to Fe-TPP, attributed to the suitable interatomic distances between the two Fe centers (ca. 4 Å), which allows for cooperative reduction, similarly to [FeNi]-CODH.

Porphyrin systems derived from other metal cores, including Co, Cu and Ni are also known.[78–82] They mostly also catalyse the reduction of CO_2 to CO with comparable selectivity and turnover. Although, Shen and co-workers have reported CH_4 as a minor product during the electrochemical reduction of an immobilized Co-protoporphyrin in water.[80,81] Most interesting is a report from Weng and co-workers, where they reported catalytic conversion of CO_2 to highly reduced hydrocarbons - CH_4 and C_2H_4 - by [Cu(TTP-OH] deposited on a nanostructured carbon electrode.[78] At -0.976 V vs real hydrogen electrode (RHE), turnover frequencies of 4.3 and 1.8 s^{-1} were recorded for CH_4 and C_2H_4, respectively. They attributed the impressive behavior to the pendant -OH groups, combined with the unique reactivity of the Cu(I) center, which work cooperatively to reduce CO_2.

1.2.3 Late Transition Metal Complexes with Macrocyclic Ligands

Catalytic CO_2 reduction with Co and Ni metals developed mostly in parallel, and the most prominent ligand sets used in combination with these later transition metals are macrocyclic N4-donor ligands. Of these, $[Ni(cyclam)]^{2+}$ and its derivatives are perhaps the most extensively explored.[83–90] This interest is driven by the behavior of the seminal complex, which on a Hg-pool electrode, showed excellent activity and selectivity for CO with a TON_{CO} of 8000 after CPE at -1.00 V vs NHE for 8 h in $KClO_4$ solution (pH 4.1). This remains a rarely surpassed benchmark for electrocatalytic CO_2 reduction under aqueous conditions.

Analysis of the cathodic path reveals that it is the $1e^-$ reduced Ni(I) species which reacts with CO_2 forming the initial adduct with CO_2. The $[Ni(cyclam)]^+$ species adsorbs onto the Hg electrode, and this is key for efficient CO_2 reaction.[88] This is because in solution, there are multiple isomers which the complex may adopt, once adsorbed onto the electrode however, the $[Ni(cyclam)]^+$ intermediate is forced to adopt the *trans-1* conformation, where all the axial amine hydrogens are out of the plane and are thus able to aid in binding of the CO_2 substrate via hydrogen bonding to the oxygen atoms. Further, the adsorption process is predicted to suppress catalyst degradation pathways, involving poisoning by CO. The degradation pathway may also be suppressed by including a CO scavenger in appropriate molar ratio to the active catalyst.

The parent structure has actually proved less amenable to improvement by appending functional groups than other catalysts from either the polypyridine or porphyrin families. Alkylation at both the N donor atoms and C backbone has been recorded as having a deleterious effect on the catalysis, the former being attributed to loss of the N-H protons, which aid binding of the CO_2 substrate and the latter more as enforcing an unfavourable conformation around the Ni center. Nonetheless, some success has been made, by careful control of the sterochemistry of the additional appendages.[85]

To date, one of the more successful reports is that of Cowan co-workers who reported strong enhancement of the catalytic current following addition of a carboxylic acid group

to the carbon backbone, see Chart 1.3. $[Ni(cyclam\text{-}COOH)]^{2+}$ is unusual in that it shows exceptional selectivity toward CO_2 even in acidic conditions in previous studies the Ni complexes all showed hydrogen production outside of a narrow pH range of 5-7. As well, under the same conditions $[Ni(cyclam\text{-}COOH)]^{2+}$ had a TON_{CO} of 591 while the $[Ni(cyclam)]^{2+}$ exhibited a TON_{CO} of just 45. The enhanced activity was correlated with protonation at the carboxylate group, which likely provided an additional local source of protons for the catalysis although there are other possible explanations.[87] More recently, catalytic CO_2 reduction to CO was observed with this complex and also the cobalt derivative at an appreciable rate (TOF, 0.73 h^{-1}), even in the absence of a mercury electrode, but in the presence of exotic ionic liquid ($BMImBF_4$ and $BMImNTf_2$) as the solvent. Removal of the mercury electrode (for obvious environmental concerns) is a key step toward optimizing the behavior.[89]

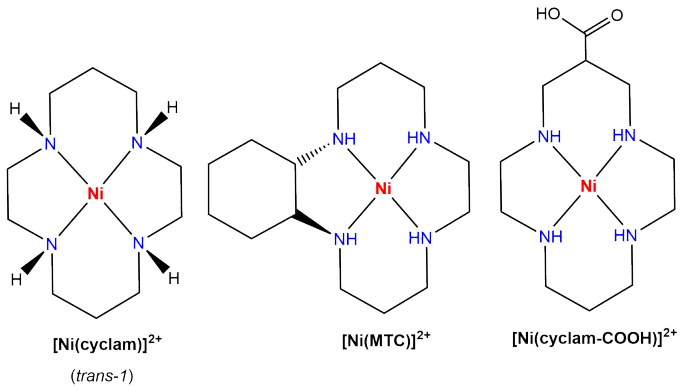

Chart 1.3: Selected Ni-cyclam complexes studied in the context of electrocatalytic CO_2 reduction.[83,85,87]

1.3 Outlook and Aims of the Thesis

The field of electrocatalytic CO_2 reduction has a history that spans almost five decades. In that time, a huge number of encouraging discoveries have been made and particularly with the advancements made in the Earth-abundant metals there is reason to be optimistic that one day catalytic CO_2 reduction may be realized on an industrially relevant scale. Despite this, a number of challenges remain and a few of the most concerning are highlighted in the following paragraphs.

First of all, while there is general consensus that Earth-abundant metals must be adopted moving forward, a lot of investigative work still regards the prohibitively expensive rare-Earth metals (Re, Ru). This work, while important in terms of providing suitable reference systems, must now be supported by increased uptake of Earth-abundant metals. In particular the literature that regards metals with the polypyridine scaffold remains badly underdeveloped for Fe and Cu, as well as for the Group-6 metals (Cr, Mo, W); probably because the initial reports were underwhelming. This is more true for the Group-6 metals, and recent field-wide reviews have also highlighted their absence from the literature. This is quite surprising, given that in nature, molybdenum plays a key role in the active site of several CO_2 reducing enzymes.[12] This leads to the primary aim of this thesis (see below) and a comprehensive discussion of the limited literature on Group-6 catalysts may be found in the introductory passage of Chapter 5. Besides this, there are unexplored opportunities in the very early transition metals, such as Sc, Ti, Ta, Zr, some of which have been shown to undergo a stochiometric reaction with CO_2, reducing it to formate and beyond.[34]

The reduction of CO_2 beyond the $2e^-$ reduction to CO and formate remains quite a rare occurrence in the literature. This perhaps makes the reduction of CO_2 to a molecule such as methanol or methane, which have potential to be used directly as chemical fuel at the moment seem unrealistic. More work is needed to investigate mechanisms which drive the reduction of CO_2, such as that of the work by Tanaka[31] and Weng[78], towards these deeply reduced products. On the other hand, CO derived from the electrolysis of CO_2 utilizes a cheap and abundant source to produce a valuable C1 building block for use in Fischer-Tropsch Chemistry[16] (SynGas) while formate/formic acid, is a promising material for fuel cells, as well as reversible hydrogen storage.[23] With this in mind, one could argue that efforts should now be directed more toward the fabrication of commercial devices.

Another potential issue is that in moving toward an industrial system the molecular catalysts must be heterogenized by binding to the electrode surface, which presents its own challenges. Firstly concerns about the stability of such hybrid systems is well founded, and there are also concerns over how the binding itself may change the operative mechanism,

which may not always be in a positive way. Also, efficient electronic communication is required between the surface-anchor-linker-catalyst relay. Quite often the active catalyst is moisture sensitive or does not function well in water, but catalysis under aqueous conditions is the most ideal situation for a number of reasons. First, water oxidation has promising potential for coupling to CO_2 reduction, for ease of design it makes sense to have a catalyst which functions as a CO_2 reduction catalyst also in water. And second, water is the best 'green' solvent, being environmentally benign, which increases the attractiveness of the process as a whole. Finally, besides Re and Ru, deep-going mechanistic studies are relatively rare for other metals, and while its not necessary to solve the complete mechanism for catalysts which exhibit poor performance, it is certainly possible that some important mechanistic details may have been overlooked, which could potentially aid future catalyst design.

Some of the challenges described here lead into the ultimate aims of the work presented in this thesis, which are two-fold. The first aim was to expand our understanding of the cathodically-induced electrochemistry of Earth-abundant Group-6 metal carbonyl electrocatalysts and, in particular, how the redox behavior is influenced by the incorporation of a range of different non-innocent ligands. This was achieved by synthesis of a range of novel complexes followed by in-depth analysis of the electrochemical behavior by cyclic voltammetry and spectroelectrochemistry, the results of which are often corroborated by DFT calculations. The effect of the electrode surface is also considered. Preliminary investigations into the catalytic ability of the novel complexes toward CO_2 reduction have been conducted. The second aim was to develop spectroelectrochemical techniques in order to better study mechanistic details. This involved the use of spectroelectrochemistry at variable temperatures, different electrode surfaces and media (e.g., NMP, room temperature ionic liquids), as well as novel combination with IR laser spectroscopy (2D-IR, TR-IR). Of course, not everything is described in this thesis (see the manuscripts in preparation), as a final accent was put on coherent story.

References

[1] S. Nangombe, T. Zhou, W. Zhang, B. Wu, S. Hu, L. Zou and D. Li, *Nat. Clim. Change*, 2018, **8**, 375–380.

[2] F. Dottori, W. Szewczyk, J.-C. Ciscar, F. Zhao, L. Alfieri, Y. Hirabayashi, A. Bianchi, I. Mongelli, K. Frieler, R. A. Betts and L. Feyen, *Nat. Clim. Change*, 2018, **8**, 781–786.

[3] J. Bartholy and R. Pongrácz, *Curr. Opin. Env. Sust.*, 2018, **30**, 123 – 132.

[4] B. P. Company, *BP Statistical Review of World Energy 2017*, 2018.

[5] A. M. Appel, J. E. Bercaw, A. B. Bocarsly, H. Dobbek, D. L. DuBois, M. Dupuis, J. G. Ferry, E. Fujita, R. Hille, P. J. A. Kenis, C. A. Kerfeld, R. H. Morris, C. H. F. Peden, A. R. Portis, S. W. Ragsdale, T. B. Rauchfuss, J. N. H. Reek, L. C. Seefeldt, R. K. Thauer and G. L. Waldrop, *Chem. Rev.*, 2013, **113**, 6621–6658.

[6] C. Beer, M. Reichstein, E. Tomelleri, P. Ciais, M. Jung, N. Carvalhais, C. Rödenbeck, M. A. Arain, D. Baldocchi, G. B. Bonan, A. Bondeau, A. Cescatti, G. Lasslop, A. Lindroth, M. Lomas, S. Luyssaert, H. Margolis, K. W. Oleson, O. Roupsard, E. Veenendaal, N. Viovy, C. Williams, F. I. Woodward and D. Papale, *Science*, 2010, **329**, 834–838.

[7] T. W. Woolerton, S. Sheard, Y. S. Chaudhary and F. A. Armstrong, *Energy Environ. Sci.*, 2012, **5**, 7470–7490.

[8] F. Marken and D. Fermin, *Electrochemical Reduction of Carbon Dioxide: Overcoming the Limitations of Photosynthesis*, The Royal Society of Chemistry, 2018, pp. 1–271.

[9] N. Armaroli and V. Balzani, *Chem. Eur. J.*, 2016, **22**, 32–57.

[10] K. E. Dalle, J. Warnan, J. J. Leung, B. Reuillard, I. S. Karmel and E. Reisner, *Chem. Rev.*, 2019, **119**, 2752–2875.

[11] L. Hammarström and S. Hammes-Schiffer, *Acc. Chem. Res.*, 2009, **42**, 1859–1860.

[12] X. Yu, D. Niks, A. Mulchandani and R. Hille, *J. Bio. Chem.*, 2017, **292**, 16872–16879.

[13] A. Majumdar, *Dalton Trans.*, 2014, **43**, 12135–12145.

[14] J.-H. Jeoung and H. Dobbek, *Science*, 2007, **318**, 1461–1464.

[15] J. Qiao, Y. Liu, F. Hong and J. Zhang, *Chem. Soc. Rev.*, 2014, **43**, 631–675.

[16] M. E. Dry, *Catal. Today*, 2002, **71**, 227–241.

[17] M. E. Dry, *Appl. Catal. A-Gen*, 1996, **138**, 319–344.

[18] G. A. Olah, *Angew. Chem. Int. Ed.*, 2005, **44**, 2636–2639.

[19] G. A. Olah, *Angew. Chem. Int. Ed.*, 2013, **52**, 104–107.

[20] I. Ganesh, *Renew. Sust. Energ. Rev.*, 2014, **31**, 221–257.

[21] A. Hamnett, *Catal. Today*, 1997, **38**, 445–457.

[22] X. Li and A. Faghri, *J. Power Sources*, 2013, **226**, 223 – 240.

[23] D. Mellmann, P. Sponholz, H. Junge and M. Beller, *Chem. Soc. Rev.*, 2016, **45**, 3954–3988.

[24] D. D. Zhu, J. L. Liu and S. Z. Qiao, *Adv. Mat.*, 2016, **28**, 3423–3452.

[25] R. Francke, B. Schille and M. Roemelt, *Chem. Rev.*, 2018, **118**, 4631–4701.

[26] J.-H. Zhou and Y.-W. Zhang, *React. Chem. Eng.*, 2018, **3**, 591–625.

[27] M. Gattrell, N. Gupta and A. Co, *J. Electroanal. Chem.*, 2006, **594**, 1 – 19.

[28] A. A. Peterson, F. Abild-Pedersen, F. Studt, J. Rossmeisl and J. K. Nørskov, *Energy Environ. Sci.*, 2010, **3**, 1311–1315.

[29] K. M. Waldie, A. L. Ostericher, M. H. Reineke, A. F. Sasayama and C. P. Kubiak, *ACS Catal.*, 2018, **8**, 1313–1324.

[30] C. Jiang, A. W. Nichols and C. W. Machan, *Dalton Trans.*, 2019, **48**, 9454–9468.

[31] K. Tanaka and T. Mizukawa, *Appl. Organometal. Chem.*, 2000, **14**, 863–866.

[32] G. Neri, J. J. Walsh, G. Teobaldi, P. M. Donaldson and A. J. Cowan, *Nat. Catal.*, 2018, **1**, 952–959.

[33] N. Elgrishi, M. B. Chambers, X. Wang and M. Fontecave, *Chem. Soc. Rev.*, 2017, **46**, 761–796.

[34] K. A. Grice, *Coord. Chem. Rev.*, 2017, **336**, 78–95.

[35] C. Finn, S. Schnittger, L. J. Yellowlees and J. B. Love, *Chem. Commun.*, 2012, **48**, 1392–1399.

[36] J. Hawecker, J. M. Lehn and R. Ziessel, *J. Chem. Soc., Chem. Commun.*, 1984, **984**, 328–330.

[37] B. P. Sullivan, C. M. Bolinger, D. Conrad, W. J. Vining and T. J. Meyer, *J. Chem. Soc., Chem. Commun.*, 1985, **985**, 1414–1416.

[38] F. P. Johnson, M. W. George, F. Hartl and J. J. Turner, *Organometallics*, 1996, **15**, 3374–3387.

[39] J. M. Smieja and C. P. Kubiak, *Inorg. Chem.*, 2010, **49**, 9283–9289.

[40] M. L. Clark, P. L. Cheung, M. Lessio, E. A. Carter and C. P. Kubiak, *ACS Catal.*, 2018, **8**, 2021–2029.

[41] J. M. Smieja, E. E. Benson, B. Kumar, K. A. Grice, C. S. Seu, A. J. M. Miller, J. M. Mayer and C. P. Kubiak, *Proc. Natl. Acad. Sci. U.S.A*, 2012, **109**, 15646–15650.

[42] C. Riplinger and E. A. Carter, *ACS Catal.*, 2015, **5**, 900–908.

[43] J. A. Keith, K. A. Grice, C. P. Kubiak and E. A. Carter, *J. Am. Chem. Soc.*, 2013, **135**, 15823–15829.

[44] E. E. Benson, M. D. Sampson, K. A. Grice, J. M. Smieja, J. D. Froehlich, D. Friebel,

J. A. Keith, E. A. Carter, A. Nilsson and C. P. Kubiak, *Angew. Chem. Int. Ed.*, 2013, **52**, 4841–4844.

[45] J. Agarwal, E. Fujita, H. F. Schaefer and J. T. Muckerman, *J. Am. Chem. Soc.*, 2012, **134**, 5180–5186.

[46] M. Bourrez, F. Molton, S. Chardon-Noblat and A. Deronzier, *Angew. Chem. Int. Ed.*, 2011, **50**, 9903–9906.

[47] D. C. Grills, M. Z. Ertem, M. McKinnon, K. T. Ngo and J. Rochford, *Coord. Chem. Rev.*, 2018, **374**, 173–217.

[48] M. Stanbury, J.-D. Compain and S. Chardon-Noblat, *Coord. Chem. Rev.*, 2018, **361**, 120–137.

[49] J. M. Smieja, M. D. Sampson, K. A. Grice, E. E. Benson, J. D. Froehlich and C. P. Kubiak, *Inorg. Chem.*, 2013, **52**, 2484–2491.

[50] J. Agarwal, T. W. Shaw, C. J. Stanton, G. F. Majetich, A. B. Bocarsly and H. F. Schaefer, *Angew. Chem. Int. Ed.*, 2014, **53**, 5152–5155.

[51] M. Stanbury, J.-D. Compain, M. Trejo, P. Smith, E. Gouré and S. Chardon-Noblat, *Electrochim. Acta*, 2017, **240**, 288–299.

[52] M. Bourrez, M. Orio, F. Molton, H. Vezin, C. Duboc, A. Deronzier and S. Chardon-Noblat, *Angew. Chem. Int. Ed.*, 2014, **53**, 240–243.

[53] G. Neri, P. M. Donaldson and A. J. Cowan, *Phys. Chem. Chem. Phys.*, 2019, **21**, 7389–7397.

[54] C. Riplinger, M. D. Sampson, A. M. Ritzmann, C. P. Kubiak and E. A. Carter, *J. Am. Chem. Soc.*, 2014, **136**, 16285–16298.

[55] C. W. Machan, C. J. Stanton, J. E. Vandezande, G. F. Majetich, H. F. Schaefer, C. P. Kubiak and J. Agarwal, *Inorg. Chem.*, 2015, **54**, 8849–8856.

[56] M. D. Sampson, A. D. Nguyen, K. A. Grice, C. E. Moore, A. L. Rheingold and C. P. Kubiak, *J. Am. Chem. Soc.*, 2014, **136**, 5460–5471.

[57] M. D. Sampson and C. P. Kubiak, *J. Am. Chem. Soc.*, 2016, **138**, 1386–1393.

[58] Q. Zeng, J. Tory and F. Hartl, *Organometallics*, 2014, **33**, 5002–5008.

[59] B. D. Rossenaar, F. Hartl, D. J. Stufkens, C. Amatore, E. Maisonhaute and J. N. Verpeaux, *Organometallics*, 1997, **16**, 4675–4685.

[60] M. V. Vollmer, C. W. Machan, M. L. Clark, W. E. Antholine, J. Agarwal, H. F. Schaefer, C. P. Kubiak and J. R. Walensky, *Organometallics*, 2015, **34**, 3–12.

[61] S. J. Spall, T. Keane, J. Tory, D. C. Cocker, H. Adams, H. Fowler, A. J. Meijer, F. Hartl and J. A. Weinstein, *Inorg. Chem.*, 2016, **55**, 12568–12582.

[62] H. Nagao, T. Mizukawa and K. Tanaka, *Inorg. Chem.*, 1994, **33**, 3415–3420.

[63] K. Tanaka and D. Ooyama, *Coord. Chem. Rev.*, 2002, **226**, 211 – 218.

[64] K. Tanaka, *Chem. Rec.*, 2009, **9**, 169–186.

[65] K. Kobayashi and K. Tanaka, *Phys. Chem. Chem. Phys.*, 2014, **16**, 2240–2250.

[66] I. Bhugun, D. Lexa and J. M. Savéant, *J. Am. Chem. Soc.*, 1996, **118**, 1769–1776.

[67] C. Costentin, S. Drouet, M. Robert and J. M. Savéant, *Science*, 2012, **338**, 90–94.

[68] C. Costentin, S. Drouet, G. Passard, M. Robert and J. M. Savéant, *J. Am. Chem. Soc.*, 2013, **135**, 9023–9031.

[69] C. Costentin, G. Passard, M. Robert and J. M. Savéant, *J. Am. Chem. Soc.*, 2014, **136**, 11821–11829.

[70] C. Costentin, M. Robert and J. M. Savéant, *Acc. Chem. Res.*, 2015, **48**, 2996–3006.

[71] C. Costentin, G. Passard, M. Robert and J. Savéant, *Proc. Natl. Acad. Sci. U.S.A*, 2014, **111**, 14990–14994.

[72] C. Costentin, M. Robert, J. M. Savéant and A. Tatin, *Proc. Natl. Acad. Sci. U.S.A*, 2015, **112**, 6882–6886.

[73] E. A. Mohamed, Z. N. Zahran and Y. Naruta, *Chem. Commun.*, 2015, **51**, 16900–16903.

[74] Z. N. Zahran, E. A. Mohamed and Y. Naruta, *Sci. Rep.*, 2016, **6**, 24533.

[75] E. M. Nichols, J. S. Derrick, S. K. Nistanaki, P. T. Smith and C. J. Chang, *Chem. Sci.*, 2018, **9**, 2952–2960.

[76] I. Azcarate, C. Costentin, M. Robert and J.-M. Savéant, *J. Am. Chem. Soc.*, 2016, **138**, 16639–16644.

[77] C. Römelt, J. Song, M. Tarrago, J. A. Rees, M. van Gastel, T. Weyhermüller, S. DeBeer, E. Bill, F. Neese and S. Ye, *Inorg. Chem.*, 2017, **56**, 4745–4750.

[78] Z. Weng, J. Jiang, Y. Wu, Z. Wu, X. Guo, K. L. Materna, W. Liu, V. S. Batista, G. W. Brudvig and H. Wang, *J. Am. Chem. Soc.*, 2016, **138**, 8076–8079.

[79] S. Meshitsuka, M. Ichikawa and K. Tamaru, *J. Chem. Soc., Chem. Commun.*, 1974, 158–159.

[80] J. Shen, R. Kortlever, R. Kas, Y. Y. Birdja, O. Diaz-Morales, Y. Kwon, I. Ledezma-Yanez, K. J. P. Schouten, G. Mul and M. T. Koper, *Nat. Commun.*, 2015, **6**, 8177.

[81] J. Shen, M. J. Kolb, A. J. Göttle and M. T. Koper, *J. Phys. Chem. C*, 2016, **120**, 15714–15721.

[82] S. Lin, C. S. Diercks, Y.-B. Zhang, N. Kornienko, E. M. Nichols, Y. Zhao, A. R. Paris, D. Kim, P. Yang, O. M. Yaghi and C. J. Chang, *Science*, 2015, **349**, 1208–1213.

[83] M. Beley, J. P. Collin, R. Ruppert and J. P. Sauvage, *J. Chem. Soc., Chem. Commun.*, 1984, 1315–1316.

[84] M. Beley, J. P. Collin, R. Ruppert and J. P. Sauvage, *J. Am. Chem. Soc.*, 1986, **108**, 7461–7467.

[85] J. Schneider, H. Jia, K. Kobiro, D. E. Cabelli, J. T. Muckerman and E. Fujita, *Energy Environ. Sci.*, 2012, **5**, 9502–9510.

[86] G. Neri, J. J. Walsh, C. Wilson, A. Reynal, J. Y. C. Lim, X. Li, A. J. P. White, N. J. Long, J. R. Durrant and A. J. Cowan, *Phys. Chem. Chem. Phys.*, 2015, **17**, 1562–1566.

[87] G. Neri, I. M. Aldous, J. J. Walsh, L. J. Hardwick and A. J. Cowan, *Chem. Sci.*, 2016, **7**, 1521–1526.

[88] Y. Wu, B. Rudshteyn, A. Zhanaidarova, J. D. Froehlich, W. Ding, C. P. Kubiak and V. S. Batista, *ACS Catal.*, 2017, **7**, 5282–5288.

[89] J. Honores, D. Quezada, M. García, K. Calfumán, J. P. Muena, M. J. Aguirre, M. C. Arévalo and M. Isaacs, *Green Chem.*, 2017, **19**, 1155–1162.

[90] E. Fujita, J. Haff, R. Sanzenbacher and H. Elias, *Inorg. Chem.*, 1994, **33**, 4627–4628.

Chapter 2

Electroanalytical Methods and Instrumentation

2.1 Cyclic Voltammetry

2.1.1 Overview

Cyclic voltammetry is a fundamental electroanalytical technique which is frequently employed in many areas of high-impact research.[1,2] The standard setup for the experiment requires three electrodes: a working (WE), counter or auxillary (CE) and a reference or pseudo-reference (RE). The WE is where the redox event of interest occurs, the CE completes the circuit, and the RE provides a stable (fixed) potential against which everything can be referenced. In the case of pseudo-reference electrodes which are subject to potential drift based on experimental conditions, an internal standard (e.g., the ferrocene/ferrocenium$^+$ redox couple) is instead used to provide the reference potential. The electrodes are most commonly held together in the same compartment (cf. three-electrode, single-compartment set-up) although it is possible to find set-ups where the electrodes may be separated from each other by glass frit or similar semi-permeable membrane.

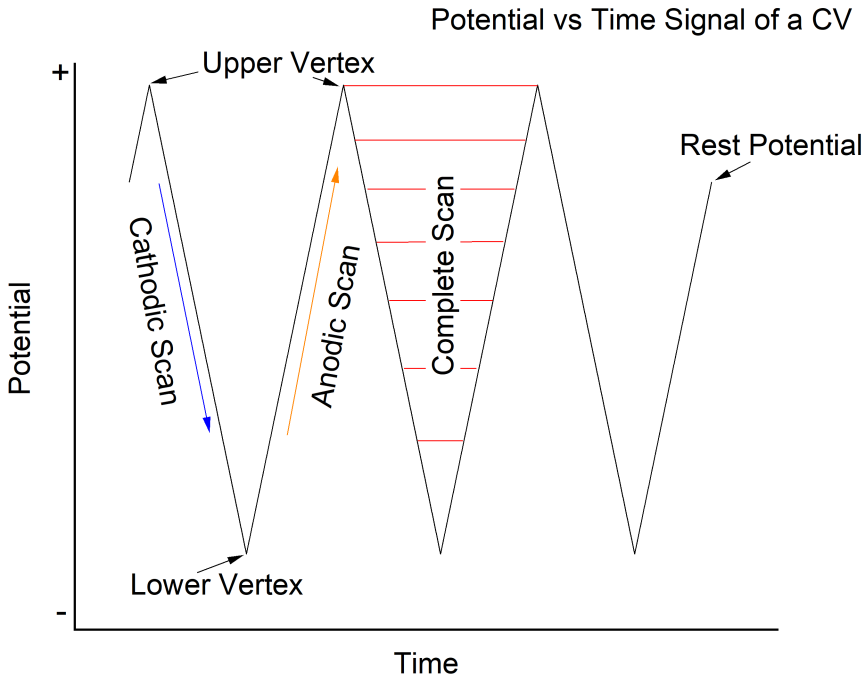

Figure 2.1: The potential vs time signal produced during cyclic voltammetry.

The technique itself involves varying the potential at the working electrode linearly with time (a potential sweep) and measuring the current response. The potential is swept from a resting potential between two upper and lower vertices (Figure 2.1), at either vertex the direction of the scan is reversed and the potential swept in the opposite direction. The potential sweep may be cycled any number of times before coming to stop again at the rest potential. The current response recorded during the scan is actually comprised of two parts, the capacitive or background current, which flows between the electrodes even in the absence of any analyte and is also related to the resistance of the cell. The other is the faradaic current, which corresponds to changes in the oxidation state of the analyte under investigation. Thus, an increase in the faradaic current is observed during a redox event, with the increase itself being termed as a peak or wave. Some electroanalytical techniques have better sensitivity as they are able to subtract the capacitive current from the faradaic. Cyclic voltammetry allows for the position (potential) of a redox event to be determined versus the stable reference potential, but also gives information about the electrochemical and chemical reversibility of the process. Additionally, altering a number of experimental conditions (e.g., temperature, scan rate (mV s^{-1})) allows more information to be recovered from the cyclic voltammogram, as well as allowing several thermodynamic and kinetic parameters to be determined.

The concept of reversibility is used to describe whether the initial species is recoverable following a redox event. A process which is described as being electrochemically reversible means there is a low activation barrier associated with the electron-transfer reaction. Conversely, an electrochemically irreversible process has a high-activation barrier. Reversible processes also exhibit a counter-wave on the reverse scan corresponding to the reverse process with a peak-to-peak current ratio of 1 (unity) and, for $1e^-$ processes at 25°C, a peak-to-peak separation (ΔE_p) of 57 mV (as defined by the Nernst equation, see Equation 2.1). On the other hand, electrochemically irreversible processes have 'sluggish' electron transfer, requiring overpotential to trigger the same current response, and thus the peak-to-peak separation increases - these are also known as quasi-reversible processes. Elec-

trochemically reversible processes are often said to exhibit 'Nernstian behavior' meaning that they obey the Nernst equation, given in Equation 2.1, where E_{cell} and E^{θ}_{cell} are the cell potentials under the conditions of interest and under standard conditions respectively, n is the number of electrons transferred in the reaction, F is Faraday's constant and Q_r is the reaction quotient. For this application, the standard potential is replaced by the formal potential and is specific to the experimental conditions; in practice, however, when the diffusion coefficients of the reduced and oxidised forms are equal it experimentally approximated as $E_{1/2}$ which is defined as the average potential of the anodic and cathodic peak potentials. The Nersnt equation provides a way of predicting how a system responds to a change in concentration or electrode potential:

$$E_{cell} = E^{\theta}_{cell} - \frac{RT}{nF} ln(Q_r) \tag{2.1}$$

When a process is described as being chemically irreversible it means that there is a follow-up chemical change (e.g., dimerization or loss of a labile ligand) accompanying the electron transfer reaction (EC), in these cases the initial species is not recoverable and simply no counter wave is observed on the reverse scan. In these cases, only the anodic ($E_{\mathrm{p,a}}$) or cathodic ($E_{\mathrm{p,c}}$) peak potentials are reported, instead of the $E_{1/2}$ values.

The scan rate (mV s^{-1}) is the rate at which the applied potential is swept and is an important parameter in cyclic voltammetry. The scan rate is inversely related to the size of the diffusion layer - as the scan rate is increased the diffusion layer shrinks. As a consequence of this, the current appears to increase as a function of the scan rate. For electrochemically reversible processes involving species which are freely diffusing in solution, this relationship may be described by the Randles-Sevcik equation (Equation 2.2), which reveals that the peak current i_p (A) increases linearly with the square root of the scan rate υ (V s^{-1}), where n is the number of electrons transferred in the redox event, A (cm^2) is the electrode surface area, D_o (cm^2 s^{-1}) is the diffusion coefficient of the oxidized analyte, and C^0 (mol cm^{-3}) is the bulk concentration of the analyte. A plot of i_p vs $\sqrt{\upsilon}$ should be linear, and any

deviation in the plot indicates either adsorption of the analyte onto the electrode surface, or quasi-reversibility (slow electron transfer):

$$i_p = 0.446nFAC^0 - \left(\frac{nF\upsilon D_o}{RT}\right)^{0.5} \tag{2.2}$$

Square-wave voltammetry is a complementary technique, which may be used in some instances to better resolve closely separated waves and also determine the $E_{1/2}$ value with greater accuracy. The current is sampled twice, before and after a redox event occurs, so it is possible to almost completely separate the capacitive current from the faradaic current, providing greater resolution.

2.1.2 Cyclic Voltammetry in the Context of Electrocatalysis

Cyclic voltammetry is used as a benchmarking technique for the preliminary assessment of catalytic properties.[3] In the first instance the catalyst (precursor) will be studied in the absence of the substrate (CO_2) to determine the feasibility of observing some catalysis and at what potential it may occur. Changes in the shape of the CV upon addition of CO_2 may then be analysed, allowing for a number of parameters relating to the catalytic efficiency to be extracted. These include (i) the overpotential required to drive catalysis at a certain rate, (ii) $i_{\mathrm{p,c}}/i_{\mathrm{p}}$, the ratio between the observed current in the absence and presence of CO_2, (iii) the apparent rate constant, (iv) turnover frequency (TOF), (v) Tafel analysis of the subsequent plots. In practice however, these kinds of analysis are made non-trivial, as a consequence of the complicated multi-electron multi-step mechanisms at work.[3]

The cyclic voltammetry under CO_2 is quite often supported by bulk electrolysis combined with gas chromatography. In bulk electrolysis an electrode with a larger surface area is charged with the potential required to trigger the catalysis and held there for a period of hours - converting the bulk solution in the vicinity of the electrode. The current and charge passed (Q) are recorded during the measurement and headspace injections are taken at regular intervals and analysed on a GC column which can be used to calculate the yields

of various gaseous and liquid (using LC now) reduction products, for example CO, H_2 or formate (LC). From these measurements the faradaic efficiency (FE, Equation 2.3) and turnover number (TON, Equation 2.4) for a particular product may be calculated.

$$FE_{CO}(\%) = \left(\frac{\text{moles of CO}}{Q(c)/2 \times 96485 \text{ (C mol}^{-1})} \right) \times 100 \tag{2.3}$$

$$TON_{CO} = \frac{\text{moles of CO}}{\text{moles of active catalyst}} \tag{2.4}$$

2.2 Spectroelectrochemistry

2.2.1 Overview

The term spectroelectrochemistry encompasses a number of techniques which allow for simultaneous, in-situ, acquisition of spectral and electrochemical data. To date a wide-range of spectral techniques have been combined with electrochemistry; including UV-Vis-NIR absorption[4,5], infrared[6], Raman[7,8], electron paramagnetic resonance (EPR)[9], NMR[10], luminescence[11], vibrational circular dichroism (VCD)[12], mass spectrometry[13], X-ray absorption[14], and epifluorescence microscopy[15]. The variety of techniques available has allowed for an even greater variety of different substrates, including proteins, molecular catalysts and batteries to be characterized under potential control.

Differently from 'pure' electrochemistry there are no standard setups for spectroelectrochemistry, which has allowed for a number of innovative cell designs to evolve naturally, facilitating investigations based on the specific needs of the spectrometer, substrate and experimental timescales.[16] Generally however these cells operate under one of two design principles; transmission or internal reflection. In the former, the optical beam is passed through an optically transparent electrode (OTE) or a perforated electrode, as well as the adjacent solution, which may or may not be thin-layer. While in the latter, the incident beam is passed to the surface of an OTE at such an angle that the beam is totally re-

flected, passing through an analyte layer in close contact with the electrode (maximum 30 μm thick).[17] One of these OTTLE cells is depicted in Figure 2.2.

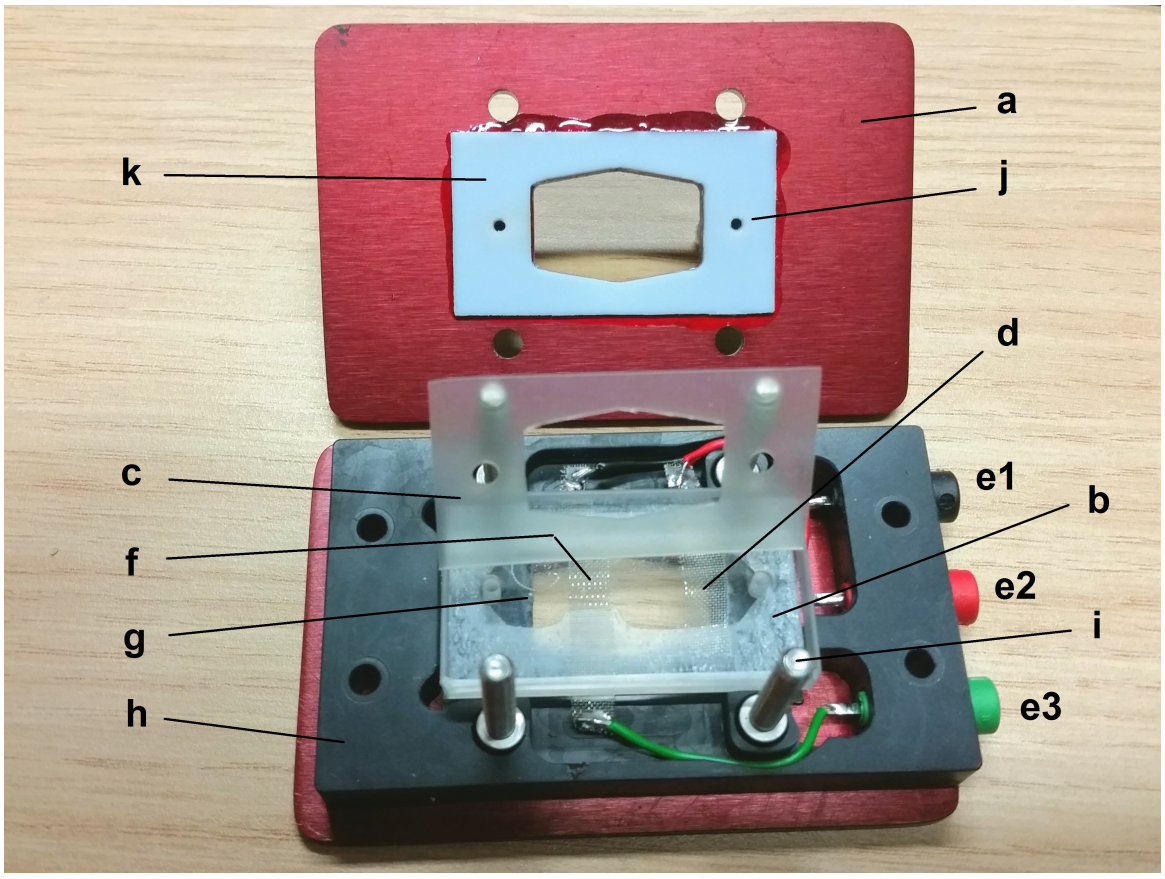

Figure 2.2: Annotated photo of an air-tight OTTLE (Optically Transparent Thin Layer Electrochemical) cell for measurements in the UV, Vis, NIR and IR regions. (a) faceplate; (b) upper CaF_2 window; (c) silicon rubber spacer protecting the filling ports; (d) Pt minigrid counter electrode; (e) external potentiostat ports – 1 pRE, 2 CE, 3 WE; (f) Pt minigrid working electrode (also Au, Cu, C); (g) Ag (or Pt) wire pseudo-reference electrode; (h) modular electrode frame holding the optical windows; (i) mounting screws; (j) filling ports; (k) smooth PTFE spacer glued to the faceplate. Reproduced with permission from ref[18].

The principle spectroelectrochemical techniques encountered in following chapters will be IR and UV-Vis/NIR absorption spectroelectrochemistry, which required the use of a transmission OTTLE (Optically Transparent Thin-Layer Electrochemical) cell, of the same design depicted in Figures 2.2 and 2.3.[19] This design is very adaptable and the base model (optimized for IR SEC) consists of a bespoke three-electrode set melt-sealed into a polyethylene spacer, sandwiched between two CaF_2 windows. The working electrode is an optically

transparent Pt minigrid (32 wires per cm), although other models with Au, Cu and graphite working electrodes have been used successfully during this work. The counter electrode is a Pt minigrid of similar design, while a Ag wire serves as the pseudo-reference electrode. This particular cell design has several advantages; (i) minimal sample volume is required to fill the cell (3 μl), (ii) rapid and complete electrolysis of the thin layer surrounding the working electrode on timescales of seconds to minutes, (iii) negligible diffusion on the timescales of the experiment, (iv) extremely air-tight - moisture and oxygen sensitive compounds may be studied with ease. It is worth noting that the cell may also be easily modified for applications in IR laser spectroscopy (2D-IR, ps-ns TR-IR) and VCD.

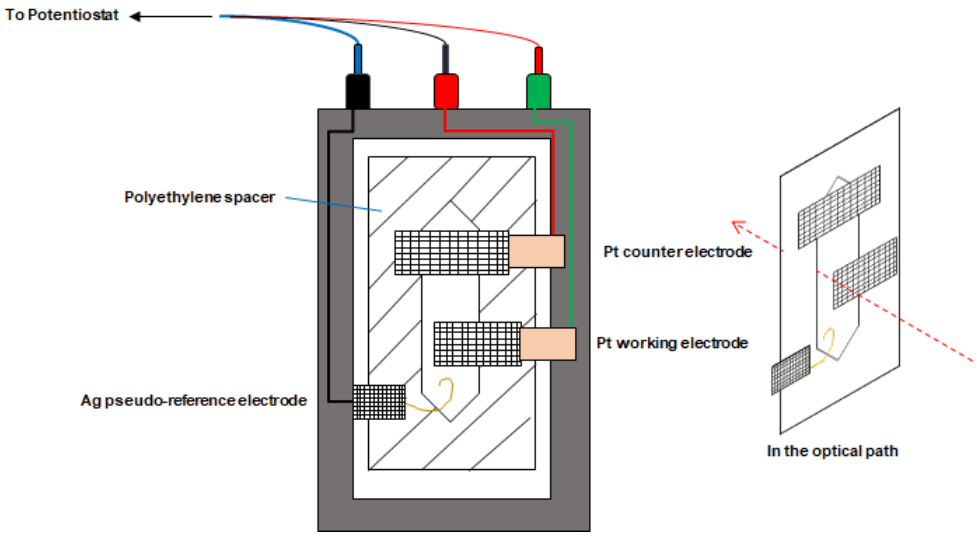

Figure 2.3: Blown-up schematic of the electrode set within an OTTLE cell (left) and the electrode set within the optical path (right). Red arrow indicates the incident light.

A cryostatted version of the OTTLE cell (Figure 2.4) was also used for the measurements presented at low temperature, which requires the use of low-freezing solvents (such as n-butyronitrile or 2-methyl-tetrahydrofuran) and modifications designed to prevent the condensation of water in the optical path.[20] The cell features three parts, (i) a bespoke, double-walled cryostat consisting of two liquid nitrogen reservoirs, evacuated mantle, heat/-cold exchanger with Pt100 thermocouple, throughput for cold nitrogen gas streaming at regulated speeds and an inner cylindrical chamber with crossed pairs of quartz/CaF_2 windows, (ii) an inner OTTLE cell with a similar arrangement of electrodes (see Figure 2.3),

which is placed into the cylindrical chamber, has a built-in heater and thermocouple, filling ports, and CaF_2 windows, (iii) an external control unit for the heaters. The cell itself is rated to continue operating down to the temperature of liquid nitrogen (77 K) however most solvent/electrolyte systems (THF/Bu_4NPF_6: 243 K, DCM/Bu_4NPF_6: 213 K, PrCN/Bu_4NPF_6: 153 K) will freeze long before reaching this temperature. It is therefore especially important to consider which is the best solvent to work in for variable temperature IR spectroelectrochemistry.

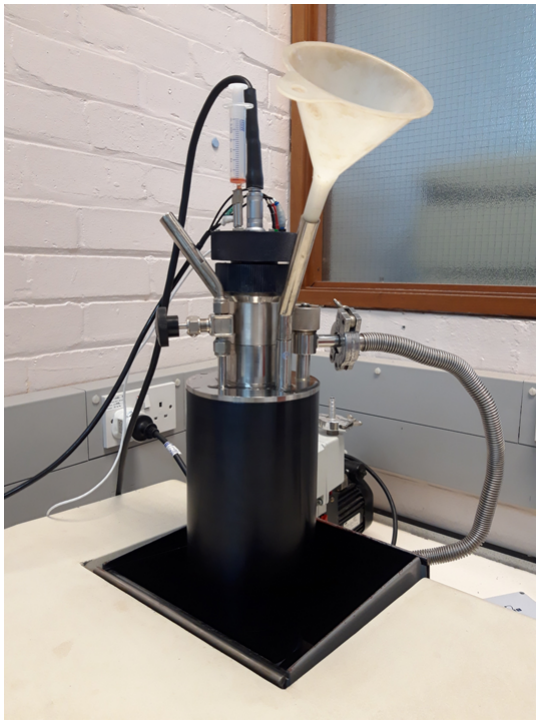

Figure 2.4: Photo of the cryostatted OTTLE cell positioned in an external MCT dectector for IR spectroelectrochemistry at variable temperature.

2.2.2 Fourier Transform Infrared Spectroscopy

All IR spectroelectrochemical measurements were conducted on a steady-state, FT-IR spectrometer (Bruker Vertex 70v) which was equipped with a DLaTGS (deuterated lanthanum α-alanine doped triglycine sulfate) detector for room temperature (298 K) measurements and an external MCT (liquid-nitrogen cooled, mercury cadmium telluride) detector for measurements at low temperature. The most common configuration of an FT-IR spectrom-

eter is based on a Michelson interferometer for optical interferometry. Figure 2.5 depicts a schematic representation of a Michelson interferometer configured for use in FT-IR. It starts with a collimated IR source, which is split by beam splitter into two beams. These beams are reflected back and recombined before being passed to the detector. One of the beams is reflected by a mirror of fixed distance from the beam splitter, while the other is reflected by a mirror which can move along a translational axis. The movement of the mirror alters the optical path length of one beam; the difference in path length between the two is known as the retardation. The retardation results in varying amounts of constructive and destructive interference once the beams are recombined, an interferogram can be generated by sampling the signal from the detector at various retardation values. The interferogram has a maximum signal at zero retardation (i.e. when the path lengths are equidistant), when a sample is present in the optical path the interferogram is modulated by its absorption bands. The 'raw' interferogram must then be processed by Fourier transform in order to extract the absorption spectrum of the sample.

An FT-IR spectrometer has several advantages over a dispersive instrument which makes it an excellent choice for conducting IR spectroelectrochemistry; the chief of these is that all wavelengths are collected simultaneously, which not only improves the signal-to-noise ratio but drastically lowers the time required to collect a single spectrum. This allows for multiple IR spectra to be collected during the course of the electrolysis, allowing the spectral changes to be observed in some detail. In the electrocatalysts presented in this thesis the carbonyl ligands provide a convenient and sensitive spectroscopic label for IR spectroelectrochemistry, which facilitates the characterization of the electronic and chemical changes upon redox activation.[21]

2.2.3 UV-Vis/NIR Absorption Spectroscopy

Finally, the UV-Vis spectroelectrochemistry presented in this thesis was conducted on a Scinco S-3100 diode-array spectrophotometer. A schematic representation of a diode array spectrophotometer may be seen in Figure 2.6. A typical spectrophotometer consists of two

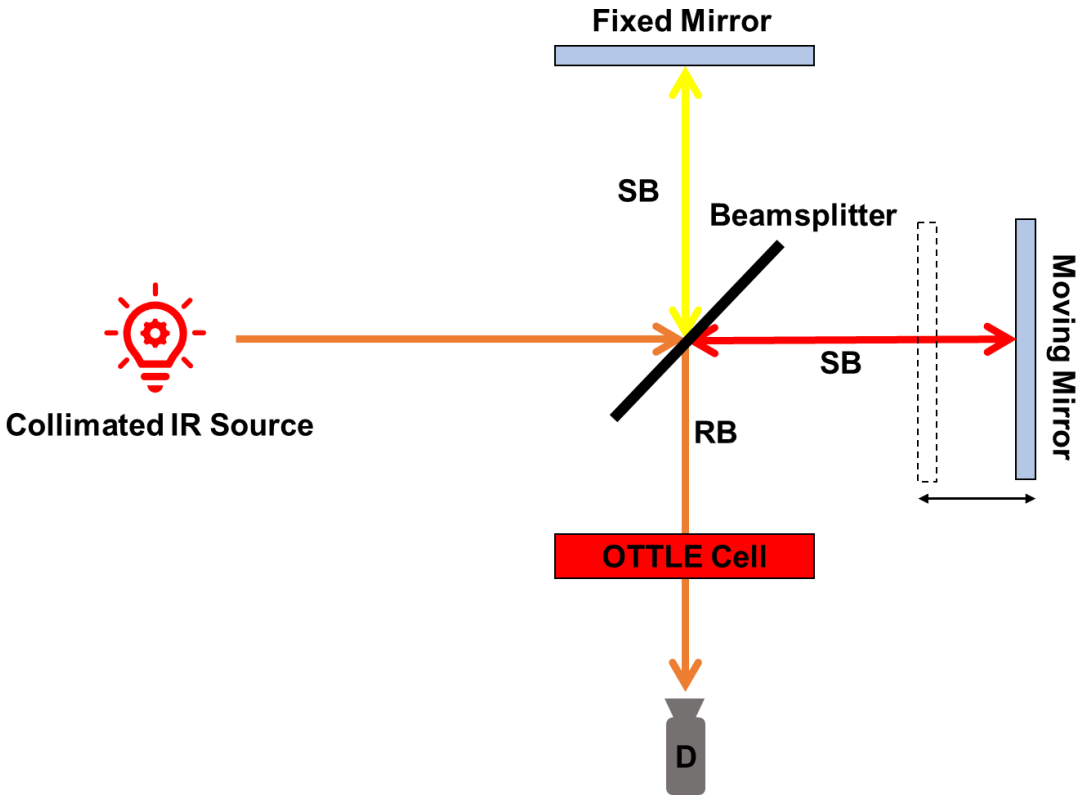

Figure 2.5: Schematic representation of a Michelson interferometer configured for FT-IR, with the sample (OTTLE cell) in place. Key: SB, split beam; RB, recombined beam; D, dectector.

light sources, a tungsten lamp, which covers the near-UV/visible/near-IR range (380-1100 nm) and a halogen lamp which covers the UV region of the spectrum (190-380 nm). The light from both lamps is focused by a series of optics, and passed through the sample (in an OTTLE cell or a cuvette). The incident light from the sample is passed to a dispersive optic, which separates the light into discrete wavelengths, and the light is then directed to shine on an assembly of photodiodes (1024 usually, each diode covering 2 nm) and the intensity of light at each wavelength may then be recorded simultaneously.

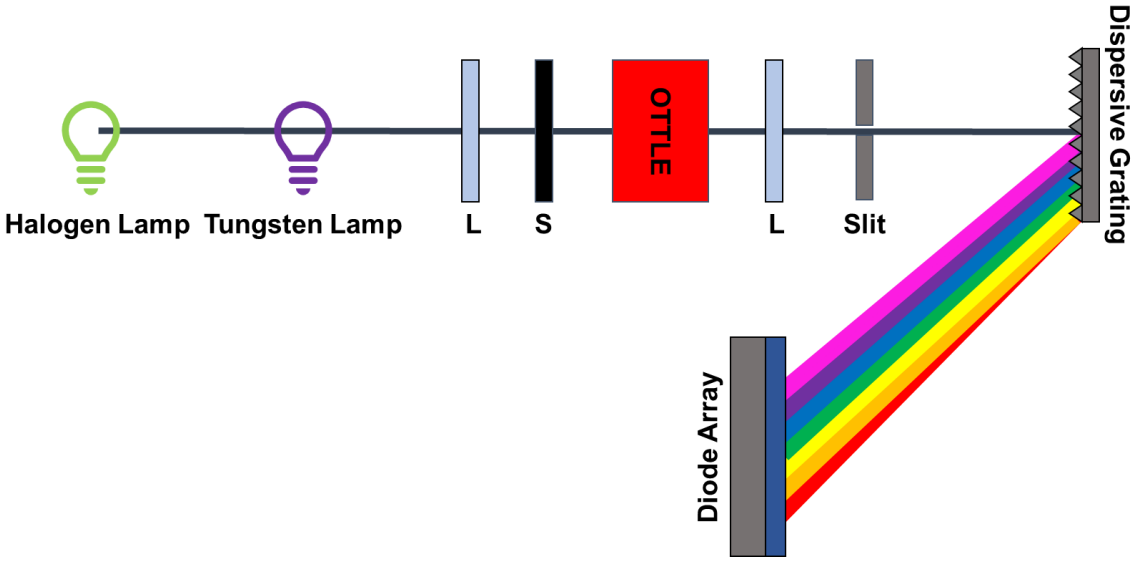

Figure 2.6: Schematic representation of a diode-array spectrophotometer configured for use in UV-Vis spectroelectrochemistry, with the sample (OTTLE cell) in place. Key: L, lense; S, shutter.

The whole spectrum may be recorded in a fraction of a second, which makes it very useful for high-throughput applications, as well as spectroelectrochemistry. The electrocatalysts that are found in subsequent chapters have rather rich UV-Vis absorption spectrums, and their reduced intermediates may also be identified from their characteristic absorption in the UV-Vis regions. Thus, an approach which combines IR and UV-Vis spectroelectrochemistry is often employed in the analysis.

References

[1] N. Elgrishi, K. J. Rountree, B. D. McCarthy, E. S. Rountree, T. T. Eisenhart and J. L. Dempsey, *J. Chem. Educ.*, 2018, **95**, 197–206.

[2] S. J. Hendel and E. R. Young, *J. Chem. Educ.*, 2016, **93**, 1951–1956.

[3] R. Francke, B. Schille and M. Roemelt, *Chem. Rev.*, 2018, **118**, 4631–4701.

[4] W. Kaim and A. Klien, *Spectroelectrochemistry*, Royal Society of Chemistry, Cambridge, 2008, pp. 1–248.

[5] R. S. Gamage, S. Umapathy and A. J. McQuillan, *J. Electroanal. Chem.*, 1990, **284**, 229–235.

[6] K. Ashley and S. Pons, *Chem. Rev.*, 1988, **88**, 673–695.

[7] D. L. Jeanmaire, M. R. Suchanski and R. P. Van Duyne, *J. Am. Chem. Soc.*, 1975, **97**, 1699–1707.

[8] D. L. Jeanmaire and R. P. Van Duyne, *J. Electroanal. Chem.*, 1977, **84**, 1–20.

[9] F. Hartl, R. P. Groenestein and T. Mahabiersing, *Collect. Czech. Chem. Commun.*, 2001, **66**, 52–66.

[10] S. Klod, F. Ziegs and L. Dunsch, *Anal. Chem.*, 2009, **81**, 10262–10267.

[11] M. Dias, P. Hudhomme, E. Levillain, L. Perrin, Y. Sahin, F. X. Sauvage and C. Wartelle, *Electrochem. Commun.*, 2004, **6**, 325–330.

[12] S. R. Domingos, H. J. Sanders, F. Hartl, W. J. Buma and S. Woutersen, *Angew. Chem. Int. Ed.*, 2014, **53**, 14042–14045.

[13] S. C. Roy and P. G. Bruce, *Solid State Ionics*, 1996, **86-88**, 1371–1378.

[14] M. R. Antonio, L. Soderholm and I. Song, *J. Appl. Electrochem.*, 1997, **27**, 784–792.

[15] F. Miomandre, C. Allain, G. Clavier, J.-F. Audibert, R. B. Pansu, P. Audebert and F. Hartl, *Electrochem. Commun.*, 2011, **13**, 574–577.

[16] W. Kaim and J. Fiedler, *Chem. Soc. Rev.*, 2009, **38**, 3373–3382.

[17] R. J. Mortimer, *Encyclopedia of Spectroscopy and Spectrometry*, 1999, 2174–2181.

[18] F. Marken and D. Fermin, *Electrochemical Reduction of Carbon Dioxide: Overcoming the Limitations of Photosynthesis*, The Royal Society of Chemistry, 2018, pp. 1–271.

[19] M. Krejčik, M. Daněk and F. Hartl, *J. Electroanal. Chem. Interfacial Electrochem.*, 1991, **317**, 179–187.

[20] T. Mahabiersing, H. Luytenn, R. Nieuwendam and F. Hartl, *Collect. Czech. Chem. Commun.*, 2003, **68**, 1687–1709.

[21] C. W. Machan, M. D. Sampson, S. A. Chabolla, T. Dang and C. P. Kubiak, *Organometallics*, 2014, **33**, 4550–4559.

Chapter 3

Solvent and Ligand Substitution Effects on the Electrocatalytic Reduction of CO_2 with [Mo(x,x′-dimethyl-2,2′-bipyridine)$(CO)_4$] (x = 4-6) Enhanced at a Gold Cathodic Surface

The content of this chapter was published in: **J. O. Taylor**, R. D. Leavey, F. Hartl, *ChemElectroChem*, 2018, **5**, 3155–3161.

3.1 Abstract

A series of molybdenum tetracarbonyl complexes with dimethyl-substituted 2,2′-bipyridine (dmbipy) ligands were investigated by cyclic voltammetry (CV) combined with spectroelectrochemistry (IR SEC) in tetrahydrofuran (THF) and *N*-methyl-2-pyrrolidone (NMP) to explore their potential in a reduced state to trigger electrocatalytic CO_2 reduction to CO. Their ability to take advantage of a low-energy, CO-dissociation two-electron ECE pathway available only at an Au cathode is addressed. A comparison is made to the reference complex bearing unsubstituted 2,2′-bipyridine (bipy). The methyl substitution in the 6,6′ position is seen to have a large positive impact on the catalytic efficiency. This behavior is ascribed to the advantageous position of the steric bulk of the methyl groups, which further facilitates CO dissociation from the one-electron reduced parent radical anion. On the contrary, the substitution in the 4,4′ position appears to have a negative impact on the catalytic performance, exerting a strong stabilizing effect on the π-accepting CO ligands, and, in THF, preventing exploitation of the low-energy dissociative pathway.

3.2 Introduction

Dwindling fossil fuel reserves and mounting year average temperatures have continued to drive the increasingly urgent need to develop renewable technologies. Despite this, continuing research efforts to produce commercially viable functionalization of CO_2 remains some distance away.[1–4]

Currently, much of the literature regarding molecular electrochemical activation of CO_2 still continues to explore the catalytic properties of the heavier members of Group-7 (Re[5–10]), Group-8 (Ru[11–18] and Os[19–21]) and Group-9 (Rh[22,23] and Ir[24–27]) triads. These "first-generation" electrocatalysts must be phased out; encouragingly, cheaper alternatives exist within the same groups – Mn[28–36] substituting Re, Fe[37–45] substituting Ru and Os, and Co substituting Rh and Ir.[46–48] However, the community's focus on late transition metals is leaving the Group-6 metals (Cr, Mo, W) rather neglected, despite the high po-

tential for the comparatively abundant metal triad to function as both high-performance alternatives to the noble metals and photostable alternatives to the hot-topic manganese carbonyls.[49–52] Indeed, two recent reviews of homogenous molecular catalysts highlighted this under-representation of Group-6 complexes.[53,54] Attention is often paid to the Re-tricarbonyl motif, which since the first accounts by Lehn and co-workers[55] has proven a robust platform from which to analyze electrocatalytic effects of a range of noninnocent a-diimine ligands.[1] Beside the emerging tetracarbonyl a-diimine catalyst precursors discussed hereinafter, complexes of the type [Mo(η^3-allyl)(α-diimine)$(CO)_2$X] (X=(pseudo)-halide) are another notable family among Group-6 carbonyls, which also involve catalytically active species along their reduction path.[56,57]

[M(bipy)$(CO)_4$] (M = Cr, Mo, W) complexes exhibit a relatively simple cathodic pathway (Scheme 1). In the primary step, they undergo reversible one-electron reduction at R1/O1, forming a stable 6-coordinate radical anion, $[M(bipy)(CO)_4]^{\bullet-}$. The radical anion is subsequently reduced by one-electron at R2, which is accompanied by rapid CO dissociation in an irreversible EC step to yield the 5-coordinate dianion, $[M(bipy)(CO)_3]^{2-}$. On the reverse scan, only the oxidation of this electron-rich species to short-lived $[M(bipy)(CO)_3]^{\bullet-}$ is seen at O2′, followed by rapid CO recoordination and recovery of the tetracarbonyl radical anion.

Recent work in our group[49] has shown that at a gold cathode the onset of the catalytic wave corresponding to CO_2 reduction by $[M(bipy)(CO)_3]^{2-}$ can be much less negative than at R2, especially in NMP. The onset of the catalytic wave now occurs at R2′, corresponding to the concomitant reduction of the transient $[M(bipy)(CO)_3]^{\bullet-}$ to the two-electron reduced catalyst $[M(bipy)(CO)_3]^{2-}$, that occurs almost 600 mV less negative than on a platinum electrode. Unlike the latter cathodic material, the gold surface is promoting dissociation of CO from $[M(bipy)(CO)_4]^{\bullet-}$. This mechanism has recently been confirmed for [Mo(bipy)$(CO)_4$] by Cowan and co-workers using SFG spectroscopy.[58] SFG is a relatively new, complex technique that involves exposing the sample at the surface of the electrode to both infrared and UV-light beams and collecting the resulting VSFG signal (in this case due to catalyt-

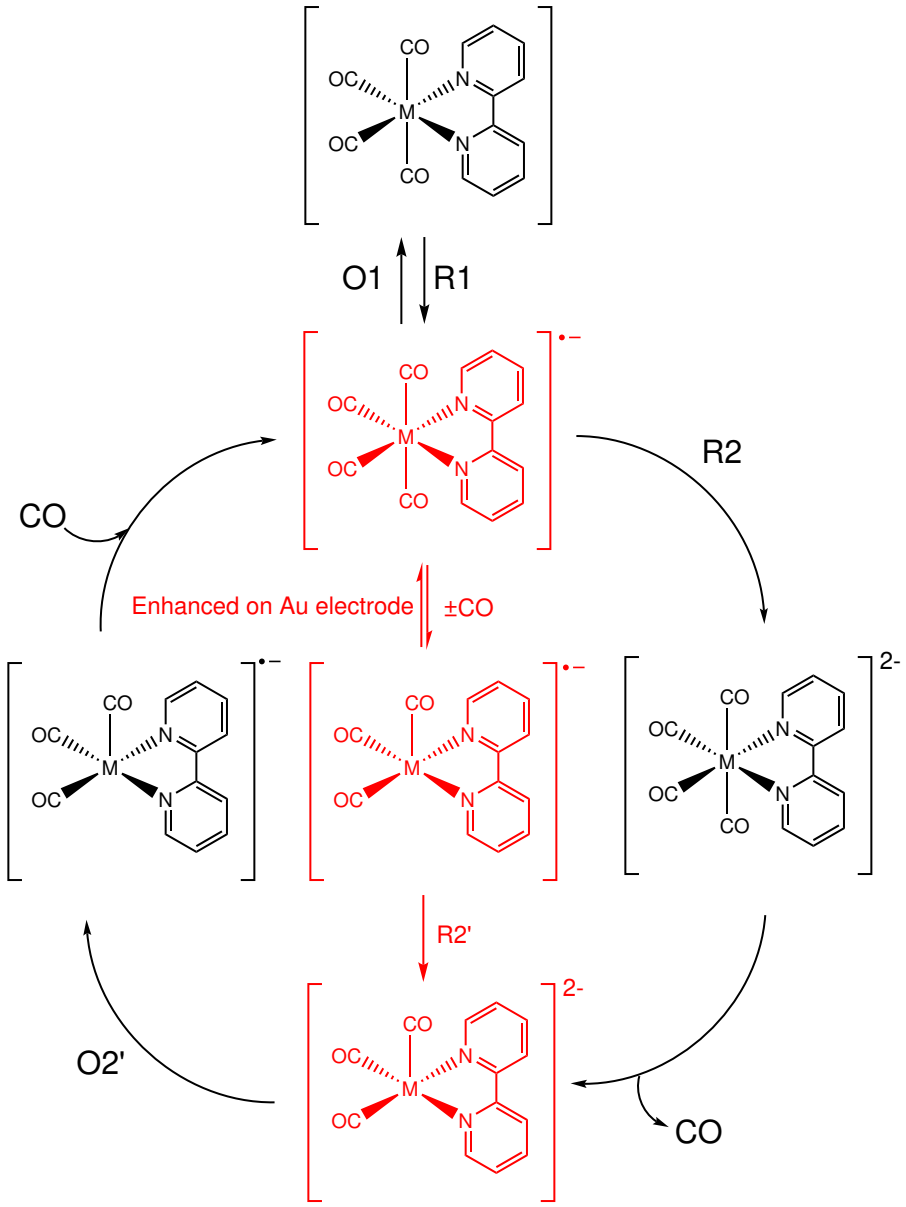

Scheme 3.1: Electrochemical reduction pathways of the $[M(bipy)(CO)_4]$ (M = Cr, Mo, W) complexes, and reoxidation of $[M(bipy)(CO)_3]^{2-}$. Highlighted in red is the alternate low-energy ECE cathodic pathway, producing the active catalytic species, $[M(bipy)(CO)_3]^{2-}$, at a potential approximately 600 mV less negative. This pathway can be easily accessed by using a gold electrode which enhances the dissociation of CO from the specifically adsorbed parent tetracarbonyl radical anion.

ically active $[Mo(bipy)(CO)_3]^{2-}$ and its protonated form, $[Mo(bipy\text{-}H)(CO)_3]^{-}$), before the onset of the second cathodic wave R2 (corresponding to the reduction of $[Mo(bipy)(CO)_4]^{\bullet-}$ specifically adsorbed at the gold electrode surface). The best catalytic performance in this respect was seen[49] with CV and IR SEC when the gold electrode was combined with the NMP electrolyte. It is likely that NMP is also aiding the carbonyl dissociation in the singly reduced state.

Hereinafter, this study is extended to encompass the three dimethylated bipy derivatives of the title compound, the goal being to ascertain (i) whether this low-energy catalytic pathway can be considered a general feature of [Mo(x,x′-dmbipy)(CO)$_4$] (x,x′-dmbipy = x,x′-dimethyl-2,2′-bipyridine, x = 4-6) complexes and what impact varying the position of the methyl groups at bipy has on the catalyst's ability to access the low-energy ECE pathway.

3.3 Experimental

Materials

Tetrahydrofuran (THF, Fisher) was freshly distilled from sodium and benzophenone (purple ketyl radicals) under a dry nitrogen atmosphere. *N*-methyl-2-pyrrolidone (NMP, anhydrous, Sigma Aldrich) was bubbled with dry argon on a frit before use. The supporting electrolyte Bu_4NPF_6 (tetrabutylammonium hexafluorophosphate, > 99.8%, Agro-Organics) was recrystallized twice from hot ethanol and dried under vacuum. All electrochemical measurements and synthetic operations were carried out under an atmosphere of dry argon using standard Schlenk techniques. Where necessary, solutions were saturated with CO_2 (99.99%, BOC) by bubbling on a frit at an atmospheric pressure.

Methods

Cyclic voltammetry (CV) was performed on a PGSTAT 302N potentiostat (Metrohm Autolab) operated with the NOVA 1.9 software. An airtight single-compartment three-electrode cell was used in all experiments. A platinum (0.4 mm) or gold (0.4 mm) microdisc polished

carefully with a 0.25 µm diamond paste (Sommer) served as the working electrode. A coiled platinum wire protected by a glass mantle served as the counter electrode. A coiled silver wire protected by a glass mantle was employed as a pseudo-reference electrode. Ferrocene (Fc) was added for the final potential scans as the internal standard, and all electrode potentials are reported against the Fc/Fc^+ couple. CV samples contained 1 mM analyte and 0.1 M supporting electrolyte.

Infrared spectroelectrochemistry (IR SEC) was performed with a Bruker Vertex 70v FT-IR spectrometer equipped with a DTLaGS detector. UV-Vis spectroelectrochemistry (UV-Vis SEC) was performed on a Scinco S-3100 diode-array spectrophotometer, in parallel with the IR monitoring. The course of the controlled-potential spectroelectrochemical experiment was recorded using thin-layer cyclic voltammetry (TL-CV) with an OTTLE cell[59] operated by the EmStat3 or EmStat3+ (PalmSens) potentiostats and the PSTrace 4.2 software. The OTTLE cell was equipped with either a Pt or Au minigrid working electrode, a platinum minigrid counter electrode, an Ag wire pseudo-reference electrode and CaF_2 windows. SEC samples contained 3 mM analyte and 0.3 M supporting electrolyte.

Synthesis of [Mo(x,x′-dmbipy)(CO)$_4$]

The studied complexes were synthesized according to slightly modified established literature procedures. $[Mo(CO)_6]$ and the x,x′-dimethyl-2,2′-bipyridine ligand of choice were dissolved in equimolar amounts in argon-saturated toluene (35 mL) and refluxed for roughly 4 h using standard Schlenk techniques. An orange powder precipitated and was isolated by filtration, then washed with hexane three times to purity confirmed by ^{1}H NMR and infrared spectroscopy.[60]

[Mo(4,4′-dimethyl-2,2′-bipyridine)(CO)$_4$]

Bright orange powder (268.6 mg, 86.5 %). FT-IR (THF, ν(CO)) 2011, 1898, 1877, 1837 cm^{-1}. ^{1}H NMR (400 MHz, CD_2Cl_2) δ 8.82 (2H, d, J = 5.3 Hz), 7.87 (2H, s), 7.14 (2H, d, J = 4.8 Hz), 2.44 (6H, s).

[Mo(5,5′-dimethyl-2,2′-bipyridine)(CO)$_4$]

Bright orange powder (338.3 mg, 79.4 %). FT-IR (THF, ν(CO)) 2011, 1899, 1879, 1839 cm^{-1}. ^{1}H NMR (400 MHz, CD_2Cl_2) δ 8.82 (2H, s), 7.90 (2H, d, J = 8.2 Hz), 7.66 (2H, d, J = 8.0 Hz), 2.35 (6H, s).

[Mo(6,6′-dimethyl-2,2′-bipyridine)(CO)$_4$]

Light red powder (129.5 mg, 30 %). FT-IR (THF, ν(CO)) 2014, 1900, 1879, 1836 cm^{-1}. ^{1}H NMR (400 MHz, CD_2Cl_2) δ 7.84 (2H, d, J = 7.6 Hz), 7.74 (2H, t, J = 7.5 Hz), 7.32 (2H, d, J=7.1 Hz), 2.95 (6H, s).

3.4 Results and Discussion

3.4.1 Cyclic Voltammetry in THF

Table 3.1: Electrode potentials of [Mo(x,x′-dmbipy)(CO)$_4$] (x = 4-6) and their reduction products in THF/Bu_4NPF_6 using a Pt microdisc electrode.

Redox Step	E / V vs Fc/Fc^+		
	x = 4	x = 5	x = 6
$[Mo(dmbipy)(CO)_4] \longrightarrow [Mo(dmbipy)(CO)_4]^{\bullet-}$ (R1)	-2.15[a]	-2.19[a]	-2.13[a]
$[Mo(dmbipy)(CO)_4]^{\bullet-} \longrightarrow [Mo(dmbipy)(CO)_4]^{2-}$ (R2)	-2.67[b]	-2.74[b]	-2.71[b]
$[Mo(dmbipy)(CO)_3]^{2-} \longrightarrow [Mo(dmbipy)(CO)_3]^{\bullet-}$ (O2′)	-2.39[c]	-2.36[c]	-2.41[c]

[a] $E_{1/2}$ values. [b] $E_{p,c}$ values. [c] $E_{p,a}$ Values. Potentials for [Mo(bipy)(CO)$_4$] are: R1: -2.07 V ($E_{1/2}$), R2: -2.73 V ($E_{p,c}$) and O2′: -2.32 V ($E_{p,a}$).[49]

Cyclic voltammetry (CV) with [Mo(x,x′-dmbipy)(CO)$_4$] was first conducted in argon-saturated THF, at Pt (Figure 3.1) and Au (Figure 3A.1, Appendix) microdiscs. The CV responses indicate that quite expectedly all three dmbipy complexes under study follow the general pathway laid out in Scheme 3.1. The methyl groups shift the cathodic potential R1 more negatively by 60-120 mV compared to the reduction of the 2,2′-bipyridine ligand[49]. This can be attributed to the electron donating effect of the methyl substituents rising the LUMO (bipy) energy. A comparable shift is reported for [Re(x,x′-dmbipy)(CO)$_3$Cl] (x =

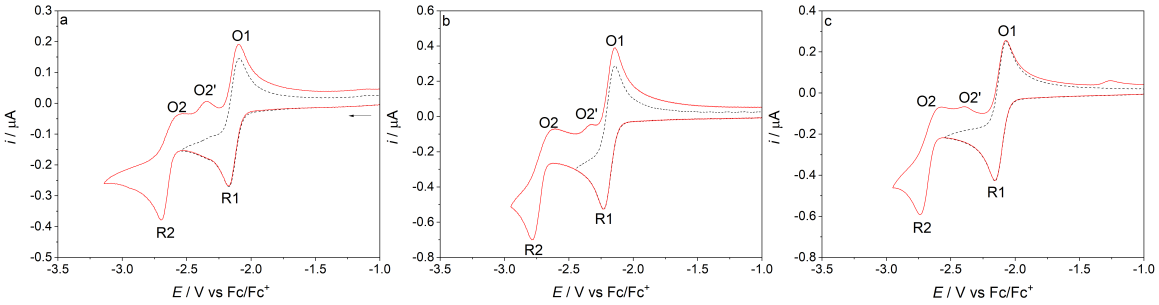

Figure 3.1: CV of [Mo(x,x′-dmbipy)$(CO)_4$] in argon-saturated THF/Bu_4NPF_6: a) x = 4, b) x = 5, c) x = 6. Scan Rate: 100 mV s^{-1}. Pt microdisc electrode. The arrow indicates the initial scan direction.

3 and 5) vs [Re(bipy)$(CO)_3$Cl].[61] The formation of the π-delocalized 5-coordinate dianion, [Mo(x,x′-dmbipy)$(CO)_4]^{2-}$, in the THF electrolyte at R2 is hardly affected, Tables 3.1 and 3A.1 (Appendix). From these observations, we can infer that migration of the methyl sites at bipy in [Mo(x,x′-dmbipy)$(CO)_4$] has only limited electronic effect on the LUMO of the parent complex and the stability of the tetracarbonyl radical anion in solution.

3.4.2 Cyclic Voltammetry in NMP

The analysis of the cathodic behavior of [Mo(x,x′-dmbipy)$(CO)_4$] in NMP/Bu_4NPF_6 by cyclic voltammetry at ambient conditions (Figure 3A.2 and Tables 3A.2-3A.3 at a Pt microdisc and at an Au microdisc, respectively (Appendix)) leads to a similar description as in THF, with the following notable differences observed. First, the parent reduction potentials (R1) are slightly less negative (130–150 mV) in NMP than in THF. Second, the cathodic wave R2′, belonging to the reduction of [Mo(x,x′-dmbipy)$(CO)_3]^{\bullet-}$, was detectable at the Au microdisc cathode on the forward cathodic scan beyond R1 for x = 4 and 5 (Figure 3A.2 (b-d)). The CO dissociation from [Mo(x,x′-dmbipy)$(CO)_4]^{\bullet-}$, responsible for the appearance of R2′, is apparently most pronounced under these conditions, in agreement with the strong electrocatalytic performance in NMP at a gold electrode surface (see below). Third, the 5-coordinate complex [Mo(x,x′-dmbipy)$(CO)_3]^{2-}$ is not the only two-electron reduced species (formed at R2 and R2′) detectable by cyclic voltammetry due to its anodic response at O2′. The continued reverse anodic scan starting beyond R2 reveals the O1/R1 peak-current ratio

to depart from unity more than in THF, especially for x = 4 and 6. A new anodic wave is seen between -1 and -1.2 V (Pt) and between -1.2 and -1.5 V (Au). Combined with IR spectroelectrochemistry (see below), the most likely assignment of this anodic wave is the oxidation of the stabilized protonated dianion keeping the tetracarbonyl coordination even after the two-electron reduction, $[Mo(x,x'\text{-dmbipy-H})(CO)_4]^-$, which appears to be the main ultimate reduction product in NMP, formed on a timescale of a few seconds.

3.4.3 Cyclic Voltammetry in CO_2-saturated THF

Using a platinum working microdisc electrode in CO_2-saturated THF, the cathodic wave R1 was passed without any evidence for the significant current growth that is usually associated with catalytic CO_2 reduction. Under these conditions, a behavior comparable to that of $[Mo(bipy)(CO)_4]$ (reproduced here in Figure 3A.3, Appendix)[49] was observed. The onset of the catalytic wave is not seen until the second reduction at R2 is passed (Figure 3.2a,c,e), producing the 5-coordinate dianion $[Mo(x,x'\text{-dmbipy})(CO)_3]^{2-}$ exclusively from the corresponding unstable tetracarbonyl dianion (the EEC path). The most active species towards CO_2 in the series proves to be $[Mo(6,6'\text{-dmbipy})(CO)_3]^{2-}$, showing the highest catalytic current (Figure 3.2c).

The catalytic performance in THF/CO_2 becomes generally enhanced at the gold microdisc electrode (Figure 3.2b,d,f). Again, R1 is passed without any obvious change compared to the reversible behavior under argon. For $[Mo(x,x'\text{-dmbipy})(CO)_4]$ (x = 4 and 5, Figure 3.2b,d), the catalytic wave remains largely associated with R2, but the catalytic activity is higher compared to that at the Pt microdisc. Only $[Mo(6,6'\text{-dmbipy})(CO)_4]$ (Figure 3.2f) shows the expected[49] shift of the catalytic wave to less negative potentials, close to the theoretical R2′ wave associated with O2′ (Figure 3.1). Apparently, in THF, the bipy substitution in the 4,4′- and 5,5′-positions is hindering the alternate low-energy pathway, presumably by strengthening Mo-CO bonds and moving the equilibrium toward the 6-coordinate radical anion, $[Mo(x,x'\text{-dmbipy})(CO)_4]^{\bullet -}$. The methyl substituents in the 6,6′-positions adjacent to the Mo-NCCN metallacycle may facilitate CO dissociation from

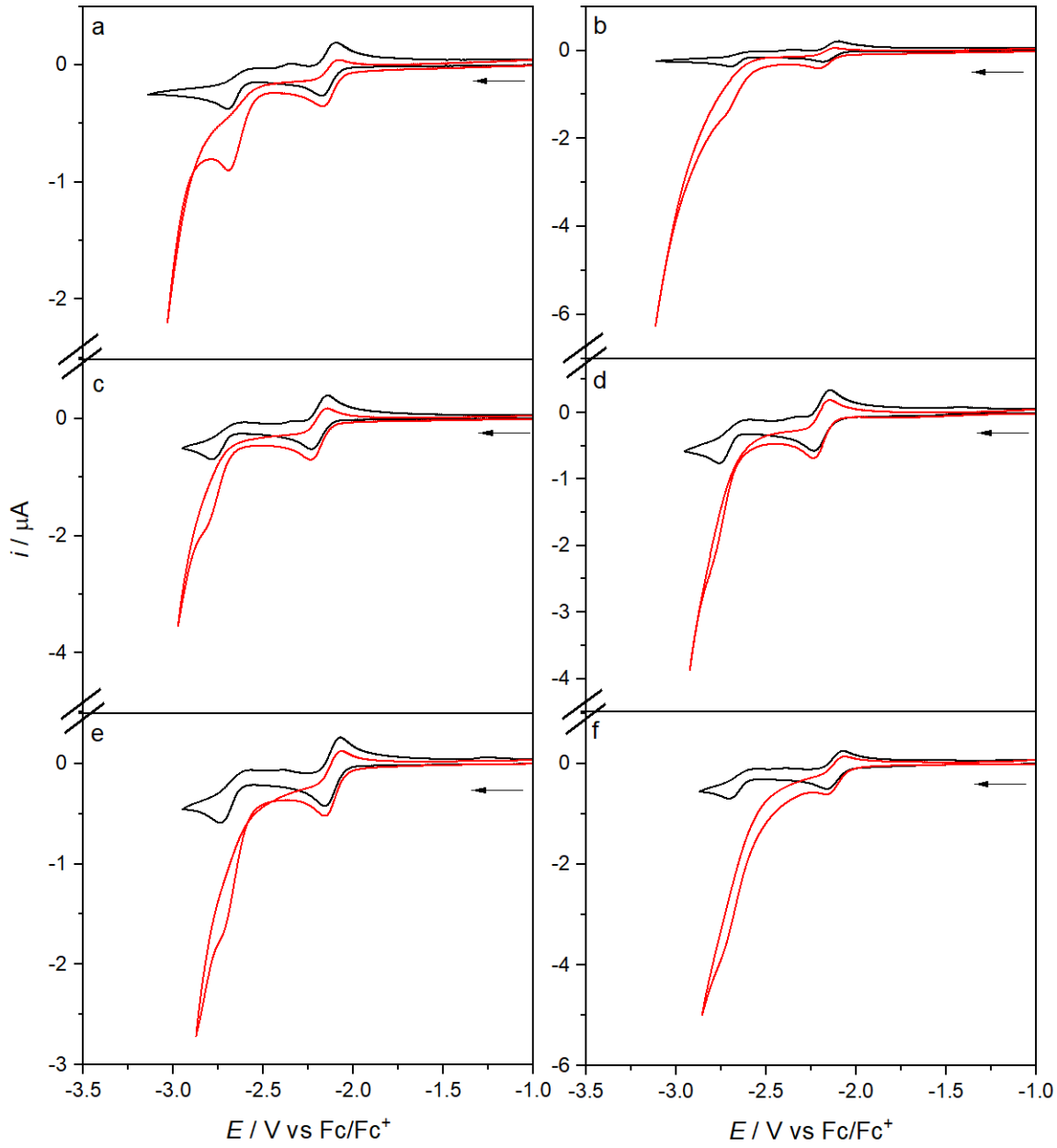

Figure 3.2: CV of [Mo(x,x′-dmbipy)$(CO)_4$] in CO_2-saturated THF/Bu_4NPF_6: a) x = 4, Pt, b) x = 4, Au, c) x = 5, Pt d) x = 5, Au, e) x = 6, Pt and f) x = 6, Au. Scan Rate: 100 mV s^{-1}. Black curves: under Argon; red curves under CO_2. Pt and Au microdisc electrodes. The arrow indicates the initial scan direction.

the latter radical anion and shift the equilibrium toward the concomitantly reducible transient $[Mo(6,6'\text{-dmbipy})(CO)_3]^{\bullet-}$ both on steric and electronic grounds, likely driven by increased stabilizing delocalization of the added electron density over the metallacycle in the 5-coordinate geometry.[62] Indeed, $[Mo(6,6'\text{-dmbipy})(CO)_4]$ responds less negatively, showing significant enhancement of the current directly behind R1, to the gold cathode than even the reference complex $[Mo(bipy)(CO)_4]$ (Figures 3.2f and 3A.3a (Appendix)).

3.4.4 Cyclic Voltammetry in CO_2-saturated NMP

In CO_2-saturated NMP, the catalytic performance at a platinum microdisc electrode (Figure 3.3) is comparable with that observed in THF, involving predominantly the high-overpotential pathway at R2. The slight enhancement in NMP can be ascribed to the ability of the two-electron reduced bipy ligand to act as a parking station for H^+, facilitating the catalytic action.[49]

Reducing $[Mo(x,x'\text{-dmbipy})(CO)_4]$ at the gold microdisc electrode in CO_2-saturated NMP (Figure 3.3b,e,f) has a remarkably strong synergetic effect, with the catalytic current exceeding more than three times the maximum values passed at the platinum microdisc electrode under the same conditions (Figure 3.3a,c,d). Moreover, the onset of the electrocatalytic process coincides with the cathodic wave R2′ seen under argon (Figure 3A.2). These experimental conditions offer the best performance but are also serving to illustrate the apparent sensitivity of the low-overpotential ECE pathway to solvent changes.

3.4.5 IR and UV-Vis Spectroelectrochemistry in THF and NMP

Infrared spectroelectrochemistry and thin-layer cyclic voltammetry largely confirm the major observations made on the sub-second timescale of conventional CV. In argon-saturated dry THF, the reduction of parent $[Mo(x,x'\text{-dmbipy})(CO)_4]$ to $[Mo(x,x'\text{-dmbipy})(CO)_4]^{\bullet-}$ at R1 is accompanied by a low-energy shift of the four ν(CO) absorption bands (Table 3.2, Figure 3.4a). For the second reduction at R2 the magnitude of the ν(CO) shift is almost doubled and the fingerprint band pattern adopts a tricarbonyl form, confirming the pres-

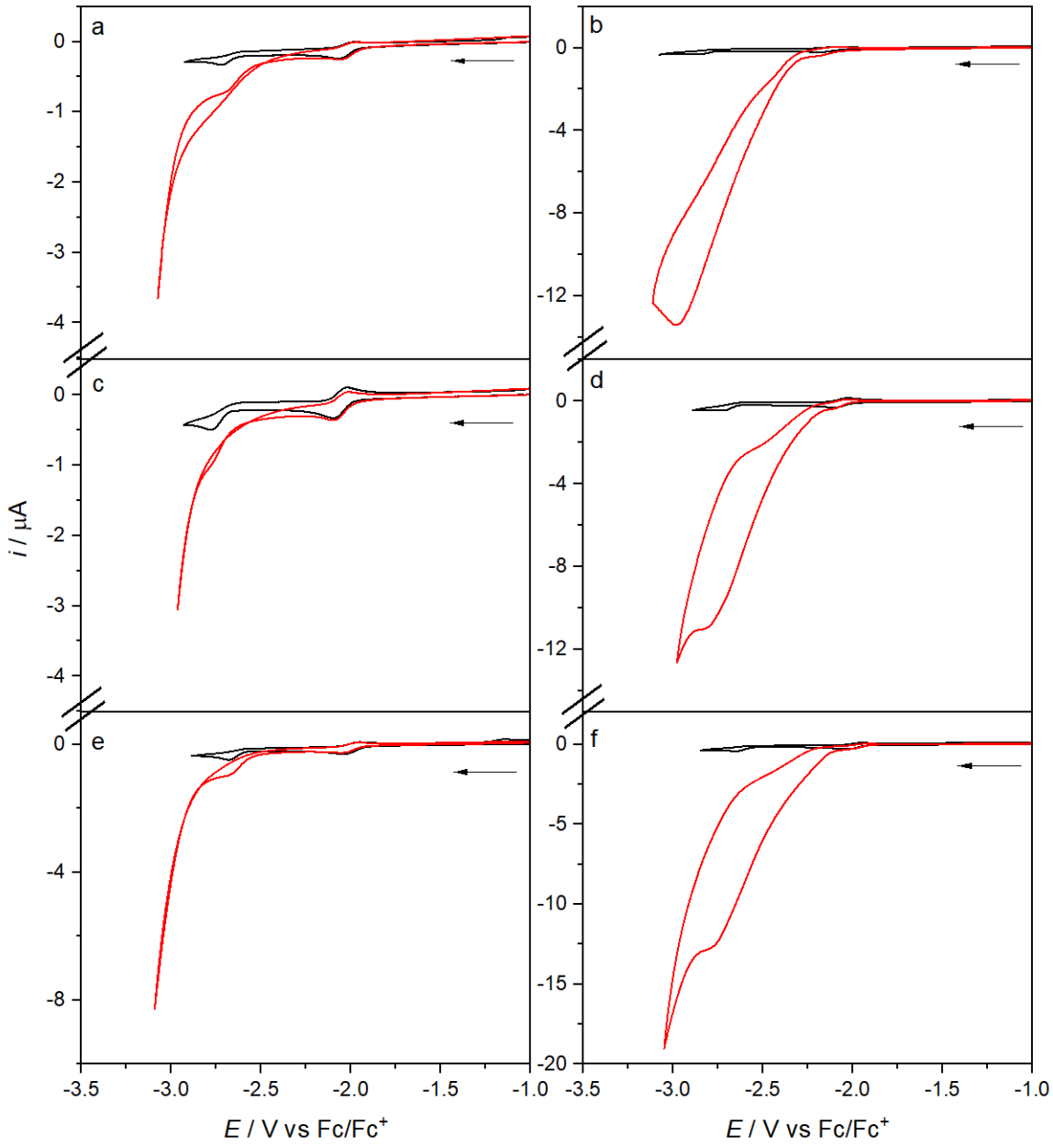

Figure 3.3: CV of [Mo(x,x′-dmbipy)$(CO)_4$] in CO_2-saturated NMP/Bu_4NPF_6: a) x = 4, Pt, b) x = 4, Au, c) x = 5, Pt d) x = 5, Au, e) x = 6, Pt and f) x = 6, Au. Scan Rate: 100 mV s^{-1}. Black curves: under Argon; red curves under CO_2. Pt and Au microdisc electrodes. The arrow indicates the initial scan direction.

Table 3.2: Infrared and UV-Vis absorption data for [Mo(x,x′-dmbipy)(CO)$_4$] (x = 4-6) and their reduction products in THF/Bu_4NPF_6, unless otherwise stated.

Complex	ν(CO) / cm^{-1}	λ_{max} / nm
[Mo(bipy)(CO)$_4$]	2012, 1900, 1882, 1840	258, 297, 393, 462
[Mo(4,4′-dmbipy)(CO)$_4$]	2011, 1898, 1877, 1837	259, 293, 402, 453
[Mo(4,4′-dmbipy)(CO)$_4$][a]	2009, 1895, 1873, 1832	259, 294, 402, 440
[Mo(5,5′-dmbipy)(CO)$_4$]	2011, 1899, 1879, 1839	-[b]
[Mo(5,5′-dmbipy)(CO)$_4$][a]	2010, 1897, 1875, 1833	-[b]
[Mo(6,6′-dmbipy)(CO)$_4$]	2014, 1900, 1879, 1836	-[b]
[Mo(6,6′-dmbipy)(CO)$_4$][a]	2013, 1898, 1874, 1829	-[b]
[Mo(bipy)(CO)$_4$]$^{\bullet-}$	1991, 1871, 1843, 1805	260, 306, 366, 463, 491, 532, <700
[Mo(4,4′-dmbipy)(CO)$_4$]$^{\bullet-}$	1991, 1869, 1841, 1802	266, 311, 370, 472, 509, 545, <700
[Mo(4,4′-dmbipy)(CO)$_4$]$^{\bullet-}$[a]	1989, 1867, 1841, 1800	266, 311, 369, 470, 510, 545, <700
[Mo(5,5′-dmbipy)(CO)$_4$]$^{\bullet-}$	1989, 1868, 1840, 1800	-[b]
[Mo(5,5′-dmbipy)(CO)$_4$]$^{\bullet-}$[a]	1988, 1865, 1839, 1798	-[b]
[Mo(6,6′-dmbipy)(CO)$_4$]$^{\bullet-}$	1994, 1873, 1844, 1801	-[b]
[Mo(6,6′-dmbipy)(CO)$_4$]$^{\bullet-}$[a]	1994, 1869, 1842, 1797	-[b]
[Mo(bipy-H)(CO)$_4$]$^{-}$[a]	1994, 1874, 1848, 1807	265, 304, 396, 509
[Mo(4,4′-dmbipy-H)(CO)$_4$]$^{-}$[a]	1994, 1871, 1845, 1802	266, 309, 398, 522
[Mo(5,5′-dmbipy-H)(CO)$_4$]$^{-}$[a]	1995, 1872, 1847, 1803	-[b]
[Mo(6,6′-dmbipy-H)(CO)$_4$]$^{-}$[a]	1996, 1874, 1845, 1798	-[b]
[Mo(bipy)(CO)$_3$]$^{2-}$	1846, 1725, 1706	258, 369, 550sh, 580, 644
[Mo(4,4′-dmbipy)(CO)$_3$]$^{2-}$	1841, 1712, 1699	264, 327, 421, 446, 543
[Mo(5,5′-dmbipy)(CO)$_3$]$^{2-}$	1840, 1721, 1703	-[b]
[Mo(6,6′-dmbipy)(CO)$_3$]$^{2-}$	1845, 1718	-[b]

[a] These values were recorded in NMP. [b] Not measured.

ence of a strongly π-delocalized[49] 5-coordinate dianion, [Mo(x,x′-dmbipy)(CO)$_3$]$^{2-}$. This characteristic behavior was also encountered for the two remaining complexes (Table 3.2).

The characteristic low-energy ν(CO) shift accompanying the formation of the stable radical anions [Mo(x,x′-dmbipy)(CO)$_4$]$^{\bullet-}$ is also seen in NMP in the course of the reduction at R1 (Table 3.2, Figure 3.4b). The ν(CO) values for the parent tetracarbonyls and the corresponding radical anions are smaller in NMP by a few wavenumbers compared to THF, and the shift magnitudes, $\Delta\nu$(CO), upon the one-electron reduction are slightly higher in the latter solvent. However, the major product of the second cathodic step at R2 in NMP is not the tricarbonyl 5-coordinate dianion seen in THF, but another two-electron-reduced

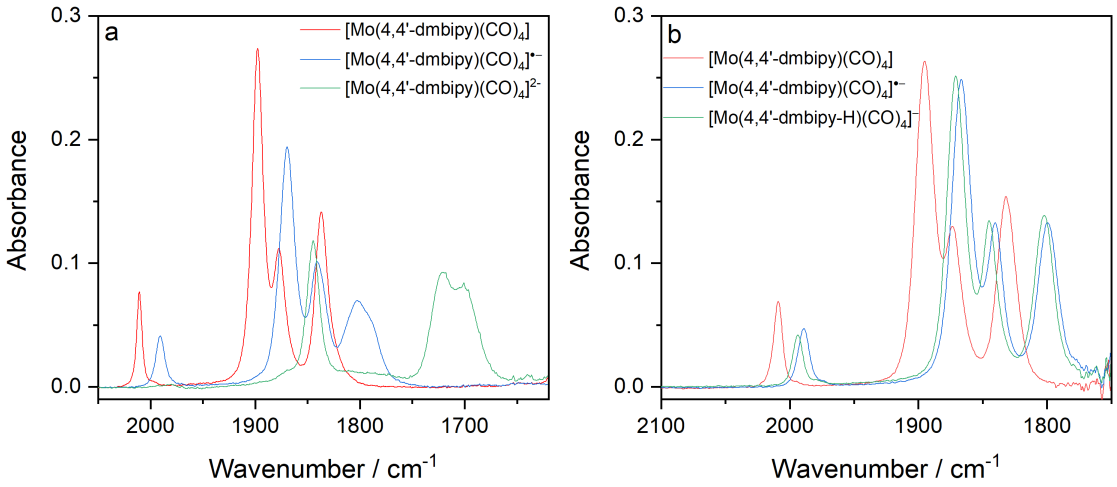

Figure 3.4: a) IR SEC monitoring of $[Mo(4,4'\text{-dmbipy})(CO)_4]$ in THF/Bu_4NPF_6 showing conversion from the parent (red) to its radical anion (blue) and finally to five-coordinate $[Mo(4,4'\text{-dmbipy})(CO)_3]^{2-}$, identified as the active CO_2 catalyst (green). b) IR SEC monitoring of $[Mo(4,4'\text{-dmbipy})(CO)_4]$ in NMP/Bu_4NPF_6 showing conversion of parent (red) to its radical anion (blue) and then to $[Mo(4,4'\text{-dmbipy-H})(CO)_4]^{-}$.

(diamagnetic) complex with the preserved parent cis tetracarbonyl ν(CO) band pattern and wavenumbers slightly larger than those recorded for the singly reduced radical anion (Table 3.2, Figure 3.4b).

UV-Vis spectral monitoring of the one-electron reduction of $[Mo(4,4'\text{-dmbipy})(CO)_4]$ in THF (Figure 3A.4a, Appendix) and NMP (Figure 3A.4b, Appendix) revealed in both solvents the broad π^*-π^* intra-ligand electronic absorption in the low-energy visible and NIR region characteristic for the 4,4′-dmbipy radical anion (Table 3.2). The electronic absorption spectrum of the two-electron-reduced species produced in NMP further distinguishes it from $[Mo(4,4'\text{-dmbipy})(CO)_3]^{2-}$, showing an intense absorption at λ_{max} = 398 nm that points to the presence of a coordinated 2,2′-bipyridine anion. These observations and a thorough comparison with the cathodic path of $[Mo(bipy)(CO)_4]$[49] lead to the assignment of the dominant ultimate two electron reduction product in NMP as the protonated anionic complex, $[Mo(4,4'\text{-dmbipy-H})(CO)_4]^{-}$. The dimethyl substitution at the bipy skeleton and the comparable ν(CO) wavenumbers (Table 3.2) point to the likely protonation of the donor nitrogen atom(s).

The stabilized protonated anionic complexes $[Mo(x,x'\text{-dmbipy-H})(CO)_4]^-$ formed in NMP (still with some water content) are oxidized much less negatively than the parent complexes $[Mo(x,x'\text{-dmbipy})(CO)_4]$ are reduced. The oxidation potentials reach ca. -1.15 V at a platinum microdisc electrode (Figure 3A.2) and ca. -1.30 V at a gold microdisc electrode. Oxidation of $[Mo(4,4'\text{-dmbipy-H})(CO)_4]^-$ was shown with thin-layer cyclic voltammetry and IR SEC to directly recover $[Mo(4,4'\text{-dmbipy})(CO)_4]$ (Figure 3A.5, Appendix). It is notable that the formation of $[Mo(4,4'\text{-dmbipy-H})(CO)_4]^-$ is not seen in NMP saturated with CO_2.

3.4.6 IR Spectroelectrochemistry in CO_2-saturated THF and NMP

The catalytic activity of the two-electron reduced complexes towards carbon dioxide reduction was examined with IR SEC for $[Mo(x,x'\text{-dmbipy})(CO)_4]$ (x = 4 and 6). In the CO_2-saturated THF electrolyte, the initial reduction of both complexes at R1, set within an OTTLE cell at the platinum or gold minigrid working electrodes, was passed smoothly, producing the stable radical anions. Sweeping the cathodic potential in the range between R1 and R2, there was very limited evidence for CO_2 reduction, reflected in the slightly diminished $^{13}CO_2$ satellite band at 2272 cm^{-1} and subordinate bicarbonate absorption at 1675 and 1638 cm^{-1} accompanying the formation of CO. This observation is fully consistent with the conventional CV responses in Figure 3.2. Reaching the negative potential of R2, the $^{13}CO_2$ satellite peak drops rapidly. The complex $[Mo(6,6'\text{-dmbipy})(CO)_4]$ is more active at the gold cathode (Figure 3.5), with evidence for the formation of formate (1605 cm^{-1}), suggesting some selectivity in the catalyst performance at different cathodic surfaces.

Strong enhancement of the catalytic CO_2-reduction resulting from the synergy between NMP and the gold cathodic surface is also apparent from the IR spectroelectrochemical monitoring of the ECE cathodic path dominating under these conditions (Figure 3.6 for the tetracarbonyl 6,6′-dmbipy complex and Figure 3A.6 (Appendix) for the 4,4′-dmbipy complex). In both cases the efficient generation of free CO adsorbed onto the cathodic surface is perceptible as a characteristic weak absorption band at 2133 (Pt) and 2130 (Au) cm^{-1} (Figures 3.6 and 3A.6). The strong NMP absorption below 1700 cm^{-1} prevents

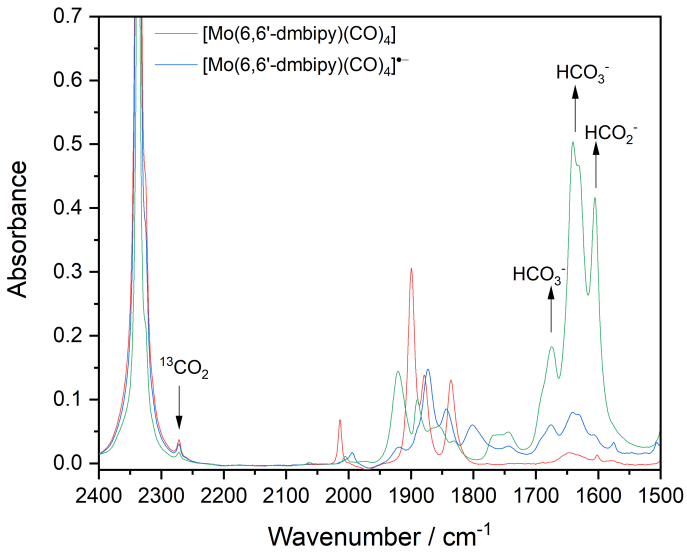

Figure 3.5: IR SEC monitoring of [Mo(6,6′-dmbipy)$(CO)_4$] reduction in CO_2-saturated THF/Bu_4NPF_6 at an Au minigrid electrode. The spectral changes correspond to the conversion of the parent complex (red) to its radical anion (blue), and finally to the situation after the catalytic wave is passed (green).

the detection of any carbonyl side products. At Au, the catalytic efficiency is highest, as evidenced by the faster decay of the $^{13}CO_2$ satellite band at 2272 cm^{-1}. For both the 4,4′-dmbipy and 6,6′-dmbipy complexes the catalytic CO_2 reduction on Au is triggered just after the conversion of the parent to its radical anion, at the cathodic potential of the experimentally observed R2′ wave (Figure 3.3).

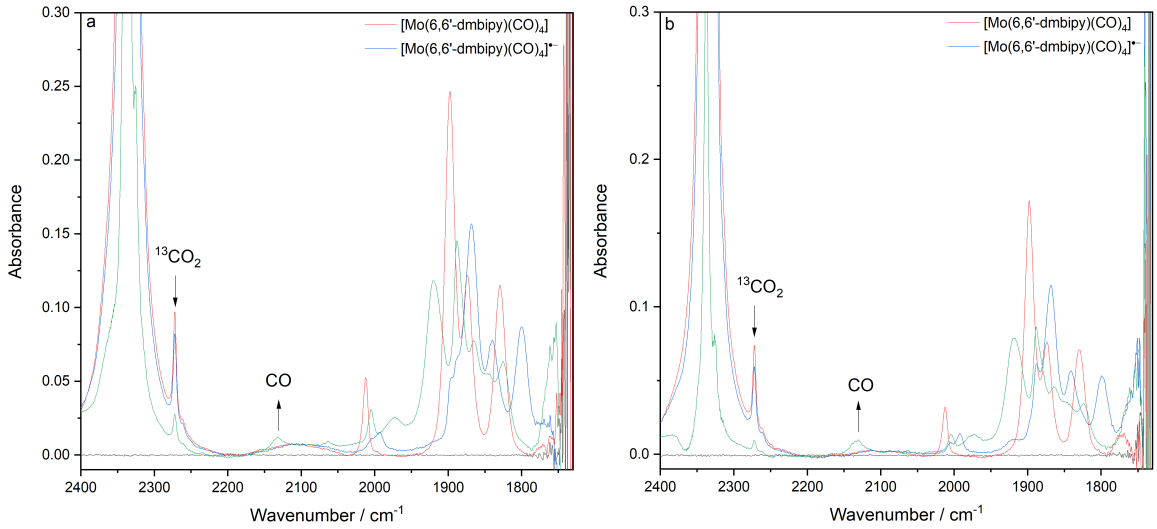

Figure 3.6: IR SEC monitoring of [Mo(6,6′-dmbipy)$(CO)_4$] reduction in CO_2-saturated NMP/Bu_4NPF_6 at (a) a Pt minigrid electrode and (b) an Au minigrid electrode. The spectral changes correspond to the conversion of the parent complex (red) to its radical anion (blue), and finally to the situation after the catalytic wave is passed (green).

3.5 Conclusions

We have shown that the judicious placement of the substituent methyl groups at the 2,2′-bipyridine ligand in [Mo(x,x′-dmbipy)$(CO)_4$] can alter the cathodic pathway leading to the two-electron reduced catalysts of the CO_2 reduction to CO, $[Mo(x,x'\text{-dmbipy})(CO)_3]^{2-}$. In THF, the substitution in the 4,4′- and 5,5′-positions favours the high-energy EEC pathway, while with the substitution in the 6,6′-positions the low-energy ECE pathway becomes dominant, involving CO dissociation from the primary radical anion. The positive response of the catalyst to the NMP solvent compared to THF is remarkable, promoting the CO-dissociation to a such a degree that the low-overpotential pathway becomes dominant for the whole x,x′-dmbipy series. In general, the effect of the solvent and the electrode on the catalytic performance play a stronger role than the substituents in determining the catalytic pathway; although the latter also needs to be considered. Promisingly, for 6,6′-dmbipy, there is a clear enhancement of the catalytic activity relative to unsubstituted [Mo(bipy)$(CO)_4$] in both THF (Figure 3A.3, compared with Figures 3.2f and 3.5) and NMP [49]. The Group-6 complexes formed by the tetracarbonyl moiety chelated by α-diimine ligands remain a

promising family of electrocatalysts suited for CO_2 conversion that deserve more attention. Our ongoing studies of these complexes also include using SFG spectroscopy to gain more insight to the cathodic surface dynamics that obviously plays a key role in these electrocatalytic processes.

3.6 Appendix to Chapter 3

3.6.1 Additional Cyclic Voltammograms

Table 3A.1: Electrode potentials of [Mo(x,x′-dmbipy)$(CO)_4$] (x = 4-6) and their reduction products in THF/Bu_4NPF_6 using a Au microdisc electrode.

Redox Step	E / V vs Fc/Fc^+		
	x = 4	x = 5	x = 6
[Mo(dmbipy)$(CO)_4$] ⟶ [Mo(dmbipy)$(CO)_4$]$^{\bullet-}$ (R1)	-2.15[a]	-2.19[a]	-2.13[a]
[Mo(dmbipy)$(CO)_4$]$^{\bullet-}$ ⟶ [Mo(dmbipy)$(CO)_4$]$^{2-}$ (R2)	-2.67[b]	-2.73[b]	-2.69[b]
[Mo(dmbipy)$(CO)_3$]$^{2-}$ ⟶ [Mo(dmbipy)$(CO)_3$]$^{\bullet-}$ (O2′)	-2.39[c]	-2.36[c]	-2.42[c]

[a] $E_{1/2}$ values. [b] $E_{p,c}$ values. [c] $E_{p,a}$ values. Potentials for [Mo(bipy)$(CO)_4$] are: R1: -2.05 V ($E_{1/2}$), R2: -2.63 V ($E_{p,c}$) and O2′: -2.32 V ($E_{p,a}$).[49]

Table 3A.2: Electrode potentials of [Mo(x,x′-dmbipy)$(CO)_4$] (x = 4-6) and their reduction products in NMP/Bu_4NPF_6 using a Pt microdisc electrode.

Redox Step	E / V vs Fc/Fc^+		
	x = 4	x = 5	x = 6
[Mo(dmbipy)$(CO)_4$] ⟶ [Mo(dmbipy)$(CO)_4$]$^{\bullet-}$ (R1)	-2.02[a]	-2.06[a]	-1.98[a]
[Mo(dmbipy)$(CO)_4$]$^{\bullet-}$ ⟶ [Mo(dmbipy)$(CO)_4$]$^{2-}$ (R2)	-2.65[b]	-2.73[b]	-2.63[b]
[Mo(dmbipy)$(CO)_3$]$^{2-}$ ⟶ [Mo(dmbipy)$(CO)_3$]$^{\bullet-}$ (O2′)	-2.41[c]	-2.37[c]	-[d]

[a] $E_{1/2}$ values. [b] $E_{p,c}$ values. [c] $E_{p,a}$ values. [d] Not observed. Potentials for [Mo(bipy)$(CO)_4$] are: R1: -1.95 V ($E_{1/2}$), R2: -2.71 V ($E_{p,c}$).[49]

Table 3A.3: Electrode potentials of [Mo(x,x′-dmbipy)$(CO)_4$] (x = 4-6) and their reduction products in NMP/Bu_4NPF_6 using a Au microdisc electrode.

Redox Step	E / V vs Fc/Fc^+		
	x = 4	x = 5	x = 6
$[Mo(dmbipy)(CO)_4] \longrightarrow [Mo(dmbipy)(CO)_4]^{\bullet-}$ (R1)	-2.02[a]	-2.06[a]	-1.99[a]
$[Mo(dmbipy)(CO)_4]^{\bullet-} \longrightarrow [Mo(dmbipy)(CO)_4]^{2-}$ (R2)	-2.63[b]	-2.69[b]	-2.64[b]
$[Mo(dmbipy)(CO)_3]^{2-} \longrightarrow [Mo(dmbipy)(CO)_3]^{\bullet-}$ (O2′)	-2.38[c]	-2.38[c]	-[d]

[a] $E_{1/2}$ values. [b] $E_{p,c}$ values. [c] $E_{p,a}$ Values. [d] Not observed. Potentials for [Mo(bipy)$(CO)_4$] are: R1: -1.95 V ($E_{1/2}$), R2: -2.71 V ($E_{p,c}$) and O2′: -2.32 V ($E_{p,a}$).[49]

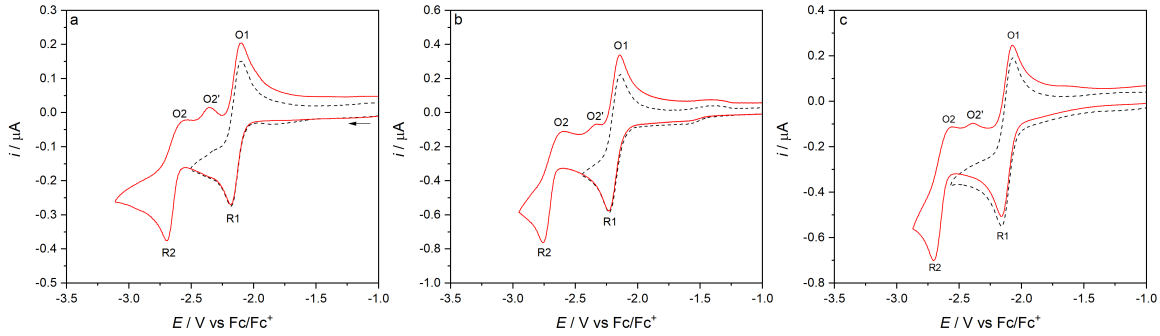

Figure 3A.1: CV of [Mo(x,x′-dmbipy)$(CO)_4$] in argon-saturated THF/Bu_4NPF_6: a) x = 4, b) x = 5, c) x = 6. Scan Rate: 100 mV s^{-1}. Au microdisc electrode. The arrow indicates the initial scan direction.

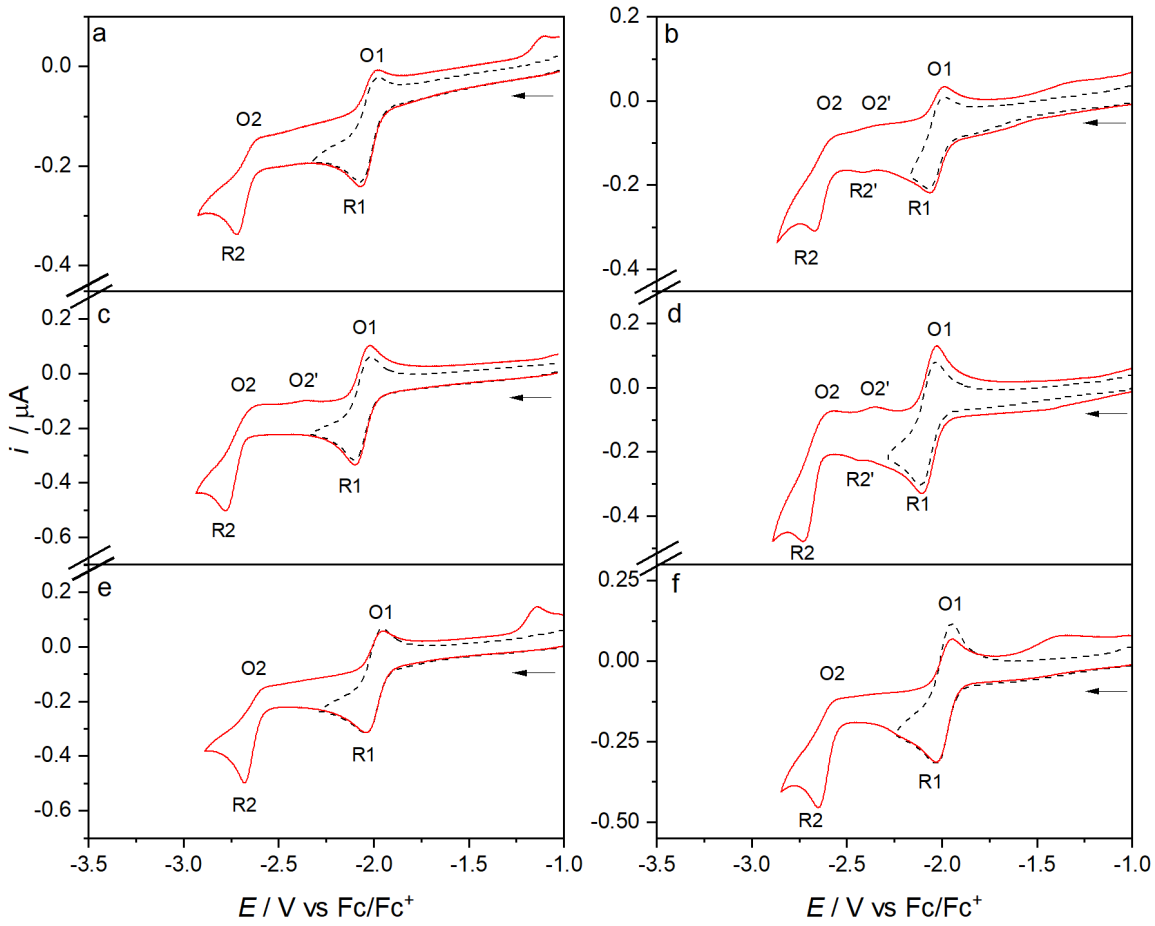

Figure 3A.2: CV of [Mo(x,x′-dmbipy)$(CO)_4$] in argon-saturated NMP/Bu_4NPF_6: a) x = 4, Pt, b) x = 4, Au, c) x = 5, Pt d) x = 5, Au, e) x = 6, Pt and f) x = 6, Au. Scan Rate: 100 mV s^{-1}. The arrow indicates the initial scan direction.

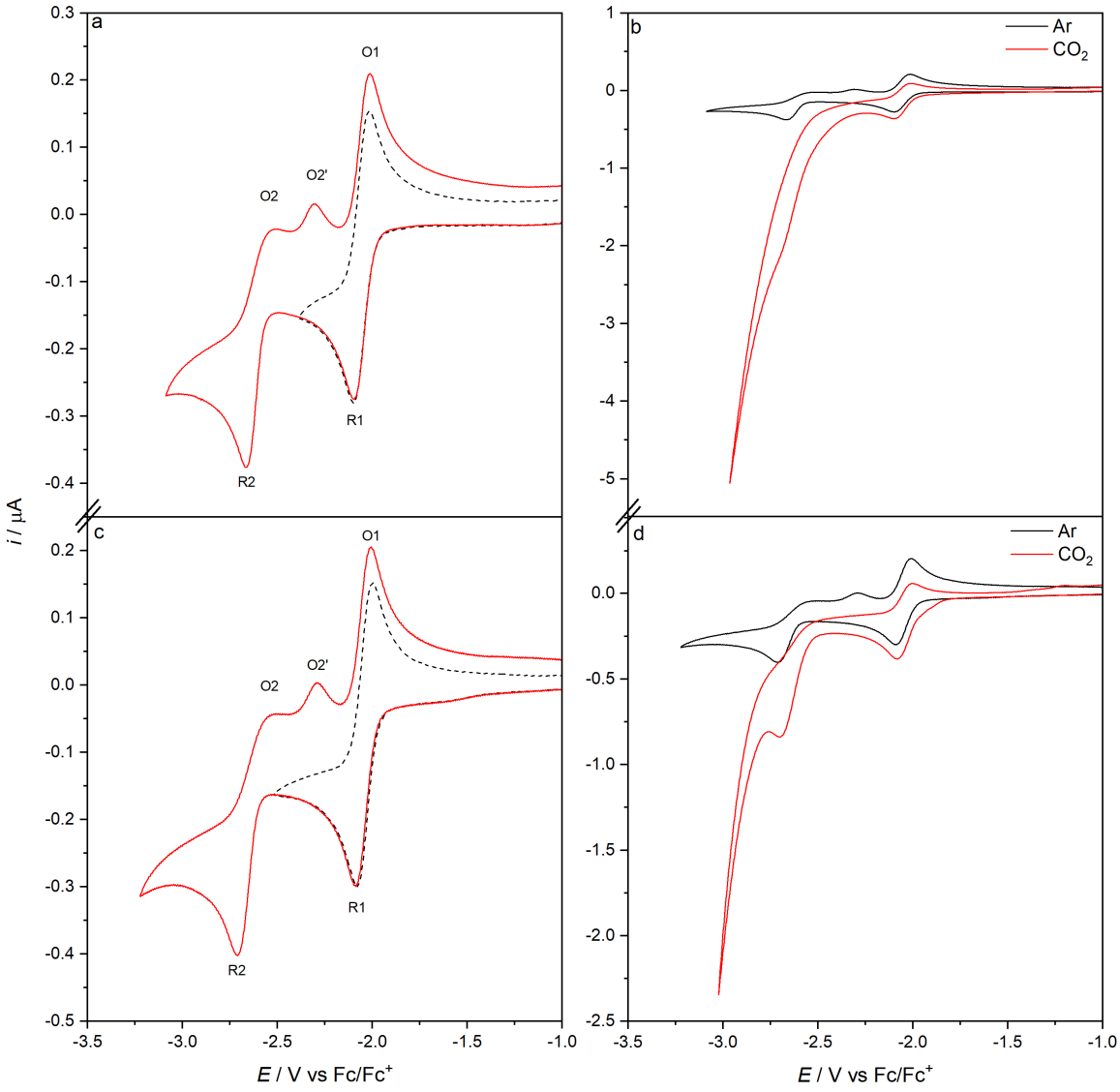

Figure 3A.3: CV of $[Mo(bipy)(CO)_4]$ in THF/Bu_4NPF_6: a) Ar, Au, b) CO_2, Au, c) Ar, Pt d) CO_2, Pt. Scan Rate: 100 mV s^{-1}.

3.6.2 Additional Spectroelectrochemical Experiments

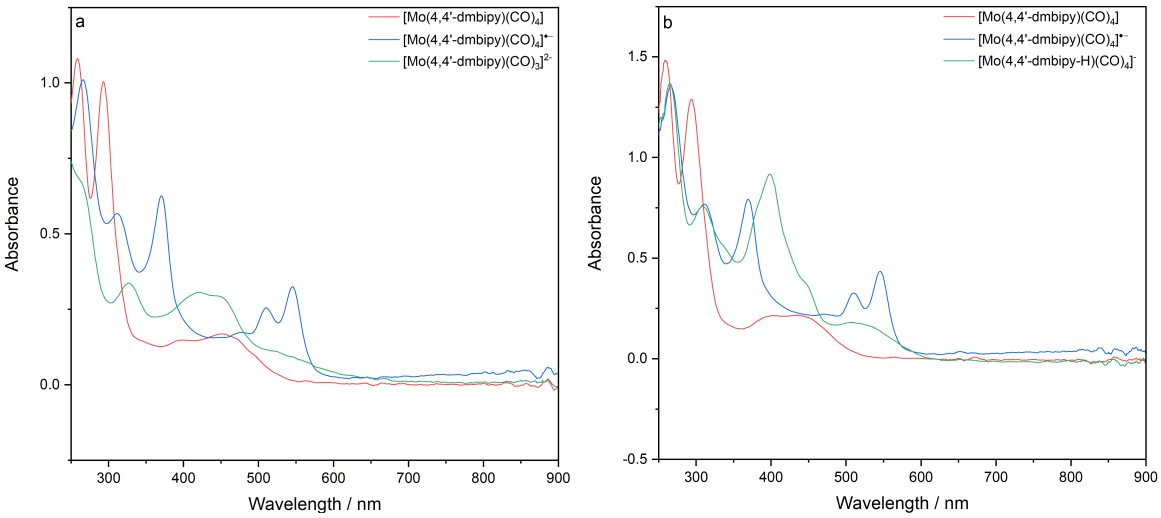

Figure 3A.4: Cathodic UV-Vis SEC in (a) THF/Bu_4NPF_6 and (b) NMP/Bu_4NPF_6, showing the conversion of parent [Mo(4,4′-dmbipy)$(CO)_4$] (red) to its radical anion (blue), and finally to dominant 5-coordinate [Mo(4,4′-dmbipy)$(CO)_3]^{2-}$ (green, in THF) or [Mo(4,4′-dmbipy-H)$(CO)_4]^{-}$ (green, in NMP).

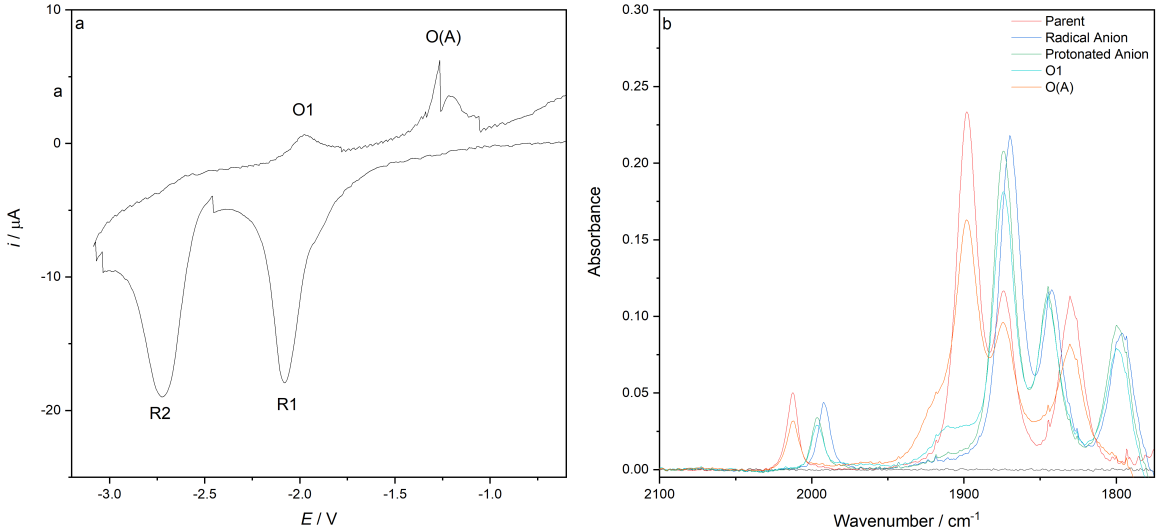

Figure 3A.5: (a) Thin-layer cyclic voltammogram of [Mo(4,4′-dmbipy)$(CO)_4$] in argon-saturated NMP/Bu_4NPF_6 (υ = 2 mV s^{-1}) recorded in ambient conditions within an OTTLE cell. It shows the stepwise one-electron reduction to [Mo(4,4′-dmbipy)$(CO)_4]^{\bullet-}$ at R1, and the latter to [Mo(4,4′-dmbipy-H)$(CO)_4]^-$ at R2. The anodic wave O(A) on the reverse scan corresponds to the oxidation of [Mo(4,4′-dmbipy-H)$(CO)_4]^-$ that leads to a substantial recovery of parent [Mo(4,4′-dmbipy)$(CO)_4$]. (b) These TL-CV processes were monitored in parallel with IR SEC; CO-stretching wavenumbers of the involved carbonyl complexes are listed in Table 2.

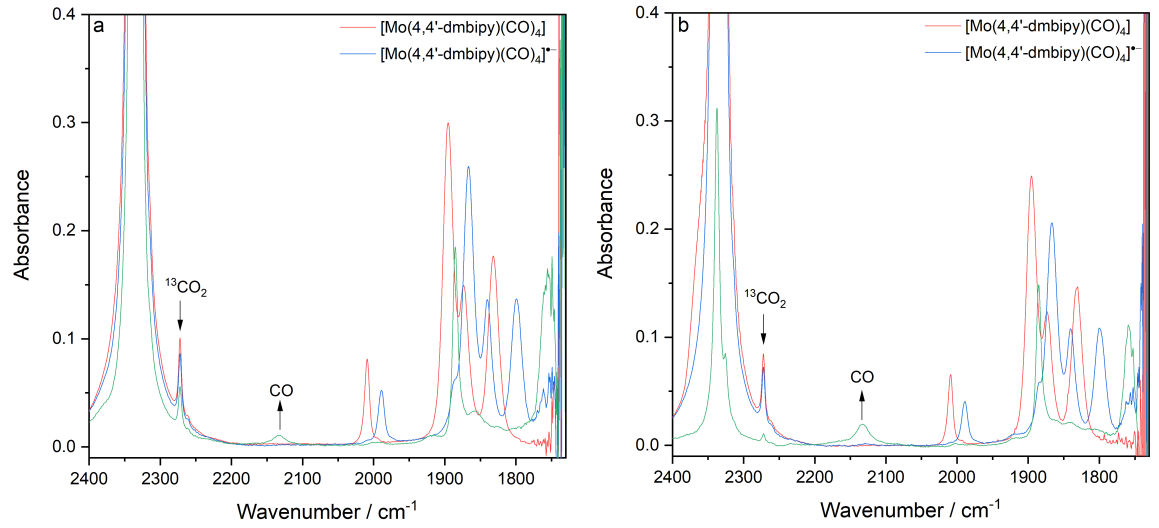

Figure 3A.6: IR SEC monitoring of [Mo(4,4′-dmbipy)$(CO)_4$] reduction in CO_2-saturated NMP/Bu_4NPF_6 at (a) a Pt minigrid electrode and (b) an Au minigrid electrode. The spectral changes correspond to the conversion of the parent complex (red) to its radical anion (blue), and finally to the situation after the catalytic wave is passed (green).

References

[1] J. Qiao, Y. Liu, F. Hong and J. Zhang, *Chem. Soc. Rev.*, 2014, **43**, 631–675.

[2] C. Costentin, M. Robert and J.-M. Savéant, *Chem. Soc. Rev.*, 2013, **42**, 2423–2436.

[3] C. Finn, S. Schnittger, L. J. Yellowlees and J. B. Love, *Chem. Commun.*, 2012, **48**, 1392–1399.

[4] K. Li, X. An, K. H. Park, M. Khraisheh and J. Tang, *Catal. Today*, 2014, **224**, 3–12.

[5] E. Portenkirchner, S. Schlager, D. Apaydin, K. Oppelt, M. Himmelsbach, D. A. M. Egbe, H. Neugebauer, G. Knör, T. Yoshida and N. S. Sariciftci, *Electrocatalysis*, 2015, **6**, 185–197.

[6] A. Maurin, C. O. Ng, L. Chen, T. C. Lau, M. Robert and C. C. Ko, *Dalton Trans.*, 2016, **45**, 14524–14529.

[7] F. Franco, C. Cometto, C. Garino, C. Minero, F. Sordello, C. Nervi and R. Gobetto, *Eur. J. of Inorg. Chem.*, 2015, **2015**, 296–304.

[8] J. K. Nganga, C. R. Samanamu, J. M. Tanski, C. Pacheco, C. Saucedo, V. S. Batista, K. A. Grice, M. Z. Ertem and A. M. Angeles-Boza, *Inorg. Chem.*, 2017, **56**, 3214–3226.

[9] N. P. Liyanage, H. A. Dulaney, A. J. Huckaba, J. W. Jurss and J. H. Delcamp, *Inorg. Chem.*, 2016, **55**, 6085–6094.

[10] A. Ge, B. Rudshteyn, J. Zhu, R. J. Maurer, V. S. Batista and T. Lian, *J. Phys. Chem. Lett.*, 2018, **9**, 406–412.

[11] F. H. Haghighi, H. Hadadzadeh, H. Farrokhpour, N. Serri, K. Abdi and H. Amiri Rudbari, *Dalton Trans.*, 2014, **43**, 11317–11332.

[12] B. A. Johnson, H. Agarwala, T. A. White, E. Mijangos, S. Maji and S. Ott, *Chem. Eur. J.*, 2016, **22**, 14870–14880.

[13] T. A. White, S. Maji and S. Ott, *Dalton Trans.*, 2014, **43**, 15028–15037.

[14] Z. Chen, C. Chen, D. R. Weinberg, P. Kang, J. J. Concepcion, D. P. Harrison, M. S. Brookhart and T. J. Meyer, *Chem. Commun.*, 2011, **47**, 12607–12609.

[15] M. Daryanavard, H. Hadadzadeh, M. Weil and H. Farrokhpour, *J. CO_2 Util.*, 2017, **17**, 80–89.

[16] H. Hadadzadeh, H. Farrokhpour, J. Simpson, J. Shakeri, M. Daryanavard and M. Shokrollahi, *New J. Chem.*, 2016, **40**, 6347–6357.

[17] D. Ghosh, K. Kobayashi, T. Kajiwara, S. Kitagawa and K. Tanaka, *Inorg. Chem.*, 2017, **56**, 11066–11073.

[18] S. Min, S. Rasul, H. Li, D. C. Grills, K. Takanabe, L.-J. Li and K.-W. Huang, *ChemPlusChem*, 2016, **81**, 166–171.

[19] M. R. M. Bruce, E. Megehee, B. P. Sullivan, H. Thorp, T. R. O'Toole, A. Downard and T. J. Meyer, *Organometallics*, 1988, **7**, 238–240.

[20] M. R. M. Bruce, E. Megehee, B. P. Sullivan, H. H. Thorp, T. R. O'Toole, A. Downard, J. R. Pugh and T. J. Meyer, *Inorg. Chem.*, 1992, **31**, 4864–4873.

[21] J. Tory, L. King, A. Maroulis, M. Haukka, M. J. Calhorda and F. Hartl, *Inorg. Chem.*, 2014, **53**, 1382–1396.

[22] P. Paul, B. Tyagi, A. K. Bilakhiya, M. M. Bhadbhade, E. Suresh and G. Ramachandraiah, *Inorg. Chem.*, 1998, **37**, 5733–5742.

[23] S. E. Witt, T. A. White, Z. Li, K. R. Dunbar and C. Turro, *Chem. Commun.*, 2016, **52**, 12175–12178.

[24] G. F. Manbeck, K. Garg, T. Shimoda, D. J. Szalda, M. Z. Ertem, J. T. Muckerman and E. Fujita, *Faraday Discuss.*, 2017, **198**, 301–317.

[25] A. Szymaszek and F. Pruchnik, *J. Organomet. Chem.*, 1989, **376**, 133–140.

[26] S. T. Ahn, E. A. Bielinski, E. M. Lane, Y. Chen, W. H. Bernskoetter, N. Hazari and G. T. R. Palmore, *Chem. Commun.*, 2015, **51**, 5947–5950.

[27] F. D. Sypaseuth, C. Matlachowski, M. Weber, M. Schwalbe and C. C. Tzschucke, *Chem. Eur. J.*, 2015, **21**, 6564–6571.

[28] M. Bourrez, F. Molton, S. Chardon-Noblat and A. Deronzier, *Angew. Chem. Int. Ed.*, 2011, **50**, 9903–9906.

[29] F. Franco, C. Cometto, L. Nencini, C. Barolo, F. Sordello, C. Minero, J. Fiedler, M. Robert, R. Gobetto and C. Nervi, *Chem. Eur. J.*, 2017, **23**, 4782–4793.

[30] S. J. Spall, T. Keane, J. Tory, D. C. Cocker, H. Adams, H. Fowler, A. J. Meijer, F. Hartl and J. A. Weinstein, *Inorg. Chem.*, 2016, **55**, 12568–12582.

[31] K. T. Ngo, M. McKinnon, B. Mahanti, R. Narayanan, D. C. Grills, M. Z. Ertem and J. Rochford, *J. Am. Chem. Soc.*, 2017, **139**, 2604–2618.

[32] D. C. Grills, J. A. Farrington, B. H. Layne, S. V. Lymar, B. A. Mello, J. M. Preses and J. F. Wishart, *J. Am. Chem. Soc.*, 2014, **136**, 5563–5566.

[33] Y. C. Lam, R. J. Nielsen, H. B. Gray and W. A. Goddard, *ACS Catal.*, 2015, **5**, 2521–2528.

[34] Q. Zeng, J. Tory and F. Hartl, *Organometallics*, 2014, **33**, 5002–5008.

[35] F. Franco, C. Cometto, F. Ferrero Vallana, F. Sordello, E. Priola, C. Minero, C. Nervi and R. Gobetto, *Chem. Commun.*, 2014, **50**, 14670–14673.

[36] G. K. Rao, W. Pell, I. Korobkov and D. Richeson, *Chem. Commun.*, 2016, **52**, 8010–8013.

[37] I. Azcarate, C. Costentin, M. Robert and J.-M. Savéant, *J. Am. Chem. Soc.*, 2016, **138**, 16639–16644.

[38] C. Costentin, S. Drouet, M. Robert and J. M. Savéant, *Science*, 2012, **338**, 90–94.

[39] A. Taheri, E. J. Thompson, J. C. Fettinger and L. A. Berben, *ACS Catal.*, 2015, **5**, 7140–7151.

[40] S. N. Pun, W. H. Chung, K. M. Lam, P. Guo, P. H. Chan, K. Y. Wong, C. M. Che, T. Y. Chen and S. M. Peng, *J. Chem. Soc., Dalton Trans.*, 2002, **0**, 575–583.

[41] E. A. Mohamed, Z. N. Zahran and Y. Naruta, *Chem. Commun.*, 2015, **51**, 16900–16903.

[42] Z. N. Zahran, E. A. Mohamed and Y. Naruta, *Sci. Rep.*, 2016, **6**, 24533.

[43] R. B. Ambre, Q. Daniel, T. Fan, H. Chen, B. Zhang, L. Wang, M. S. G. Ahlquist, L. Duan and L. Sun, *Chem. Commun.*, 2016, **52**, 14478–14481.

[44] M. Hammouche, D. Lexa, M. Momenteau and J. M. Saveant, *J. Am. Chem. Soc.*, 1991, **113**, 8455–8466.

[45] C. Costentin, G. Passard, M. Robert and J. M. Savéant, *J. Am. Chem. Soc.*, 2014, **136**, 11821–11829.

[46] S. Roy, B. Sharma, J. Pécaut, P. Simon, M. Fontecave, P. D. Tran, E. Derat and V. Artero, *J. Am. Chem. Soc.*, 2017, **139**, 3685–3696.

[47] N. Elgrishi, M. B. Chambers and M. Fontecave, *Chem. Sci.*, 2015, **6**, 2522–2531.

[48] D. C. Lacy, C. C. L. McCrory and J. C. Peters, *Inorg. Chem.*, 2014, **53**, 4980–4988.

[49] J. Tory, B. Setterfield-Price, R. A. W. Dryfe and F. Hartl, *ChemElectroChem*, 2015, **2**, 213–217.

[50] F. Franco, C. Cometto, F. Sordello, C. Minero, L. Nencini, J. Fiedler, R. Gobetto and C. Nervi, *ChemElectroChem*, 2015, **2**, 1372–1379.

[51] M. L. Clark, K. A. Grice, C. E. Moore, A. L. Rheingold and C. P. Kubiak, *Chem. Sci.*, 2014, **5**, 1894–1900.

[52] D. Sieh, D. C. Lacy, J. C. Peters and C. P. Kubiak, *Chem. Eur. J.*, 2015, **21**, 8497–8503.

[53] N. Elgrishi, M. B. Chambers, X. Wang and M. Fontecave, *Chem. Soc. Rev.*, 2017, **46**, 761–796.

[54] R. Francke, B. Schille and M. Roemelt, *Chem. Rev.*, 2018, **118**, 4631–4701.

[55] J. Hawecker, J. M. Lehn and R. Ziessel, *J. Chem. Soc., Chem. Commun.*, 1984, **984**, 328–330.

[56] J. Tory, G. Gobaille-Shaw, A. M. Chippindale and F. Hartl, *J. Organomet. Chem.*, 2014, **760**, 30–41.

[57] D. E. Ryan, D. J. Cardin and F. Hartl, *Coord. Chem. Rev.*, 2017, **335**, 103–149.

[58] G. Neri, P. M. Donaldson and A. J. Cowan, *J. Am. Chem. Soc.*, 2017, **139**, 13791–13797.

[59] M. Krejčik, M. Daněk and F. Hartl, *J. Electroanal. Chem. Interfacial Electrochem.*, 1991, **317**, 179–187.

[60] P. N. Baxter and J. A. Connor, *J. Organomet. Chem.*, 1995, **486**, 115–121.

[61] S. A. Chabolla, E. A. Dellamary, C. W. Machan, F. A. Tezcan and C. P. Kubiak, *Inorg. Chim. Acta*, 2014, **422**, 109–113.

[62] F. Hartl, P. Rosa, L. Ricard, P. Le Floch and S. Záliš, *Coord. Chem. Rev.*, 2007, **251**, 557–576.

Chapter 4

Photo-assisted Electrocatalytic Reduction of CO_2: A New Strategy for Reducing Catalytic Overpotentials

The content of this chapter was published in: **J. O. Taylor**, Y. Wang, F. Hartl, *ChemCatChem*, 2020, **12**, 386–393.

4.1 Abstract

Electrochemical and photochemical reduction of CO_2 are both well-established, independent catalytic routes toward producing added-value chemicals. The potential for any cross-reactivity has, however, hardly been explored so far. In this report, we assess a system primarily using spectroelectrochemical monitoring, where photochemistry assists the cathodic activation of precursor complexes [Mn(2,2′-bipyridine)$(CO)_3$Br] and [Mo(6,6′-dimethyl-2,2′-bipyridine)$(CO)_4$] to lower the catalytic overpotential needed to trigger the electrocatalytic reduction of CO_2 to CO. Following the complete initial one-electron reduction of the parent complexes, the key photochemical cleavage of the Mn−Mn and Mo−CO bonds in the reduction products, [Mn(2,2′-bipyridine)$(CO)_3]_2$ and [Mo(6,6′-dimethyl-2,2′-bipyridine)$(CO)_4]^{\bullet-}$, respectively, generates the $2e^-$-reduced, 5-coordinate catalysts, [Mn(2,2′-bipyridine)$(CO)_3]^-$ and [Mo(6,6′-dimethyl-2,2′-bipyridine)$(CO)_3]^{2-}$ appreciably closer to the initial cathodic wave (R1). Experiments under CO_2 confirm the activity of both electrocatalysts under the photoirradiation with 405 nm and 365 nm light, respectively. This remarkable achievement corresponds to a ca. 500 mV positive shift of the catalytic onset compared to the exclusive standard electrocatalytic activation.

4.2 Introduction

The recent environmental concerns stemming from the anthropogenic emission of CO_2 is the main driving force behind academic efforts to develop both homogeneous and heterogeneous catalytic systems converting CO_2 into valuable chemicals.[1] These systems can broadly be classified as either electrocatalytic,[2] photocatalytic[3] or photoelectrocatalytic.[4] In all three cases transition metal α-diimine complexes have emerged as the leading class of catalytic systems, boasting both high levels of selectivity and activity.[5–7] *fac*-[Re(bipy)$(CO)_3$Cl] (bipy = 2,2′-bipyridine), is a prime example, having first been identified as an electrocatalyst by Lehn and co-workers,[8] and two decades later as a photocatalyst by Ishitani and coworkers.[9] The way in which the Re(I) polypyridyl field has developed highlights one of the discernible

flaws in the current approach; catalysts are always explored independently as either a photocatalyst or an electrocatalyst. This leads to the primary goal of this report, which is to investigate the possibility of combining the electrochemical reactivity of a catalyst precursor with the photochemical reactivity of its singly reduced intermediates, Schemes 4.1 and 4.2. The expectation is that the active $2e^-$-reduced catalyst can be produced and actively maintained at a lower overpotential close to its reoxidation. To our knowledge, this is a unique, yet unexplored way to address the sometimes rather negative reduction potentials along the reduction path of these complexes needed to generate the electrocatalyst, which we have termed as photo-assisted electrochemical reduction. In recent years, catalysts based on the unsustainable Earth-rare metals (Re, Ru, Rh, Ir)[2] have been relegated to benchmark status, as the community refocuses efforts on the Earth-abundant metals such as Mn,[10–15] Fe[16–18] and more recently the Group-6 triad (Cr, Mo, W).[19–26] For this reason, two viable catalyst precursors, *fac*-[Mn(bipy)$(CO)_3$Br] (**1**) and [Mo(6,6′-dmbipy)$(CO)_4$] (6,6′-dmbipy = 6,6′-dimethyl-2,2′-bipyridine) (**2**) have been selected for this investigation.

In the very first reports, the reduction of [Mn(bipy)$(CO)_3$Br] in dry organic solvents was noted to not trigger electrocatalytic CO_2 conversion.[27] It was not until Deronzier,[10] and later Kubiak,[12] and their co-workers revealed that the presence of small amounts (typically 5%) of Brønsted or Lewis acids were required for an efficient catalytic reaction to occur, that any serious attention was devoted to the Mn-based family of catalysts. Despite a similar molecular structure, [Mn(bipy)$(CO)_3$Br] exhibits quite different electrochemical reactivity to its Re analogue. [Mn(bipy)$(CO)_3$Br] initially undergoes $1e^-$ reduction (at the cathodic wave R1) to the corresponding, unstable radical anion that quickly loses Br^- to form a 5-coordinate radical. As the radical is reducible at less negative potentials than the parent compound, it quickly converts electrochemically (ECE) to the 5-coordinate anion, $[Mn(bipy)(CO)_3]^-$. At this stage the 5-coordinate anion reacts via zero-electron coupling with the yet unreduced parent to form $[Mn(bipy)(CO)_3]_2$. The resulting dimer must be reduced at more negative potentials to recover the 5-coordinate anion (at the cathodic wave R(D)). The dominant catalytic response of CO_2 converting to CO is seen at R(D), coinciding with the formation of

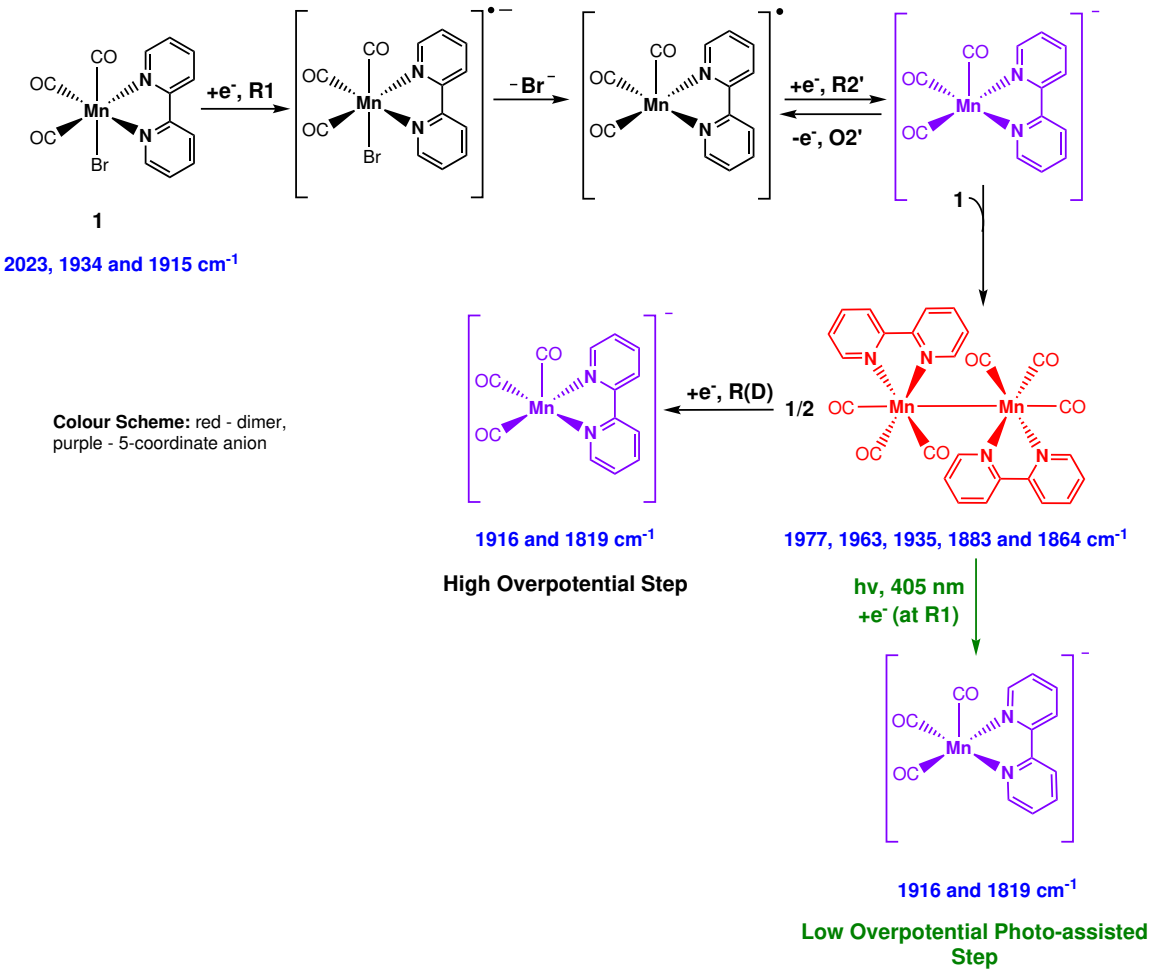

Scheme 4.1: Cathodic pathway of **1** under ambient conditions. The photo-assisted electrochemical reduction is highlighted in green.

the $[Mn(bipy)(CO)_3]^-$ catalyst. In selected cases (for 4,4′-dmbipy replacing the bipy ligand), some catalytic response was actually noted[10] already at R1, and there is now convincing evidence for a second catalytic pathway based on the Mn−Mn dimer.[11,28]

Ideally, $[Mn(bipy)(CO)_3]^-$ should remain stable at R1, avoiding the secondary dimerization. Kubiak and co-workers succeeded in eliminating the dimerization by introducing bulky 6,6′-dimesityl-bipy (6,6′-mesbipy) into the catalyst.[29,30] However, the catalytic response was not seen at R1, but shifted to more negative potentials where the undesired, stable Mn(I)-bicarbonate product is reduced. This is a case that advocates for the use of photo-assisted electrochemical reduction. A potential complication is, to our knowledge,

only the photochemistry of parent [Mn(bipy)$(CO)_3$Br] is known, which undergoes fac-to-mer isomerisation followed by optical population of an LLCT/MLCT excited state, Mn-Br bond cleavage and dimer formation.[31] The photochemistry of the dimer [Mn(bipy)$(CO)_3]_2$ has not been extensively investigated, but it was exploited in the past by Ishitani,[32,33] while the photochemistry of the related dimers $[Mn(CO)_5]_2$ and [(bipy)$(CO)_3$Mn−Mn$(CO)_5$] were investigated more thoroughly.[34–37] Optical excitation of these dimers with photons of ca. 400 nm wavelength results, through various means, in the population of a dissociative $^3\sigma_{MM}\sigma^*_{MM}$ excited state, which induces homolysis of the Mn−Mn bond and, in turn, yields the corresponding 5-coordinate Mn radicals.

Experimental and theoretical studies of closely related [Re(bipy)$(CO)_3]_2$ have revealed[38] that there is no low-lying σ^*_{MM} orbital in this dimer and optical excitation in the visible region (400–800 nm) results in population of MLCT excited states, the lowest one corresponding to σ_{MM}(d,p) $\longrightarrow$ π^*(bipy) charge transfer (seen as an intense absorption band at $\lambda_{max} = 808$ nm in THF). The quantum yield for the homolysis of the Re−Re bond from the corresponding triplet excited state is very low ($< 10^{-5}$) in this case.[39] Molecular orbitals with a σ^*_{MM}(d) contribution are high-lying (LUMO+8 – as a minor component, LUMO+17, LUMO+27 – as a significant component, and classical LUMO+28) and a more efficient Re−Re bond cleavage therefore requires UV radiation. To summarize, following the electrochemical production of [Mn(bipy)$(CO)_3]_2$, irradiation with photons of a sufficiently high energy to yield the 5-coordinate radicals theoretically allows access to the catalytic agent already at R1, via the cathodic conversion of the amply long-lived radical species[38] to the corresponding 5-coordinate anion at this potential (Scheme 4.1).

The other target complex, [Mo(6,6′-dmbipy)$(CO)_4$], has only recently been introduced as an electrocatalyst for CO_2 reduction.[19] The first report on this Group-6 metal tetracarbonyl α-diimine family regarded [Mo(bipy)$(CO)_4$], a catalyst precursor that initially was not considered very promising, as only a very limited catalytic performance was seen at a very negative reduction potential of R2, triggered by the generation of $2e^-$ reduced $[Mo(bipy)(CO)_3]^{2-}$.[21] It was later discovered that this particular family was quite sen-

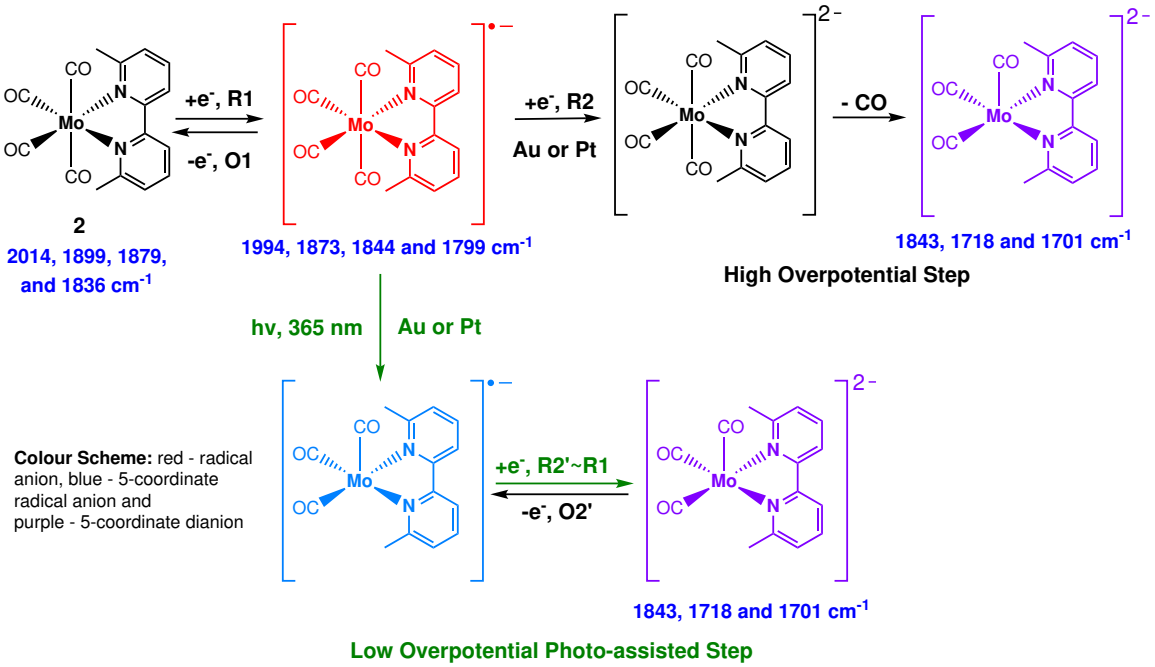

Scheme 4.2: Cathodic pathway of **2** under ambient conditions. The photo-assisted electrochemical reduction is highlighted in green.

sitive to the cathodic material employed. On an Au cathode, the catalytic onset becomes shifted to a much less negative overpotential; in addition, sterically demanding substituents on bipy together with solvent variation can further improve the catalytic performance.[19,26] The initial $1e^-$ reduction of [Mo(6,6′-dmbipy)$(CO)_4$] produces the stable 6-coordinate radical anion $[Mo(6,6'\text{-dmbipy})(CO)_4]^{\bullet-}$; its irreversible reduction at R2 produces transient $[Mo(6,6'\text{-dmbipy})(CO)_4]^{2-}$ quickly losing CO to yield the active catalyst, $[Mo(6,6'\text{-dmbipy})(CO)_3]^{2-}$. The latter dianion is reoxidized on the reverse anodic scan at O2′ to $[Mo(6,6'\text{-dmbipy})(CO)_3]^{\bullet-}$ (Scheme 4.2). This observation allows one to estimate the position of the forward reduction wave, R2′, only scarcely observable directly.[26] The preceding work[26] confirms that when using a Pt cathode, the catalytic response is seen exclusively at R2, while replacement with an Au cathode causes the onset of the catalytic CO_2 reduction to appear in the vicinity of R2′. The origin of this phenomenon has been explained[40] by the co-existence of $[Mo(6,6'\text{-dmbipy})(CO)_4]^{\bullet-}$ with a small amount of $[Mo(6,6'\text{-dmbipy})(CO)_3]^{\bullet-}$. At the Au surface the equilibrium is shifted more toward the 5-coordinate member of the

radical pair. As $[Mo(6,6'\text{-dmbipy})(CO)_3]^{\bullet-}$ is reducible to $[Mo(6,6'\text{-dmbipy})(CO)_3]^{2-}$ at R2′ < R2, the early onset of the catalytic wave has the origin in the CO dissociation facilitated by the cathodic Au surface.

It was tempting to enhance this process with photodissociation, especially at a cathodic Pt surface where it was hardly observed as thermally driven. While the photochemistry of the strongly air- and moisture-sensitive 6-coordinate radical anions is poorly known, the photodissociation of CO from the neutral parent tetracarbonyl complexes is well understood. Under irradiation with UV light (λ_{exc} = 365 nm), the complexes of this type are known to undergo CO dissociation from an optically populated ^{1}MLCT state.[41–43] Resonance Raman studies on $[W(bpym)(CO)_4]^{\bullet-}$ (bpym = 2,2′-bipyrimidine) have revealed that the MLCT absorption band becomes blue-shifted compared to the neutral parent compound.[44] However, it has remained open-ended whether the MLCT photoexcitation in the singly reduced state similarly initiates the CO dissociation to directly generate the 5-coordinate radical anion. The aim of this work is to probe the CO photodissociation from $[Mo(6,6'\text{-dmbipy})(CO)_4]^{\bullet-}$ at the applied cathodic potential of R2′ to form the transient $[Mo(6,6'\text{-dmbipy})(CO)_3]^{\bullet-}$ concomitantly reducible to $[Mo(6,6'\text{-dmbipy})(CO)_3]^{2-}$ thereby providing access to the catalytic activation of CO_2 at a considerably reduced overpotential regardless of the cathodic metal surface.

As stated, our primary goal in this study is to investigate the possibility of photo-assisted electrochemical reduction of CO_2 already at, or close to the parent cathodic wave R1, that is, at a significantly reduced overpotential: first, to prove the formation of the catalyst in the absence of CO_2 and then to explore the CO_2 activation under the same conditions. In both selected cases, $[Mn(bipy)(CO)_3Br]$ and $[Mo(6,6'\text{-dmbipy})(CO)_4]$, the negatively shifted second electrochemical reduction step generating the active catalyst was tested for replacement by the controlled photoirradiation, allowing the catalyst to form.

4.3 Experimental

Materials and Methods

Tetrahydrofuran (THF, Fisher) was freshly distilled from sodium/benzophenone (soluble purple ketyl radicals). Prior to use, the solvent was bubbled with dry argon (BOC, 99.9%) on a frit. The supporting electrolyte, tetrabutylammonium hexafluorophosphate (Bu_4NPF_6, $>$ 99.8%, Acros-Organics) was recrystallized twice from hot ethanol and then dried under vacuum. The supporting electrolyte was dried prior to use once more at 120 °C for 12 h. All electrochemical measurements were conducted under an atmosphere of dry argon, or CO_2 (BOC, 99.9%), using standard Schlenk techniques. Prior to electrocatalytic experiments, solutions were saturated with CO_2 by bubbling on a frit at the atmospheric pressure. [Mn(2,2′-bipyridine)$(CO)_3$Br] (**1**) (ref.[10]), [Mn(2,2′-bipyridine)$(CO)_3$(OTf)] (ref[45]) and [Mo(6,6′-dimethyl-2,2′-bipyridine)$(CO)_4$] (**2**) (ref.[19]) were synthesised in house according to the established literature procedures. ^{1}H NMR spectra were measured on a Bruker 400 MHz Nanobay spectrometer. The identity and purity of the studied complexes were confirmed by a combination of IR spectroscopy, ^{1}H NMR spectroscopy and cyclic voltammetry. [Mn(2,2′-bipyridine)$(CO)_3$Br]: IR (THF), ν(CO) at 2023, 1934 and 1915 cm^{-1}. [Mn(2,2′-bipyridine)$(CO)_3$(OTf)]: IR (THF), ν(CO) at 2043 and 1943 cm^{-1}; ^{1}H NMR (400 MHz, $CDCl_3$) δ 9.28 (2H, d, J = 5.2 Hz), 8.16 (4H, m, J = 8 Hz), 7.32 (2H, t, J = 6 Hz). [Mo(6,6′-dimethyl-2,2′-bipyridine)$(CO)_4$]: IR (THF), ν(CO) at 2014, 1899, 1879 and 1836 cm^{-1}; ^{1}H NMR (400 MHz, CD_2Cl_2) δ 7.84 (2H, d, J = 7.6 Hz), 7.74 (2H, t, J = 7.5 Hz), 7.32 (2H, d, J = 7.1 Hz), 2.95 (6H, s).

Cyclic Voltammetry

Cyclic voltammograms were recorded on a PGSTAT302N potentiostat (Metrohm Autolab) under an atmosphere of dry argon using a standard configuration of an airtight, three-electrode, single-compartment cell. Pt, Au or Cu microdiscs (all d = 0.4 mm), polished by 0.25-μm diamond paste (Kemet), served as the working electrode; the auxiliary and pseudo-

reference electrodes were made of coiled Pt and Ag wires, respectively, protected by a glass mantle. Ferrocene (Fc) served as the internal potential reference for these measurements and was added just before the ultimate voltammetric scan. The solutions prepared for cyclic voltammetry contained 1 mM analyte and 10^{-1} M Bu_4NPF_6.

Infrared and UV-Vis Spectroelectrochemistry

Infrared spectroelectrochemical experiments were performed on a Bruker Vertex 70v FT-IR spectrometer, equipped with a DTLaGS detector. UV-Vis spectroelectrochemical experiments were conducted on a Scinco S-3100 diode-array spectrophotometer. The electrochemical response in the form of a thin-layer cyclic voltammogram (TL-CV) at $\upsilon = 2$ mV s^{-1} was recorded during both IR and UV-Vis monitoring of the controlled-potential electrolyses with an EmStat3 potentiostat (PalmSens). The spectroelectrochemical measurements were conducted with an optically transparent thin-layer electrochemical (OTTLE) cell (Spectroelectrochemistry Reading).[46] The cell was equipped with either a Pt, Au or Cu minigrid working electrode, a Pt minigrid auxiliary electrode, an Ag microwire pseudo-reference electrode and CaF_2 optical windows. The solutions prepared for spectroelectrochemistry contained 3 mM analyte and 3×10^{-1} M Bu_4NPF_6.

Photochemistry

In-situ irradiation of the masked active cathodic space of the OTTLE cell during the cathodic electrolyses was accomplished using a light-emitting diode (LED) driver (ThorLabs). A 405-nm LED (M405L4) was used for [Mn(bipy)$(CO)_3$Br] and a 365-nm LED (M365L2) for [Mo(6,6′-dmbipy)$(CO)_4$] experiments, both equipped with a collimating lens. The LED was placed in front of the cell window and switched on to a maximum power once the initial $1e^-$ electrochemical reduction of the parent complex was complete. Samples were irradiated and spectra recorded at 5 or 10 min intervals, up to a maximum of 45 min total irradiation time; this was sufficient in most cases to convert 60-70% of the starting material to the further reducible photoproduct, as revealed by IR spectral monitoring.

4.4 Results and Discussion

The primary method of investigation in this report is IR spectroelectrochemistry at ambient conditions, conducted with a purpose-built OTTLE cell that permits the combination of in-situ irradiation with an LED source and spectroscopic monitoring of the electrochemistry required for this project.

4.4.1 Photo-assisted Electrochemical Reduction of [Mn(bipy)(CO)$_3$Br]

To reiterate from the introductory section, the electrochemical activation of [Mn(bipy)(CO)$_3$Br] (**1**) has been reported extensively. In THF, cyclic voltammetry (Figure 4A.1, Appendix) reveals two irreversible cathodic waves, R1 ($E_{p,c}$ = -1.91 V vs Fc/Fc$^+$), due to the overall parent-to-dimer conversion (ECEC) process, and R(D) ($E_{p,c}$ = -2.11 V) where the dimer further reduces to form the 2e$^-$-reduced [Mn(bipy)(CO)$_3$]$^-$ at the cathode. It is now widely accepted that the latter 5-coordinate anion is the dominant active electrocatalyst at R(D). IR spectroelectrochemistry, (Figure 4A.2, Appendix) provides an unambiguous assignment of the reduced species. At R1, the parent-to-dimer reduction is confirmed by the replacement of the ν(CO) bands of **1** at 2023, 1934 and 1915 cm^{-1} with five (of the six possible) ν(CO) bands of [Mn(bipy)(CO)$_3$]$_2$ at 1977, 1963, 1935, 1883 and 1864 cm^{-1}. While at R(D), two low-lying broad absorbances at 1916 and 1819 cm^{-1} are characteristic of the highly π-delocalized, fluxional 5-coordinate anion.[47]

Figure 4.1 then shows the result of the alternative photo-assisted 2e$^-$ electrochemical reduction experiment at R1. In the first instance, the dimer is electrogenerated from **1** via the same ECEC cathodic path. Thus, instead of further increasing the overpotential towards R(D), photoirradiation at 405 nm triggers the conversion of the dimer to the 5-coordinate anion already at R1. The catalyst remains 'locked' in the active 2e$^-$-reduced form, with an additional electrochemical energy cost of further reducing the dimer almost completely negated. The UV-Vis absorption spectra of parent **1**, the dimer and the 5-coordinate anion are depicted in Figure 4A.3 (Appendix). The visible electronic absorption

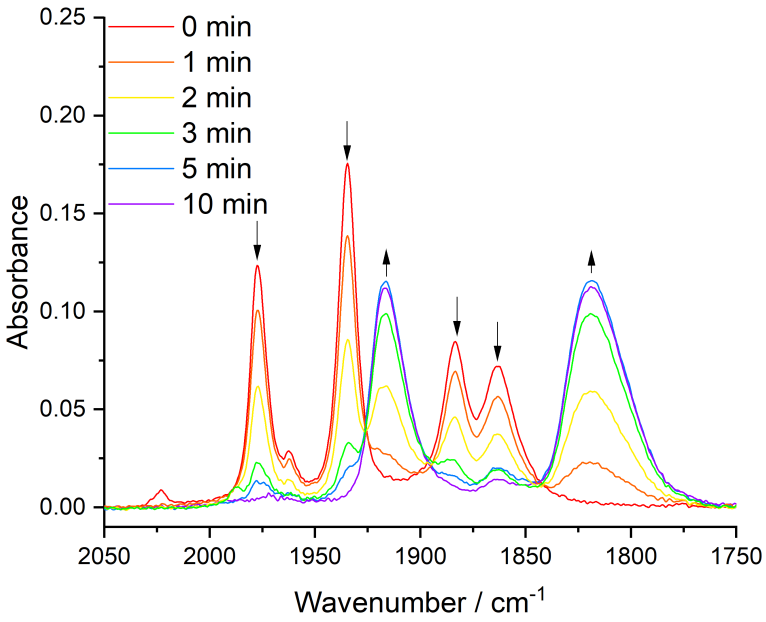

Figure 4.1: IR SEC monitoring of the photo-assisted electrochemical reduction of **1** at R1, which ultimately yields the 5-coordinate anion $[Mn(bipy)(CO)_3]^-$ (↑), following 405 nm irradiation of electrogenerated $[Mn(bipy)(CO)_3]_2$ (↓) over the course of several minutes. Conditions: THF/Bu_4NPF_6, an OTTLE cell (Pt mesh cathode), T = 298 K.

of $[M(bipy)(CO)_3]_2$ (M = Mn and Re[38]) is very similar and we consider the same MLCT assignment as reported for M = Re. Irradiation into two separate bands of $[Mn(bipy)(CO)_3]_2$ at λ_{max} = 398 and 832 nm was attempted.

Only the high-energy excitation with λ_{exc} = 405 nm led to the Mn−Mn bond cleavage, giving access to the dissociative $^3\sigma_{MM}\sigma^*_{MM}$ state. The low-energy excitation most likely populates the $\sigma_{MM}(d)\pi^*$ (bipy) charge transfer state with a high energetic barrier to cross to the dissociative $^3\sigma_{MM}\sigma^*_{MM}$ state, hence keeping the Mn−Mn bond intact. Comparison of the relative IR ν(CO) absorbances of the dimer and $[Mn(bipy)(CO)_3]^-$ formed during the standard electrochemical (Figure 4A.2) and photo-assisted (Figure 4.1) processes at R(D) and R1, respectively, reveals that not all the electrogenerated dimer molecules are converted into the 5-coordinate anion along the photo-assisted route. Instead, upon the 405 nm photoexcitation the dimer seems to follow a parallel photodecarbonylation pathway, which is accounting for the lower ν(CO) band intensities of the 5-coordinate anion in Figure 4.1, compared to the IR spectral changes in Figure 4A.2 (Appendix). Aside from this, in

THF, a still significant amount of the dimer is successfully converted to the 5-coordinate anion. It is worth noting that when the same experiment was tried in the ionic liquid, [BMIM][OTF], hardly any of the dimer was successfully converted to the 5-coordinate anion. This may well be attributed to the enhanced dipole in this unusual solvent.

The presence of either 5% trifluoroethanol (TFE) or methanol (MeOH) in the Ar-saturated electrolyte does not impact the photo-assisted conversion process at R1 significantly (Figures 4A.4 and 4A.5, Appendix). With CO_2 dissolved in the dry THF/Bu_4NPF_6 electrolyte, the 5-coordinate anion can again be produced from the dimer via the standard ECE cathodic process at R(D) (Figure 4A.6, Appendix) or the photo-assisted process at R1 (Figure 4A.7, Appendix), and no conversion of CO_2 is observed in either case. As expected, the electrocatalytic reduction of CO_2 is observed only with the Brønsted acids (TFE or MeOH) added to the electrolyte. Along the standard electrochemical route, only a limited CO_2 conversion is noticed at R1 (Figure 4.2 and Figure 4A.8, Appendix), where **1** is again converted to the dimer by the ECEC mechanism. It is only when R(D) is passed and the 5-coordinate anion reformed (but not detected in this case due to its rapid reaction with CO_2) that the electrocatalytic process begins in earnest, as testified primarily by the decreasing reference satellite $^{13}CO_2$ peak. The primary product of the CO_2 reduction is CO in this case.[10] Another species was also observed, exhibiting a C=O stretch at 1694 cm^{-1} in THF/TFE (Figure 4.2) or 1665 cm^{-1} in THF/MeOH (Figure 4A.8, Appendix) so far unreported in the literature to the best of our knowledge. These wavenumbers are attributed to subordinate bicarbonate usually accompanying the main CO product.

This assignment is supported by experiments with isotopically labelled $^{13}CO_2$ (Figure 4A.9, Appendix), which reveal an isotopic shift of almost 50 cm^{-1} in line with the ^{13}C=O stretch. The varying position of this band in the IR spectra points to an interaction of the bicarbonate side product with the Brønsted acids used. Encouragingly, CO accompanied by bicarbonate, and some formate were formed also during the photo-assisted electrochemical reduction of **1** at R1 in the presence of CO_2/5% TFE (Figure 4.3) or CO_2/5% MeOH (Figure 4A.10, Appendix), proving that the electrocatalytic CO_2 reduction occurs successfully

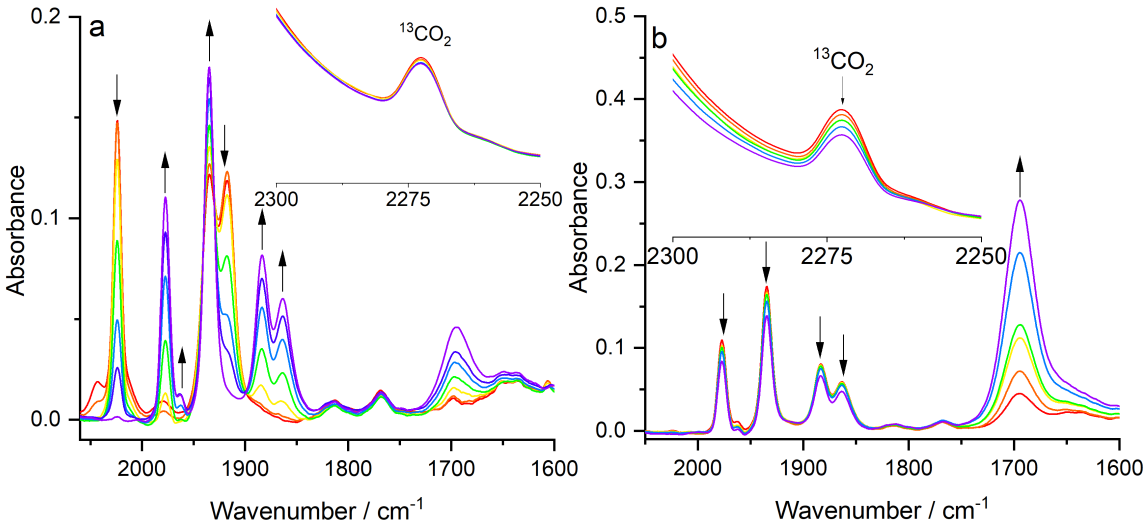

Figure 4.2: IR SEC monitoring of (a) the standard electrochemical reduction of $[Mn(bipy)(CO)_3Br]$ (**1**) (↓) to $[Mn(bipy)(CO)_3]_2$ (↑) at R1, and (b) the dimer (↓) to the catalyst $[Mn(bipy)(CO)_3]^-$ at R(D) (detectable only under argon, cf. Figure 4A.4a, Appendix), triggering electrocatalytic reduction of CO_2. Inset: the $^{13}CO_2$ satellite peak used as a reference. Conditions: CO_2-saturated THF/Bu_4NPF_6 containing 5% TFE, an OTTLE cell (Pt mesh cathode), $T = 298$ K.

at the lower overpotential under these conditions. However, compared to the standard electrocatalytic process at R(D) (Figure 4.2 and Figure 4A.8, Appendix), markedly less CO_2 reacted on the photo-assisted electrocatalytic activation at R1 in the same time interval.

At this stage we cannot identify the reason for the observed difference with certainty. However, the somewhat disappointing lower catalytic performance under CO_2 is assumed to be a result of the above-mentioned parallel photodecomposition reaction of the dimer, which prevents the full recovery of the catalyst in each redox cycle. In this way, the $^{13}CO_2$ experiment was particularly important to exclude any CO that may be produced via photodecarbonylation. If the dimer were photostable in this respect the performance along the standard and photo-assisted electrocatalytic routes should have been comparable. Nevertheless, as a proof of concept, the $[Mn(bipy)(CO)_3]^-$ catalyst is no doubt active at the cathodic wave R1 of precursor **1** in the photo-assisted mode.

The related complex, $[Mn(bipy)(CO)_3(OTf)]$ (OTf = $CF_3SO_3^-$) was also investigated during the course of this study. This derivative is reducible at a significantly less negative

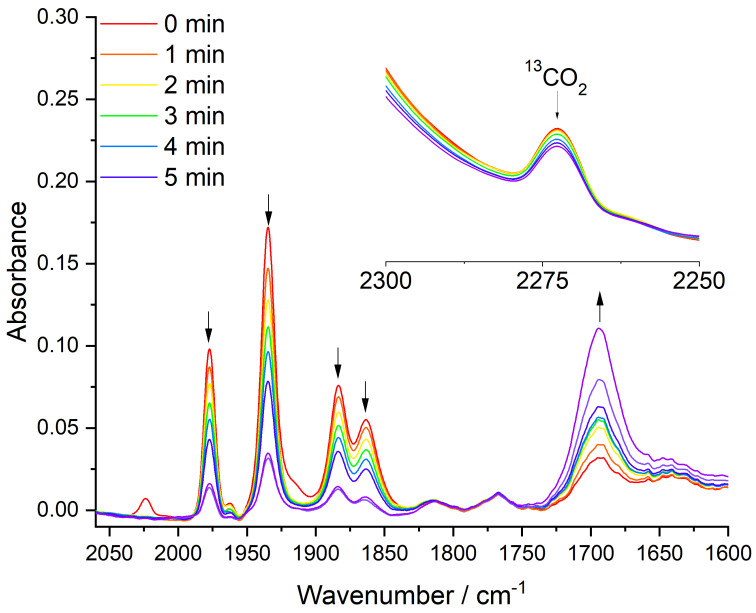

Figure 4.3: IR SEC monitoring of the photo-assisted electrochemical reduction of $[Mn(bipy)(CO)_3]_2$ (↓) pre-formed from **1** at R1, to the catalyst $[Mn(bipy)(CO)_3]^-$ at the same cathodic potential (detectable under argon, cf. Figure 4A.4b, Appendix), triggering electrocatalytic reduction of CO_2. Inset: the $^{13}CO_2$ satellite peak used as a reference. Conditions: CO_2-saturated THF/Bu_4NPF_6 containing 5% TFE, an OTTLE cell (Pt mesh cathode), λ_{exc} = 405 nm (irradiation times in minutes), T = 298 K.

cathodic potential compared to R1 of **1**, viz. $E_{p,c}$ = -1.32 V vs Fc/Fc^+ ($\Delta E_{p,c}$ = +0.59 V), see Figure 4A.11 (Appendix). The latter value is actually less negative than the anodic potential for the reoxidation of $[Mn(bipy)(CO)_3]^-$, viz. $E_{p,a}$ = -1.64 V vs Fc/Fc^+, which represents the limiting value for the dimer-based photo-assisted cathodic process. Thus, in order to keep the 5-coordinate anion stable during the photo-assisted measurement it was necessary to set the potential slightly more negative of R1, that is, in the vicinity of R2′ (Scheme 4.1). Despite the less negative reduction potential, spectroelectrochemistry confirms that the Mn-OTf complex (ν(CO) at 2043 and 1943br cm^{-1}) converts again to $[Mn(bipy)(CO)_3]_2$ at R1, which reduces further at R(D) to give the stable 5-coordinate anion (Figure 4A.12, Appendix). Importantly, $[Mn(bipy)(CO)_3]^-$ can also be produced with the photo-assistance already at R2′ (around 1.55 V vs Fc/Fc^+) from transient $[Mn(bipy)(CO)_3]$ (Figure 4A.13, Appendix).

4.4.2 Photo-assisted Electrochemical Reduction of [Mo(6,6′-dmbipy)(CO)$_4$]

The electrochemical activation of **2** under both Ar and CO_2 has already been extensively described elsewhere, using again a combination of CV and IR/UV-Vis spectroelectrochemistry.[19] To refresh, on the cathodic scan two separate reduction steps can be observed (Figure 4A.14, Appendix). The first one (R1) is the reversible 1e$^-$ reduction producing stable [Mo(6,6′-dmbipy)(CO)$_4$]$^{\bullet-}$. In THF/Bu_4NPF_6 at a Pt cathode, this process lies at $E_{1/2}$ = -2.13 V vs Fc/Fc$^+$. The subsequent irreversible reduction of the 6-coordinate radical anion at $E_{p,c}$ = -2.71 V (R2) produces the 5-coordinate dianion, [Mo(6,6′-dmbipy)(CO)$_3$]$^{2-}$. On the reverse anodic scan, the wave O2′ is observed at $E_{p,a}$ = -2.41 V, which corresponds to 1e$^-$ oxidation of the 5-coordinate dianion to the corresponding reactive 5-coordinate radical anion. At an Au cathodic surface, the catalytic CO_2 reduction does not start at R2 but already in the vicinity of the R2′/O2′ redox couple of the tricarbonyl species. As before, infrared spectroelectrochemistry offers clarity on the nature of the reduced species (Figure 4A.15, Appendix). At R1, the low energy shift of the four ν(CO) bands of the parent cis-isomer at 2014, 1899, 1879 and 1836 cm^{-1} become red-shifted by roughly 30 cm^{-1} to 1994, 1873, 1844 and 1799 cm^{-1}. The retention of the ν(CO) tetracarbonyl band pattern advocates for the stable radical anionic structure. The subsequent cathodic conversion from the 6-coordinate radical anion to [Mo(6,6′-dmbipy)(CO)$_3$]$^{2-}$ (formally a π-delocalized $(CO)_3Mo^{-I}$−bipy$^-$ species) at R2 is proved by the appearance of three low-energy ν(CO) bands at 1843, 1718 and 1701 cm^{-1}.

Importantly, the photo-assisted electrochemical reduction of **2** (Figure 4.4), when irradiating the primary 6-coordinate radical anion with 365 nm light, generates the 5-coordinate dianion already at R2′, that is, about 400 mV less negatively than the standard electrolysis at the cathodic wave R2, regardless of the metallic cathodic surface – at Pt (Figure 4.4), Au (Figure 4A.16, Appendix) or Cu (Figure 4A.17, Appendix). This behavior presents a significant advantage over the standard cathodic path, where only the Au cathodic surface has been shown to promote limited CO dissociation from [Mo(6,6′-dmbipy)(CO)$_4$]$^{\bullet-}$, opening the chance for the 5-coordinate dianion to be produced at R2′. In this study, only the

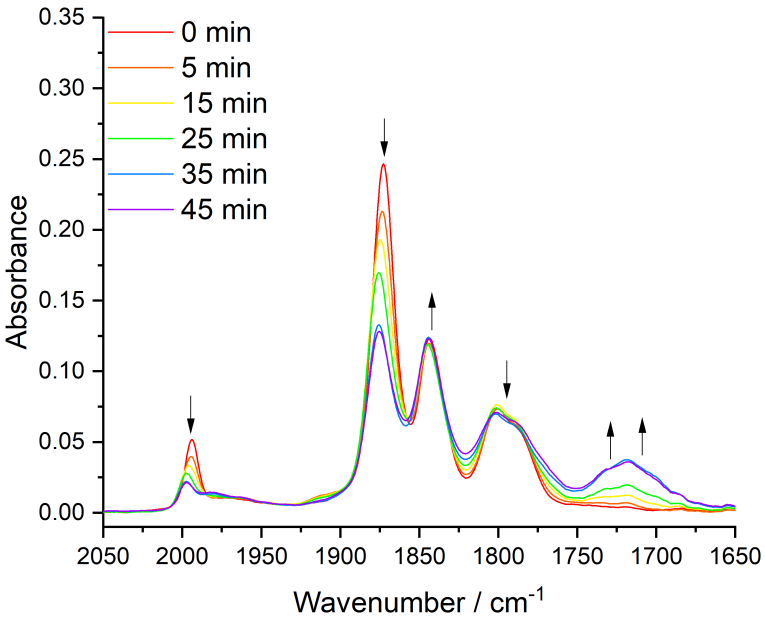

Figure 4.4: IR SEC monitoring of the photo-assisted electrochemical conversion of [Mo(6,6′-dmbipy)$(CO)_4]^{\bullet-}$ (↓), pre-formed from **2** at the cathodic wave R1, to the 5-coordinate dianion, [Mo(6,6′-dmbipy)$(CO)_3]^{2-}$ (↑) at the cathodic wave R2′. Conditions: Ar-saturated THF/Bu_4NPF_6, an OTTLE cell (Pt mesh cathode), λ_{exc} = 365 nm (irradiation times in minutes), T = 298 K.

365 nm irradiation of the tetracarbonyl radical anion was attempted, as this wavelength has the best cross-sectional overlap with the anticipated MLCT band of interest, see the UV-Vis spectrum of the radical anion (Figure 4A.18, Appendix). Unexpectedly, the 5-coordinate dianion itself is photoreactive at λ_{exc}= 365 nm (Figure 4A.19, Appendix) under the applied cathodic potential of R2, converting quickly to a secondary, yet unassigned species absorbing at 1864 and 1712br cm^{-1}. The small shift and little change in the ν(CO) band pattern point to a species having a similar molecular and electronic structure as the original [Mo(6,6′-dmbipy)$(CO)_3]^{2-}$.

In the presence of CO_2, there is no catalytic response of **2** when reduced at R1/R2′ using a Pt cathode, on the standard electrochemical route (Figure 4A.20, Appendix). It is only when the cathodic potential is swept to R2, that the catalytic reduction of CO_2 becomes evidenced by the major production of CO accompanied by bicarbonate (1676 and 1641 cm^{-1}) and subordinate formate (1607 cm^{-1}).[19] The formation of an inactive tetracarbonyl complex (ν(CO) at 2005, 1885, 1867 and 1829 cm^{-1}) is ascribed to moisture

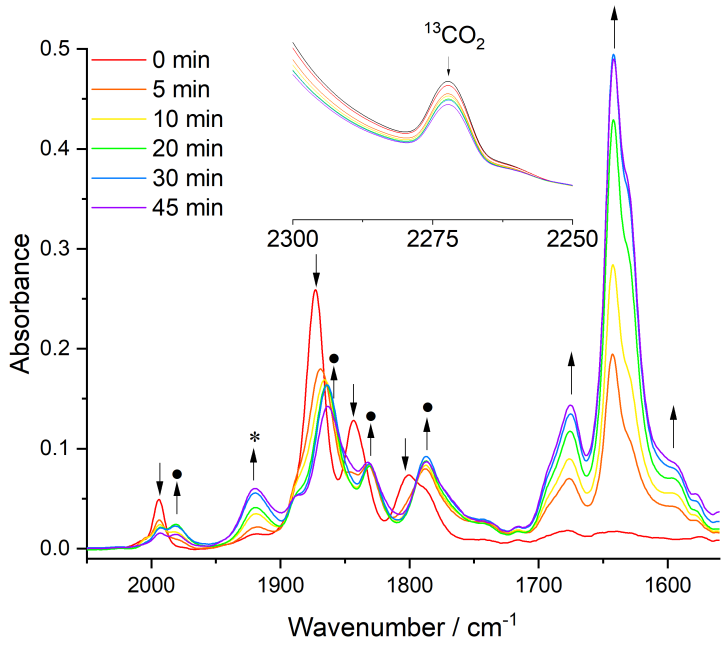

Figure 4.5: IR SEC monitoring of the photo-assisted electrochemical reduction of [Mo(6,6′-dmbipy)$(CO)_4]^{\bullet-}$ (↓) at R2′ to transient [Mo(6,6′-dmbipy)$(CO)_3]^{2-}$ that reduces a part of CO_2 to CO (accompanied by bicarbonate) and free formate. The labels • denote an ultimate tetracarbonyl product. Inset: the $^{13}CO_2$ satellite peak serving as a reference. Conditions: CO_2-saturated THF/Bu_4NPF_6, an OTTLE cell (Pt mesh cathode), λ_{exc} = 365 nm (irradiation times in minutes), T = 298 K.

present in the CO_2-saturated electrolyte, and is representing the major deactivation path for the catalyst [Mo(6,6′-dmbipy)$(CO)_3]^{2-}$. The latter wavenumbers are larger compared to [Mo(6,6′-dmbipy-H)$(CO)_4]^-$ under argon[19] (Table 1), which may reflect some interaction of the protonated anion with CO_2. The minor ν(CO) band at 1920 cm^{-1} detected during the experiment is diagnostically important for the catalytic process taking place.[26] Using the photo-assisted electrochemical reduction (Figure 4.5), an almost identical set of CO_2-originated products form already at R2′, again proving the advantage of this method. However, the ratio of the products is changed slightly as less formate seems to form along this route. Once formed, the 5-coordinate dianion reacts rapidly with CO_2, and the same also applies for the photoproduct detected during the experiment under argon, which, differently from **1**, eliminates parallel photoreactivity as a drawback in this case.

Differently from the standard electrochemical reduction at R2 under CO_2, the inactive

tetracarbonyl complex absorbing at 2005, 1885, 1867 and 1829 cm^{-1} was not observed, which ultimately led to a more efficient conversion of CO_2. Notably, a different tetracarbonyl product formed in the course of the photo-assisted electrocatalysis, with ν(CO) at 1980, 1864, 1831 and 1784 cm^{-1}. The values are smaller than the ν(CO) wavenumbers of precursor $[Mo(6,6'\text{-dmbipy})(CO)_4]^{\bullet-}$ (1994, 1873, 1844 and 1799 cm^{-1}). The identity of this resulting reduced tetracarbonyl species is unknown as yet. The growing ν(CO) band at 1920 cm^{-1}, which is marking the electrocatalytic reduction of CO_2 at R2 in Figure 4A.20 (Appendix) is also seen for the photo-assisted process at R2′ (Figure 4.5, denoted with asterisk).

Table 4.1: IR absorption data for complexes **1** and **2** and their reduction products. Measured in THF/Bu_4NPF_6 within an OTTLE cell.

Complex	ν(CO) / cm^{-1}
$[Mn(bipy)(CO)_3Br]$ (**1**)	2023, 1934, 1915
$[Mn(bipy)(CO)_3(OTf)]$	2043, 1943br
$[Mn(bipy)(CO)_3]_2$	1977, 1963, 1935, 1883, 1864
$[Mn(bipy)(CO)_3]^-$	1916, 1819
$[Mo(6,6'\text{-dmbipy})(CO)_4]$ (**2**)	2014, 1899, 1879, 1836
$[Mo(6,6'\text{-dmbipy})(CO)_4]^{\bullet-}$ ($[\mathbf{2}]^{\bullet-}$)	1994, 1873, 1844, 1799
$[Mo(6,6'\text{-dmbipy-H})(CO)_4]^{-}$[a]	1996, 1874, 1845, 1798
Unassigned Complex[b]	2005, 1885, 1867, 1829
Unassigned Complex[c]	1980, 1864, 1831, 1784
$[Mo(6,6'\text{-dmbipy})(CO)_3]^{2-}$	1843, 1718, 1701
Unassigned Complex[d]	1864, 1712br

[a] In *N*-methyl-2-pyrrolidone.[19] [b] A tetracarbonyl complex formed upon electrochemical reduction of $[\mathbf{2}]^{\bullet-}$ at R2 in THF under CO_2. Most likely an adduct of protonated $[Mo(6,6'\text{-dmbipy-H})(CO)_4]^-$ (Ref.[19]) with CO_2. [c] A tetracarbonyl complex formed upon the photo-assisted electrochemical reduction of $[\mathbf{2}]^{\bullet-}$ at R2′ in THF under CO_2. [d] A tricarbonyl complex formed upon photoirradiation of $[Mo(6,6'\text{-dmbipy})(CO)_3]^{2-}$ in THF.

4.5 Conclusions

We have shown how combined photo- and electrochemical reactivity of catalyst precursors can be exploited in attempts to specifically target a high-overpotential catalyst of CO_2 reduction along the reduction path of two reference parent complexes of Earth-abundant

transition metals, [Mn(bipy)$(CO)_3$Br] and [Mo(6,6′-dmbipy)$(CO)_4$]. In terms of the required overpotential, the dissociative photoexcitation of the $1e^-$ reduced intermediates, viz. $[Mn(bipy)(CO)_3]_2$ and $[Mo(6,6'\text{-dmbipy})(CO)_4]^{\bullet -}$, respectively, assists the electrochemical reduction by replacing the second cathodic step at a highly negative electrode potential. Thereby effectively 'locking' the $2e^-$-reduced catalyst in the active form at (Mn) or close to (Mo) the parent reduction potential, or more precisely close to its reoxidation potential, which is almost unheard of for these catalysts. Despite the positives, the behavior is obviously complex, and more work is needed to understand particularly the details of photochemistry behind the cleavage of the Mn−Mn and Mo−CO bonds, respectively, in the $1e^-$ reduced catalyst precursors. There is a clear potential for the powerful photo-assisted alternative to the exclusively electrocatalytic cathodic process. This pilot study demonstrates that the onset of the electrocatalytic reduction of CO_2 to CO can be shifted to a lower energy significantly, depending on the redox properties of the catalyst. The presented exploratory work is believed to serve as an inspiration for the community to search for other cases where photo-assisted electrochemical activation may successfully be applied to trigger, and facilitate, electron-transfer-based catalytic processes.

4.6 Appendix to Chapter 4

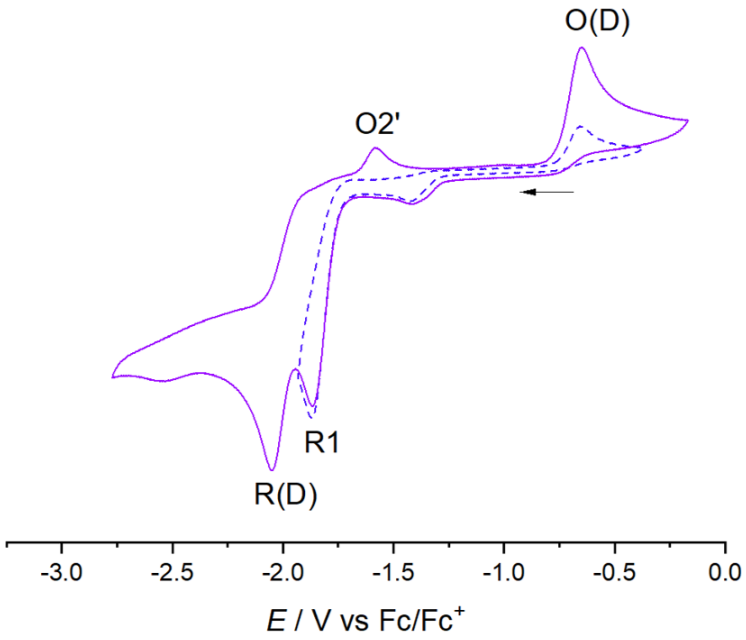

Figure 4A.1: Cyclic voltammogram of $[Mn(bipy)(CO)_3Br]$. Conditions: Ar-saturated THF/Bu_4NPF_6, Pt microdisc electrode, $\upsilon = 100$ mV s^{-1}, $T = 298$ K. Legend: R1 - reduction of the parent complex; R(D) and O(D) - reduction and oxidation of $[Mn(bipy)(CO)_3]_2$; O2′ – oxidation of $[Mn(bipy)(CO)_3]^-$. Arrow indicates the initial scan direction.

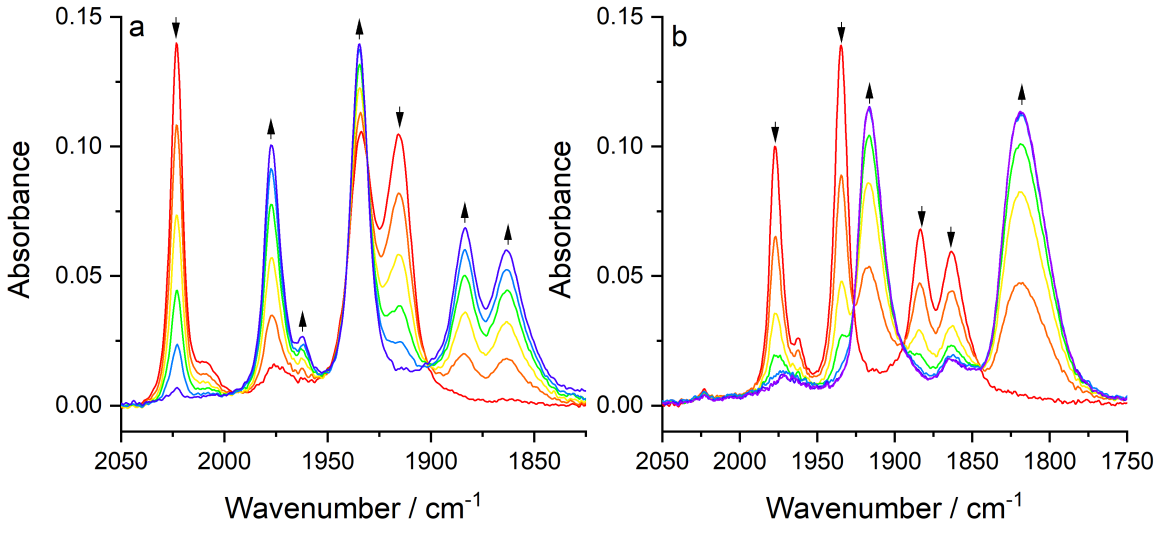

Figure 4A.2: IR SEC monitoring of $[Mn(bipy)(CO)_3Br]$ during (a) the initial reduction at R1 producing the dimer $[Mn(bipy)(CO)_3]_2$, and (b) the subsequent dimer reduction at R(D) to give the 5-coordinate anion $[Mn(bipy)(CO)_3]^-$. Conditions: Ar-saturated THF/Bu_4NPF_6, an OTTLE cell (Pt-mesh cathode), $T = 298$ K.

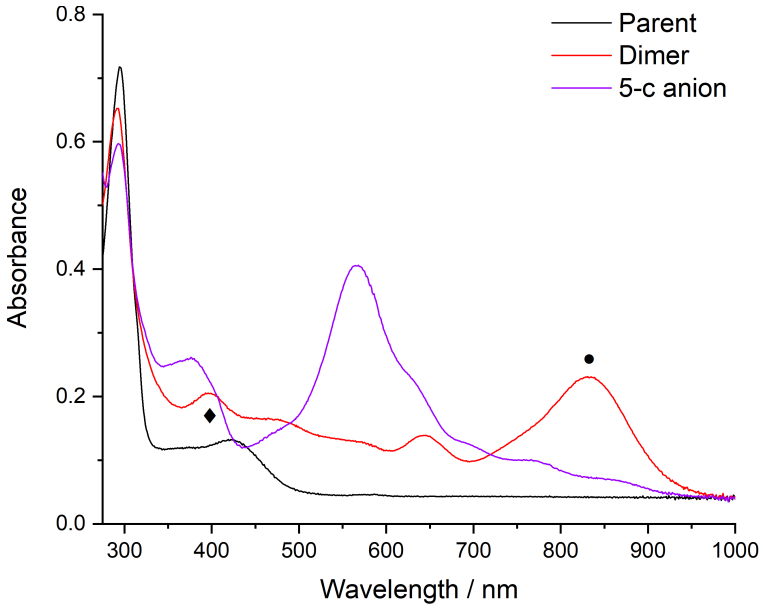

Figure 4A.3: UV-Vis spectra of parent $[Mn(bipy)(CO)_3Br]$ (black), the dimer $[Mn(bipy)(CO)_3]_2$ (red) and the 5-coordinate anion, $[Mn(bipy)(CO)_3]^-$ (purple). The label ♦ denotes the irradiation wavelength used for the dimer to cleave the Mn–Mn bond; the label • indicates the optical excitation with no photoreaction observed. Conditions: Ar-saturated THF/Bu_4NPF_6, an OTTLE cell (Pt mesh cathode), $T = 298$ K.

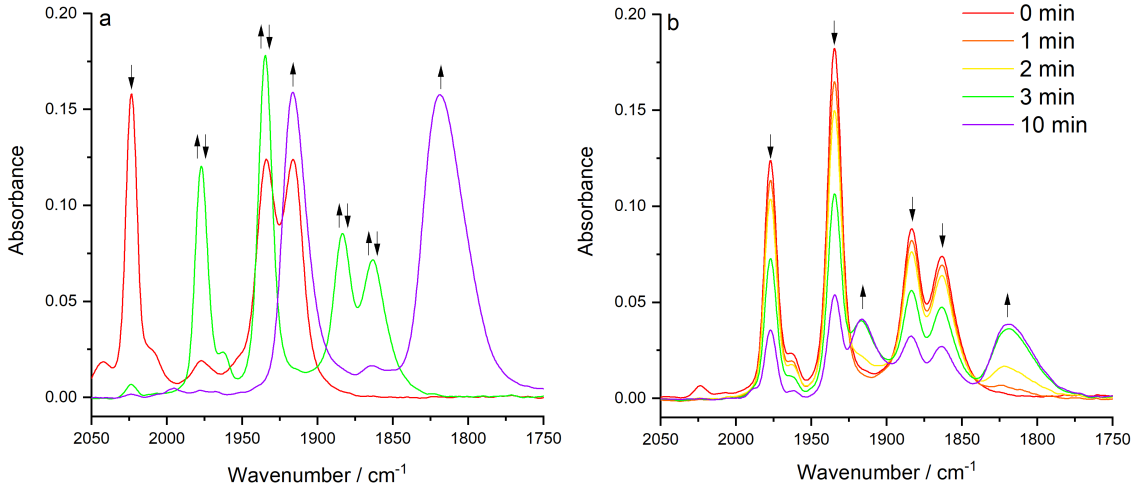

Figure 4A.4: IR SEC monitoring of (a) the standard electrochemical reduction of $[Mn(bipy)(CO)_3Br]$ (**1**) (↓) to $[Mn(bipy)(CO)_3]_2$ (↑↓) at R1, and the dimer to $[Mn(bipy)(CO)_3]^-$ (↑) at R(D), and (b) the photo-assisted electrochemical reduction of $[Mn(bipy)(CO)_3]_2$ (↓) pre-formed from **1** at R1, to $[Mn(bipy)(CO)_3]^-$ (↑) at the same cathodic potential. Conditions: Ar-saturated THF/Bu_4NPF_6 containing 5% TFE, an OTTLE cell (Pt mesh cathode), $\lambda_{exc} = 405$ nm (irradiation times in minutes), $T = 298$ K.

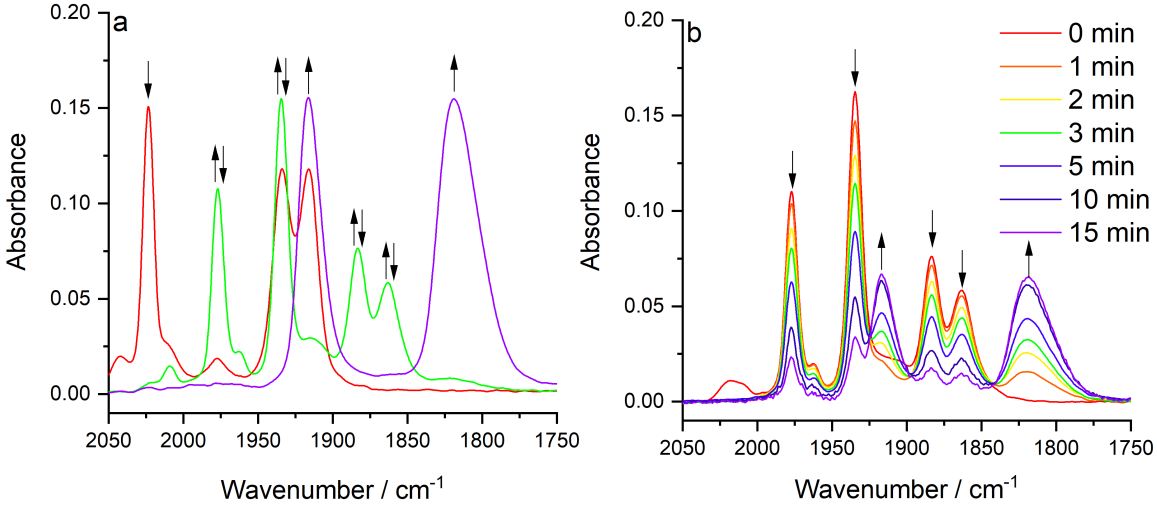

Figure 4A.5: IR SEC monitoring of (a) the standard electrochemical reduction of $[Mn(bipy)(CO)_3Br]$ (**1**) (↓) to $[Mn(bipy)(CO)_3]_2$ (↑↓) at R1, and the dimer to $[Mn(bipy)(CO)_3]^-$ (↑) at R(D), and (b) the photo-assisted electrochemical reduction of $[Mn(bipy)(CO)_3]_2$ (↓) pre-formed from **1** at R1, to $[Mn(bipy)(CO)_3]^-$ (↑) at the same cathodic potential. Conditions: Ar-saturated THF/Bu_4NPF_6 containing 5% MeOH, an OTTLE cell (Pt mesh cathode), $\lambda_{exc} = 405$ nm (irradiation times in minutes), $T = 298$ K.

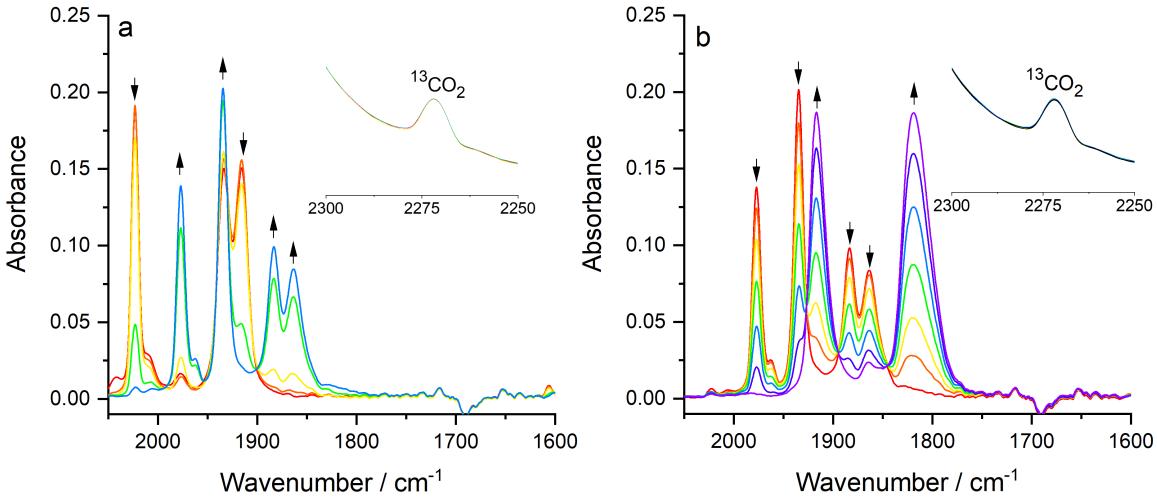

Figure 4A.6: IR SEC monitoring of the electrochemical reduction of (a) **1** (↓) at the cathodic wave R1 to $[Mn(bipy)(CO)_3]_2$ (↑), and (b) the dimer (↓) to $[Mn(bipy)(CO)_3]^-$ (↑) at the cathodic wave R(D). Insets: the $^{13}CO_2$ satellite peak used as a reference. Conditions: CO_2-saturated dry THF/Bu_4NPF_6, an OTTLE cell (Pt mesh cathode), $T = 298$ K. No catalytic activation of CO_2 was observed under these conditions.

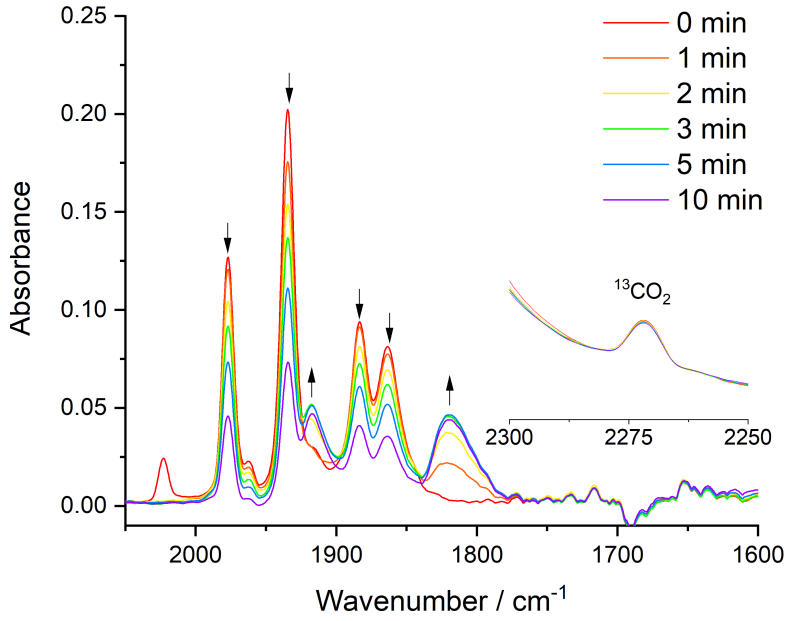

Figure 4A.7: IR SEC monitoring of the photo-assisted electrochemical reduction of $[Mn(bipy)(CO)_3]_2$ (↓) pre-formed from **1** at R1, to $[Mn(bipy)(CO)_3]^-$ (↑) at the same cathodic potential. Inset: the $^{13}CO_2$ satellite peak used as a reference. Conditions: CO_2-saturated dry THF/Bu_4NPF_6, an OTTLE cell (Pt mesh cathode), λ_{exc} = 405 nm (irradiation times in minutes), T = 298 K. No catalytic activation of CO_2 was observed under these conditions.

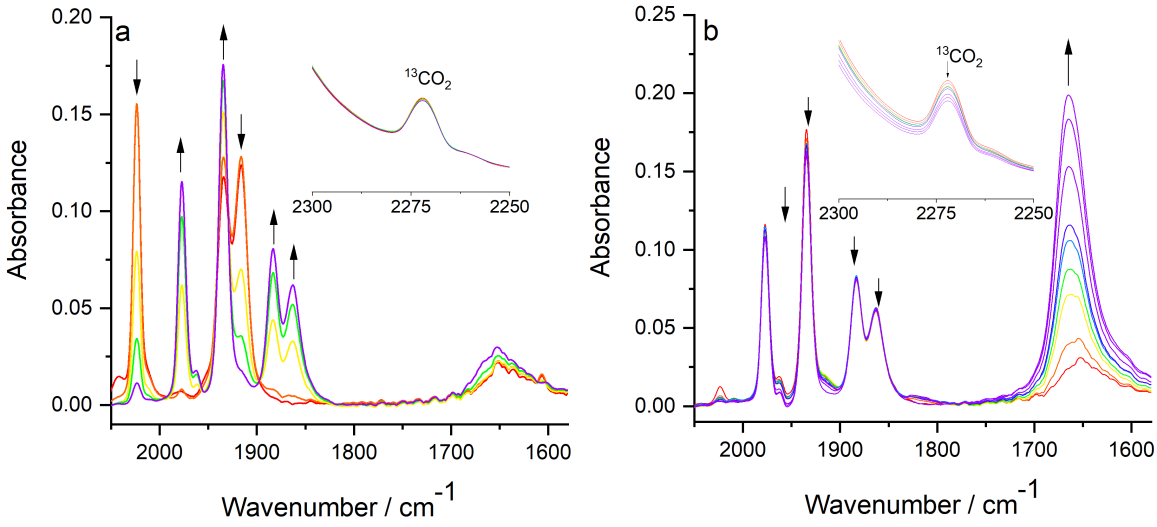

Figure 4A.8: IR SEC monitoring of (a) the standard electrochemical reduction of $[Mn(bipy)(CO)_3Br]$ (**1**) (↓) to $[Mn(bipy)(CO)_3]_2$ (↑) at R1, and (b) the dimer (↓) to $[Mn(bipy)(CO)_3]^-$ (↑) at R(D) (cf. Figure 4A.5a), triggering electrocatalytic reduction of CO_2. Inset: the $^{13}CO_2$ satellite peak used as a reference. Conditions: CO_2-saturated THF/Bu_4NPF_6 containing 5% MeOH, an OTTLE cell (Pt mesh cathode), T = 298 K.

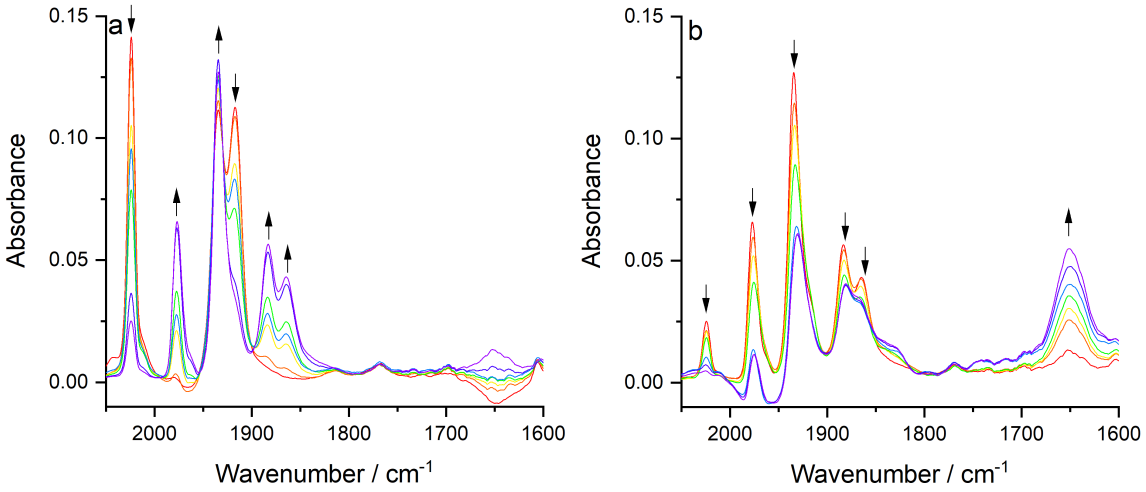

Figure 4A.9: IR SEC monitoring of (a) the standard electrochemical reduction of $[Mn(bipy)(CO)_3Br]$ (**1**) (↓) to $[Mn(bipy)(CO)_3]_2$ (↑) at R1, and (b) the dimer (↓) to $[Mn(bipy)(CO)_3]^-$ (↑) at R(D) (cf. Figure 4A.5a), triggering electrocatalytic reduction of $^{13}CO_2$. Conditions: $^{13}CO_2$-saturated THF/Bu_4NPF_6 containing 5% TFE, an OTTLE cell (Pt mesh cathode), T = 298 K.

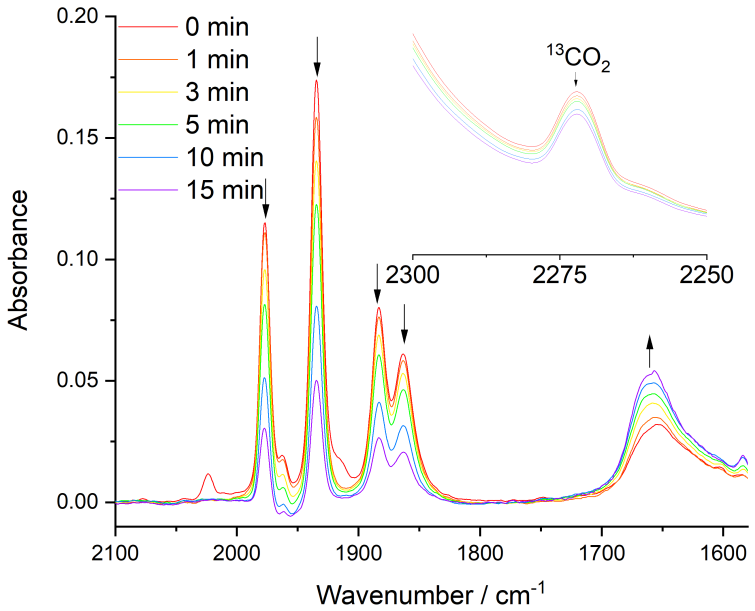

Figure 4A.10: IR SEC monitoring of the photo-assisted electrochemical reduction of $[Mn(bipy)(CO)_3]_2$ (↓) pre-formed from **1** at R1, to $[Mn(bipy)(CO)_3]^-$ at the same cathodic potential (cf. Figure 4A.5b, Appendix), triggering electrocatalytic reduction of CO_2. Inset: the $^{13}CO_2$ satellite peak used as a reference. Conditions: CO_2-saturated THF/Bu_4NPF_6 containing 5% MeOH, an OTTLE cell (Pt mesh cathode), λ_{exc} = 405 nm (irradiation times in minutes), T = 298 K.

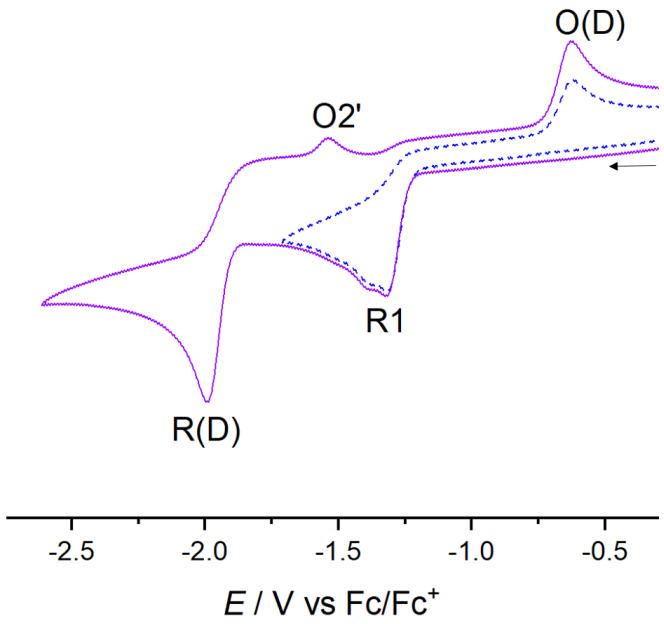

Figure 4A.11: Cyclic voltammogram of $[Mn(bipy)(CO)_3(OTf)]$. Conditions: Ar-saturated THF/Bu_4NPF_6, Pt microdisc electrode, $\upsilon = 100$ mV s^{-1}, $T = 298$ K. Legend: R1 – reduction of the parent complex; R(D) and O(D) – reduction and oxidation of $[Mn(bipy)(CO)_3]_2$; O2′ – oxidation of $[Mn(bipy)(CO)_3]^-$. Arrow indicates the initial scan direction.

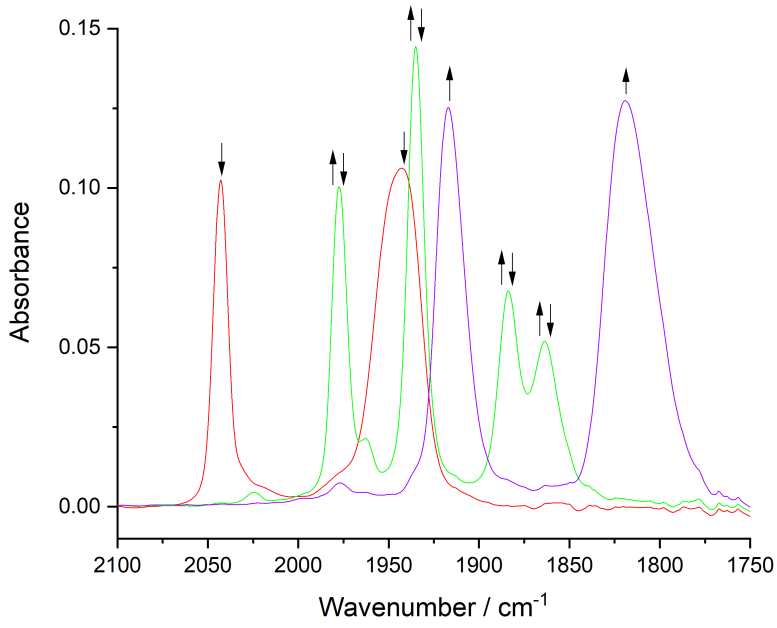

Figure 4A.12: IR SEC monitoring of (a) the standard electrochemical reduction of $[Mn(bipy)(CO)_3(OTf)]$ (**1**) (↓) to $[Mn(bipy)(CO)_3]_2$ (↑↓) at R1, and the dimer to $[Mn(bipy)(CO)_3]^-$ (↑) at R(D). Conditions: Ar-saturated THF/Bu_4NPF_6, an OTTLE cell (Pt mesh cathode), $T = 298$ K.

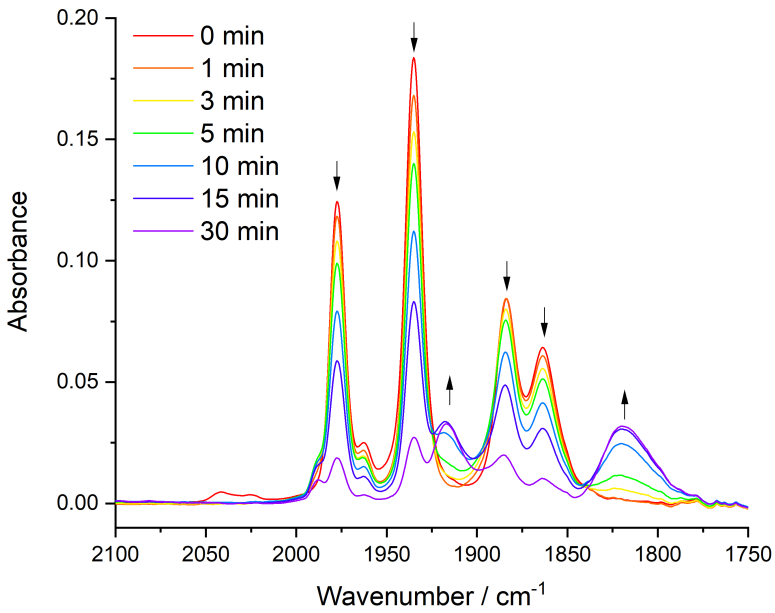

Figure 4A.13: IR SEC monitoring of the photo-assisted electrochemical reduction of $[Mn(bipy)(CO)_3(OTf)]$ (↓) at R2′ which ultimately yields the 5-coordinate anion $[Mn(bipy)(CO)_3]^-$ (↑), following 405-nm irradiation of electrogenerated $[Mn(bipy)(CO)_3]_2$ (↓) over the course of several minutes. Some photodecarbonylation of the dimer has also taken place. Conditions: Ar-saturated THF/Bu_4NPF_6, an OTTLE cell (Pt mesh cathode), T = 298 K.

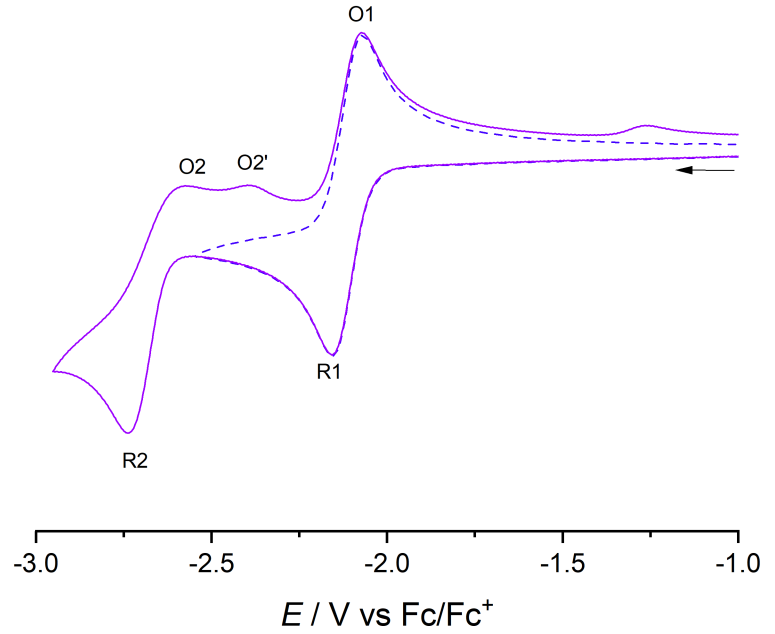

Figure 4A.14: Cyclic voltammogram of $[Mo(6,6'\text{-dmbipy})(CO)_4]$. Conditions: Ar-saturated THF/Bu_4NPF_6, Pt microdisc electrode, υ = 100 mV s^{-1}, T = 298 K. Legend: R1 – reduction of the parent complex; R2 - reduction of $[Mo(6,6'\text{-dmbipy})(CO)_4]^{\bullet-}$; O2′ – oxidation of $[Mo(6,6'\text{-dmbipy})(CO)_3]^{2-}$. Arrow indicates the initial scan direction.

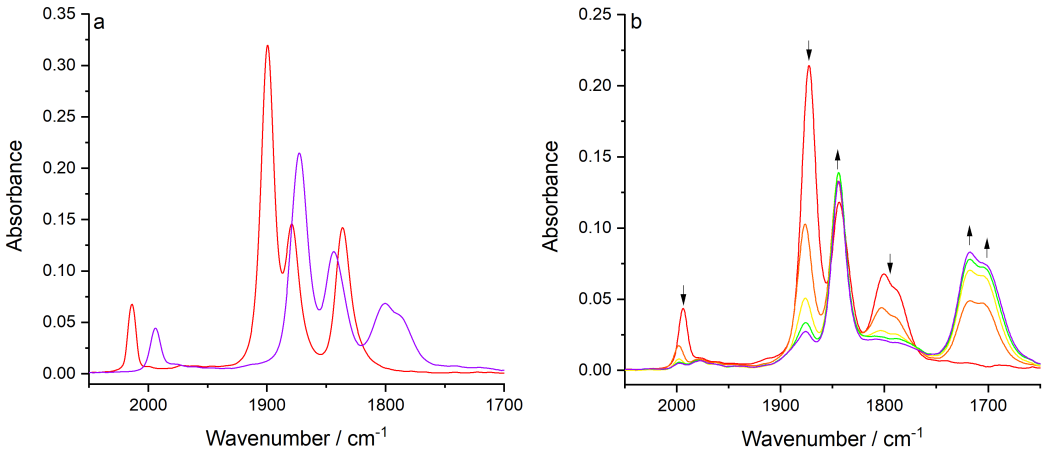

Figure 4A.15: IR SEC monitoring of (a) reduction of [Mo(6,6′-dmbipy)$(CO)_4$] at R1 (see Figure 4A.14) to [Mo(6,6′-dmbipy)$(CO)_4]^{\bullet-}$, and (b) reduction of the radical anion at R2 to 5-coordinate dianion, [Mo(6,6′-dmbipy)$(CO)_3]^{2-}$. Conditions: Ar-saturated THF/Bu_4NPF_6, OTTLE cell (Pt mesh cathode), T = 298 K.

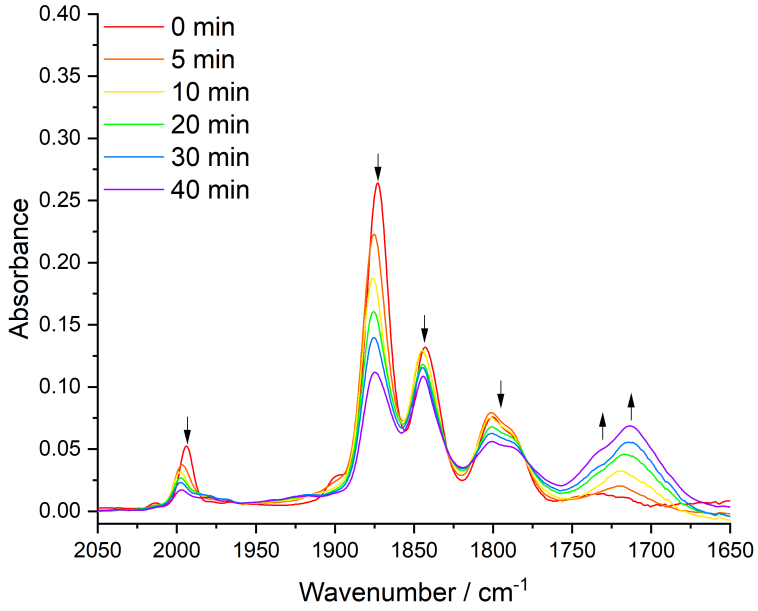

Figure 4A.16: IR SEC monitoring of the photo-assisted electrochemical reduction of [Mo(6,6′-dmbipy)$(CO)_4]^{\bullet-}$ (↓) at R2′ to the 5-coordinate dianion [Mo(6,6′-dmbipy)$(CO)_3]^{2-}$ (↑). Conditions: Ar-saturated THF/Bu_4NPF_6, OTTLE cell (Au mesh cathode), λ_{exc} = 365 nm (irradiation times in minutes), T = 298 K.

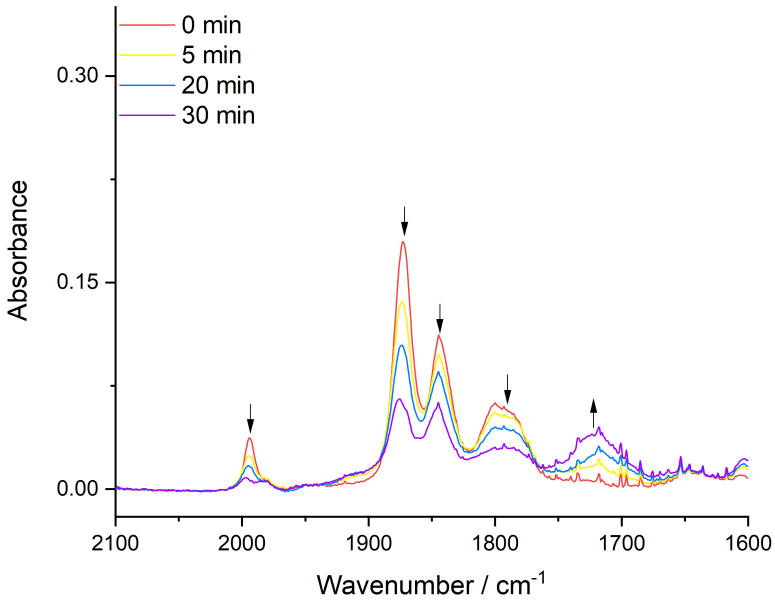

Figure 4A.17: IR SEC monitoring of the photo-assisted electrochemical reduction of [Mo(6,6′-dmbipy)$(CO)_4]^{\bullet-}$ (↓) at R2′ to the 5-coordinate dianion [Mo(6,6′-dmbipy)$(CO)_3]^{2-}$ (↑). Conditions: Ar-saturated THF/Bu_4NPF_6, OTTLE cell (Cu mesh cathode), λ_{exc} = 365 nm (irradiation times in minutes), T = 298 K.

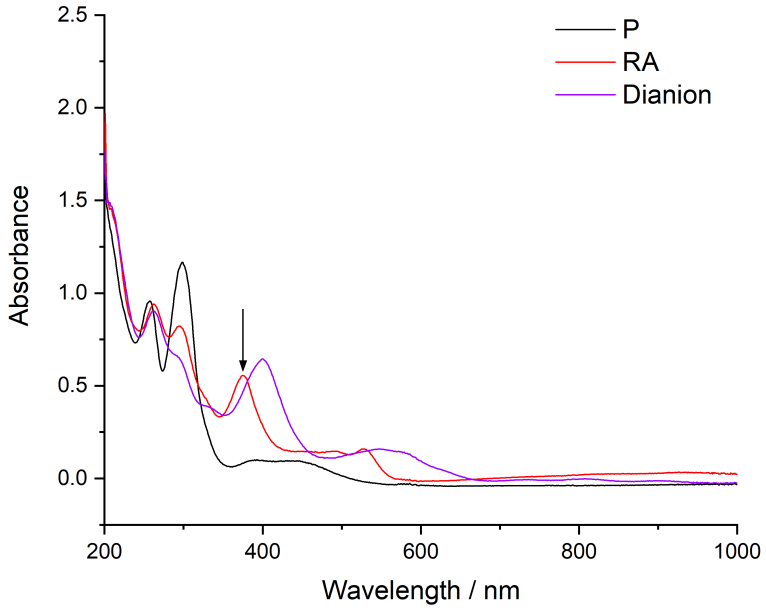

Figure 4A.18: UV-Vis absorption spectra of parent [Mo(6,6′-dmbipy)$(CO)_4$] (**2**, black), the radical anion [Mo(6,6′-dmbipy)$(CO)_4]^{\bullet-}$ (red) and the 5-coordinate dianion [Mo(6,6′-dmbipy)$(CO)_3]^{2-}$ (purple). The arrow indicates the LED irradiation wavelength (365 nm) used to optically populate the MLCT excited state of the $1e^-$ reduced radical anion. Conditions: Ar-saturated THF/Bu_4NPF_6, an OTTLE cell (Pt mesh cathode), T = 298 K.

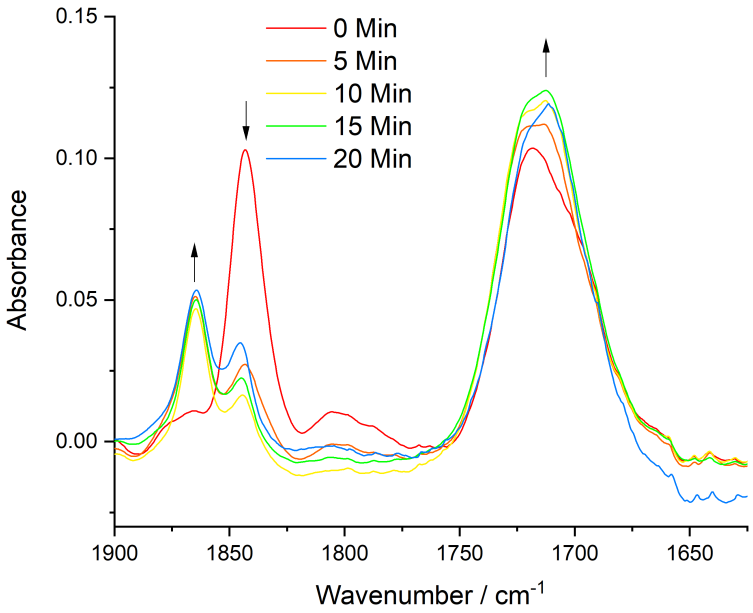

Figure 4A.19: IR SEC monitoring of the photochemical (λ_{exc} = 365 nm) transformation of the 5-coordinate dianion, $[Mo(6,6'\text{-dmbipy})(CO)_3]^{2-}$ (↓), at R2 to an unknown tricarbonyl photoproduct (↑). Conditions: THF/Bu_4NPF_6, OTTLE cell (Pt mesh cathode), T = 298 K.

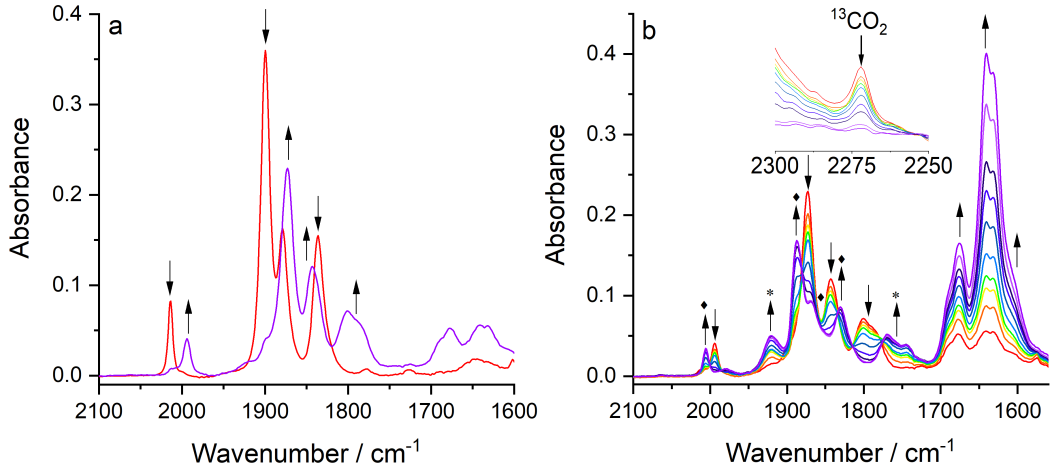

Figure 4A.20: IR spectral monitoring of (a) the initial reduction of **2** at R1 producing the radical anion $[Mo(6,6'\text{-dmbipy})(CO)_4]^{\bullet -}$, and (b) the subsequent cathodic step at R2 triggering the catalytic conversion of CO_2 to CO and formate, with some amount of accompanying bicarbonate also formed. The labels ♦ denote an inactive tetracarbonyl complex, most likely an adduct of protonated anion, $[Mo(6,6'\text{-dmbipy-H})(CO)_4]^-$ with CO_2, replacing $[Mo(6,6'\text{-dmbipy})(CO)_3]^{2-}$ (see Figure 4A.15). Unassigned carbonyl side products are labelled with asterisk. Conditions: CO_2-saturated THF/Bu_4NPF_6, an OTTLE cell (Pt mesh cathode), T = 298 K.

References

[1] N. Armaroli and V. Balzani, *Chem. Eur. J.*, 2016, **22**, 32–57.

[2] R. Francke, B. Schille and M. Roemelt, *Chem. Rev.*, 2018, **118**, 4631–4701.

[3] K. Li, X. An, K. H. Park, M. Khraisheh and J. Tang, *Catal. Today*, 2014, **224**, 3–12.

[4] J. Zhao, X. Wang, Z. Xu and J. S. C. Loo, *J. Mater. Chem. A*, 2014, **2**, 15228.

[5] K. A. Grice, *Coord. Chem. Rev.*, 2017, **336**, 78–95.

[6] N. Elgrishi, M. B. Chambers, X. Wang and M. Fontecave, *Chem. Soc. Rev.*, 2017, **46**, 761–796.

[7] C. Jiang, A. W. Nichols and C. W. Machan, *Dalton Trans.*, 2019, **48**, 9454–9468.

[8] J. Hawecker, J. M. Lehn and R. Ziessel, *J. Chem. Soc., Chem. Commun.*, 1984, **984**, 328–330.

[9] H. Takeda, K. Koike, H. Inoue and O. Ishitani, *J. Am. Chem. Soc.*, 2008, **130**, 2023–2031.

[10] M. Bourrez, F. Molton, S. Chardon-Noblat and A. Deronzier, *Angew. Chem. Int. Ed.*, 2011, **50**, 9903–9906.

[11] M. Bourrez, M. Orio, F. Molton, H. Vezin, C. Duboc, A. Deronzier and S. Chardon-Noblat, *Angew. Chem. Int. Ed.*, 2014, **53**, 240–243.

[12] J. M. Smieja, M. D. Sampson, K. A. Grice, E. E. Benson, J. D. Froehlich and C. P. Kubiak, *Inorg. Chem.*, 2013, **52**, 2484–2491.

[13] M. Stanbury, J.-D. Compain, M. Trejo, P. Smith, E. Gouré and S. Chardon-Noblat, *Electrochim. Acta*, 2017, **240**, 288–299.

[14] M. Stanbury, J.-D. Compain and S. Chardon-Noblat, *Coord. Chem. Rev.*, 2018, **361**, 120–137.

[15] D. C. Grills, M. Z. Ertem, M. McKinnon, K. T. Ngo and J. Rochford, *Coord. Chem. Rev.*, 2018, **374**, 173–217.

[16] H. Rao, L. C. Schmidt, J. Bonin and M. Robert, *Nature*, 2017, **548**, 74–77.

[17] R. B. Ambre, Q. Daniel, T. Fan, H. Chen, B. Zhang, L. Wang, M. S. G. Ahlquist, L. Duan and L. Sun, *Chem. Commun.*, 2016, **52**, 14478–14481.

[18] C. Costentin, M. Robert and J. M. Savéant, *Acc. Chem. Res.*, 2015, **48**, 2996–3006.

[19] J. O. Taylor, R. D. Leavey and F. Hartl, *ChemElectroChem*, 2018, **5**, 3155–3161.

[20] J. O. Taylor, F. L. Veenstra, A. M. Chippindale, M. J. Calhorda and F. Hartl, *Organometallics*, 2019, **38**, 1372–1390.

[21] M. L. Clark, K. A. Grice, C. E. Moore, A. L. Rheingold and C. P. Kubiak, *Chem. Sci.*, 2014, **5**, 1894–1900.

[22] F. Franco, C. Cometto, F. Sordello, C. Minero, L. Nencini, J. Fiedler, R. Gobetto and C. Nervi, *ChemElectroChem*, 2015, **2**, 1372–1379.

[23] L. Rotundo, C. Garino, R. Gobetto and C. Nervi, *Inorg. Chim. Acta*, 2018, **470**, 373–378.

[24] K. A. Grice and C. Saucedo, *Inorg. Chem.*, 2016, **55**, 6240–6246.

[25] J. Tory, G. Gobaille-Shaw, A. M. Chippindale and F. Hartl, *J. Organomet. Chem.*, 2014, **760**, 30–41.

[26] J. Tory, B. Setterfield-Price, R. A. W. Dryfe and F. Hartl, *ChemElectroChem*, 2015, **2**, 213–217.

[27] F. P. Johnson, M. W. George, F. Hartl and J. J. Turner, *Organometallics*, 1996, **15**, 3374–3387.

[28] G. Neri, P. M. Donaldson and A. J. Cowan, *Phys. Chem. Chem. Phys.*, 2019, **21**, 7389–7397.

[29] M. D. Sampson, A. D. Nguyen, K. A. Grice, C. E. Moore, A. L. Rheingold and C. P. Kubiak, *J. Am. Chem. Soc.*, 2014, **136**, 5460–5471.

[30] M. D. Sampson and C. P. Kubiak, *J. Am. Chem. Soc.*, 2016, **138**, 1386–1393.

[31] G. J. Stor, S. L. Morrison, D. J. Stufkens and A. Oskam, *Organometallics*, 1994, **13**, 2641–2650.

[32] H. Takeda, H. Koizumi, K. Okamoto and O. Ishitani, *Chem. Commun.*, 2014, **50**, 1491–1493.

[33] H. Takeda, H. Kamiyama, K. Okamoto, M. Irimajiri, T. Mizutani, K. Koike, A. Sekine and O. Ishitani, *J. Am. Chem. Soc.*, 2018, **140**, 17241–17254.

[34] T. J. Meyer and J. V. Caspar, *Chem. Rev.*, 1985, **85**, 187–218.

[35] M. Sarakha and G. Ferraudi, *Inorg. Chem.*, 2002, **38**, 4605–4607.

[36] H. Cho, K. Hong, M. L. Strader, J. H. Lee, R. W. Schoenlein, N. Huse and T. K. Kim, *Inorg. Chem.*, 2016, **55**, 5895–5903.

[37] D. Stufkens, T. van der Graaf, G. Stor and A. Oskam, *Coord. Chem. Rev.*, 1991, **111**, 331–336.

[38] E. Fujita and J. T. Muckerman, *Inorg. Chem.*, 2004, **43**, 7636–7647.

[39] Y. Hayashi, S. Kita, B. S. Brunschwig and E. Fujita, *J. Am. Chem. Soc.*, 2003, **125**, 11976–11987.

[40] G. Neri, P. M. Donaldson and A. J. Cowan, *J. Am. Chem. Soc.*, 2017, **139**, 13791–13797.

[41] J. Vichova, F. Hartl and A. Vlcek, *J. Am. Chem. Soc.*, 1992, **114**, 10903–10910.

[42] S. Záliš, I. R. Farrell and A. Vlček, *J. Am. Chem. Soc.*, 2003, **125**, 4580–4592.

[43] A. Vlček, *Coord. Chem. Rev.*, 2002, **230**, 225–242.

[44] W. Kaim, S. Kohlmann, A. J. Lees, T. L. Snoeck, D. J. Stufkens and M. M. Zulu, *Inorg. Chim. Acta*, 1993, **210**, 159–165.

[45] E. Hevia, J. Pérez, L. Riera, V. Riera and D. Miguel, *Organometallics*, 2002, **21**, 1750–1752.

[46] M. Krejčik, M. Daněk and F. Hartl, *J. Electroanal. Chem. Interfacial Electrochem.*, 1991, **317**, 179–187.

[47] F. Hartl, P. Rosa, L. Ricard, P. Le Floch and S. Záliš, *Coord. Chem. Rev.*, 2007, **251**, 557–576.

Chapter 5

Group-6 Metal Complexes as Electrocatalysts of CO_2 Reduction: Strong Substituent Control over the Reduction Path of [Mo(η^3-allyl)(x,x′-dimethyl-2,2′-bipyridine)$(CO)_2$(NCS)] (x = 4-6)

The content of this chapter was published in: **J. O. Taylor**, F. L. P. Veenstra, A. M. Chippindale, M. J. Calhorda, F. Hartl, *Organometallics*, 2019, **38**, 1372-1390.

5.1 Abstract

A series of complexes [Mo(η^3-allyl)(x,x′-dmbipy)$(CO)_2$(NCS)] (dmbipy = dimethyl-2,2′-bipyridine; x= 4-6) have been synthesized and their electrochemical reduction investigated using combined cyclic voltammetry (CV) and variable-temperature spectroelectrochemistry (IR/UV-Vis SEC) in tetrahydrofuran (THF) and butyronitrile (PrCN), at gold and platinum electrodes. The experimental results, strongly supported by density functional theory (DFT) calculations, indicate that the general cathodic path of these Group-6 organometallic complexes is closely related to that of the intensively studied class of Mn tricarbonyl α-diimine complexes, which, themselves, have recently been identified as important smart materials for catalytic CO_2 reduction. The dimethyl substitution on the 2,2′-bipyridine ligand backbone has presented new insights into this emerging class of catalysts. For the first time, the $2e^-$ reduced 5-coordinate anions [Mo(η^3-allyl)(x,x′-dmbipy)$(CO)_2$]$^-$ were directly observed with infrared spectroelectrochemistry (IR SEC). The role of steric and electronic effects in determining the reduction-induced reactivity was also investigated. For the 6,6′-dmbipy, the primary $1e^-$ reduced radical anions exhibit unusual stability, radically changing the follow-up cathodic path. The 5-coordinate anion [Mo(η^3-allyl)(6,6′-dmbipy)$(CO)_2$]$^-$ remains stable at low temperature in strongly coordinating butyronitrile and does not undergo dimerization at elevated temperature, in sharp contrast to reactive [Mo(η^3-allyl)(4,4′-dmbipy)$(CO)_2$]$^-$ that tends to dimerize in a reaction with the parent complex. The complex with the 5,5′-dmbipy ligand combines both types of reactivity. Under aprotic conditions, the different properties of [Mo(η^3-allyl)(x,x′-dmbipy)$(CO)_2$]$^-$ are also reflected in their reactivity toward CO_2. Preliminary CV and IR SEC results reveal differences in the strength of CO_2 coordination at the free axial position. Catalytic waves attributed to the generation of the 5-coordinate anions were observed using CV, but only a modest catalytic performance toward the production of formate was demonstrated by IR SEC. For 6,6′-dmbipy, a stronger catalytic effect was observed for the Au cathode, compared to Pt.

5.2 Introduction

Atmospheric levels of anthropogenic CO_2 have continued to increase unabated for several years, driving a concurrent rise in yearly average temperatures and extreme weather patterns.[1] Although it has an obvious damaging impact on the environment, CO_2 itself has potential to become a sustainable source of carbon-based fuels and chemical feedstocks for Fischer-Tropsch chemistry. To fulfill this potential, CO_2 must first be reduced electro- or photochemically, converting it from a harmful by-product of industry to compounds with the aforementioned applications.[2,3] However, the direct electrochemical reduction to $CO_2^{\bullet -}$ is hindered by large overpotentials and one must take advantage of proton-coupled reduction pathways.[3,4] An exception is a dinuclear Cu(I) catalyst reported recently by Bowman and co-workers, which reduces CO_2 from the air to oxalate isolated as a lithium salt.[5]

In comparison, the proton-coupled paths have significantly reduced energy barriers to catalysis but they must be promoted by homogeneous or heterogeneous (Cu) transition-metal catalysts. The effect of the catalyst is two-fold, enabling reduction of CO_2 at much lower overpotentials whilst also allowing one to handle a larger number of proton- and electron transfer steps facilitating the transformation to more complex and valuable reduction products such as formaldehyde, methanol or methane.[6] Of the many homogeneous transition metal electrocatalysts of CO_2 reduction known in the literature, the most widely studied have been those based on the noble metals, Re[7–12], Ru[13–15], Rh[16] and Ir.[17,18] Although first reported almost 40 years ago, they are still offering up both interesting redox properties and synthetic challenges. The high costs of these metals, as well as a strong competition for the limited supply from the electronics industry, largely preclude the possibility of any industrial-scale system. Thus, efforts now focus on the more Earth-abundant metals, Mn, Fe, Co,[19] and Ni.[20,21] Highly promising are the systems of [Mn(α-diimine)$(CO)_3$X] (X = (pseudo)-halide), which only recently have been found to be catalytically active at potentials similar to the analogous complexes of rhenium, in the presence of Brønsted or Lewis acids.[22–28] The Fe-porphyrin systems are also highly efficient catalysts of CO_2 reduction,

but synthetically challenging to prepare.[29–31]

Surprisingly, and despite the analogues found in nature, the Group-6 metal triad (Cr, Mo, W) has largely been ignored by the wider community. This has been highlighted in several recent comprehensive reviews of the field.[32–34] Preliminary studies of Group-6 complexes show a potential to catalytically reduce CO_2 with a comparable activity and efficiency to that of the widely studied Group-7 systems. Recently, it was reported that Group-6 hexacarbonyl complexes can behave catalytically toward CO_2.[35] This is highly unusual, as most catalysts reported to date bear a redox-active ligand acting as both an electron reservoir and a parking place for the protons required for catalysis. The hexacarbonyl is reduced by $2e^-$ to form $[M(CO)_5]^{2-}$ that can bind CO_2 and transform to $[M(CO)_5(CO_2)]^{2-}$. Under anhydrous conditions, the major product of the reduction is CO. Interestingly, addition of water or another proton source inhibits the activity of the catalyst, most likely due to competing formation of H_2 from $[M(CO)_5H]^-$. A comparison with $[M(CO)_5]^-$ (M = Re or Mn), formed by the reduction of the corresponding decacarbonyl dimers, shows that the Group-7 metals are not active toward CO_2 in this manner. Instead, they simply bind CO_2 and require a noninnocent ligand to trigger the reduction. The difference in their reactivity may simply be explained by the fact that the Group-6 $[M(CO)_5]^{2-}$ species are better reducing agents, because of the negative charge experiencing less nuclear charge than the comparable Group-7 species. Apart from this, the limited literature regarding Group-6 catalysts has mostly focused on the family of $[M(\alpha\text{-diimine})(CO)_4]$ catalysts.[36–40] The first of these studied as a catalyst of CO_2 reduction was $[Mo(bipy)(CO)_4]$ (bipy = 2,2′-bipyridine).[36,37] The parent complex is reduced in two consecutive $1e^-$ steps to form, first, the corresponding radical anion and then the catalytically active 5-coordinate species, $[Mo(bipy)(CO)_3]^{2-}$. The latter is isoelectronic with the Group-7 catalysts, $[M(bipy)(CO)_3)]^-$ (M = Re, Mn), formed by $2e^-$ (ECE) reduction of $[M(bipy)(CO)_3X]$ (X = (pseudo)-halide).

Unlike their Group-7 cousins, $[Mo(\alpha\text{-diimine})(CO)_4]$ (α-diimine = 2,2′-bipyridine (bipy) and x,x′-dimethyl-bipyridine (dmbipy, x = 4-6) show higher sensitivity to the cathodic material.[37,39] This can be exploited in the form of a low-energy pathway only accessible with

the use of a gold cathode that facilitates CO dissociation from the usually stable radical anion, $[Mo(bipy)(CO)_4]^{\bullet-}$, converting it to $[Mo(bipy)(CO)_3]^{\bullet-}$. The latter 5-coordinate complex is reducible to the dianionic catalyst at a cathodic potential only slightly more negative than the initial reduction of the neutral tetracarbonyl parent, thereby bypassing the energetically demanding formation of the unstable dianion, $[Mo(bipy)(CO)_4]^{2-}$. This CO dissociation-first pathway is similar to the low-energy protonation-first pathway reported for $[Mn(bipy)(CO)_3Br]$.[41] These observations have been confirmed by Cowan and co-workers using sum frequency generation (SFG) spectroscopy.[42,43]

One can also alter the pathway that these Group-6 tetracarbonyl catalysts follow, by substitution on the 2,2′-bipyridine rings.[39] Advantageous positioning of steric bulk at the 6,6′-position can enhance the CO dissociation from the primary radical anion, improving the catalytic activity, while substitution at the 4,4′-position suppresses the CO dissociation, forcing the catalyst to follow the higher-energy reduction-first pathway. Smart choice of the solvent and electrolyte, especially turning to *N*-methyl-pyrrolidone (NMP), can improve the catalytic efficiency remarkably. Nervi and co-workers[38] have described a comparable catalytic action for [M(α-diimine)$(CO)_4$] (M = Mo, W; α-diimine = 4,6-diphenyl-bipy, 4-dimethoxyphenyl-6-phenyl-bipy). A higher catalytic activity toward conversion of CO_2 to CO and a unique activation pathway have also been reported for the complexes [M(2,2′-dipyridylamine)$(CO)_4$] (M = Mo and W), in which the catalytic center resides at the bidentate ligand rather than at the metal.[38] The unusual cathodic behavior of $[W(dpa)(CO)_4]$ has been rationalized with the help of quantum mechanical calculations. The $1e^-$ reduction of the parent complex induces a rearrangement of the dpa ligand with one of the pyridine rings rotating away from the metal center, which facilitates the reduction of CO_2.[44]

Inspired by the promising performance of the Group-6 tetracarbonyl catalysts, the related complex, [Mo(η^3-allyl)(bipy)$(CO)_2$X] (X = (pseudo)-halide), was identified as a precursor to the catalytically active 5-coordinate anion, $[Mo(\eta^3\text{-allyl})(bipy)(CO)_2]^-$.[45,46] In an analogous fashion to the well-studied catalyst precursor $[Mn(bipy)(CO)_3Br]$, the radical anion [Mo(η^3-allyl)(bipy)$(CO)_2$(NCS)], formed by the initial one-electron reduction ($E_{p,c}$ = -1.99

V vs Fc/Fc^+), is very unstable at room temperature. The concomitant dissociation of the NCS^- ligand yields the 5-coordinate radical [Mo(η^3-allyl)(bipy)$(CO)_2$] that can be reduced at the applied electrode potential of the parent complex to [Mo(η^3-allyl)(bipy)$(CO)_2]^-$. This anion reacts with an as-yet-non-reduced parent, forming the dimer [Mo(η^3-allyl)(bipy)$(CO)_2]_2$, the final step of the ECEC pathway. Here, the similarity with the Mn-catalysts appears to end. In the original paper,[46] it was claimed that the 5-coordinate anion had been detected by infrared (IR) spectroelectrochemistry; however, this assignment was only tentative. The main issue to be clarified in this work is under exactly what conditions an IR-detectable quantity of the 5-coordinate anionic catalyst can be formed. Indeed, the dimer-like species produced in this instance appear to be more reactive than the related hexacarbonyl Mn-Mn bound dimers and can only be detected on the relatively short timescale of cyclic voltammetry. The subsequent reduction of the Mo−Mo dimer in the presence of CO_2 is then associated with catalytic current, and IR monitoring at the catalytic wave reveals the formation of CO and free formate.

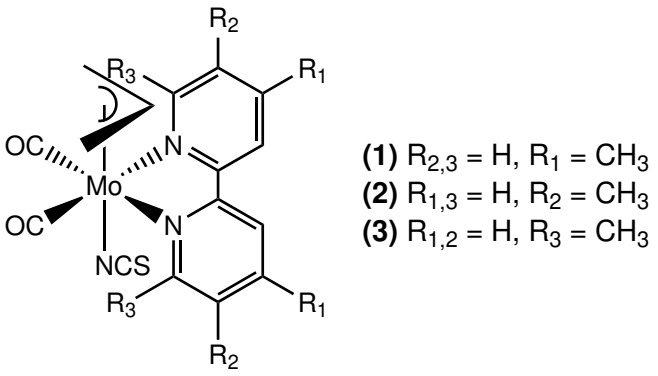

Chart 5.1: General molecular structures of the studied complexes [Mo(η^3-allyl)(x,x′-dmbipy)$(CO)_2$(NCS)] **1** (x = 4), **2** (x = 5), and **3** (x = 6).

Hereinafter, the study of the original (allyl)Mo-bipy complex is extended to the series of three x,x′-dmbipy derivatives (Chart 5.1), with the following goals: (i) to identify (by IR spectroelectrochemistry) the 5-coordinate anions [Mo(η^3-allyl)(x,x′-dmbipy)$(CO)_2]^-$, the proposed active catalysts in these systems, which were misassigned for the reference bipy complex; (ii) to assess the catalytic performance of the 5-coordinate anions via cyclic

voltammetry (CV) and infrared spectroelectrochemistry (IR SEC); (iii) to investigate the steric and electronic consequences of the dimethyl substitution at the x = x′ = 4, 5, and 6 positions of the 2,2′-bipyridine ligand on the cathodic paths; (iv) to probe the variation of the cathodic material, Pt and Au, and its impact on the reduction potentials, cathodic pathways, and catalytic performance, in analogy with $[Mo(CO)_{4-n}(x,x'\text{-dmbipy})]$ (n = 0,1; x = 4-6).

5.3 Experimental

Materials and Methods

All syntheses and electrochemical measurements were conducted under a strictly inert atmosphere of dry argon, using standard Schlenk techniques. Solvents were freshly distilled under N_2 from a mixture of Na/benzophenone (tetrahydrofuran, THF), P_2O_5 (acetonitrile, MeCN) or CaH_2 (butyronitrile, PrCN, and dichloromethane, DCM). The electrolyte, tetrabutylammonium hexafluorophosphate (Bu_4NPF_6, Acros-Organics), was recrystallized twice from hot ethanol and dried under vacuum at 80 °C. All other reagents were purchased from Sigma-Aldrich and used as received. The precursor $[Mo(\eta^3\text{-allyl})(MeCN)_2(CO)_2(NCS)]$ was prepared according to the literature procedure.[47] All the $[Mo(\eta^3\text{-allyl})(x,x'\text{-dmbipy})(CO)_2(NCS)]$ complexes were prepared by facile thermal substitution of the labile acetonitrile ligands in $[Mo(\eta^3\text{-allyl})(MeCN)_2(CO)_2(NCS)]$. For the electrocatalytic studies, solvents were saturated with CO_2 (BOC, < 99.99%) at atmospheric pressure by short bubbling on a frit.

General Synthesis of $[Mo(\eta^3\text{-allyl})(x,x'\text{-dmbipy})(CO)_2(NCS)]$

Under argon, a three-necked round-bottom flask was charged with $[Mo(\eta^3\text{-allyl})(CO)_2(MeCN)_2(NCS)]$ (230 mg, 0.69 mmol) and the appropriate x,x′-dimethyl-2,2′-bipyridine ligand (x = 4-6) in a small excess (typically 0.78 mmol). After the addition of dry deaerated DCM (10 mL), the mixture was refluxed at 50 °C for 2 h. The solution was then allowed to cool to ambient temperature and its volume was reduced by half. The

remaining solution was transferred to a Schlenk vessel, followed by the addition of hexane (5 x 10 mL) to precipitate the crude product that was further purified by extraction with hexane and column chromatography on silica, using dichloromethane:hexane 10:1 (v/v) as an eluent. The yields of a red microcrystalline powder varied between 35% and 55%. X-ray-quality crystals were grown by vapour diffusion in hexane/DCM.

[Mo(η^3-allyl)(4,4′-dmbipy)(CO)$_2$(NCS)] (1)

The precursor complex [Mo(η^3-allyl)(MeCN)$_2$(CO)$_2$(NCS)] (230 mg, 0.69 mmol) and 4,4′-dmbipy (151 mg, 0.82 mmol) reacted to afford **1** (168 mg, 55%). ^{1}H NMR (400 MHz, CD_2Cl_2): δ 8.55 (2H, d, J = 6 Hz), 7.85 (2H, s), 7.27 (2H, d, J = 5.6 Hz), 3.08 (2H, d, J = 6.4 Hz), 2.93 (1H, m), 2.54 (6H, s), 1.34 (2H, d, J = 6 Hz); (400 MHz, $(CD_3)_2SO$) δ 8.67 (2H, d, J = 5.2 Hz), 8.48 (2H, s), 7.53 (2H, d, J = 5.6 Hz), 3.26 (2H, d, J = 6.8 Hz), 3.19 (1H, m), 2.52 (6H, s), 1.42 (2H, d, J = 9.2 Hz). IR (THF): ν(CO) 1949, 1869 cm^{-1}, ν(CN) of NCS$^-$ 2076 cm^{-1}.

[Mo(η^3-allyl)(5,5′-dmbipy)(CO)$_2$(NCS)] (2)

The precursor complex [Mo(η^3-allyl)(MeCN)$_2$(CO)$_2$(NCS)] (220 mg, 0.66 mmol) and 5,5′-dmbipy (150 mg, 0.82 mmol) reacted to afford **2** (132 mg, 43%). ^{1}H NMR (400 MHz, CD_2Cl_2): δ 8.52 (2H, s), 7.87 (2H, d, J = 8 Hz), 7.75 (2H, d, J = 8 Hz), 3.12 (2H, d, J = 8 Hz), 2.96 (1H, m), 2.40 (6H, s), 1.36 (2H, d, J = 8 Hz); (400 MHz, $(CD_3)_2SO$) δ 8.64 (2H, s), 8.42 (2H, d, J = 10 Hz), 8.05 (2H, d, J = 10 Hz), 3.40 (2H, d, J = 8 Hz), 3.19 (1H, m), 2.48 (6H, s), 1.40 (2H, d, J = 8 Hz). IR (THF): ν(CO) 1951, 1871 cm^{-1}, ν(CN) of NCS$^-$ 2076 cm^{-1}.

[Mo(η^3-allyl)(6,6′-dmbipy)(CO)$_2$(NCS)] (3)

The precursor complex [Mo(η^3-allyl)(MeCN)$_2$(CO)$_2$(NCS)] (230 mg, 0.69 mmol) and 6,6′-dmbipy (143 mg, 0.78 mmol) reacted to afford **3** (109 mg, 36%). ^{1}H NMR (400 MHz, CD_2Cl_2): δ 7.82 (3H, m), 7.38 (2H, d, J = 8.4 Hz), 7.24 (1H, s), 2.94 (6H, s), 2.62 (3H, m),

1.19 (2H, d, J = 8 Hz); (400 MHz, $(CD_3)_2SO$): δ 8.45 (2H, d, J = 8 Hz), 8.18 (2H, t, J = 24 Hz), 7.72 (2H, d, J = 8 Hz), 2.99 (6H, s), 2.90 (1H, m), 2.80 (2H, d, J = 8 Hz), 1.30 (2H, d, J = 8 Hz). IR (THF): ν(CO) 1948, 1866 cm^{-1}; ν(CN) of NCS^- 2074 cm^{-1}.

X-ray Structure Determination

A crystal of [Mo(η^3-allyl)(x,x′-dmbipy)$(CO)_2$(NCS)] was quickly mounted under Paratone-N oil and flash-cooled to 150 K in a stream of nitrogen in an Oxford Cryostream cooler. Single-crystal x-ray intensity data were collected using an Agilent Gemini S Ultra diffractometer (Mo Kα radiation (λ = 0.71073 Å). The data were reduced within the CrysAlisPro software.[48] The structure was solved using the program Superflip,[49] and all non-hydrogen atoms were located. Least-squares refinements were performed using the CRYSTALS suite of programs.[50] The non-hydrogen atoms were refined anisotropically. Each hydrogen atom of the ligands was placed geometrically at a C-H distance of 0.95 Å and a U_{iso} of 1.2-1.5 times the value of U_{iso} of the parent C atom. The positions of the hydrogen atoms were then refined with riding constraints. In the case of [Mo(η^3-allyl)(6,6′-dmbipy)$(CO)_2$(NCS)], several disordered solvent molecules (DCM), which could not be modeled satisfactorily, were also present within the structure. The PLATON SQUEEZE software enabled the contribution to diffraction of the four disordered solvent molecules to be calculated, and thus it was possible to produce solvent-free diffraction intensities.[51]

Cyclic Voltammetry

Cyclic voltammograms were recorded on a PGSTAT 302N potentiostat (Metrohm Autolab) under an atmosphere of argon or carbon dioxide, using an airtight three-electrode single-compartment cell. A Pt (0.4 mm) or Au (0.4 mm) microdisc electrode polished by a 0.25-μm diamond paste (Sommer) served as the working electrode; the counter and pseudo-reference electrodes were made of coiled Pt and Ag wires, respectively, protected by a glass mantle. Ferrocene (Fc), serving as the internal reference, was added just before the final potential scan. Occasionally, decamethylferrocene (Fc*) served this purpose to avoid an

overlap of the standard system with the nearby Mo(II)-NCS oxidation; $E_{1/2}$ = 0.48 V vs Fc/Fc^+ (in THF). The CV samples contained 1 mM analyte and 0.1 M tetrabutylammonium hexafluorophosphate (Bu_4NPF_6) as the supporting electrolyte.

IR and UV-Vis Spectroelectrochemistry

Infrared spectroelectrochemical experiments were performed on a Bruker Vertex 70v FT-IR spectrometer, equipped with either a DTLaGS detector (measurements at 298 K) or linked to an external Biorad FTS 60 MCT detector (measurements at 223 K). UV-Vis spectroelectrochemical experiments were conducted on a Scinco S-3100 diode array spectrophotometer. The electrochemical response in the form of a thin-layer cyclic voltammogram (TL-CV) at υ = 2 mV s^{-1} was recorded during both IR and UV-Vis monitoring of the controlled-potential electrolysis with an EmStat3 potentiostat (PalmSens). The spectroelectrochemical measurements were conducted with an optically transparent thin-layer electrochemical (OTTLE) cell (Spectroelectrochemistry Reading) in the room-temperature[52] and the cryostatted low-temperature[53] versions. Both OTTLE cells were equipped with a Pt minigrid working electrode, a Pt minigrid counter electrode, an Ag wire pseudo-reference electrode and CaF_2 windows. The room-temperature OTTLE cell was also used with an Au minigrid working electrode. The SEC samples contained 3 mM analyte and 0.3 M Bu_4NPF_6.

Computational Studies

Density functional theory (DFT) calculations[54] were performed, using the Amsterdam Density Functional (ADF) program.[55–57] Geometries were optimized with gradient correction, without symmetry constraints, using the Local Density Approximation (LDA) of the correlation energy (Vosko-Wilk-Nusair)[58] and the Generalized Gradient Approximation (Becke's[59] exchange and Perdew's[60,61] correlation functionals). Unrestricted calculations were performed for open-shell complexes. Solvent was considered in all geometry optimizations and single-point calculations, in accordance with the COSMO approach implemented in ADF. Tetrahydrofuran (THF) was always chosen, except for the PrCN-coordinated reduced com-

plexes (Scheme 5.1) that were modeled with acetonitrile. Relativistic effects were treated with the ZORA approximation.[62] Triple-ζ Slater-type orbitals (STOs) were used to describe all the valence electrons of H, O, C, N, S, and Mo. A set of two polarization functions was added to H (single-ζ 2s, 2p), O, C, N, S (single-ζ, 3d, 4f), and Mo (5d, 4f). Frequency calculations were performed to obtain the vibrational spectra and to check that intermediates were minima in the potential energy surface. Time-dependent DFT calculations[63–65] with spin-orbit coupling (SOPERT) were performed to determine the excitation energies.[66] The energy decomposition analysis (EDA)[67,68] was performed on single-point calculations in the gas phase over the solvent-optimized geometries.

The x-ray structures described above were used for the calculations on parent x,x′-dmbipy complexes **1-3** and all the others were modeled after them. The more important isomers of each species were considered, as well as different spin states, when relevant. To check the effect of two possible isomers in solution, frequencies and absorption spectra were calculated for both, and the differences were much smaller than differences to other complexes of the same ligand. Three-dimensional representations of the structures and molecular orbitals were obtained with Chemcraft.[69]

5.4 Results and Discussion

5.4.1 Characterization and Crystal Structure Analysis

Infrared spectra of dicarbonyl complexes **1-3** show the two ν(CO) absorption bands close to 1950 and 1870 cm^{-1} (see Table 5.2). Compared with the ν(CO) modes of the unsubstituted-bipy reference, [Mo(η^3-allyl)(bipy)(CO)$_2$(NCS)], the wavenumbers of **1-3** do not deviate significantly, reflecting the limited electronic effect of the methyl substitution on the CO π-back-donation. The two CO-stretching wavenumbers are almost identical for **2** and only slightly smaller for **1**. The largest ν(CO) drop in the series (up to 5 cm^{-1}) is caused by the inductive effect of the donor methyl substituents at 6,6′-dmbipy. The ν(CN) mode of the axial thiocyanato ligand in **1** and **2** also remains positioned near 2080 cm^{-1} (in PrCN) and

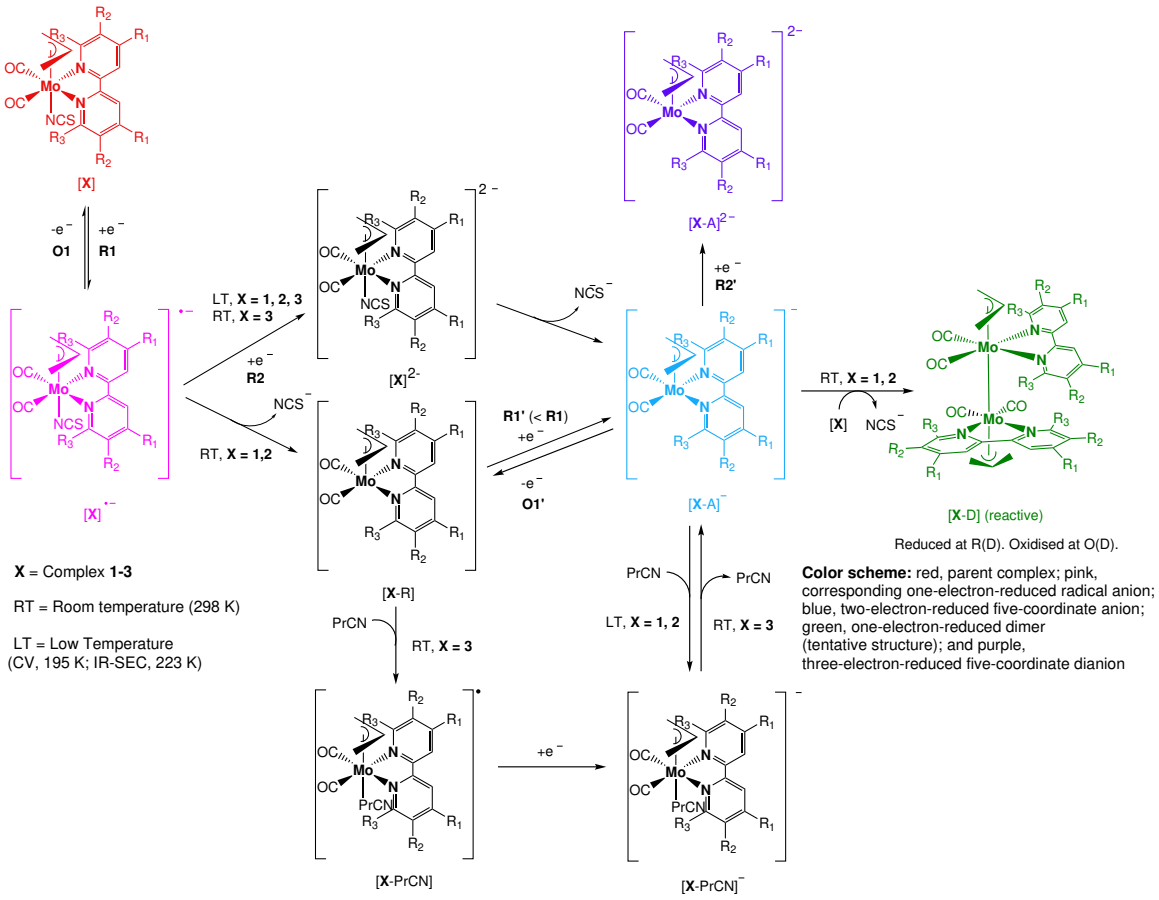

Scheme 5.1: General cathodic pathways of complex **X** (**X** = **1**-**3**), based on the evidence from cyclic voltammetry (colored molecular structures). The evidence for radical [**X**-PrCN] and anion [**X**-PrCN]$^-$ (**X** = **1** and **2**) comes solely from IR spectroelectrochemistry.

2075 cm^{-1} (in THF), compared to the reference bipy complex. The CO π-back-donation increases, and thiocyanate π-donation decreases at lower temperatures, both in PrCN and THF.

The crystal structures of **1**-**3** (shown in Figure 5.1 for **1** and **3**, and Figure 5A.1 in the Appendix for **2**) reveal that these complexes all adopt the type A pseudo-octahedral structure encountered in most [Mo(η^3-allyl)(L∩L)(CO)$_2$X] complexes (L∩L = chelating bidentate ligand, X = monodentate anionic ligand), including [Mo(η^3-allyl)(bipy)(CO)$_2$(NCS)],[70] also known as the equatorial isomer. The type A structure is symmetric, characterized by both L∩L donor atoms appearing in the trans position to the carbonyl ligands, defining the equatorial plane. The less-symmetric type B structure (axial isomer), where the

η^3-allyl and one CO ligand are trans to the L∩L donor atoms, is only seen in rare instances,[71–74] but is particularly common for larger, more sterically hindered donor ligands or those with strong π-accepting properties such as the 2,6-xylyl-bian ligand (where bian = bis(2,6-dimethylphenyl)-acenaphthenequinonediimine).[46,74] As is found in practically all the complexes in this family, the open face of the allyl ligand in **1-3** lies over the equatorial CO ligands. While almost linear in the reference bipy complex,[46] the structure of the NCS^- ligand is bent in the dmbipy complexes, toward the 4,4′-dmbipy ligand in **1**, while away from the 6,6′-dmbipy ligand in **3**, forced by packing interactions (Figure 5.1). The bond angle between the equatorial CO ligands is compressed in **3** (76°), relative to **1** (82°). In the reference bipy complex, this angle is 78°, the midway point between the two extremes.[46] In addition to this, the two rings in chelated 6,6′-dmbipy in **3** are not coplanar, but have a dihedral angle around the NCCN moiety of -7.2°. In **1**, the corresponding angle is 0°. These observations indicate that the methyl groups in the 6,6′-positions exert a stronger steric impact over the rest of the complex. Corresponding crystallographic data for **1-3** are presented in Tables 5A.1 and 5A.2 in the Appendix.

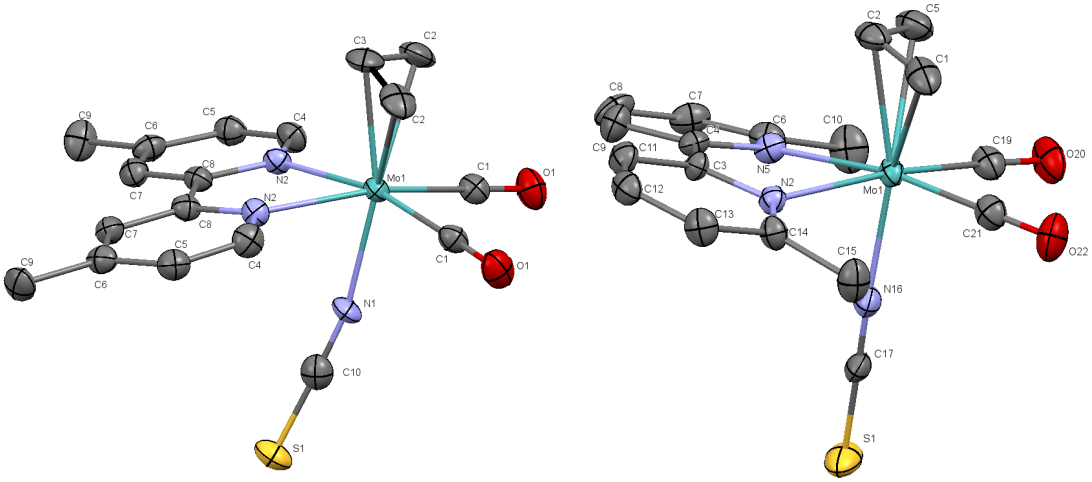

Figure 5.1: An ORTEP view (50% thermal probability) of the molecular structures of [Mo(η^3-allyl)(4,4′-dmbipy)$(CO)_2$(NCS)] (**1**, left) and [Mo(η^3-allyl)(6,6′-dmbipy)$(CO)_2$(NCS)] (**3**, right) determined by single-crystal x-ray analysis. Hydrogen atoms have been omitted for clarity.

DFT calculations[54] using the ADF program[55–57] were performed on **1-3** in order to understand the role of the methyl substituents and to calibrate the method used to identify

the species detected in the spectroelectrochemical experiments. The equatorial isomer is indeed always preferred, the energy difference increasing as the methyl substituents approach the metal: 0.67, 0.86, and 5.45 kcal mol^{-1} for **1**, **2**, and **3**, respectively (Tables 5A.3 and 5A.4 in the Appendix). Substituents in adjacent positions to the donor N atoms give rise to a distortion of the coordinated dmbipy ligand in the equatorial isomer (Figure 5.1) but also lead to severe repulsion with the allyl hydrogen atoms. This is reflected in the binding energy of each dmbipy to the [Mo(η^3-allyl)$(CO)_2$(NCS)] fragment, which is ∼41 kcal mol^{-1} for **1** and **2**, but only 33 and 27 kcal mol^{-1} for the equatorial and axial isomers of **3**. The structural parameters are well-reproduced (Tables 5A.5 and 5A.2 in the Appendix).

A fragment decomposition analysis helps to understand the origin of the lower binding energy of the 6,6′-dmbipy ligand compared to the 4,4′- and 5,5′-derivatives (Table 5A.6 in the Appendix). Indeed, the ca. 8 kcal mol^{-1} difference results from two sources. The first one is the extra energy needed to distort the fragments from their optimized geometry to the geometry that they have in the complex. The Mo fragment requires ca. 0.5 kcal mol^{-1}, and the dmbipy ligands require ca. 2.5 kcal mol^{-1}. The second contribution is the loss of covalent interaction between the two fragments (ca. 5 kcal mol^{-1}). These intrinsic differences will play a role in the reactivity of the complexes.

5.4.2 Cyclic Voltammetry

Cyclic voltammetry of **1-3** was conducted at room temperature (298 K) and low temperature (195 K) at an Au microdisc electrode in argon-saturated THF/Bu_4NPF_6 (Figures 5.2-5.4) and PrCN/Bu_4NPF_6 (Figures 5A.2-5A.4 in the Appendix). Reference measurements at a Pt microdisc electrode are depicted in Figures 5A.5-5A.7 (THF) and Figures 5A.8-5A.10 (PrCN) in the Appendix. The redox potentials obtained for **1-3** with the Au microdisc are summarized in Table 5.1. Redox potentials measured for the series **1-3** on a Pt microdisc are summarized in Table 5A.7 in the Appendix.

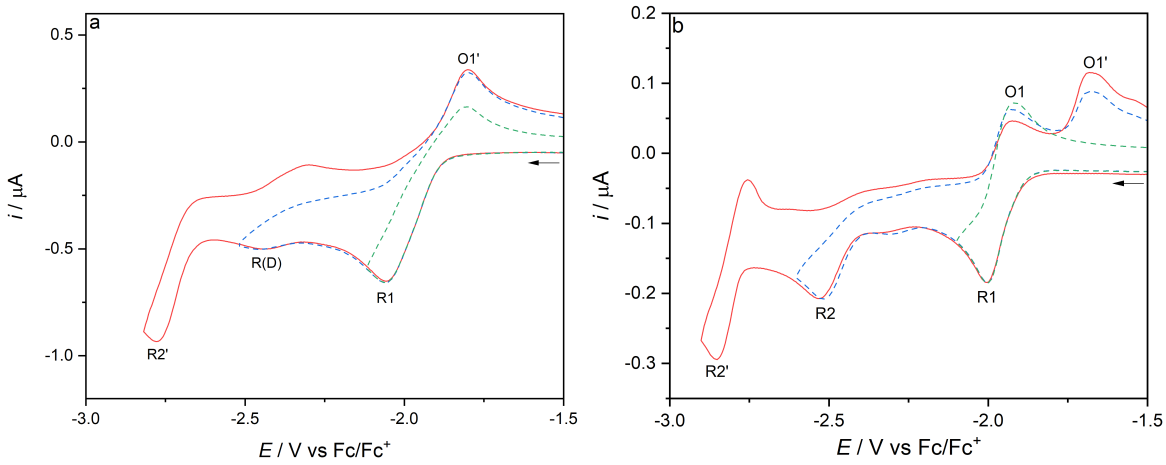

Figure 5.2: Cyclic voltammetry of **1**, in THF/Bu_4NPF_6 (a) at room temperature and (b) at low (195 K) temperature. υ: 100 mV s^{-1}. Au microdisc electrode. The arrow indicates the initial scan direction.

The redox behavior of **1** closely resembles that reported[46] for the reference complex [Mo(η^3-allyl)(bipy)$(CO)_2$(NCS)]. In the anodic region, **1** undergoes reversible, formally Mo-based $1e^-$ oxidation, producing the cationic species [Mo^{III}(η^3-allyl)(4,4′-dmbipy)$(CO)_2$(NCS)]$^+$, even in strongly coordinating PrCN. This result proves that the donor ability of the dmbipy ligand is sufficient to stabilize the higher oxidation state. Despite this, the influence of the methyl substituents on the actual anodic potential is negligible. On the slow cathodic scan at υ = 100 mV s^{-1}, **1** undergoes irreversible dmbipy-based reduction to [**1**]$^{\bullet-}$, in weakly coordinating THF at $E_{p,c}$ = -2.06 V (R1 in Figure 5.2). In PrCN, this irreversible process occurs less negatively at $E_{p,c}$ = -1.99 V. Reversing the scan direction just behind the initial cathodic wave in either solvent exposes a nearby irreversible anodic wave at $E_{p,a}$ = -1.82 V (THF) or $E_{p,a}$ = -1.92 V (PrCN); this process is designated O1′. From a comparison with both the reference bipy complex and the cathodic cyclic voltammogram of [Mn(bipy)$(CO)_3$Br],[22] O1′ can be assigned to the oxidation of the 5-coordinate anion [Mo(η^3-allyl)(4,4′-dmbipy)$(CO)_2$]$^-$ ([**1**-A]$^-$ in Scheme 5.1), classifying the initial reduction at R1 as a formally $2e^-$ process. The initial $1e^-$ reduction of **1** forms unstable [**1**]$^{\bullet-}$ that readily loses the axial monodentate ligand NCS^- (see the spectroelectrochemical section for support) and converts to the corresponding 5-coordinate radical, [Mo(η^3-allyl)(4,4′-dmbipy)$(CO)_2$] ([**1**-R])

readily reducible at R1′ < R1 (ECE) to [**1**-A]$^-$. This 5-coordinate anion is detectable by its irreversible oxidation at O1′ but also its 1e$^-$ reduction to [Mo(η^3-allyl)(4,4′-dmbipy)(CO)$_2$]$^{2-}$ ([**1**-A]$^{2-}$) at R2′ (becoming reversible at 195 K, $E_{1/2}$ = -2.80 V (THF)), similar to the redox behavior of [Mn(bipy)(CO)$_3$]$^-$ under argon.[22] The wave R2′ was poorly resolved in PrCN at the edge of the accessible potential window.

The new cathodic wave R(D) in the room-temperature CV of **1**, observed at $E_{p,c}$ = -2.46 V (in THF) and -2.36 V (in PrCN), can be attributed to the reduction of the Mo−Mo bonded dimer [Mo(η^3-allyl)(4,4′-dmbipy)(CO)$_2$]$_2$ ([**1**-D] in Scheme 5.1) formed on the selected timescale from the unreduced parent complex by its electron-transfer reaction with [**1**-A]$^-$ electrogenerated at R**1** by the irreversible ECE process. The reduction of [**1**-D] appears reversible on the CV timescale of seconds; however, ultimately it should reproduce [**1**-A]$^-$. This route has been reported for reference [Mn(bipy)(CO)$_3$]$_2$.[22] However, [**1**-D] exhibits inherent secondary reactivity, revealed by IR SEC in the following section, preventing us from obtaining clear spectroscopic evidence for this process. The oxidation of [**1**-D] is visible on the reverse anodic scan in THF as a weak anodic wave O(D) at $E_{p,a}$ = -1.17 V, beyond the oxidation of [**1**-A]$^-$ at O1′ that triggers the ECEC dimerization process, similar to that at R1 via 5-coordinate radical [**1**-R] (Scheme 5.1). The latter species probably binds back the liberated NCS$^-$ ligand; the concomitant oxidation (O1′ < O1) reproduces parent **1** that reacts with yet nonoxidized [**1**-A]$^-$ to form dimer [**1**-D] detected more positively by its oxidation at O(D). Differently from the cathodic dimerization route, the donor solvent (especially PrCN) may play a role in the intimate mechanism of the anodic dimerization.

At sufficiently low temperatures, parent radical anion [**1**]$^{\bullet-}$ formed at R1 becomes stable, resulting in a reversible R1/O1 couple, $E_{1/2}$ = -1.93 V (THF, Figure 5.2) or -1.96 V (PrCN, Figures 5A.2 and 5A.8 in the Appendix). [**1**-A]$^-$ is then formed only at the newly observed irreversible cathodic wave R2, $E_{p,c}$ = -2.53 V (THF) or -2.55 (PrCN), upon rapid dissociation of NCS$^-$ from 6-coordinate [**1**]$^{2-}$. The quasi-reversible reduction of [**1**-A]$^-$ to 5-coordinate dianion occurs again at R2′, $E_{p,c}$ = -2.85 V (THF). Compared to room-temperature CV, the reverse oxidation of [Mo(η^3-allyl)(4,4′-dmbipy)(CO)$_2$]$^-$ is shifted upon

cooling more positively (> 100 mV) from the parent reduction at R1. The anodic ECEC dimerization process is observable at low temperatures only in THF (a minor O(D) wave at -1.17 V).

Table 5.1: Redox potentials of complexes **1**-**3** and their reduction products (see Scheme 5.1) from cyclic voltammetry at an Au microdisc electrode at 298 K.

	Redox Potentials [V vs Fc/Fc^+]						
Solvent	Mo(II)/(III)	R1	R2	R2′	O1′	R(D)	O(D)
	$E_{1/2}$	$E_{p,c}$	$E_{p,c}$	$E_{p,c}$	$E_{p,a}$	$E_{p,c}$	$E_{p,a}$
[Mo(η^3-allyl)(bipy)(CO)$_2$(NCS)][c]							
THF	0.20	-1.99	-	-2.82	-1.74	-2.52	[e]
PrCN	0.22	-1.95	-2.59	-2.77	-1.74	[e]	-0.80
PrCN[b]	[d]	-1.88[a]	-2.58[b]	[f]	-1.58	[e]	-0.63
[Mo(η^3-allyl)(4,4′-dmbipy)(CO)$_2$(NCS)] (1)							
THF	0.18	-2.06	-	-2.78	-1.82	-2.46	-1.18
THF[b]	0.22	-1.96[a]	-2.53	-2.80[a]	-1.68	[e]	-1.17
PrCN	0.22	-1.99	-	[f]	-1.74	-2.36	[e]
PrCN[b]	0.22	-1.96[a]	-2.55	[f]	-1.54	[e]	-1.16
[Mo(η^3-allyl)(5,5′-dmbipy)(CO)$_2$(NCS)] (2)							
THF	0.15	-2.14	-	-2.90	-1.81	-2.50	-1.18
THF[b]	0.17	-2.07[a]	-2.60	-2.94[a]	-1.73	[e]	-1.17
PrCN	0.22	-2.04	-	[f]	-1.73	-2.33	[e]
PrCN[b]	0.23	-1.99[a]	-2.52	[f]	-1.62	-	[e]
[Mo(η^3-allyl)(6,6′-dmbipy)(CO)$_2$(NCS)] (3)							
THF	0.26	-2.02[a]	-2.57	-2.94	-1.84	-	-
THF[b]	0.28	-1.98[a]	-2.60	-2.82[a]	-1.66	-	-
PrCN	0.32	-1.93[a]	-2.45	[f]	-1.73	-	-
PrCN[b]	0.28	-1.94[a]	-2.56	[f]	-1.54	-	-

[a] $E_{1/2}$ value (anodic counter wave observed). [b] Measured at 195 K.[c] Reference complex measured at a Pt Electrode. [d] Not measured.[e] Not observable.[f] Beyond the accessible cathodic potentional window of PrCN/Bu_4NPF_6.

The analysis of the redox behavior of **2** under ambient conditions (Figure 5.3, THF) and Figures 5A.3 and 5A.9 in the Appendix, PrCN) leads to a description that is largely comparable to that of **1** (Table 5.1, Table 5A.7, and Scheme 5.1), with only minor differences in the electrode potential values of each redox process. It is noteworthy that the reference complex [Mo(η^3-allyl)(bipy)$(CO)_2$(NCS)] with the less-donating bipy ligand[46] showed a partially reversible reduction to the corresponding radical anion at R1 in PrCN at room temperature

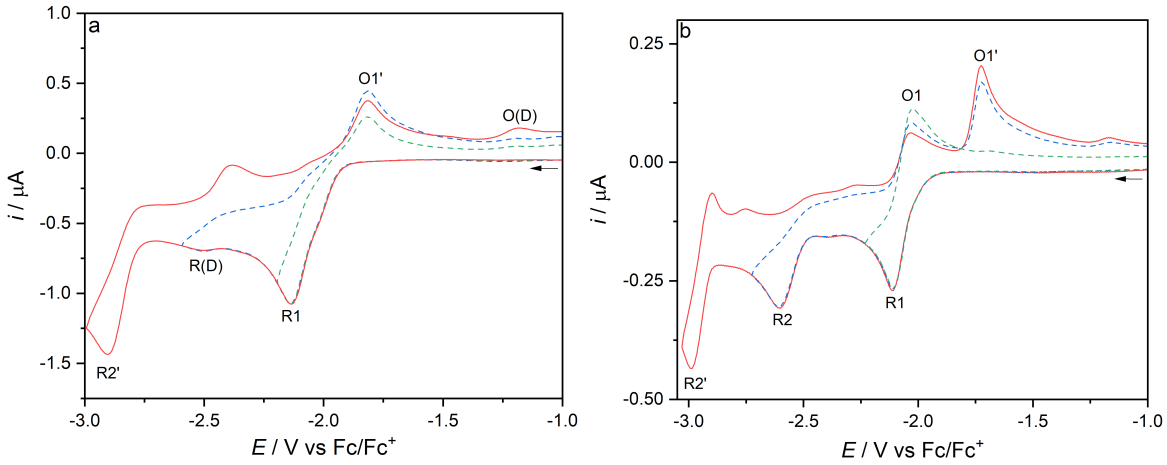

Figure 5.3: Cyclic voltammetry of **2**, in THF/Bu_4NPF_6 (a) at room temperature and (b) at low (195 K) temperature. υ: 100 mV s^{-1}. Au microdisc electrode. The arrow indicates the initial scan direction.

already at υ = 100 mV s^{-1}, while the radical anions of **1** and **2** are more reactive and not observable under the same experimental conditions, as revealed by the absent counter wave O1.

The redox behavior of **3** (Figure 5.4, and Figures 5A.5 and 5A.10) strongly differs from that of **1** and **2**. The formally metal-based oxidation becomes quasi-reversible and markedly positively shifted to $E_{1/2}$ = 0.26 V (THF) or 0.32 V (PrCN); the anodic potential in PrCN is more positive, by 100 mV, than that of the reference complex with the unsubstituted bipy ligand, whereas complexes **1** and **2** oxidize at slightly less-positive potentials (Table 5.1, and Table 5A.7 in the Appendix). In the cathodic range, the reduction of parent **3** at R1 to radical anion $[\mathbf{3}]^{\bullet-}$ at $E_{1/2}$ = -2.03 V (THF) or -1.93 V (PrCN) is reversible at υ = 100 mV s^{-1} already at room temperature (Figure 5.4). This difference has several implications for following the cathodic path. Unlike **1** and **2**, there is no evidence for the formation (absent O1′) of 5-coordinate anion [**3**-A]$^-$, until the irreversible wave R2 at $E_{p,c}$ = -2.57 V (THF) or -2.45 (PrCN) is passed, where the latter is directly produced by NCS^- dissociation from the transient 6-coordinate dianion. On the reverse anodic scan initiated beyond R2, the anodic wave O1′ is clearly seen at $E_{p,a}$ = -1.84 V (THF) or -1.73 V (PrCN). The absence of [**3**-A]$^-$ at R1 also prevents the formation of dimer [**3**-D], which is reflected in the absence of its

R(D) and O(D) signatures. The absent anodic wave O(D) indicates that the dimerization reaction between [**3**-A]$^-$ and parent **3** (reformed at O1′) is inhibited. The 5-coordinate anion is further reduced to [**3**-A]$^{2-}$ at R2′, $E_{p,c}$ = -2.94 V (THF). At low temperatures, R2′ takes on the reversible character and slightly shifts to $E_{1/2}$ = -2.82 V (Figure 5.4b).

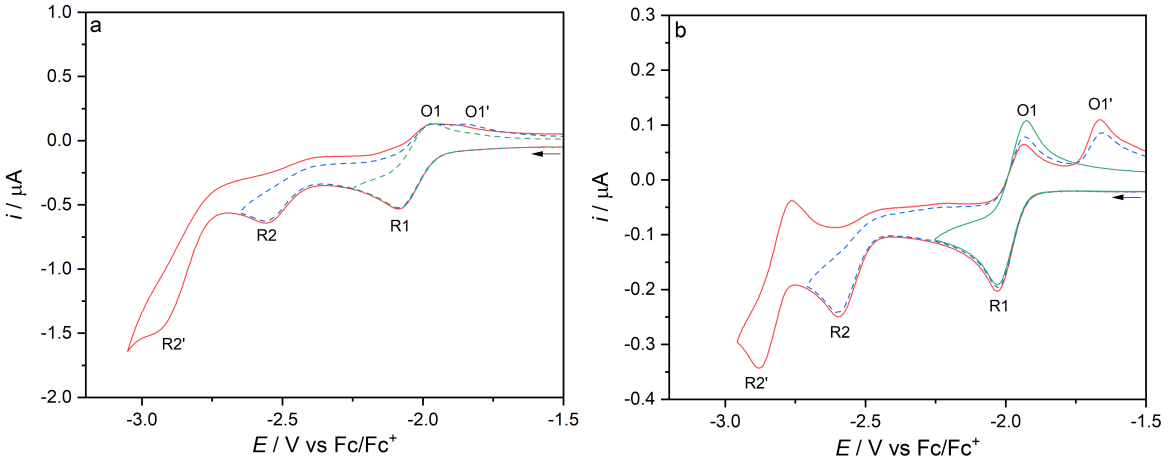

Figure 5.4: Cyclic voltammetry of **3**, in THF/Bu_4NPF_6 (a) at room temperature and (b) at low (195 K) temperature. υ: 100 mV s^{-1}. Au microdisc electrode. The arrow indicates the initial scan direction.

On electronic grounds, the addition of methyl groups to bipy in the 4,4′-positions (**1**) and 5,5′-positions (**2**) increases the electron donation toward the Mo∩bipy metallacycle and the axial Mo−NCS bond, as evidenced by the more negative reduction potentials, destabilizing the corresponding radical anions compared to the reference complex with 2,2′-bipyridine. The magnitude of the R1 potential shift is comparable to that reported for [Mo(x,x′-dmbipy)$(CO)_4$] (x = 4-6) and [Re(x,x′-dmbipy)$(CO)_3$Cl] (x = 3-5) versus their respective bipy counterparts.[39,75] The redox behavior following the donor substitution in the 6,6′-position (**3**) is extremely unusual, resulting in an apparently stable radical anion formed upon 1e$^-$ reduction. In addition, it also stabilizes [**3**-A]$^-$ and hinders the follow-up dimerization involving this 2e$^-$ reduced species and parent **3**. A similar inhibiting effect on the dimerization was reported by Kubiak and co-workers for [Mn(6,6′-dimesityl-bipy)$(CO)_3$]$^-$ stabilized by the large substituents in the vicinity of the Mn∩bipy metallacycle.[24]

5.4.3 Computational Studies

The behavior of **1-3** upon electrochemical reduction, and the nature of the reduction products formed, as revealed by the preceding CV studies, were investigated in detail with quantum chemical calculations (Amsterdam Density Functional, ADF).[55–57] The initial $1e^-$ reduction of **1-3** leads to the formation of corresponding radical anions; only $[\mathbf{3}]^{\bullet-}$ has been found sufficiently stable under ambient conditions (Figure 5.4). The geometry optimization (Table 5A.4, Appendix) reveals that the axial isomer is preferred for $[\mathbf{1}]^{\bullet-}$ and $[\mathbf{2}]^{\bullet-}$ by < 1 kcal mol^{-1}, while the less-strained equatorial form remains significantly favored by $[\mathbf{3}]^{\bullet-}$ (ca. 6 kcal mol^{-1}). The binding energy of the NCS^- ligand in each anion is 7.8 ($[\mathbf{1}]^{\bullet-}$), 6.8 ($[\mathbf{2}]^{\bullet-}$), and 10.74 ($[\mathbf{3}]^{\bullet-}$) kcal mol^{-1}, suggesting that thiocyanate will be less easily released by $[\mathbf{3}]^{\bullet-}$, which is consistent with the CV observations. The effect of the reduction on the structure is observed in the shortening of the central $C_1{-}C_1'$ bond of the bidentate ligand (from 1.476 Å to 1.428 Å in **1**), reflecting the dominant localization of the complex LUMO on x,x′-dmbipy, and in the lengthening of the carbonyl C−O distances (Figure 5.5 and Figures 5A.11-5A.12 in the Appendix).

The HOMO of **1** (Figure 5.6) is bonding between the metal and the π-acceptor carbonyls and allyl, but π-antibonding between Mo and the axial π-donor thiocyanate, being mainly a Mo orbital. Hence, the $1e^-$ oxidation of **1-3** is formally $Mo^{II} \longrightarrow Mo^{III} + e^-$. Therefore, strong σ-donation from x,x′-dmbipy (x = 4-6) is needed to stabilize $[\mathbf{1}]^+$-$[\mathbf{3}]^+$, as observed (see the following spectroelectrochemical section). The LUMO and LUMO+1 of **1** are largely localized on 4,4′-dmbipy, both being bonding between C1 and C1′. Therefore, shortening of this distance is expected upon the reduction.

The identification of the diverse carbonyl complexes formed along the cathodic pathways can be most effective by analysis of the vibrational stretching modes of the CO ligands (Table 5A.8 in the Appendix). The calculated wavenumbers are practically independent of the methyl substitution pattern. The absorption maxima of the symmetric modes for **1**, **2**, and **3** reside at 1882, 1883, and 1881 cm^{-1}, respectively, and the absorption maxima of

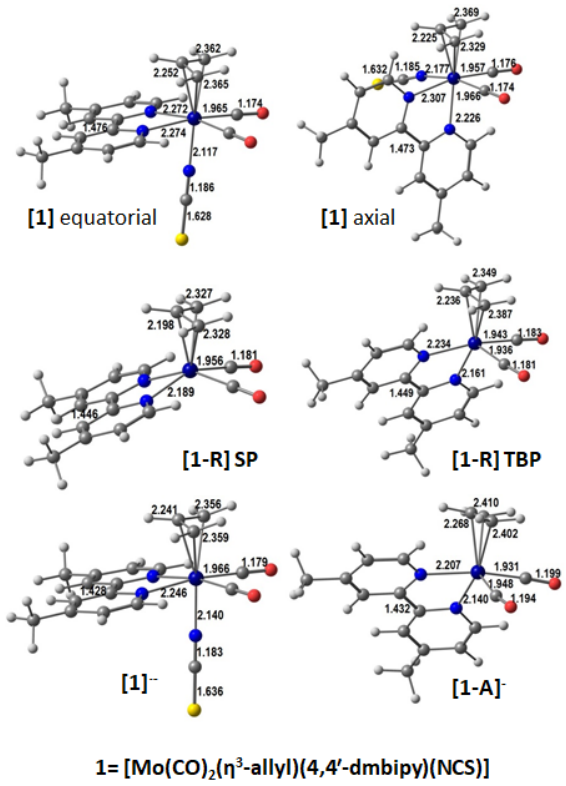

Figure 5.5: DFT-optimized structures of the parent complex [Mo(η^3-allyl)(4,4′-dmbipy)(CO)$_2$(NCS)], **1** (the equatorial isomer (top left) and the axial isomer (top right), 1e$^-$ reduced radical anion [**1**]$^{\bullet-}$ (bottom left), 5-coordinate radical [**1**-R] (the SP isomer (left) and the TBP isomer (right), and 2e$^-$ reduced 5-coordinate anion [**1**-A]$^-$ (bottom right), with the relevant bond lengths (given in Å).

the antisymmetric modes for **1**, **2**, and **3** reside at 1800, 1801, and 1800 cm^{-1}, respectively. Frequency calculations need a scaling factor to reproduce experimental values. These calculated values are ca. 0.97 of the experimental ones, in very good agreement. Interestingly, the trend in the neutral and singly reduced species is the same (the largest wavenumbers found for **2**). In THF, the experimental wavenumbers for **1** are 1949 and 1869 cm^{-1} and the experimental wavenumbers for [**1**]$^{\bullet-}$ are 1926 and 1831 cm^{-1} (Table 5.2, in the following section). Application of the 0.97 factor converts these values to 1891 and 1813 cm^{-1} and 1868 and 1776 cm^{-1}, respectively; these values are very close to those calculated (see Table 5A.8).

The electronic absorption of **1**-**3** in the visible spectral region, having a charge-transfer

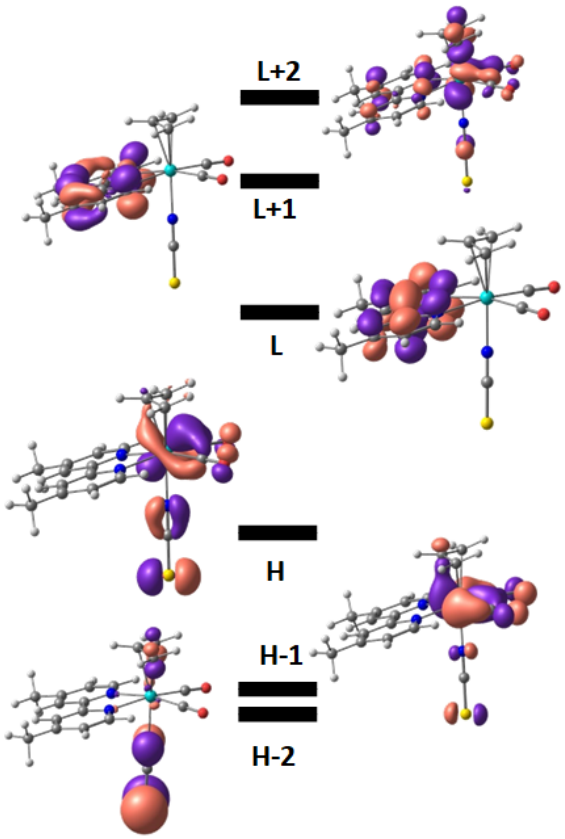

Figure 5.6: DFT-calculated frontier orbitals in the parent complex [Mo(η^3-allyl)(4,4′-dmbipy)$(CO)_2$(NCS)], **1**. The HOMO-LUMO (H-L) gap is 1.574 eV.

character, was investigated with time-dependent density functional theory (TDDFT) calculations and the results are presented in Table 5A.9 in the Appendix. The calculated frontier molecular orbitals of **1-3** are shown in Figure 5.6, and Figures 5A.13 and 5A.14 in the Appendix, respectively. The calculated complex **1** exhibits two major absorptions at 506 and 452 nm (Table 5A.9), in relatively good agreement with the experimental UV-Vis spectra showing an asymmetric absorption band between 400-550 nm with a shallow absorption maximum at 470 nm. These visible optical excitations result from the HOMO-to-LUMO+1 and HOMO-3-to-LUMO transitions, respectively. The lowest-energy HOMO-to-LUMO+1 is essentially a (M-L)L′CT transition from occupied π^*(Mo–NCS) to π^*(4,4′-dmbipy) (see Figure 5.6). Model complex **2** also exhibits two transitions at 506 nm (HOMO-to-LUMO+1, 54%, and HOMO-to-LUMO+2, 43%) and 444 nm (HOMO-3-to-LUMO), also close to the experimental λ_{max} value of 470 nm. Their nature is close to that described for **1**, involving

excitation from π^*(Mo–NCS) to π^*(5,5′-dmbipy) but also to π^*(Mo-allyl) (a small component). The MOs involved are shown in Figure 5A.13 (Appendix). Complex **3** shows three electronic absorptions in the visible region, one at 471 nm (very weak) and two at 456 (HOMO-3-to-LUMO) and 449 nm (HOMOto-LUMO+3, 67%, HOMO-to-LUMO+2, 29%). Inspecting these orbitals (Figure 5A.14, Appendix) points again to photoinduced charge transfer from π^*(Mo−NCS) to π^*(6,6′-dmbipy) and π^*(Mo-allyl).

The concomitant loss of the thiocyanate anion from the initial radical anion will afford the transient 5-coordinate radicals [Mo(η^3-allyl)(x,x′-dmbipy)$(CO)_2$] (x = 4-6; [**X**-R] in Scheme 5.1). Their structure has been derived from parent equatorial and axial isomers; this approach yielded geometries close to a square plane (SP) or a trigonal bipyramid (TBP), respectively. The latter was the most stable one, by a negligible 0.4 kcal mol^{-1} for [**1**-R] and [**2**-R], while the square-planar geometry was more strongly preferred for [**3**-R] (ca. 5 kcal mol^{-1}). Radical [**3**-R] was less stable than [**1**-R] and [**2**-R], by ca. 10 kcal mol^{-1}. The structure of [**1**-R] exhibits, for the two geometries calculated, larger carbonyl C−O and 4,4′-dmbipy inter-ring C−C bond lengths than that calculated for [**1**]$^{\bullet-}$, and smaller Mo−C(allyl) bond lengths (these are merely trends, the absolute differences being small; see Figure 5.5). These changes indicate that the loss of the NCS^- anion leads to stronger delocalization of the additional electron from the dominantly 4,4′-dmbipy radical anion in [**1**]$^{\bullet-}$ over the Mo-bis(carbonyl) unit in [**1**-R] (Figure 5.7).

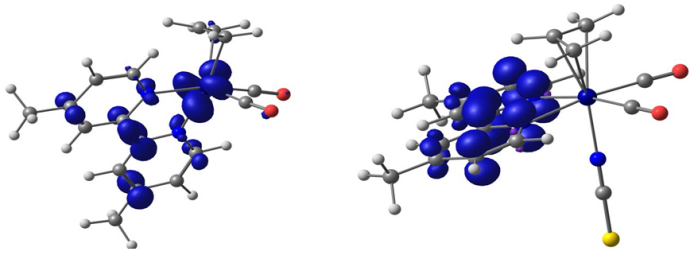

Figure 5.7: DFT-calculated spin density in the 5-coordinate radical [Mo(η^3-allyl)(4,4′-dmbipy)$(CO)_2$], [**1**-R] (left), and precursor 6-coordinate radical anion, [**1**]$^{\bullet-}$ (right).

Because of their role in the reactivity characterizing the cathodic path, the frontier orbitals of [**1**-R], as well as the spin density distribution in the 5-coordinate radical, are

important. The orbitals of [**1**-R] are depicted in Figure 5A.15 in the Appendix. The spin density in the radicals is delocalized over the metal and the 4,4′-dmbipy ligand, with practically no contributions from the allyl and the carbonyls, as shown for [**1**-R] in Figure 5.7 (left), and for [**2**-R] and [**3**-R] in Figures 5A.16 and 5A.17 in the Appendix, respectively.

The direct 1e$^-$ reduction of 5-coordinate radicals [**X**-R] (X = **1**, **2**, **3**), formed at the irreversible cathodic wave R1 (Figure 5.2a), produces 5-coordinate anions [**X**-A]$^-$ that, in principle, may exist in closed-shell singlet or open-shell triplet states. As expected, the former alternative is more stable in all three cases, by 16.9 and 19.2 kcal mol^{-1} for [**1**-A]$^-$ and [**2**-A]$^-$, but by only 11.8 kcal mol^{-1} for [**3**-A]$^-$, emphasizing again the differences exhibited by the 6,6′-dmbipy derivatives. The addition of the second electron leads to longer Mo−C(allyl) bonds, compared not only to precursors [**X**-R] but also to neutral parent compounds **X**, suggesting allyl loss as a possible decomposition pathway. The C−O bonds lengthen, while the C−C inter-ring bond in reduced x,x′-dmbipy slightly shortens. The structure of [**1**-A]$^-$ is shown in Figure 5.5; the others for **X** = **2** and **3** can be found in Figures 5A.11 and 5A.12, respectively. The calculated frequencies of parent **X** shift by 26-30 cm^{-1} for ν(CO)s and 37-40 cm^{-1} for $\nu(\mathrm{CO})_\mathrm{a}$ when reduction occurs and radical anions [**X**]$^{\bullet-}$ are formed (Table 5A.8). Interestingly, the loss of the thiocyanate ligand has practically no effect on the stretching frequencies when going from [**3**]$^{\bullet-}$ to [**3**-R] ($<$ 5 cm^{-1} for both modes). This effect on the π-back-donation to the carbonyl ligand is understandable, as the dissociation of the π-donor thiocyanate is compensated by the increased π-delocalization of the added electron from 4,4′-dmbipy to the $(\mathrm{CO})_2$Mo-dmbipy metallacycle. For the 4,4′-dmbipy and 5,5′-dmbipy ligands, the consequence of the thiocyanate dissociation is not so small, since the $\nu(\mathrm{CO})_\mathrm{s}$ mode shifts by 7 and 5 cm^{-1}, respectively (for the axial geometry). As can be seen in Table 5A.8, the reduction from the 5-coordinate radicals to the corresponding anions has more dramatic effects: the shifts reaching ca. 90 cm^{-1} for the derivatives of **1** and **2**, and ca. 50 for cm^{-1} those of **3**. This difference testifies that the added second electron largely resides on the Mo dicarbonyl unit due to the extensive π-delocalization of the frontier orbitals in [**X**-A]$^-$. This characteristic bonding property is clearly evidenced by the

nature of the calculated frontier orbitals depicted in Figure 5.8 for [**3**-A]$^-$, and Figures 5A.18 and 5A.19 in the Appendix for [**1**-A]$^-$ and [**2**-A]$^-$, respectively. The strongly π-delocalized situation applies in all three cases for the HOMO and LUMO. The LUMO+1 and LUMO+2 are dominantly x,x′-dmbipy-localized while the HOMO-1 and HOMO-2 reside on the Mo-dicarbonyl unit. The molecular orbitals of the five-coordinate anions are indeed very similar in nature to those of the radical precursors (α-orbitals), as can be seen for [**1**-R] and [**1**-A]$^-$ in Figures 5A.15 and 5A.18 (Appendix), respectively.

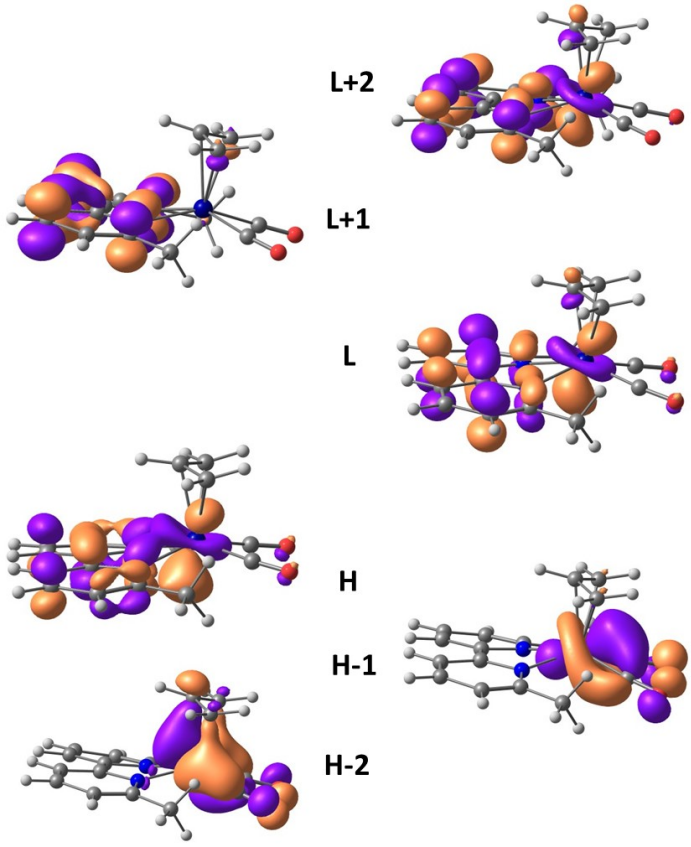

Figure 5.8: DFT-calculated frontier orbitals of the 5-coordinate anion [Mo(η^3-allyl)(6,6′-dmbipy)(CO)$_2$], [**3**-A]$^-$.

Two other reduced species are also formed, depending on the x,x′-dmbipy ligand. First, the existence of the 6-coordinate anion [Mo(η^3-allyl)(4,4′-dmbipy)(CO)$_2$(PrCN)]$^-$, [**1**-PrCN]$^-$, is not obvious from the preceding CV studies but strong evidence for its participation comes from the IR SEC described in the following section. This low-temperature

complex of PrCN and 2e$^-$ reduced [**X**-A]$^-$ in the equatorial conformation was only observed for [**1**-PrCN]$^-$ (Figure 5.9) and [**2**-PrCN]$^-$ (Figure 5A.20 in the Appendix); the absence of [**3**-PrCN]$^-$ (Figure 5A.20) may be explained by stronger stabilizing π-delocalization in the closer-to-square pyramidal structure of [**3**-A]$^-$, as well as by the steric hindrance by the adjacent methyl substituents. For [**1**-PrCN]$^-$, the axial and equatorial isomers, both as diamagnetic or paramagnetic species, were explored, but only the diamagnetic equatorial isomers could be calculated with PrCN coordinated in the original position of the thiocyanate ligand in parent **1** (Figure 5.9). The 4,4′-dmbipy inter-ring C−C distance of 1.399 Å is significantly shorter, compared to the values calculated for both diamagnetic [**1**-A]$^-$ (1.432 Å) and paramagnetic [**1**]$^{\bullet -}$ (1.426 Å), where 4,4′-dmbipy is considered to be formally 1e$^-$ reduced. This may lead to the conclusion that both added electrons in [**1**-PrCN]$^-$ reside largely in the lowest π^*-(dmbipy) orbital. On the other hand, the calculated wavenumbers of the ν(CO) and PrCN ν(CN) modes in [**X**-PrCN]$^-$ are still too low and too high, respectively, compared to the experimental values for stable 6-coordinate [**1**-PrCN]$^-$ (Table 5.2), which indicates only rather weak interactions of [**X**-A]$^-$ with PrCN, as also reflected in positive binding energies, with regard to the isolated components.

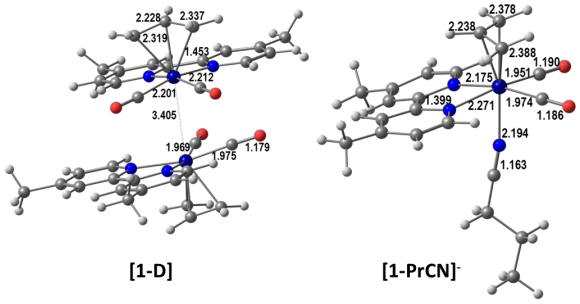

Figure 5.9: DFT-optimized structures of the 6-coordinate anion [Mo(η^3-allyl)(4,4′-dmbipy)(CO)$_2$(PrCN)]$^-$, [**1**-PrCN]$^-$ (the stable equatorial isomer, right) and the staggered Mo−Mo dimer, [**1**-D] (left), with relevant bond lengths (Å).

The 5-coordinate radical and anionic species, [**X**-R] and [**X**-A]$^-$, in the TBP geometry do not have obvious occupied frontier orbitals to form a Mo−Mo bond, but the SP conformers feature the SOMO and HOMO, respectively, with a strong contribution of 4 d_z^2, as reflected in the orbital contour plots (Figure 5A.21 in the Appendix, for **X** = 1). Therefore,

it is easy to imagine two radicals forming a Mo−Mo bond, in [**1**-D], by sharing electrons. This is equivalent to the formation of the dimer by the reaction between the $2e^-$ reduced anion and the neutral parent complex after the loss of the thiocyanate (via donation of $2e^-$ from $[\mathbf{1}\text{-A}]^-$ to the empty orbital of **1**). The dimer obtained, [**1**-D] (Figure 5.9), displays a very long Mo−Mo bond but is a true intermediate (see the ν(CO) wavenumbers in Table 5A.8). Other bond lengths are within normal values. A similar dimer could be obtained for **2** (Figure 5A.20). A definitive answer to the true nature of the dimer would require a more extensive analysis of possible alternatives and more experimental information.

The $2e^-$ reduction of **1** and **3** to corresponding 5-coordinate anions $[\mathbf{X}\text{-A}]^-$ (Scheme 5.1) was also performed under a CO_2 atmosphere, and there was evidence of a different reactivity (see the following SEC section). Therefore, we used DFT calculations to look for derivatives of the 5-coordinate anion with CO_2, both as equatorial and axial isomers of the adduct $[\mathbf{1}\text{-}CO_2]^-$. The equatorial isomer (Figure 5.10) was more stable, by 7.2 kcal mol^{-1}, than the axial one (Table 5A.3).

The narrow O−C−O angle in $[\mathbf{1}\text{-}CO_2]^-$ of ca. 125° is consistent with a strong electronic reduction accompanying the coordination of CO_2 caused by the electron transfer from formally dianionic 4,4′-dmbipy seen, for example, in $[\mathbf{1}\text{-PrCN}]^-$. This is evidenced by a strong elongation of the C1-C1′ inter-ring distance from 1.399 Å in the latter anion to 1.466 Å in $[\mathbf{1}\text{-}CO_2]^-$. This value is very close to 1.476 Å for neutral 4,4′-dmbipy in **1**. The C=O bonds in the reduced CO_2 ligand are elongated to 1.273 Å/1.275 Å, which reflects their weakening. There is still significant electron density on the two carbonyl ligands, as revealed by the calculated CO-stretching wavenumbers of 1831 and 1714 cm^{-1} for the symmetric and asymmetric mode, respectively.

5.4.4 IR and UV-Vis Absorption Spectroelectrochemistry at Low Temperature

Molecular spectroelectrochemistry is commonly used in combination with conventional cyclic voltammetry (CV) to assign major redox products. In this work, IR and UV-Vis spec-

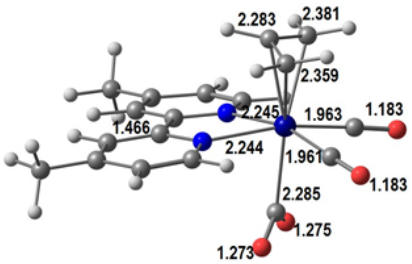

Figure 5.10: DFT-optimized structure of [Mo(η^3-allyl)(4,4′-dmbipy)$(CO)_2(CO_2)$]$^-$, [**1**-CO_2]$^-$.

troscopy, in combination with thin-layer cyclic voltammetry (TL-CV), is very convenient to unravel the reduction paths of **1-3**, in association with the insight from the conventional CV and the predictive power of the relevant DFT data in the preceding sections. The focus is placed on analysis of the IR stretching pattern and wavenumbers of the carbonyl ligands, the CN-stretching modes of the NCS^- and PrCN ligands, and the electronic absorption of the reduced x,x′-dmbipy ligands.

All three parent complexes are smoothly oxidized to the corresponding (radical) cations that are stable at 298-223 K. The corresponding CO- and CN-stretching wavenumbers and visible electronic absorption are summarized in Table 5A.10 in the Appendix. The IR spectral changes are supportive of the depopulation of the π^*(Mo−NCS) HOMO of the parent complexes, with a strong impact on the Mo-to-CO π-back-donation, strongly reduced in the formally Mo(III) products. It is important to note that the thermal stability of $[X]^+$ (X = **1-3**) is significantly higher, compared to the cationic complex with the unsubstituted bipy ligand,[46] proving the stronger donor ability of all three dimethylated x,x′-dmbipy ligand isomers. This result indicates that any major differences in the cathodic behavior of **1-3** should have their origin in the steric properties of the metallacycle imposed by the methyl substituents at x,x′-dmbipy (x = 4-6).

Table 5.2: IR and UV-Vis absorption data for complexes [Mo(η^3-allyl)(x,x′-dmbipy)(CO)$_2$(NCS)], **1** (x = 4), **2** (x = 5) and **3** (x = 6), and their reduction products (Scheme 5.1). Reference compounds containing the non-methylated bipyridine ligand are also included.

	ν(CO)/ cm^{-1}		ν(CN) / cm^{-1}		λ_{max}
Complex	Exp	DFT[h]	Exp	DFT[h]	/ nm
[Mo(η^3-allyl)(bipy)(CO)$_2$(NCS)][a]	1950, 1868	-	2079	-	351, 478
[Mo(η^3-allyl)(bipy)(CO)$_2$(NCS)][a,c]	1946, 1864	-	2085	-	-
[Mo(η^3-allyl)(bipy)(CO)$_2$(NCS)][b]	1951, 1871	-	2075	-	340, 501
[Mo(η^3-allyl)(4,4′-dmbipy)(CO)$_2$(NCS)][a]	1949, 1866	-	2080	-	475
[Mo(η^3-allyl)(4,4′-dmbipy)(CO)$_2$(NCS)][a,c]	1949, 1863	-	2084	-	-
[Mo(η^3-allyl)(4,4′-dmbipy)(CO)$_2$(NCS)][b]	1949, 1869	1882, 1800	2076	2056	490
[Mo(η^3-allyl)(4,4′-dmbipy)(CO)$_2$(NCS)][b,d]	1948, 1868	-	2078	-	-
[Mo(η^3-allyl)(5,5′-dmbipy)(CO)$_2$(NCS)][a]	1950, 1867	-	2080	-	470
[Mo(η^3-allyl)(5,5′-dmbipy)(CO)$_2$(NCS)][a,c]	1947, 1863	-	2085	-	-
[Mo(η^3-allyl)(5,5′-dmbipy)(CO)$_2$(NCS)][b]	1951, 1871	1883, 1801	2076	2056	-
[Mo(η^3-allyl)(6,6′-dmbipy)(CO)$_2$(NCS)][a]	1946, 1862	-	2078	-	460
[Mo(η^3-allyl)(6,6′-dmbipy)(CO)$_2$(NCS)][a,c]	1944, 1860	-	2082	-	-
[Mo(η^3-allyl)(6,6′-dmbipy)(CO)$_2$(NCS)][b]	1948, 1866	1881, 1800	2074	2054	-
[Mo(η^3-allyl)(bipy)(CO)$_2$(NCS)]$^{\bullet-}$[a,c]	1920, 1829	-	2079	-	-
[Mo(η^3-allyl)(4,4′-dmbipy)(CO)$_2$(NCS)]$^{\bullet-}$[a,c]	1922, 1832	1855, 1763	2089	2070	388, 494, 538, >600
[Mo(η^3-allyl)(4,4′-dmbipy)(CO)$_2$(NCS)]$^{\bullet-}$[b,d]	1926, 1831	-	2084	-	-
[Mo(η^3-allyl)(5,5′-dmbipy)(CO)$_2$(NCS)]$^{\bullet-}$[a,c]	1921, 1832	1853, 1761	2085	2072	394, 492, 528, >600
[Mo(η^3-allyl)(6,6′-dmbipy)(CO)$_2$(NCS)]$^{\bullet-}$[a,c]	1920, 1829	1855, 1764	2089	2069	396, 489, 518, >600
[Mo(η^3-allyl)(6,6′-dmbipy)(CO)$_2$(NCS)]$^{\bullet-}$[b]	1925, 1834	-	2089	-	-
[Mo(η^3-allyl)(6,6′-dmbipy)(CO)$_2$(NCS)]$^{\bullet-}$[a]	1923, 1833	-	-	-	-
[Mo(η^3-allyl)(bipy)(CO)$_2$(PrCN)]$^{-}$[a]	1893, 1796	-	2147[i]	-	-
[Mo(η^3-allyl)(4,4′-dmbipy)(CO)$_2$(PrCN)]$^{-}$[a,c]	1896, 1797	1797, 1705	2148[i]	2229	350
[Mo(η^3-allyl)(5,5′-dmbipy)(CO)$_2$(PrCN)]$^{-}$[a,c]	1897, 1789	1781, 1687	2148[i]	2313	360
[Mo(η^3-allyl)(6,6′-dmbipy)(CO)$_2$(PrCN)]$^{-}$[a]	1904, 1789	1816, 1715	2148[i]	2247	-
[Mo(η^3-allyl)(bipy)(CO)$_2$]$_2$[b]	1891, 1778, 1757	-	-	-	369, 581
		-	-	-	-
[Mo(η^3-allyl)(4,4′-dmbipy)(CO)$_2$]$_2$[b]	1891, 1766, 1759	1775, 1787, 1844, 1858	-	-	-
[Mo(η^3-allyl)(5,5′-dmbipy)(CO)$_2$]$_2$[b]	1892, 1779, 1757	1777, 1789, 1844, 1858	-	-	-
[Mo(η^3-allyl)(4,4′-dmbipy)(CO)$_2$]$^{-}$[b,d]	1815, 1722	1741, 1658[e]	-	-	-
[Mo(η^3-allyl)(5,5′-dmbipy)(CO)$_2$]$^{-}$[a,c]	1789, 1693	1742, 1658[e]	-	-	590
[Mo(η^3-allyl)(5,5′-dmbipy)(CO)$_2$]$^{-}$[b]	1820, 1730	-	-	-	-
[Mo(η^3-allyl)(6,6′-dmbipy)(CO)$_2$]$^{-}$[a,c]	1797, 1700[g]	1803, 1702[f]	-	-	420, 550
[Mo(η^3-allyl)(6,6′-dmbipy)(CO)$_2$]$^{-}$[a]	1807, 1700	-	-	-	-
[Mo(η^3-allyl)(6,6′-dmbipy)(CO)$_2$]$^{-}$[b]	1792, 1680	-	-	-	-

[a] Measured in PrCN. [b] Measured in THF. [c] Measured at 223 K. [d] Measured at 268 K. [e] Derived from axial isomer. [f] Derived from equatorial isomer. [g] Broad absorption bands. [h] Some DFT data from Table 5A.8 is reproduced. [i] CN stretching mode of the PrCN ligand. [j] Values at Au minigrid, at Pt minigrid: 1801 and 1717 cm^{-1}.

It is prudent to start the description of the cathodic behavior in the studied series of complexes with the low-temperature spectroelectrochemistry of **3** that displays arguably the most straightforward redox behavior, as revealed by CV (Figure 5.4). This is because [Mo(η^3-allyl)(6,6′-dmbipy)$(CO)_2$(NCS)]$^{\bullet-}$ ([**3**]$^{\bullet-}$) is perfectly stable in PrCN at low temperature; then, passing the reversible reduction step R1 at 223 K, only the radical anion is detected. The sole product is easily assignable from the distinctive high-energy shift of the ν(CN) band of NCS^- from 2069 cm^{-1} to 2089 cm^{-1} and the accompanying low-energy shift of the two ν(CO) bands from 1943 and 1859 cm^{-1} to 1919 and 1829 cm^{-1}, respectively (Figure 5.11a). These values show reasonable agreement with those procured from the DFT calculations (Table 5A.8 and Table 5.2, with a scaling factor of 0.97). The corresponding UV-Vis-NIR spectral changes recorded during the initial reduction (Figure 5A.22, Appendix) confirm the presence of the 6,6′-dmbipy radical anion by its characteristic intraligand π-π^* absorption at 396 nm, bifurcated π^*-π^* at 489 and 518 nm, and low-lying π^*-π^* at $>$ 600 nm,[37,76] which is consistent with the bipy-based LUMO of parent **3** (Figure 5A.14).

The radical anion, [**3**]$^{\bullet-}$, was smoothly reduced in the following, irreversible 1e^- cathodic step at R2 generating the 5-coordinate anion [Mo(η^3-allyl)(6,6′-dmbipy)$(CO)_2$]$^-$, [**3**-A]$^-$ (Scheme 5.1). This process is recognized by the appearance of free NCS^- absorbing at 2050 cm^{-1}, and two low-lying broad ν(CO) bands at 1797 and 1700 cm^{-1}, which are characteristic of a negatively charged dicarbonyl 5-coordinate species. The experimental wavenumbers are in a very good agreement with the DFT values calculated for the equatorial square-pyramidal structure (Table 5.2) stabilized by strongly delocalized π-bonding in the metallacycle. This is the first time that reliable IR ν(CO) values have been reported for 2e^- reduced [Mo(η^3-allyl)(α-diimine)$(CO)_2$]$^-$. In the published pioneering work,[46] the IR absorption of the more reactive anion [Mo(η^3-allyl)(bipy)$(CO)_2$]$^-$ (detected by conventional CV analysis) was confused with products of thermal dimerization reactions (Scheme 5.1, and spectroelectrochemistry below). In the visible spectral region, [**3**-A]$^-$ exhibits the characteristic absorption between 450 nm and 600 nm (Figure 5A.23 in the Appendix) belonging

to π-π^* electronic excitation[77] between the delocalized frontier orbitals of the Mo-dmbipy metallacycle (Figure 5.8).

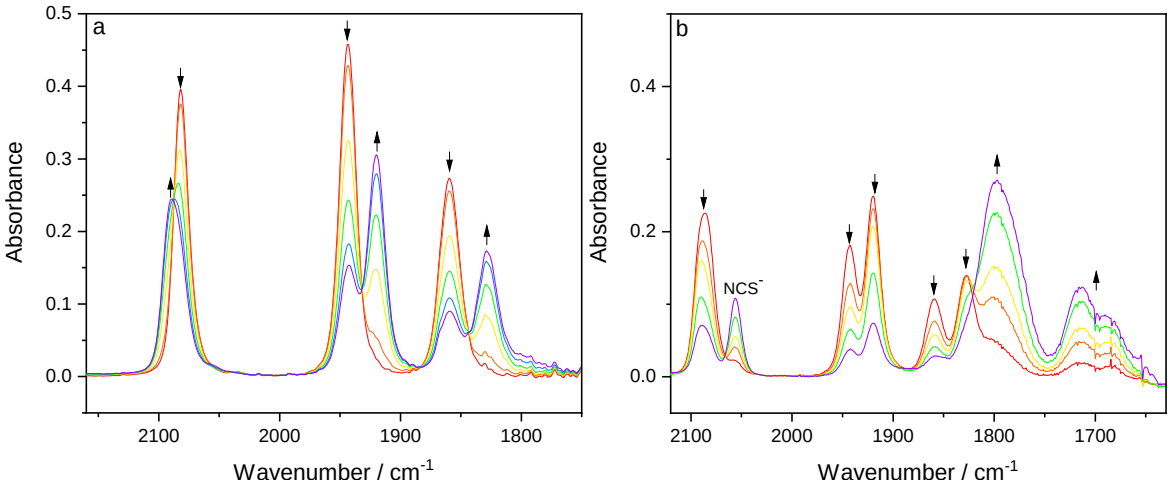

Figure 5.11: IR SEC monitoring of (a) the initial 1e$^-$ reduction of [Mo(η^3-allyl)(6,6′-dmbipy)(CO)$_2$(NCS)], **3** (↓) at R1 to stable [**3**]$^{\bullet-}$ (↑) and (b) the following reduction at R2 showing the conversion of [**3**]$^{\bullet-}$ (↓) to [**3**-A]$^-$ (↑) and free NCS$^-$. Conditions: a cryostatted OTTLE cell, PrCN/Bu$_4$NPF$_6$, 223 K.

In the preceding CV section, radical anions [**1**]$^{\bullet-}$ and [**2**]$^{\bullet-}$ were found to convert under ambient conditions within seconds to the corresponding 5-coordinate anions already at the initial cathodic wave R1 (Figures 5.2a and 5.3a, respectively). However, for [**3**]$^{\bullet-}$, this ECE process is too slow to be detected on the CV timescale (Figure 5.4a). Therefore, the reduction of **3** at R1 and subsequent reactivity of its radical anion were studied by IR SEC at variable temperatures. At 223 K, [**3**]$^{\bullet-}$ remained stable. However, gradual temperature elevation to 273 K at the constantly applied cathodic potential R1 resulted in its complete conversion to 2e$^-$ reduced [**3**-A]$^-$ (Figure 5.12). This is the high-T ECE equivalent of the low-T EEC path at the cathodic potential R2 (Figure 5.11b). Reasons for the unusually high stability of [**3**]$^{\bullet-}$ are briefly discussed in the preceding DFT section.

Compared to **3**, the cathodic behavior of **1** under the same SEC conditions is affected by both the higher thermal reactivity of [**1**]$^{\bullet-}$ and the different steric properties of the 4,4′-dmbipy ligand. Despite appearing stable on the CV timescale (Figure 5.2), the low temperature of 223 K set in the OTTLE cell was insufficient to completely stabilize the

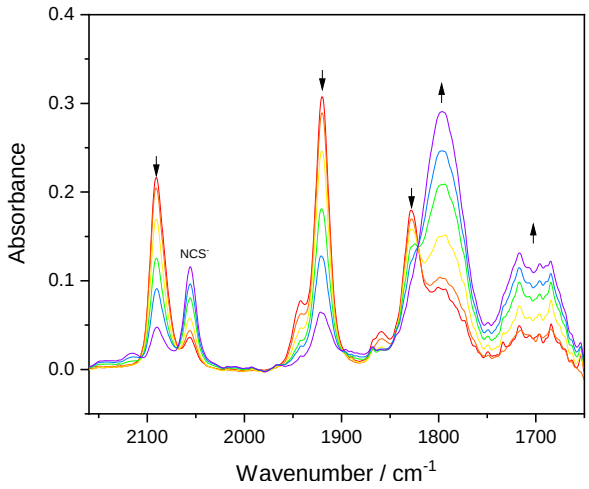

Figure 5.12: Controlled potential IR SEC monitoring of the thermal conversion of [Mo(η^3-allyl)(6,6′-dmbipy)(CO)$_2$(NCS)]$^{\bullet-}$, [**3**]$^{\bullet-}$ (↓) to [**3**-A]$^-$ (↑) and free NCS$^-$ between 223 K and 298 K. Conditions: a cryostatted OTTLE cell, PrCN/Bu$_4$NPF$_6$, 223 K.

radical anion. IR monitoring of the electrolysis at R1 revealed the simultaneous appearance of [**1**]$^{\bullet-}$ as the primary reduction product, and another dicarbonyl complex assigned as the PrCN-substituted 6-coordinate anion, [**1**-PrCN]$^-$ (Figure 5.13, Scheme 5.1) that replaces, in the strongly cooled coordinating solvent, the 2e$^-$ reduced 5-coordinate anion, [**1**-A]$^-$, in contrast to **3** and [**3**-A]$^-$. The radical anion [**1**]$^{\bullet-}$ is once again identified by the ca. 5 cm^{-1} high-energy shift of the ν(CN) mode of coordinated NCS$^-$ and the low-energy shift of the two ν(CO) modes by some 20-30 cm^{-1}, in this case from 1946 and 1862 cm^{-1} to 1922 and 1832 cm^{-1}. The presence of the singly reduced 4,4′-dmbipy ligand in [**1**]$^{\bullet-}$ has been confirmed by the parallel UV-Vis monitoring of the reduction course (Figure 5A.24 in the Appendix).

The new axial PrCN ligand in the second observed reduction product, [**1**-PrCN]$^-$, is typically recognized in the IR spectrum by its low-intensity ν(CN) absorption at 2147 cm^{-1} (Figure 5.13). The liberated NCS$^-$ ligand absorbs again at 2050 cm^{-1}. The accompanying ν(CO) bands at 1898 and 1797 cm^{-1} of [**1**-PrCN]$^-$ are much narrower, compared to those of the 5-coordinate [**3**-A]$^-$ (Figure 5.11) and [**1**-A]$^-$ (see Figure 5.14). A significant difference in ν(CO) wavenumbers and bandwidth was also encountered for related 2e$^-$ reduced anions [Re(bipy)(CO)$_3$]$^-$ and [Re(bipy)(CO)$_3$(PrCN)]$^-$.[78] The ν(CO) wavenumbers do not corre-

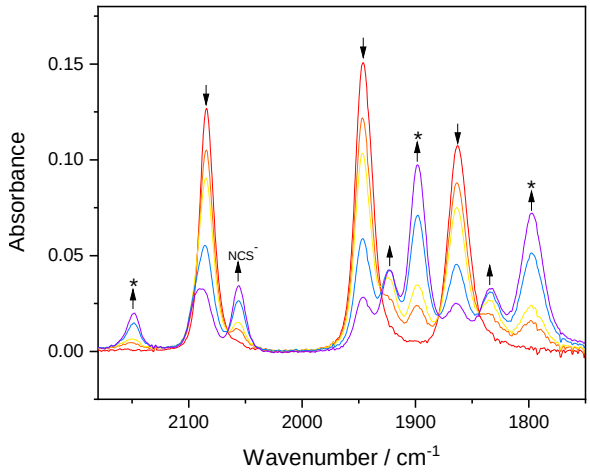

Figure 5.13: IR SEC monitoring of the electrochemical reduction of [Mo(η^3-allyl)(4,4′-dmbipy)$(CO)_2$(NCS)]$^{\bullet-}$, **1** (↓) at R1 forming [**1**]$^{\bullet-}$ (↑) and 6-coordinate [**1**-PrCN]$^-$ (*). Conditions: a cryostatted OTTLE cell, PrCN/Bu_4NPF_6, 223 K.

spond with any 1e$^-$ reduced radical species, being much smaller than those of [**1**]$^{\bullet-}$ (Table 5.2). On the other hand, they are much larger, compared to [**1**-A]$^-$ (Table 5.2), because the second added electron in the latter π-delocalized anion largely resides on the $Mo(CO)_2$ moiety while in 6-coordinate [**1**-PrCN]$^-$ it is on the (formally dianionic) bipy ligand (see the preceding DFT section).

The UV-Vis spectra corresponding to the IR SEC situation in Figure 5.13 also indicate the presence of two reduced species, one of which must be [**1**]$^{\bullet-}$ absorbing at 388, 494, 538, and >650 nm. The electronic absorption arising at ∼350 nm is then assigned to [**1**-PrCN]$^-$; importantly, the characteristic metallacycle π-π^* absorption of [**X**-A]$^-$ at 500-600 nm (Table 5.2) is absent in this case (Figure 5A.24), which is consistent with the IR SEC results. The comparison of the reduction paths of complexes **1** and **3** clearly reveals that the 6,6′-dmbipy ligand hinders coordination of PrCN to the Mo center of [**X**-A]$^-$, probably not only for steric but also electronic reasons. Data in Table 5A.8 testify that [**1**-A]$^-$ prefers a different structure than [**3**-A]$^-$, with an impact on the π-delocalization in the Mo-dmbipy metallacycle stabilizing the 5-coordinate geometry of the 2e$^-$ reduced species. An alternative structure of 6-coordinate [**1**-PrCN]$^-$ has been suggested by DFT calculations on its possible triplet states. The paramagnetic equatorial form appears to be quite stable, revealing a

changed η^2-allyl coordination and a stronger Mo-PrCN bond. A detailed investigation of this interesting alternative was beyond the scope of this work, but attention will be paid to it in the follow-up studies.

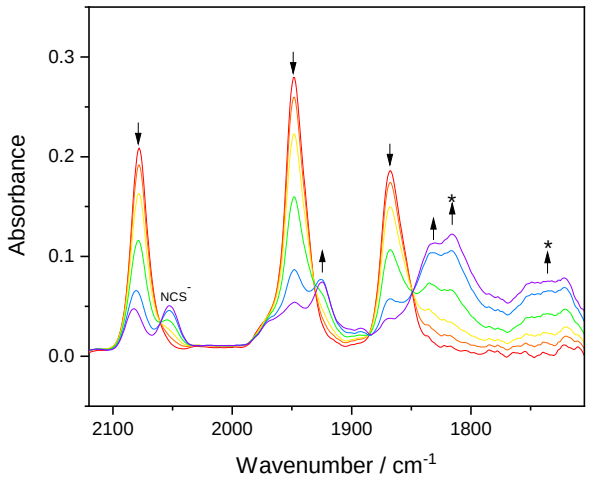

Figure 5.14: IR SEC monitoring of the electrochemical reduction of [Mo(η^3-allyl)(4,4′-dmbipy)$(CO)_2$(NCS)]$^{\bullet-}$, **1** (↓) at R1 forming [**1**]$^{\bullet-}$ (↑) and 5-coordinate [**1**-A]$^-$ (*) as a weak adduct with THF. Conditions: a cryostatted OTTLE cell, THF/Bu_4NPF_6, 268 K.

Conducting the reduction of **1** in weakly coordinating THF at 268 K induces a very similar behavior as described above for **3** in the chilled PrCN electrolyte (Figure 5.14). In addition to intermediate [**1**]$^{\bullet-}$, the main product formed at the cathodic wave R1 is now the 5-coordinate anion [**1**-A]$^-$ absorbing in the ν(CO) region at 1815 and 1722 cm^{-1}. The wavenumbers are much smaller, compared to 6-coordinate [**1**-PrCN]$^-$ (see above). On the other hand, both values are slightly larger than those determined for 5-coordinate [**1**-A]$^-$ in chilled PrCN and in THF at ambient temperature (Table 5.2), while they should be smaller according to the DFT calculations. This difference can be explained by the formation of a weak adduct of [**1**-A]$^-$ with THF, causing slightly decreased electron density on the carbonyl ligands. Much larger ν(CO) wavenumbers can be anticipated in this regard for ordinary 6-coordinate anion with coordinated THF, [**1**-THF]$^-$.[79]

The course of the reduction of **2** at R1 in PrCN at 223 K (Figure 5A.25 in the Appendix) combines the features observed for **1** and **3**, with the parallel production of radical anion [**2**]$^{\bullet-}$ (ν(CO) at 1921, 1831 cm^{-1}), and 6-coordinate anion [**2**-PrCN]$^-$ (ν(CO) at 1897, 1789

cm^{-1}) in a thermal equilibrium with 5-coordinate anion [**2**-A]$^-$ (ν(CO) 1789, 1692 cm^{-1}). This product distribution was confirmed by the parallel UV-Vis monitoring (Figure 5A.26 in the Appendix). The visible region is dominated by the characteristically broad absorption of the 5-coordinate anion at ∼600 nm. This experiment presents the most convincing evidence for the median position of the 5,5′-dimethyl substitution at the redox active bipy ligands in the studied series.

5.4.5 IR and UV-Vis Absorption Spectroelectrochemistry at Ambient Temperature

The discussion of the generally more complicated cathodic paths and reactivity induced by the added electrons at room temperature will be based on IR spectroelectrochemical results obtained in weakly coordinating THF and strongly coordinating PrCN. It focuses on the participation of peculiar dimerization reactions of **1** and **2**, which are inhibited by cooling the electrolyte solution (see the preceding section).

It is convenient to start the description and discussion of the cathodic behavior at 298 K again with **3** bearing the sterically demanding 6,6′-dmbipy ligand. Notably, the reduction path in THF mirrors the temperature-controlled conversion of 1e$^-$ reduced [**3**]$^{\bullet-}$ in PrCN at R1 to 2e$^-$ reduced 5-coordinate [**3**-A]$^-$ via [**3**-R] (Figure 5.12). Thus, during the reduction of **3** at R1, only a small amount of [**3**]$^{\bullet-}$ (ν(CN): 2087 cm^{-1}, and ν(CO): 1924, 1835 cm^{-1}) is initially detected (Figure 5.15), the transient species being readily converted to stable 2e$^-$ reduced [**3**-A]$^-$ (ν(CO): 1792, 1680 cm^{-1}). This process may involve an intermediate (a contact species) absorbing at 1900 cm^{-1}, differently from the instant low-temperature ECE path. It is worth mentioning that the wavenumbers of [**3**-A]$^-$ in this experiment are somewhat smaller than those measured in PrCN at 223 K (Table 5.2). This observation indicates a weak interaction between [**3**-A]$^-$ and PrCN at the low temperature. The spectral variability in the ν(CO) region is thus a common feature in the entire series of [**X**-A]$^-$.

The cathodic path of **3** leading to [**3**-A]$^-$ in PrCN at 298 K (Figure 5A.27 in the Appendix) is less straightforward than in THF. The initially detectable reduced species

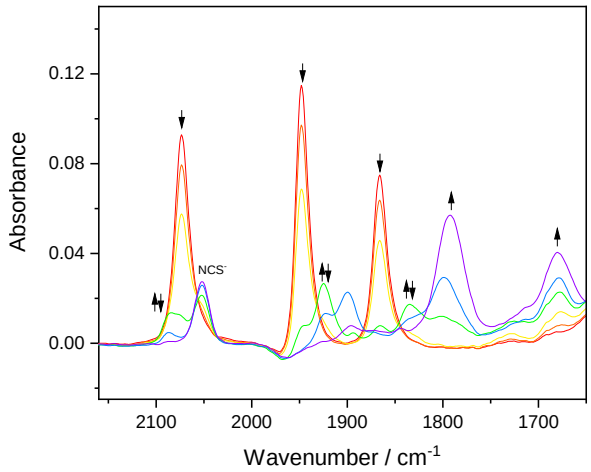

Figure 5.15: IR SEC monitoring of the initial reduction of [Mo(η^3-allyl)(6,6′-dmbipy)$(CO)_2$(NCS)], **3** (↓) at R1 to 5-coordinate [**3**-A]$^-$ (↑) via intermediate [**3**]$^{\bullet-}$ (↑↓). Conditions: OTTLE cell, THF/Bu_4NPF_6, 298 K.

shows two ν(CO) bands at 1923 and 1797 cm^{-1}, being accompanied by free thiocyanate absorbing at 1950 cm^{-1}. The absence of the ν(CN) absorption of the coordinated thiocyanate (typically above the parent absorption at 2074 cm^{-1}) excludes the formation of [**3**]$^{\bullet-}$. The higher stability of the reduced dicarbonyl complex formed, compared to [**3**]$^{\bullet-}$ in THF (Figure 5.15), supports its tentative assignment as the solvento radical [Mo(η^3-allyl)(6,6′-dmbipy)$(CO)_2$(PrCN)], [**3**-PrCN]. As anticipated, the concomitant reduction of this complex produces [**3**-PrCN]$^-$ (ν(CO) at 1904 and 1789 cm^{-1}) that was not detected along the straightforward ECE route at 223 K (Figure 5.12). Therefore, it is not surprising that the 2e$^-$ reduced 6-coordinate anion also is unstable at 298 K and converts gradually to 5-coordinate [**3**-A]$^-$ (ν(CO) at 1807 and 1700 cm^{-1}). The described peculiar cathodic path also includes a contact species (ν(CO) absorption at 1832 and 1733 cm^{-1}), arising from the coexistence of [**3**-PrCN] and [**3**-A]$^-$. This absorbance disappears during the follow-up reduction of [**3**-PrCN] to [**3**-PrCN]$^-$, the latter converting ultimately to genuine [**3**-A]$^-$. The main factor responsible for the different reduction paths of **3** in PrCN at 223 and 298 K, and in THF at 298 K, is the (in)stability of [**3**]$^{\bullet-}$ as the primary 1e$^-$ reduction product. It is also noteworthy that the ν(CO) wavenumbers of [**3**-PrCN] (1923, 1797 cm^{-1}) are very similar to those calculated (using the scaling factor of 0.97) for the equatorial isomer of

5-coordinate radical [**3**-R] (Table 5A.8). This means that, compared to THF, where [**3**-R] is directly reducible to [**3**-A]$^-$, the 5-coordinate radical becomes stabilized by a weak bonding interaction with PrCN. There is no evidence for its secondary dimerization (Scheme 5.1), pointing to the protective role of the 6,6′-dmbipy ligand.

Reducing **1** in THF at 298 K, the first cathodic step at the electrode potential of R1 already shows a striking difference from the reduction of **3** that converts under the same conditions of thin-layer electrolysis exclusively to 5-coordinate anion [**3**-A]$^-$ (typically broad ν(CO) bands at 1792 and 1680 cm^{-1}). For **1**, the corresponding anionic species, [**1**-A]$^-$, was only detected at 268 K as a weak adduct with THF (Table 5.2). Instead, at room temperature, no [**1**-A]$^-$ was formed at R1 and the dominant product (apart from minor [**1**]$^{\bullet -}$ still detectable in the thin-solution layer of the OTTLE cell) showed an unusual IR spectral pattern of three narrow ν(CO) bands at 1891, 1778, and 1759 cm^{-1} (Figure 5.16). These values of absorption maxima reasonably agree with the ν(CO) wavenumbers obtained with DFT for the staggered structure of the Mo−Mo bound dimer [Mo(η^3-allyl)(4,4′-dmbipy)(CO)$_2$]$_2$, [**1**-D] (Figure 5.9, and Tables 5.2 and 5A.8). The calculated intensity pattern of the four ν(CO) modes for [**1**-D], 1858 (medium), 1844 (strong), 1787 (strong), and 1775 (weak), has been encountered[80] for the tetracarbonyl dimer [Ru(iPr-dab)(CO)$_2$(Me)]$_2$ (iPr-dab = 1,4-diisopropyl-1,4-diaza-buta-1,3-diene)].

For **1**, the exact molecular structure of the dimeric end-product showing the different ν(CO) intensity pattern ([**1**-D′]), is unknown at present. However, it is assumed to be closely related to the metal-metal bound dimers represented by [Ru(iPr-dab)(CO)$_2$(Me)]$_2$ and [Mn(bipy)(CO)$_3$]$_2$, resulting from the general ECEC cathodic route shown also in Scheme 5.1, which has been based on the evidence gained from faster CV analysis. A strong argument for a different, reinforced structure of [**1**-D′] is its subsequent reduction that does not convert it to 5-coordinate anion, [**1**-A]$^-$, which is a typical ECE step for both Ru−Ru and Mn−Mn dimers, but most likely to singly reduced [**1**-D′]$^-$. For [Mo(η^3-allyl)(bipy)(CO)$_2$(NCS)], with a cathodic behavior closest to that of **1**, the equivalent of [**1**-D′] absorbs in the IR CO-stretching region at 1891, 1778, and 1757 cm^{-1}.[46] The sub-

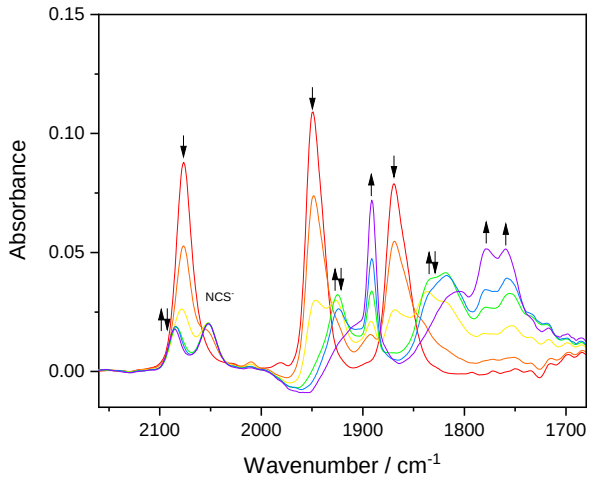

Figure 5.16: IR SEC monitoring of the initial reduction of [Mo(η^3-allyl)(4,4′-dmbipy)(CO)$_2$(NCS)], **1** (↓) at R1 to intermediate [**1**]$^{\bullet-}$ (↑↓) concomitantly converting to [Mo(η^3-allyl)(4,4′-dmbipy)(CO)$_2$]$_2$-related dimer [**1**-D′] (↑). Conditions: OTTLE cell, THF/Bu_4NPF_6, 298 K.

sequent reduction shifts these values down to 1844, 1723, and 1700(sh) cm^{-1}. The latter wavenumbers were assigned incorrectly to [Mo(η^3-allyl)(bipy)(CO)$_2$]$^-$, which is actually hardly seen in THF at 298 K, similar to [**1**-A]$^-$. It remains a challenge to prepare, isolate, and characterize [**1**-D′] in a follow-up study.

Reducing **1** at room temperature in PrCN (Figure 5A.28, Appendix), dimer [**1**-D′] is again the dominant product, suggesting that, under ambient conditions, there is a strong driving force to form this species. The intimate mechanism is slightly different from that in THF, with [**1**-PrCN], and [**1**-A]$^-$ in a weak contact with PrCN, being involved as intermediate species. Much like at low temperature in PrCN (see above), reduction of **2** in THF at 298 K (Figure 5A.29, Appendix) represents an intermediate case between the routes of **1** and **3**, producing ultimately a mixture of both the 5-coordinate anion and a dimer. The [Mo(η^3-allyl)(5,5′-dmbipy)(CO)$_2$]$_2$ related dimer, [**2**-D′], is revealed by the three ν(CO) bands at 1892 (sharp), 1780 and 1761 cm^{-1}; the ν(CO) wavenumbers of [Mo(η^3-allyl)(5,5′-dmbipy)(CO)$_2$]$^-$ (1820, 1730 cm^{-1}) point to its weak interaction with THF. A very similar cathodic path is followed by **2** in PrCN (Figure 5A.30, Appendix).

5.4.6 Cyclic Voltammetry and IR Spectroelectrochemistry under a CO_2 Atmosphere

The CV study of **1** and **3** was repeated in CO_2-saturated weakly coordinating THF at both Pt and Au cathodes, to probe the catalytic activity of the complexes toward CO_2 reduction and identify the catalyst. For both complexes the initial cathodic wave R1 (Table 5.1 and Table 5A.7, Appendix) remains unchanged, excluding any thermal reaction or adsorption effects. Inspecting the CV of **1** at an Au cathode in CO_2-saturated THF (Figure 5.17), the reduction at R1 does not produce any detectable 5-coordinate anions [**1**-A]$^-$ that would be reoxidized (under Ar) at the anodic wave O1′ (Figure 5.2). The adduct of the anion with CO_2, [**1**-CO_2]$^-$, has been calculated (Figure 5.10) and analyzed with DFT. Some catalytic current enhancement is not seen already at R1 but at a more negative potential close to the reduction of dimer [**1**-D] at R(D). This observation indicates that either further reduction of [**1**-CO_2]$^-$ or its transformation product at a potential close to R(D) is needed to trigger the catalytic process, or that the dimerization seen for [**1**-A]$^-$ in THF under argon cannot be inhibited under CO_2 and the concomitant dimer reduction is needed to regenerate catalyst [**1**-CO_2]$^-$. The first route resembles tricarbonyl Mn-iPr-dab (iPr-dab = 1,4-diisopropyl-1,4-diaza-buta-1,3-diene) complexes forming 2e$^-$ reduced 5-coordinate anions via an ECE mechanism, which react with CO_2 to form a Mn-bicarbonate intermediate reducible some 600 mV more negatively than the parent complex, to restore the catalytic activity.[81] IR monitoring of the electrolysis at R1 was needed to collect supporting evidence for either pathway (see below).

The cathodic behavior of **3** in THF in the presence of excess CO_2 on the short timescale of CV is straightforward, given the relative stability of singly reduced radical anions [**3**]$^{\bullet-}$ formed at R1 and further reducible to [**3**-A]$^-$ at R2 (Figure 5.18). Similar to [**1**-A]$^-$, also [**3**-A]$^-$ reacts with CO_2 to form initially [**3**-CO_2]$^-$, triggering the catalytic CO_2 reduction at R2. The higher catalytic current on Au (Figure 5.18a) compared to Pt (Figure 5.18b) indicates an involvement of the cathodic surface in the catalytic process. The increased catalytic

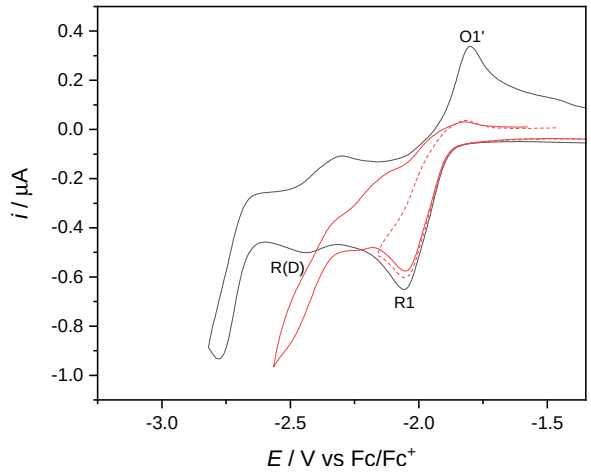

Figure 5.17: Cyclic voltammetry (CV) of [Mo(η^3-allyl)(4,4′-dmbipy)$(CO)_2$(NCS)], (**1**) in CO_2-saturated (red) or Ar-saturated (black) THF/Bu_4NPF_6 at an Au microdisc electrode. υ = 100 mV s^{-1}.

efficiency may result from a strong stabilizing interaction between the gold surface and [**3**-A]$^-$, which has recently been proven for the [Mo(bipy)$(CO)_4$] family of catalysts.[42] Compared to [Mo(η^3-allyl)(bipy)$(CO)_2$(NCS)],[46] the anionic catalyst derived from **3** operates with higher efficiency, that is, with a higher catalytic current flowing at a lower overpotential. This difference can be ascribed to a higher stability of [**3**-A]$^-$, as [Mo(η^3-allyl)(bipy)$(CO)_2]^-$ was hardly detectable by in-situ IR spectroscopy. In this case, IR SEC of **3** on the timescale of minutes was expected to provide evidence for the catalytic activity of [**3**-A]$^-$ toward CO_2 already at the cathodic wave R1 (consistent with Figure 5.15).

The reduction of **1** at R1 in CO_2-saturated THF monitored by IR spectroscopy led to a mixture of detectable products. The ν(CO) absorption at 1893 and 1760 cm^{-1} almost certainly belongs to dimer [**1**-D′] (Figure 5.16), which supports the dimerization process observed with CV (Figure 5.17). As expected, there is no 5-coordinate [**1**-A]$^-$ observed in the IR spectra at room temperature (Figure 5.14). However, compared to Figure 5.16, representing the cathodic route of **1** in THF under argon, the ν(CO) absorptions at 1910 and 1802 cm^{-1}, seen in Figure 5A.31 in the Appendix, are not much different from the wavenumbers predicted for the 6-coordinate anion [**1**-CO_2]$^-$ (1905, 1780 cm^{-1}), using the difference between the ν(CO) values measured and calculated for [**1**-A]$^-$ (Table 5.2, 90 and

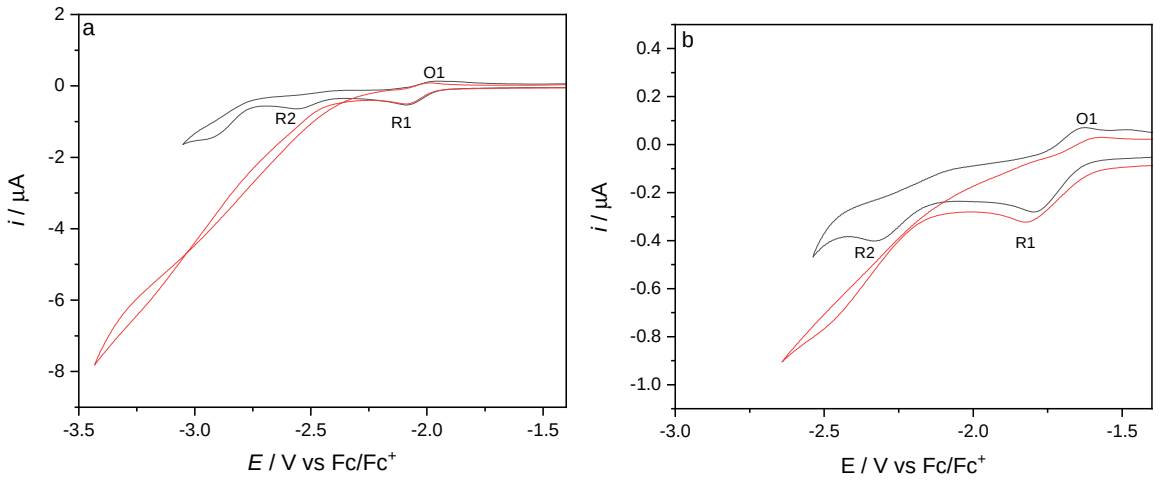

Figure 5.18: Cyclic voltammetry (CV) of [Mo(η^3-allyl)(6,6′-dmbipy)(CO)$_2$(NCS)], (**3**) in CO_2-saturated (red) or Ar-saturated (black) THF/Bu_4NPF_6 at (a) Au microdisc electrodes and (b) Pt microdisc electrodes. υ = 100 mV s^{-1}.

58 cm^{-1}), and the ν(CO) values calculated for [**1**-CO_2]$^-$. Another comparison of ν(CO) wavenumbers measured and calculated for [**1**]$^{\bullet-}$ (Table 5.2), and measured for [**1**-CO_2]$^-$ (see above), predicts the values calculated for [**1**-CO_2]$^-$ to be 1843 and 1734 cm^{-1}, which are reasonably close to the values of 1831 and 1714 cm^{-1} calculated for the DFT-optimized structure of [**1**-CO_2]$^-$ depicted in Figure 5.10. The interaction between [**1**-A]$^-$ and CO_2 has also been revealed by conventional cyclic voltammetry (Figure 5.17). In Figure 5A.31, there is a concurrent appearance of small bands at 1674 and 1641 cm^{-1} indicating the formation of free bicarbonate anion (and, indirectly, CO). At the same time, a small amount of free formate (1600 cm^{-1}) starts to appear from the very beginning of the thin-layer electrolysis of **1** at R1. The limited reductive conversion of dissolved CO_2, testified by only a small decrease in the intensity of the satellite $^{13}CO_2$ peak, is in agreement with the relative stability of [**1**-CO_2]$^-$ under the aprotic conditions. The formation of [**1**-D′] can also be considered as an inhibiting factor.

In argon-saturated THF at 298 K, **3** forms at R1 2e$^-$ reduced [**3**-A]$^-$ with the smallest IR ν(CO) wavenumbers of 1792 and 1680 cm^{-1} indicating the absence of any interaction with the weak donor solvent (Figure 5.15). The presence of CO_2 in the THF electrolyte has some impact on the ν(CO) wavenumbers of the 5-coordinate anion, which slightly

increase to 1801/1792 cm^{-1} and 1697/1673 cm^{-1} (Figure 5.19a). The behavior does not correspond with the formation of [**3**-CO_2]$^-$ previously observed for **1** with a less hindered Mo-dmbipy metallacycle. Rather, [**3**-CO_2]$^-$ interacts only weakly with CO_2, similar to PrCN at variable temperature (Figures 5.11 and 5.12). Moving the cathodic potential from R1 more negatively, toward R2 (in the ordinary CV of **3**), results in IR spectral changes (Figure 5.19b), revealing some catalytic conversion of CO_2 to free formate and CO (flanked by the characteristic absorption of the bicarbonate anion). The ν(CO) absorption of [**3**-CO_2]$^-$ becomes diminished while there is a continuous growth of ν(CO) absorption labeled by an asterisk in Figure 5.19b, which most likely corresponds to the inactive dimer, [**3**-D′], which is also seen for **1**, representing a deactivation route.

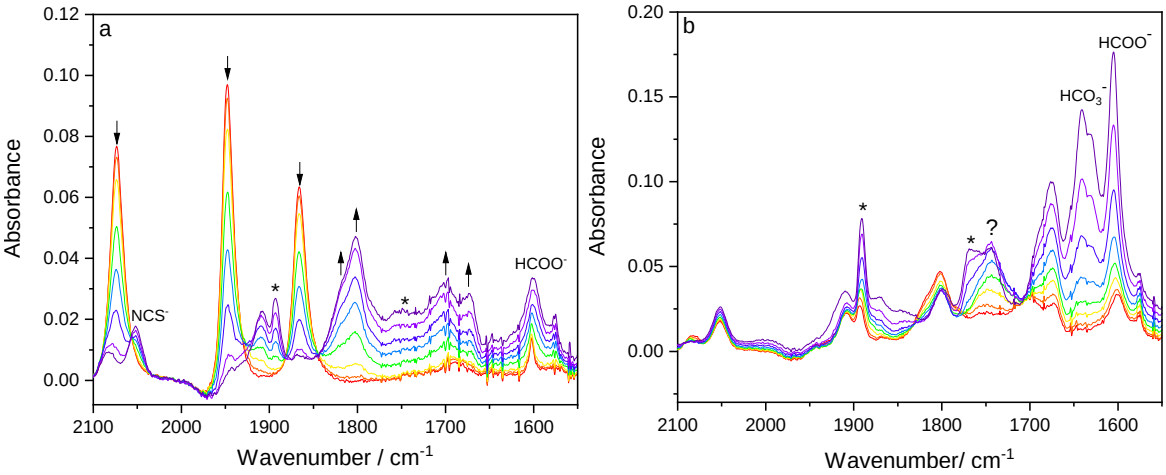

Figure 5.19: IR spectroelectrochemistry of [Mo(η^3-allyl)(6,6′-dmbipy)$(CO)_2$(NCS)], (**3**) in CO_2-saturated THF/Bu_4NPF_6 showing (a) the conversion of the parent complex at R1 to [**3**-A]$^-$ weakly interacting with CO_2 (↑), and (b) IR spectral changes accompanying further cathodic potential shift toward the cathodic wave R2.

5.5 Conclusions

The position of the methyl substituents in the studied series of x,x′-dmbipy (x = 4-6) complexes plays a key role in determining the cathodic paths at variable temperature. There is a direct linear relationship between the position of the methyl group and the stability of both the 1e$^-$ reduced primary radical anion and 2e$^-$ reduced 5-coordinate anionic complex, increasing in the direction of x = 4 < 5 < 6. This trend reflects an interplay of

both steric (dmbipy planarity, Mo−NCS packing) and electronic (Mo−NCS bond strength, delocalized π-bonding) factors. At the cathodic wave R1, the reduction of **1** produces the unstable radical anions and the 5-coordinate anions. The latter product converts to an unreactive dimer that may also exist in its reduced form; the molecular structure of the end-product, seen in both THF and PrCN, remains to be elucidated. This behavior excludes an unsupported Mo−Mo bond between 5-coordinate radical units. Radical anions derived from **3** are most stable, surprisingly more than the congeners with unsubstituted bipy as a weaker donor ligand. At ambient temperature, $[\mathbf{3}]^{\bullet-}$ transform exclusively to the 5-coordinate anion (in a CE step) that hardly bind donor solvents or dimerize. The key differences in the cathodic paths of **1** and **3**, in particular, the different coordinating ability of $2e^-$ reduced $[\mathbf{X}\text{-A}]^-$, also persist in the presence of CO_2 dissolved in the thin solution layer of the electrolyte. Further differences and enhanced catalytic activity can be expected upon the addition of Brønsted or Lewis acids, to complete the comparative study stimulated by the development in the field of the electrocatalytic CO_2 reduction with $[Mn(R\text{-bipy})(CO)_3X]$. Variation of the α-diimine nature and backbone substitution, as well as probing substituents on the allyl ligand, are a few possible routes that warrant attention to continue the investigation of the peculiar redox behavior, reactivity, and catalytic activity of this challenging yet largely unexplored family of organometallic compounds.

5.6 Appendix to Chapter 5

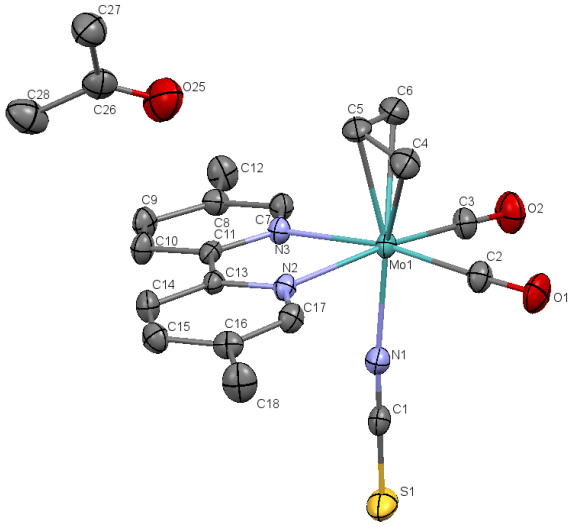

Figure 5A.1: An ORTEP view (50% thermal probability) of the molecular structure of [Mo(η^3-allyl)(5,5′-dmbipy)$(CO)_2$(NCS)] (**2**) determined by single-crystal x-ray analysis. Hydrogen atoms have been omitted for clarity. The crystal structure also contains one molecule of the solvent, acetone.

Table 5A.1: Crystallographic data for **1**-**3**.

Complex	**3** with 6,6′-dmbipy	**2** with 5,5′-dmbipy	**1** with 4,4′-dmbipy
Formula	C18H17MoN3O2S [+solvent]	C18H17MoN3O2S + [C3H6O]	C18H17MoN3O2S
M_r	435.35[a]	489.39	435.36
Crystal System	orthorhombic	monoclinic	orthorhombic
Space Group	*Pbca*	$P2_{1/c}$	Pnam
Z	8	4	4
a/Å	15.0540(5)	10.3391(4)	15.2602(5)
b/Å	14.6980(4)	19.3368(5)	8.3477(3)
c/Å	17.9270(5)	11.5027(4)	14.2157(4)
α/°	90	90	90
β/°	90	105.951(3)	90
γ/°	90	90	90
V/Å^3	3966.6(2)	2211.13(13)	1810.89(11)
ρ_{calc}/g cm^{-1}	1.458[a]	1.470	1.597
Crystal habit	Red plate	Red plate	Red block
Crystal dimensions /mm	0.03×0.06×0.07	0.036×0.053×0.100	0.050×0.055×0.060
Radiation	Mo Kα	Mo Kα	Mo Kα
T/K	150	150	150
μ/mm^{-1}	0.781[a]	0.713	0.856
R(F), R_w(F)	0.0463, 0.0374	0.0398, 0.0156	0.0512, 0.0313
CCDC Code	1862264	1862263	1862262

[a] Excludes solvent.

Table 5A.2: Selected bond lengths (Å) and angles (°) for **1**-**3**.

Complex	**3** with 6,6′-dmbipy	**2** with 5,5′-dmbipy	**1** with 4,4′-dmbipy
Mo(1)−N(2)	2.296(2)	2.254(1)	2.240(2)
Mo(1)−N(3)	2.289(2)	2.237(1)	2.240(2)
Mo(1)−C(4)	2.341(3)	2.325(2)	2.331(2)
Mo(1)−C(5)	2.232(3)	2.220(2)	2.214(3)
Mo(1)−C(6)	2.338(3)	2.339(2)	2.331(2)
Mo(1)−C(2)	1.949(3)	1.978(2)	1.958(2)
Mo(1)−C(3)	1.953(3)	1.951(2)	1.958(2)
C(2)−O(1)	1.166(4)	1.155(2)	1.161(3)
C(3)−O(2)	1.156(3)	1.157(2)	1.161(1)
Mo(1)−N(1)	2.135(2)	2.149(1)	2.135(2)
N(1)−C(1)	1.162(3)	1.160(2)	1.186(2)
C(1)−S(1)	1.626(3)	1.626(2)	1.614(1)
N(2)−Mo(1)−N(3)	72.80(8)	72.95(5)	72.90(8)
C(2)−Mo(1)−C(3)	76.10(12)	80.67(7)	82.59(13)

Table 5A.3: DFT-calculated energies (kcal mol^{-1}) for **1**, **2**, and **3** (= **X**), their radical anions $[\mathbf{X}]^{\bullet-}$ and derived 5-coordinate radicals [**X**-R], 5-coordinate anions $[\mathbf{X}\text{-A}]^-$ (obtained by the loss of thiocyanate), 6-coordinate anions $[\mathbf{X}\text{-PrCN}]^-$ and $[\mathbf{X}\text{-CO}_2]^-$, and dimers [**X**-D]. (For the molecular structures see Scheme 5.1).

Complex	**1** / kcal mol^{-1}	**2** / kcal mol^{-1}	**3** / kcal mol^{-1}	Others
X eq	-6330.74	-6329.63	-6323.25	
X ax	-6330.07	-6328.77	-6317.80	
$[\mathbf{X}]^{\bullet-}$ eq	-6393.97	-6391.81	-6387.50	
$[\mathbf{X}]^{\bullet-}$ ax	-6394.79	-6392.86	-6381.65	
[**X**−R] SP	-5823.55	-5822.38	-5814.17	
[**X**-R] TBP	-5823.98	-5822.82	-5809.34	
$[\mathbf{X}\text{-A}]^-$ diamag.	-5895.45	-5895.03	-5883.54	
$[\mathbf{X}\text{-A}]^-$ paramag.	-5878.54	-5875.86	-5871.77	
$[\mathbf{X}\text{-PrCN}]^-$ eq, diamag.	-7471.01	-7431.32	-7467.35	
[**X**-D]	-11658.23	-11656.03	-	
$[\mathbf{X}\text{-CO}_2]^-$ eq	-6435.03			
$[\mathbf{X}\text{-CO}_2]^-$ ax	-6427.82			
x,x′-dmbipy	-3836.23			
[**X**-(x,x′-dmbipy)]				-2453.28
PrCN				-1593.63
CO_2				-531.74
SCN^-				-526.59

Table 5A.4: DFT-calculated relative energies (kcal mol^{-1}) for **1**, **2**, and **3** (= **X**), their radical anions [**X**]$^{\bullet-}$ and derived 5-coordinate radicals [**X**-R], 5-coordinate anions ([**X**-A]$^{-}$) (obtained by the loss of thiocyanate), 6-coordinate anions [**X**-PrCN]$^{-}$ and dimers [**X**-D]. (For the molecular structures see Scheme 5.1).

Complex	**1** / kcal mol^{-1}	**2** / kcal mol^{-1}	**3** / kcal mol^{-1}
X eq	0	1.11	7.29
X ax	0.67	1.97	12.94
ΔE	0.67	0.86	5.45
[**X**]$^{\bullet-}$ eq	0.82	2.98	7.29
[**X**]$^{\bullet-}$ ax	0	1.93	13.14
ΔE	0.82	1.05	-5.95
[**X**-R] SP	0.43	1.60	9.81
[**X**-R] TBP	0	1.16	14.64
ΔE	0.43	0.44	-4.83
[**X**-A]$^{-}$ TBP	0	0.42	11.91
[**X**-PrCN]$^{-}$	0	-0.31	3.66
[**X**-D]	0	2.20	-
ΔE_1 [a]	10.27	10.39	
ΔE_2 [b]	-41.37	-42.04	

[a] $\Delta E_1 = E([\mathbf{X}\text{-D}])$ - $2E([\mathbf{X}\text{-R}])$. [b] $\Delta E_2 = E([\mathbf{X}\text{-D}])$ - $E([\mathbf{X}\text{-A}])$-$E([[\text{X}]\ \text{eq})$-$E(\text{SCN}^{-})]$.

Table 5A.5: Relevant DFT-calculated distances (Å) in **1**, **2**, and **3** (= **X**), as well as their radical anions $[\mathbf{X}]^{\bullet-}$ and derived 5-coordinate radicals [**X**-R] and reduced $[\mathbf{X}\text{-A}]^{-}$ (obtained by the loss of thiocyanate).

Complex		**X**		$[\mathbf{X}]^{\bullet-}$		[**X**-R]		$[\mathbf{X}\text{-A}]^{-}$
	Exp(eq)	equat	axial	equat	axial	SP	TBP	from ax
Complex **1**								
Mo−C_1	2.331	2.362	2.369	2.356	2.382	2.327	2.349	2.41
Mo−C_2	2.214	2.252	2.225	2.241	2.237	2.198	2.236	2.268
Mo−C_3	2.331	2.365	2.329	2.359	2.348	2.328	2.387	2.402
Mo−C(O)	1.958	1.965	1.957	1.966	1.953	1.956	1.943	1.931
Mo−C(O)	1.958	1.966	1.966	1.966	1.956	1.956	1.936	1.948
Mo−N (trans CO)	2.24	2.272	2.307	1.396	2.29	2.188	2.234	2.207
Mo−N	2.24	2.274	2.226	1.396	2.181	2.189	2.161	2.14
C−C (inter-ring bipy)	1.489	1.476	1.473	1.428	1.428	1.446	1.449	1.432
Mo−N(CS)	2.134	2.117	2.177	2.14	2.218	-	-	-
N−C	1.186	1.186	1.185	1.183	1.183	-	-	-
C−S	1.614	1.628	1.632	1.636	1.641	-	-	-
Complex **2**								
Mo−C_1	2.339	2.363	2.368	2.355	2.385	2.327	2.352	2.408
Mo−C_2	2.22	2.254	2.225	2.241	2.238	2.199	2.235	2.268
Mo−C_3	2.325	2.367	2.328	2.358	2.352	2.328	2.384	2.401
Mo−C(O)	1.951	1.966	1.957	1.966	1.952	1.955	1.942	1.931
Mo−C(O)	1.978	1.966	1.966	1.966	1.966	1.956	1.937	1.949
Mo−N (trans CO)	2.237	2.273	2.312	2.244	2.293	2.191	2.24	2.207
Mo−N	2.254	2.276	2.229	2.246	2.179	2.193	2.163	2.141
C−C (inter-ring bipy)	1.473	1.471	1.468	1.43	1.431	1.446	1.449	1.434
Mo−N(CS)	2.148	2.116	2.177	2.143	2.224	-	-	-
N−C	1.16	1.186	1.186	1.183	1.183	-	-	-
C−S	1.626	1.628	1.632	1.637	1.642	-	-	-
Complex **3**								
Mo−C_1	2.338	2.37	2.36	2.361	2.352	2.325	nc[a]	2.326
Mo−C_2	2.232	2.252	2.239	2.244	2.238	2.201	nc	2.211
Mo−C_3	2.341	2.37	2.347	2.363	2.344	2.317	nc	2.328
Mo−C(O)	1.953	1.956	1.945	1.957	1.948	1.954	nc	1.961
Mo−C(O)	1.949	1.955	1.963	1.956	1.957	1.954	nc	1.961
Mo−N (trans CO)	2.289	2.333	2.365	2.297	2.322	2.234	nc	2.185
Mo−N	2.296	2.331	2.273	2.293	2.25	2.235	nc	2.187
C−C (inter-ring bipy)	1.483	1.482	1.478	1.433	1.428	1.454	nc	1.421
Mo−N(CS)	2.135	2.112	2.273	2.136	2.199	-	-	-
N−C	1.162	1.186	1.186	1.184	1.184	-	-	-
C−S	1.626	1.627	1.632	1.636	1.639	-	-	-

[a] Not converged.

Table 5A.6: Energy decomposition for the interaction between the x,x′-dmbipy ligand and the [Mo(η^3-allyl)(CO)$_2$(NCS)] fragment in the equatorial isomer of **1**-**3** (energies in kcal mol^{-1}).

Complex	**1** / kcal mol^{-1}	**2** / kcal mol^{-1}	**3** / kcal mol^{-1}
ΔE_{Pauli}	134.40	134.26	127.73
ΔE_{elec}	-120.49	-120.26	-112.02
ΔE_{oi}	-69.36	-69.28	-64.36
ΔE_{int}	-55.44	-55.28	-48.65
ΔE_{prep}	10.45	10.42	9.97
ΔE_{prep}	2.08	1.81	4.51
ΔE_{prep}	12.53	12.23	14.48
ΔE_{ligand}	**-42.91**	**-43.05**	**-34.17**

In the EDA,[67,68] the interaction energy (ΔE_{int}) is considered as the sum of Pauli repulsion (ΔE_{Pauli}), electrostatic (ΔE_{elec}) and orbital interactions (ΔE_{oi}). ΔE_{Pauli} represents the repulsion between occupied orbitals of the fragments, ΔE_{elec} the electrostatic interaction between fragments, and ΔE_{oi} the 2-electron stabilizing interactions between occupied levels of one fragment and empty levels of the other. ΔE_{elec} is an attractive term and ΔE_{oi} is related to covalent bond formation. To calculate the bond energy (ΔE), another term must be considered, that is the reorganization or preparation energy (ΔE_{prep}). It corresponds to the difference between the energy of each fragment as it is in the complex and being allowed to relax to the lowest energy geometry.

Table 5A.7: Redox potentials of complexes **1**-**3** and their reduction products (see Scheme 5.1) from cyclic voltammetry at an Pt microdisc electrode at 298 K.

	Redox Potentials [V vs Fc/Fc^+]						
Solvent	Mo(II)/(III)	R1	R2	R2′	O1′	R(D)	O(D)
	$E_{1/2}$	$E_{p,c}$	$E_{p,c}$	$E_{p,c}$	$E_{p,a}$	$E_{p,c}$	$E_{p,a}$
	[Mo(η^3-allyl)(4,4′-dmbipy)$(CO)_2$(NCS)] (1)						
THF	0.15	-1.79	-	-2.58	-1.48	-2.23	[c]
THF[b]	0.18	-1.64[a]	-2.26	-2.50[a]	-1.35	[c]	[c]
PrCN	0.20	-2.05	-	[d]	-1.77	-2.37	[c]
PrCN[b]	0.25	-1.91[a]	-2.63	[d]	-	[c]	[c]
	[Mo(η^3-allyl)(5,5′-dmbipy)$(CO)_2$(NCS)] (2)						
THF	0.17	-1.95	-	-2.89	-1.57	-2.58	-1.13
THF[b]	0.20	-1.94[a]	-2.54	-2.82[a]	-1.54	[c]	[c]
PrCN	0.21	-2.05	-	[d]	-1.73	-2.61	[c]
PrCN[b]		-1.91[a]	-2.65	[d]	-1.57	[c]	[c]
	[Mo(η^3-allyl)(6,6′-dmbipy)$(CO)_2$(NCS)] (3)						
THF	0.26	-1.88[a]	-2.56		-1.47	-	-
THF[b]	0.34	-1.84[a]	-2.43	-2.58[a]	-1.27	-	-
PrCN	0.31	-1.81[a]	-2.37	[d]	-1.74	-	-
PrCN[b]	0.35	-1.79[a]	-2.46	[d]	-1.41	-	-

[a] $E_{1/2}$ value (anodic counter wave observed). [b] Measured at 195 K.[c] Not observable. [d] Beyond the accessible cathodic potentional window of PrCN/Bu_4NPF_6.

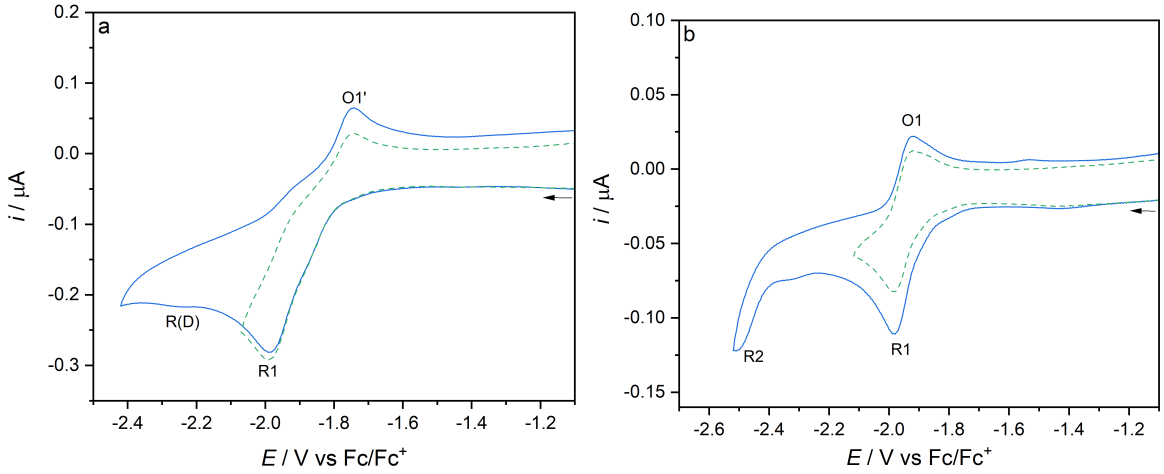

Figure 5A.2: Cyclic voltammetry of [Mo(η^3-allyl)(4,4′-dmbipy)$(CO)_2$(NCS)] (**1**) at (a) room temperature and (b) 195 K in PrCN/Bu_4NPF_6. Au microdisc electrode. Scan rate: 100 mV s^{-1}.

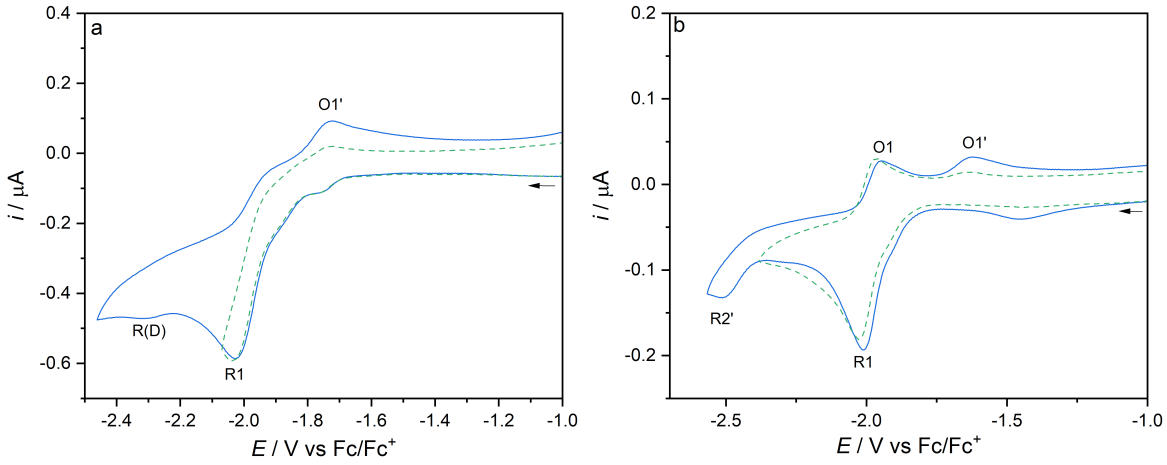

Figure 5A.3: Cyclic voltammetry of [Mo(η^3-allyl)(5,5′-dmbipy)(CO)$_2$(NCS)] (**2**) at (a) room temperature and (b) 195 K in PrCN/Bu$_4$NPF$_6$. Au microdisc electrode. Scan rate: 100 mV s^{-1}.

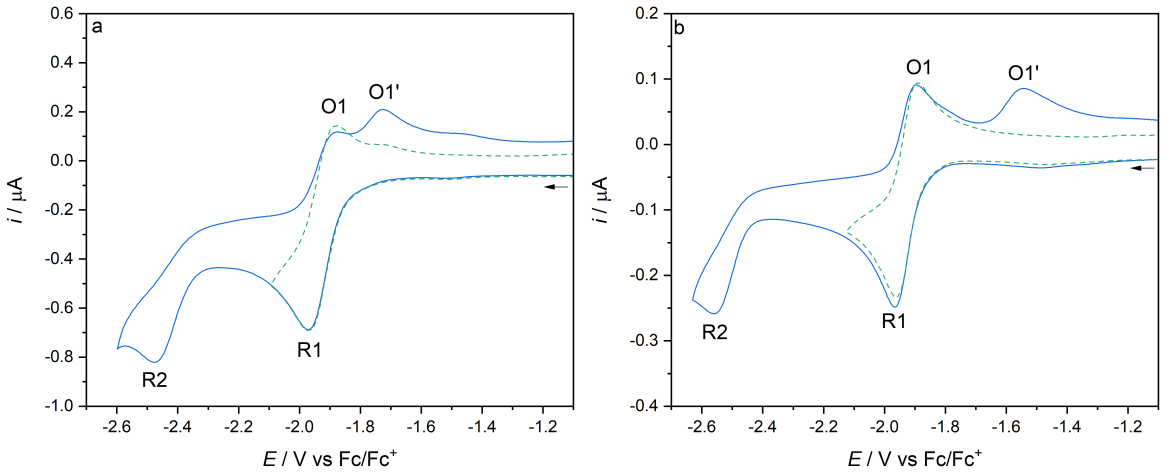

Figure 5A.4: Cyclic voltammetry of [Mo(η^3-allyl)(6,6′-dmbipy)(CO)$_2$(NCS)] (**3**) at (a) room temperature and (b) 195 K in PrCN/Bu$_4$NPF$_6$. Au microdisc electrode. Scan rate: 100 mV s^{-1}.

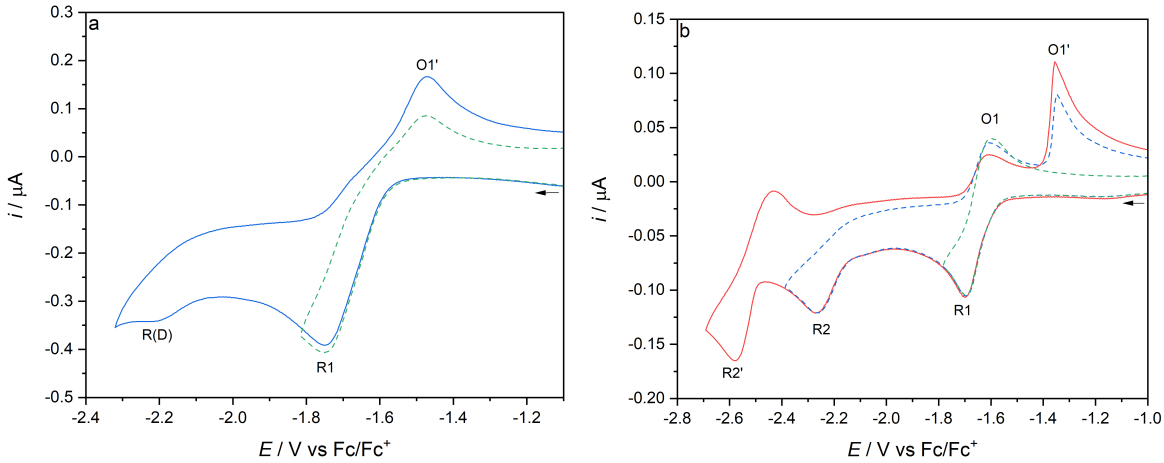

Figure 5A.5: Cyclic voltammetry of [Mo(η^3-allyl)(4,4′-dmbipy)$(CO)_2$(NCS)] (**1**) at (a) room temperature and (b) low temperature (195 K) in THF/Bu_4NPF_6. Pt microdisc electrode. Scan rate: 100 mV s^{-1}.

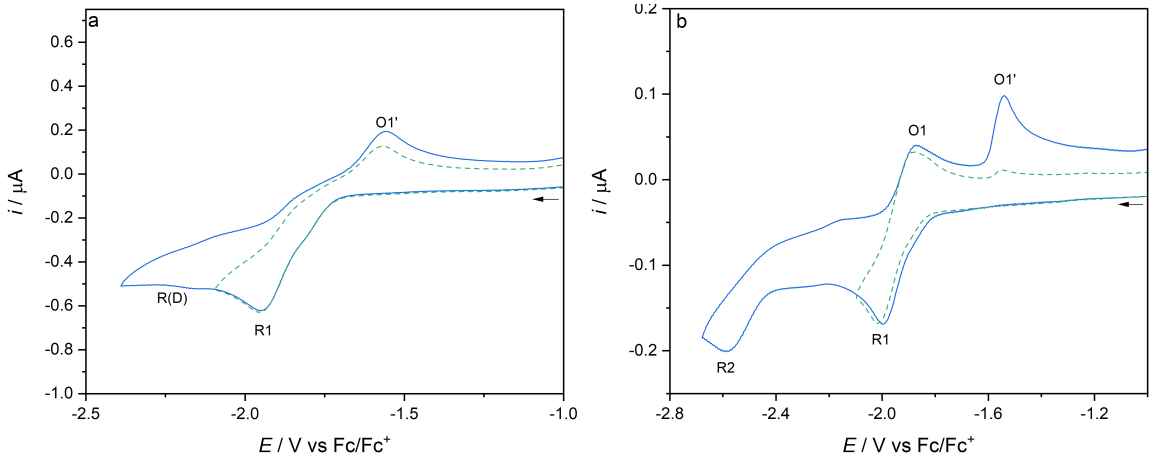

Figure 5A.6: Cyclic voltammetry of [Mo(η^3-allyl)(5,5′-dmbipy)$(CO)_2$(NCS)] (**2**) at (a) room temperature and (b) 195 K in THF/Bu_4NPF_6. Pt microdisc electrode. Scan rate: 100 mV s^{-1}.

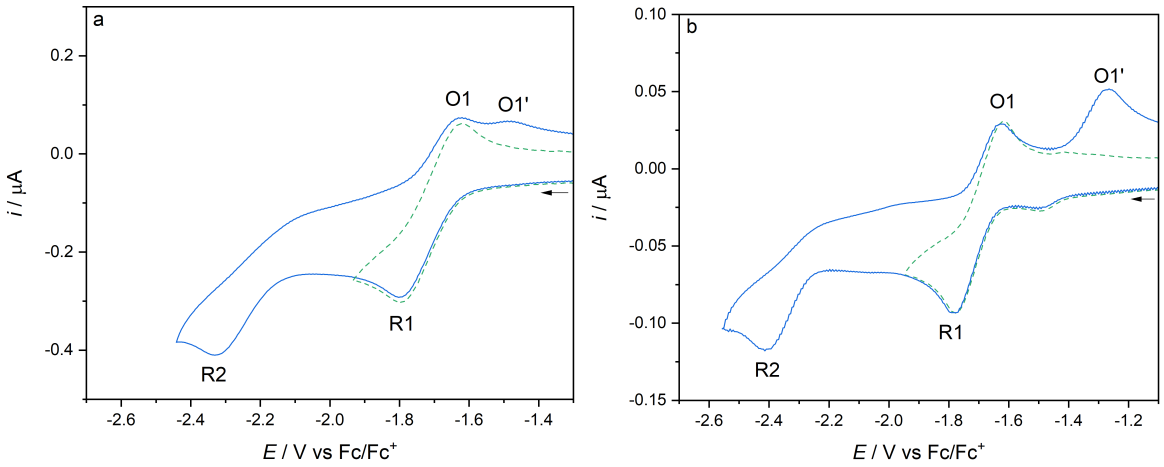

Figure 5A.7: Cyclic voltammetry of [Mo(η^3-allyl)(6,6′-dmbipy)$(CO)_2$(NCS)] (**3**) at (a) room temperature and (b) 195 K in THF/Bu_4NPF_6. Pt microdisc electrode. Scan rate: 100 mV s^{-1}.

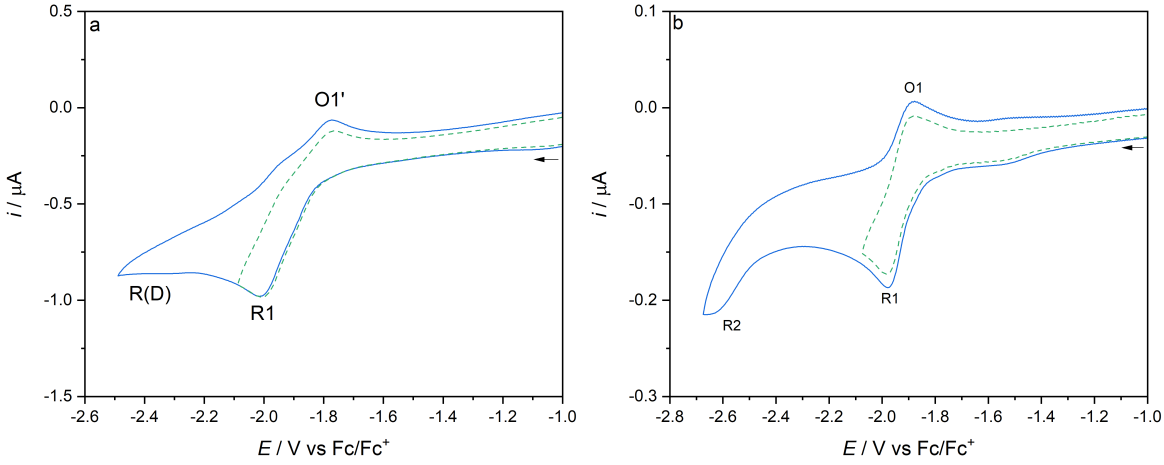

Figure 5A.8: Cyclic voltammetry of [Mo(η^3-allyl)(4,4′-dmbipy)$(CO)_2$(NCS)] (**1**) at (a) room temperature and (b) 195 K in PrCN/Bu_4NPF_6. Pt microdisc electrode. Scan rate: 100 mV s^{-1}.

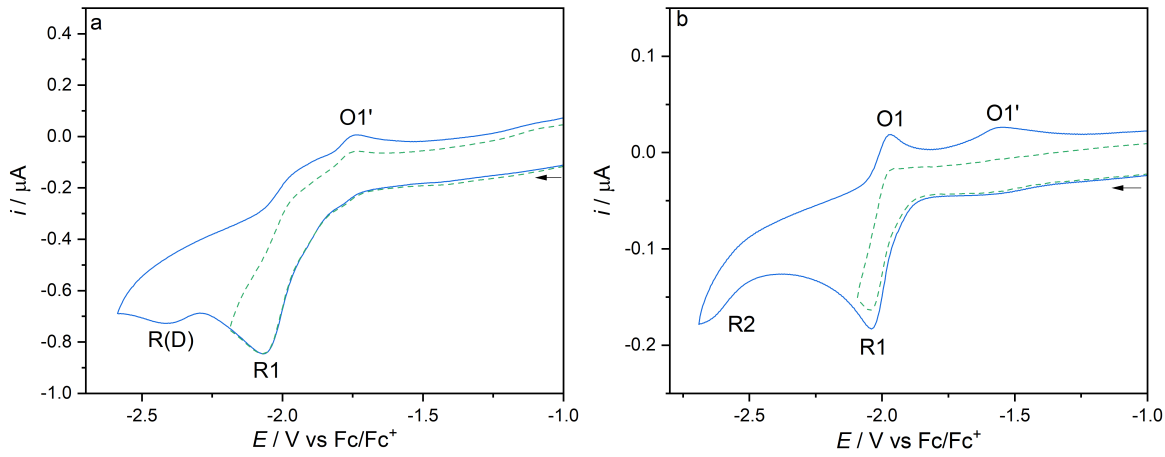

Figure 5A.9: Cyclic voltammetry of [Mo(η^3-allyl)(5,5′-dmbipy)(CO)$_2$(NCS)] (**2**) at (a) room temperature and (b) 195 K in PrCN/Bu_4NPF_6. Pt microdisc electrode. Scan rate: 100 mV s^{-1}.

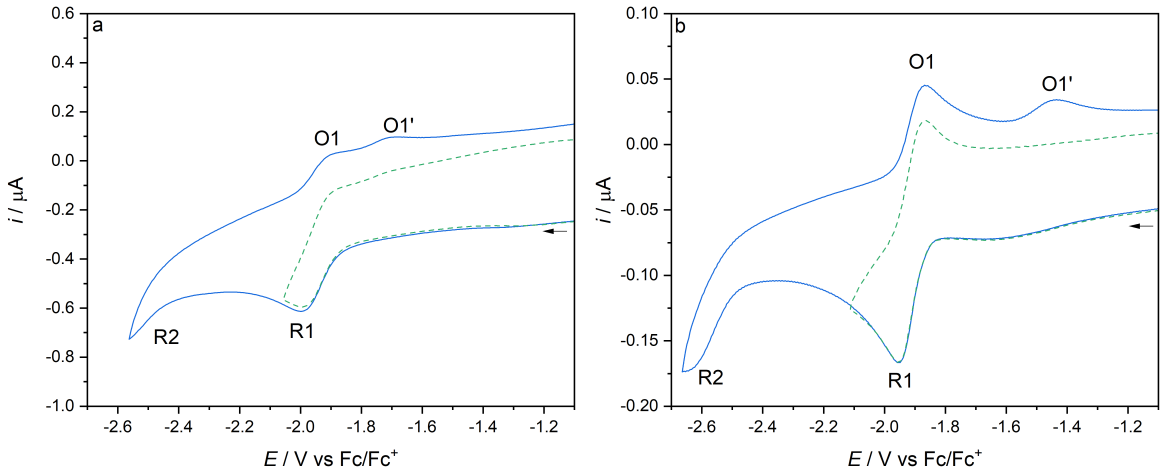

Figure 5A.10: Cyclic voltammetry of [Mo(η^3-allyl)(6,6′-dmbipy)(CO)$_2$(NCS)] (**3**) at (a) room temperature and (b) 195 K in PrCN/Bu_4NPF_6. Pt microdisc electrode. Scan rate: 100 mV s^{-1}.

Table 5A.8: DFT (ADF)-calculated frequencies of the symmetric and antisymmetric CO-stretching modes and the CN-stretching mode of thiocyanate (in cm^{-1}) in **1**-**3** (= **X**) and their reduction products (see Scheme 5.1).

Complex	**X**	$[\mathbf{X}]^{\bullet-}$		[**X**-R]		$[\mathbf{X}\text{-A}]^{-}$		$[\mathbf{X}\text{-PrCN}]^{-}$	[**X**-D]
	Equat	Equat	Axial	SP	TBP	SP	TBP		
1									
ν_s(C≡O)	1882	1855	1841	1856	1834	-	1741	1797	1858, 1844
ν_a(C≡O)	1800	1763	1750	1754	1746	-	1656	1705	1787, 1775[a]
ν(N≡C)	2056	2070	2070	-	-	-	-	2229	
2									
ν_s(C≡O)	1883	1853	1839	1851	1834	-	1742	1781	1859, 1844
ν_a(C≡O)	1801	1761	1748	1754	1746	-	1658	1687	1789, 1777[a]
ν(N≡C)	2056	2072	2068	-	-	-	-	2313	
3									
ν_s(C≡O)	1881	1855	1852	1852	-	1803		1816	-
ν_a(C≡O)	1800	1764	1759	1760	-	1702		1715	-
ν(N≡C)	2054	2069	-	-	-	-		2347	-

[a] Four calculated ν(CO) modes of the dimer.

Table 5A.9: Calculated and experimental excitation energies (eV), composition (%) and oscillator strengths (OS).

No.	λ/nm	E/eV	Composition(%)	λ/nm (exp)	OS
			[Mo(η^3-allyl)(4,4′-dmbipy)(CO)$_2$(NCS)] (1)		
1	506	2.45	H $\longrightarrow$ L + 1 (97)	490 (THF)	0.029
2	452	2.75	H-3 $\longrightarrow$ L (97)		0.082
3	347	3.57	H-2 $\longrightarrow$ L + 3 (70), H-2 $\longrightarrow$ L + 2 (23)		0.204
4	313	3.96	H-5 $\longrightarrow$ L (63), H-4 $\longrightarrow$ L + 1 (24)		0.476
5	300	4.13	H-4 $\longrightarrow$ L + 1 (71), H-5 $\longrightarrow$ L (17)		0.301
			[Mo(η^3-allyl)(5,5′-dmbipy)(CO)$_2$(NCS)] (2)		
1	506	2.44	H $\longrightarrow$ L + 1 (54), H $\longrightarrow$ L + 2 (43)	480 (THF)	0.022
2	444	2.79	H-3 $\longrightarrow$ L (97)		0.081
3	385	3.22	H-2 $\longrightarrow$ L + 2 (42), H-2 $\longrightarrow$ L + 1 (42), H-2 $\longrightarrow$ L + 3 (15)		0.087
4	354	3.50	H-2 $\longrightarrow$ L + 3 (82), H-2 $\longrightarrow$ L + 1 (7)		0.228
5	329	3.77	H-4 $\longrightarrow$ L (30), H-3 $\longrightarrow$ L + 3 (26), H $\longrightarrow$ L + 4 (19), H-5 $\longrightarrow$ L(13)		0.354
6	325	3.81	H $\longrightarrow$ L + 4 (77), H-4 $\longrightarrow$ L (14)		0.129
7	324	3.83	H-3 $\longrightarrow$ L + 3 (71), H-4 $\longrightarrow$ L (12), H-5 $\longrightarrow$ L (7)		0.250
			[Mo(η^3-allyl)(6,6′-dmbipy)(CO)$_2$(NCS)] (3)		
1	471	2.63	H $\longrightarrow$ L + 2 (68), H $\longrightarrow$ L + 3 (31)	460 (THF)	0.005
2	456	2.72	H-3 $\longrightarrow$ L (98)		0.040
3	449	2.76	H $\longrightarrow$ L + 3 (67), H $\longrightarrow$ L + 2 (29)		0.014
4	355	3.49	H-2 $\longrightarrow$ L + 2 (72), H-2 $\longrightarrow$ L + 3 (22)		0.328
5	339	3.65	H-3 $\longrightarrow$ L + 2 (50), H-4 $\longrightarrow$ L (18), H-5 $\longrightarrow$ L (18), H-3 $\longrightarrow$ L + 3 (10)		0.135
6	332	3.73	H-3 $\longrightarrow$ L + 2 (48), H-4 $\longrightarrow$ L (21), H-5 $\longrightarrow$ L (17)		0.277

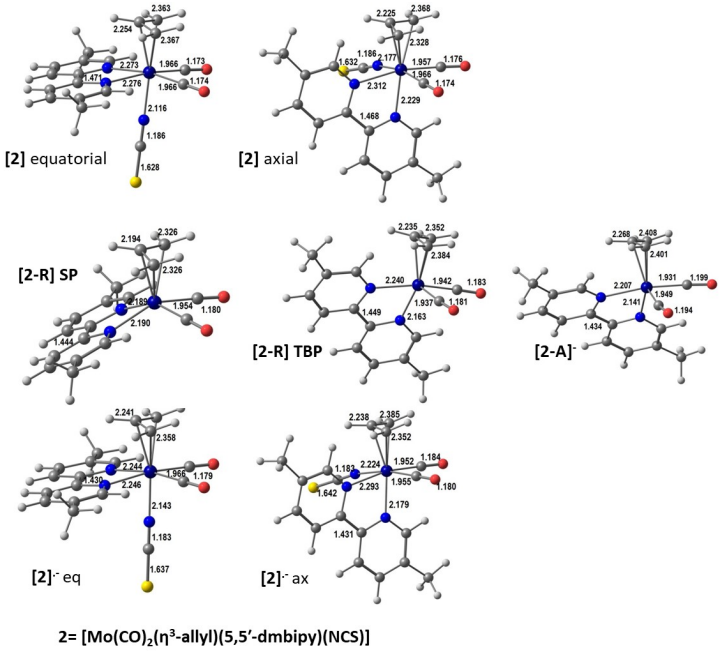

Figure 5A.11: DFT-optimized structures of the parent complex [Mo(η^3-allyl)(5,5′-dmbipy)$(CO)_2$(NCS)] (**2**) (the equatorial isomer (top left) and the axial isomer (top right)), $1e^-$ reduced radical anion $[\mathbf{2}]^{\bullet -}$ (bottom left, equatorial isomer, bottom right, axial isomer) , 5-coordinate radical [**2**-R] (the SP isomer (center left), the TBP isomer (center right), and $2e^-$ reduced 5-coordinate anion $[\mathbf{2}\text{-A}]^-$ (center far right), with the relevant bond lengths (Å).

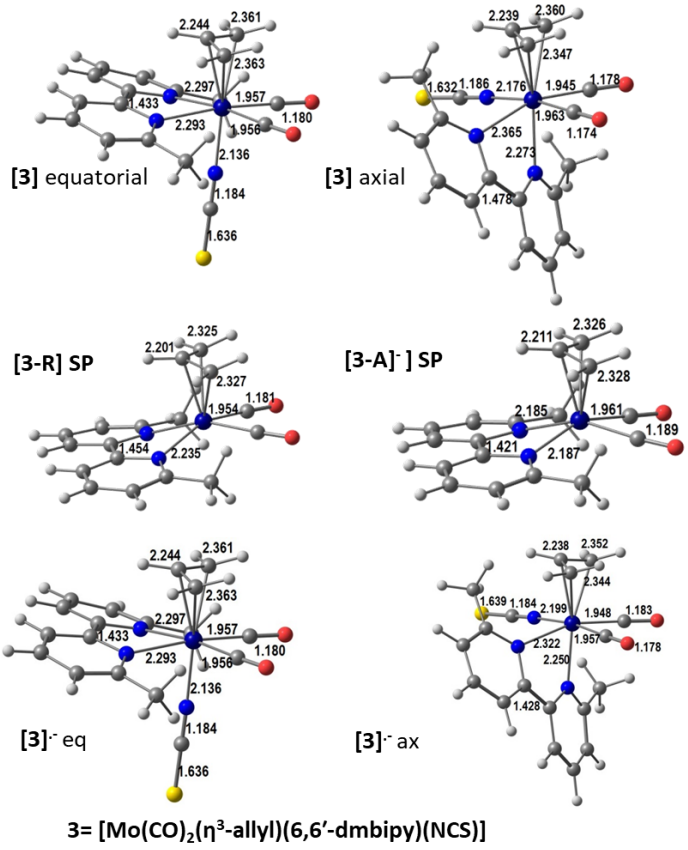

Figure 5A.12: DFT-optimized structures of the parent complex [Mo(η^3-allyl)(6,6′-dmbipy)$(CO)_2$(NCS)] (**3**) (the equatorial isomer (top left) and the axial isomer (top right), $1e^-$ reduced radical anion $[\mathbf{3}]^{\bullet -}$ (bottom left, equatorial isomer, bottom right axial isomer), 5-coordinate radical [**3**-R] (the SP isomer (center left) and $2e^-$ reduced 5-coordinate anion [**3**-A]$^-$ (center right), with the relevant bond lengths (Å).

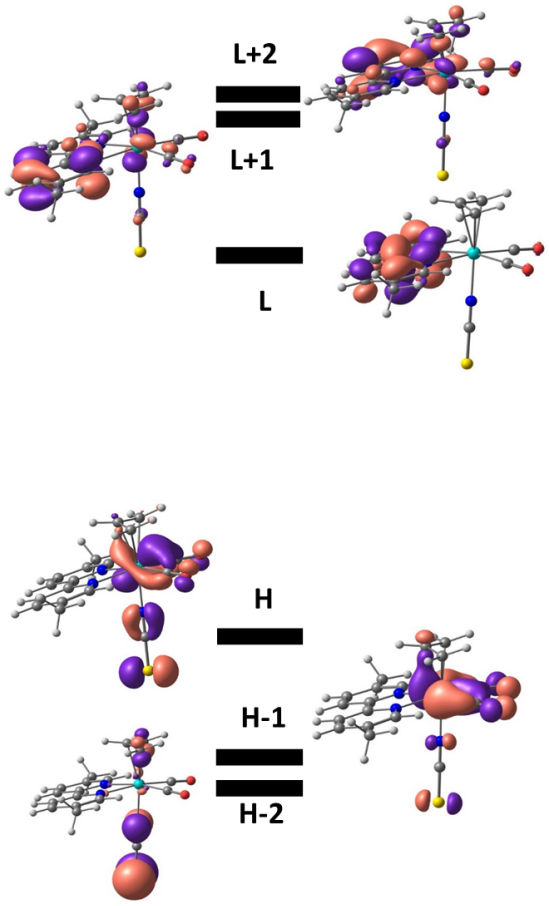

Figure 5A.13: DFT-calculated frontier orbitals of the parent complex [Mo(η^3-allyl)(5,5′-dmbipy)$(CO)_2$(NCS)] (**2**). The HOMO-LUMO (H-L) gap is 1.616 eV.

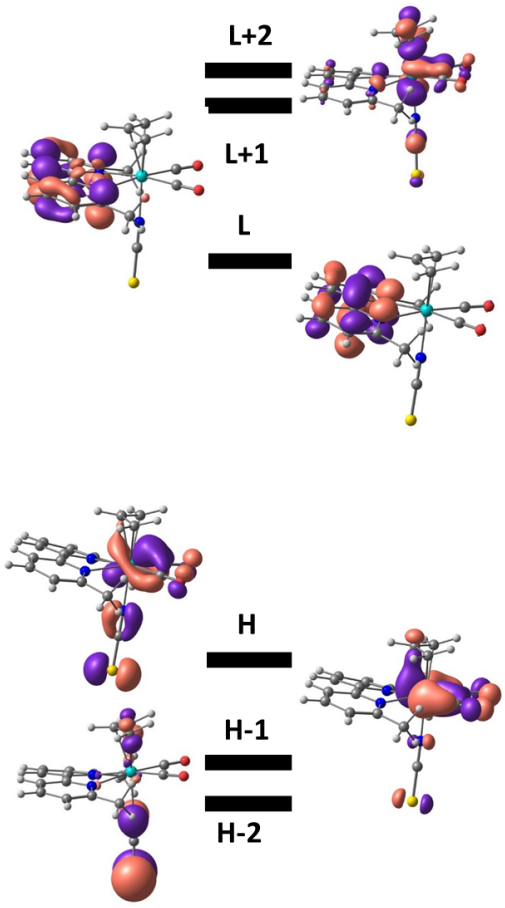

Figure 5A.14: DFT-calculated frontier orbitals of the parent complex [Mo(η^3-allyl)(6,6′-dmbipy)$(CO)_2$(NCS)] (**3**). The HOMO-LUMO (H-L) gap is 1.592 eV.

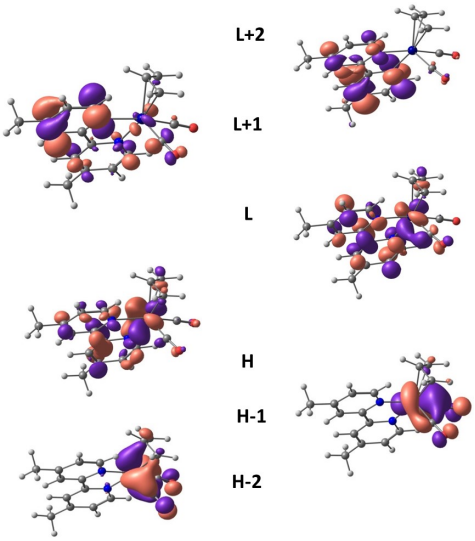

Figure 5A.15: DFT-calculated α-spin frontier orbitals of the 5-coordinate radical [Mo(η^3-allyl)(4,4′-dmbipy)$(CO)_2$], [**1**-R].

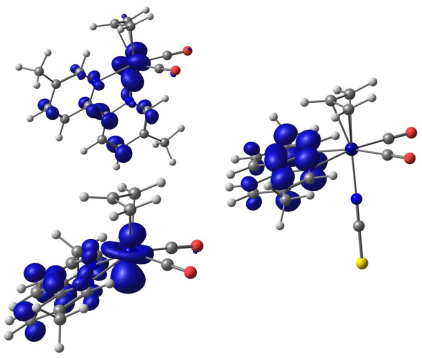

Figure 5A.16: DFT-calculated spin densities in the 5-coordinate radical [Mo(η^3-allyl)(5,5′-dmbipy)$(CO)_2$], [**2**-R] (the TBP isomer (top left) and the SP isomer (bottom left)), and radical anion $[\mathbf{2}]^{\bullet-}$ (right).

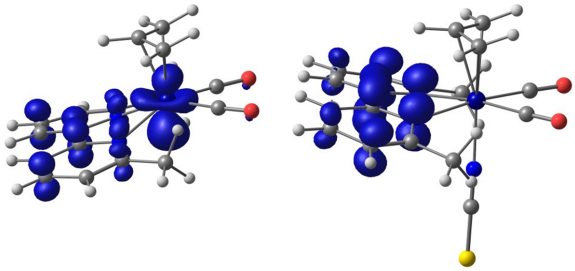

Figure 5A.17: DFT-calculated spin densities the 5-coordinate radical [Mo(η^3-allyl)(6,6′-dmbipy)$(CO)_2$], [**3**-R] (the SP isomer, left) and radical anion $[\mathbf{3}]^{\bullet-}$ (right).

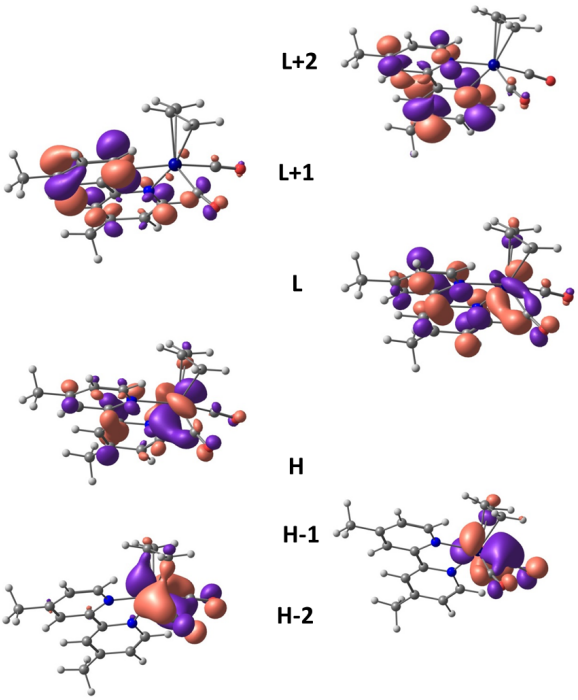

Figure 5A.18: DFT-calculated frontier orbitals of the 5-coordinate anion [Mo(η^3-allyl)(4,4′-dmbipy)$(CO)_2$]$^-$, [**1**-A]$^-$.

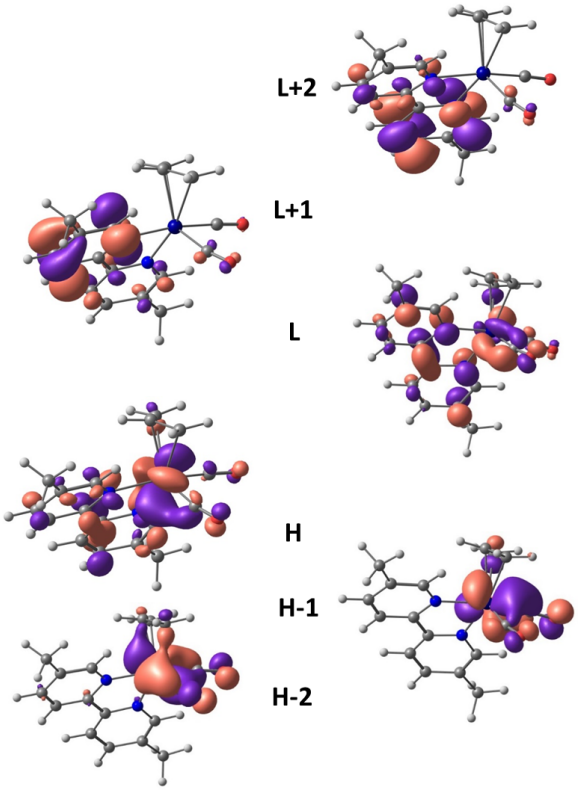

Figure 5A.19: DFT-calculated frontier orbitals of the 5-coordinate anion [Mo(η^3-allyl)(5,5′-dmbipy)$(CO)_2$]$^-$, [**2**-A]$^-$.

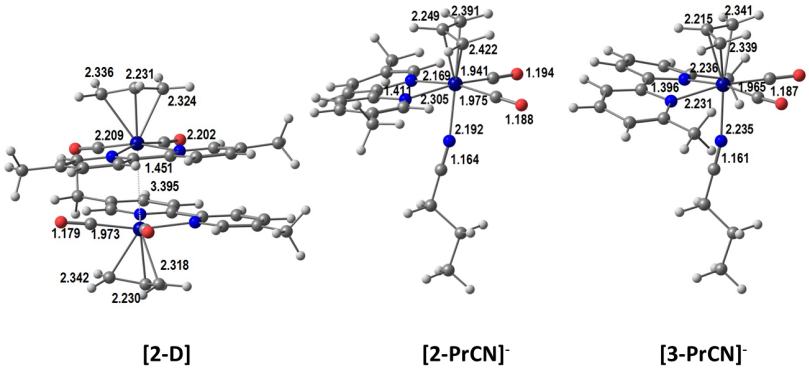

Figure 5A.20: DFT-optimized structures of the Mo−Mo dimer [Mo(η^3-allyl)(5,5′-dmbipy)$(CO)_2$]$_2$, [**2**-D] (left), the 6-coordinate anions [Mo(η^3-allyl)(5,5′-dmbipy)$(CO)_2$(PrCN)]$^-$, [**2**-PrCN]$^-$ (the equatorial isomer, center), and [Mo(η^3-allyl)(6,6′-dmbipy)$(CO)_2$(PrCN)]$^-$, [**3**-PrCN]$^-$ (the equatorial isomer, right), with relevant bond lengths (Å).

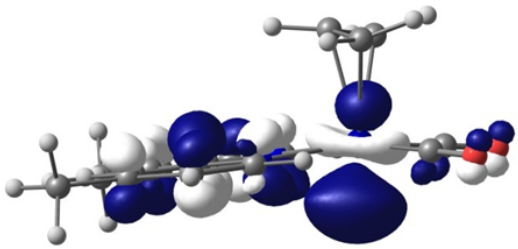

Figure 5A.21: DFT-calculated SOMO of the SP radical fragment [Mo(η^3-allyl)(4,4′-dmbipy)$(CO)_2$], [**1**-R′], used to form dimer [**1**-D].

Table 5A.10: IR and UV-Vis absorption data for complexes [Mo(η^3-allyl)(x,x′-dmbipy)(CO)$_2$(NCS)], **1** (x = 4), **2** (x = 5) and **3** (x = 6), and 1e$^-$ oxidized [Mo(η^3-allyl)(x,x′-dmbipy)(CO)$_2$(NCS)]$^+$, [**1**]$^+$-[**3**]$^+$. Reference compounds containing the non-methylated bipyridine ligand are also included.

Complex	ν(CO) / cm^{-1}	ν(CN) / cm^{-1}	λ_{max} / nm
[Mo(η^3-allyl)(bipy)(CO)$_2$(NCS)][a]	1950, 1866	2083	[f]
[Mo(η^3-allyl)(bipy)(CO)$_2$(NCS)][b]	1947, 1864	2085	[f]
[Mo(η^3-allyl)(4,4′-dmbipy)(CO)$_2$(NCS)][c]	1949, 1869	2076	490
[Mo(η^3-allyl)(4,4′-dmbipy)(CO)$_2$(NCS)][d]	1949, 1866	2080	475
[Mo(η^3-allyl)(5,5′-dmbipy)(CO)$_2$(NCS)][c]	1951, 1971	2076	480
[Mo(η^3-allyl)(5,5′-dmbipy)(CO)$_2$(NCS)][d]	1949, 1866	2080	470
[Mo(η^3-allyl)(6,6′-dmbipy)(CO)$_2$(NCS)][c]	1948, 1866	2074	460
[Mo(η^3-allyl)(6,6′-dmbipy)(CO)$_2$(NCS)][d]	1946, 1862	2078	460
[Mo(η^3-allyl)(bipy)(CO)$_2$(NCS)]$^+$[a]	2069, 2028[e]	2028[e]	[f]
[Mo(η^3-allyl)(bipy)(CO)$_2$(NCS)]$^+$[b]	2069, 2019	2034	[f]
[Mo(η^3-allyl)(4,4′-dmbipy)(CO)$_2$(NCS)]$^+$[c]	2065, 2022[e]	2022[e]	375, 560
[Mo(η^3-allyl)(4,4′-dmbipy)(CO)$_2$(NCS)]$^+$[d]	2067, 2024[e]	2024[e]	380, 550
[Mo(η^3-allyl)(5,5′-dmbipy)(CO)$_2$(NCS)]$^+$[c]	2067, 2022[e]	2022[e]	395, 570
[Mo(η^3-allyl)(5,5′-dmbipy)(CO)$_2$(NCS)]$^+$[d]	2068, 2024[e]	2024[e]	370, 543
[Mo(η^3-allyl)(6,6′-dmbipy)(CO)$_2$(NCS)]$^+$[c]	2059, 2019[e]	2019[e]	375, 585
[Mo(η^3-allyl)(6,6′-dmbipy)(CO)$_2$(NCS)]$^+$[d]	2059, 2019[e]	2019[e]	400, 553

[a] Measured in MeCN. [b] Measured in PrCN at 183 K.[c] Measured in THF. [d] Measured in PrCN. [e] Broad aband, due to strong overlap of ν_a(CO) and ν(CN) of NCS$^-$. [f] Not measured.

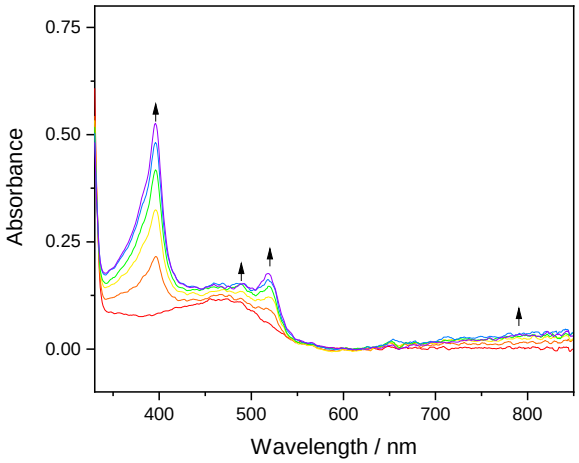

Figure 5A.22: Cathodic UV-Vis spectroelectrochemistry of [Mo(η^3-allyl)(6,6′-dmbipy)$(CO)_2$(NCS)] (**3**) in $PrCN/Bu_4NPF_6$ at 223 K, showing its conversion to stable radical anion $[\mathbf{3}]^{\bullet-}$ (↑) at the cathodic wave R1, using a cryostatted OTTLE cell.

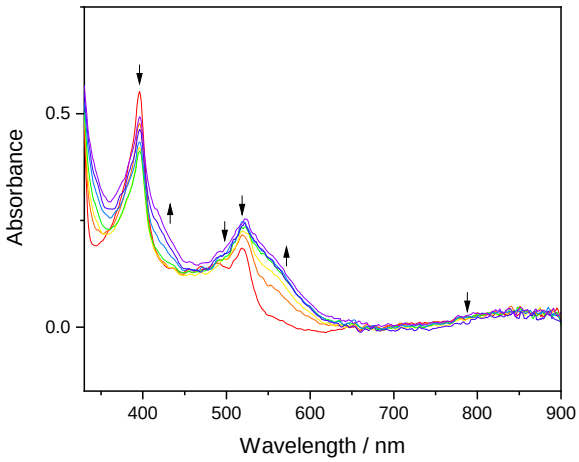

Figure 5A.23: Cathodic UV-Vis spectroelectrochemistry of [Mo(η^3-allyl)(6,6′-dmbipy)$(CO)_2$(NCS)] (**3**) in $PrCN/Bu_4NPF_6$ at 223 K, showing the conversion of $[\mathbf{3}]^{\bullet-}$ (↓) to 5-coordinate anion $[\mathbf{3}\text{-A}]^-$ (↑) at the cathodic wave R2. The electrolysis was conducted in a cryostatted OTTLE cell.

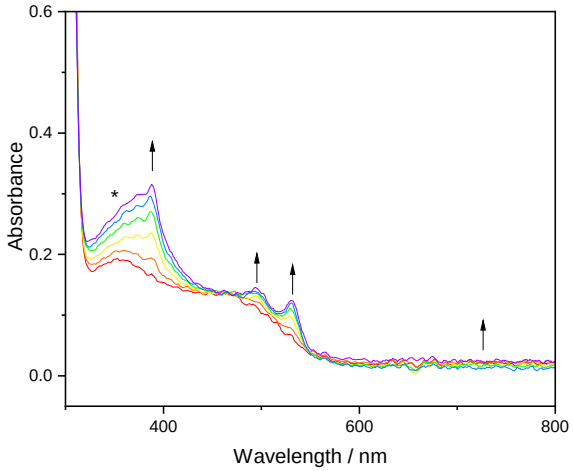

Figure 5A.24: UV-Vis spectral changes recorded during the electrochemical reduction of [Mo(η^3-allyl)(4,4′-dmbipy)$(CO)_2$(NCS)] (**1**) at 223 K in PrCN/Bu_4NPF_6 within a cryostatted OTTLE cell. In line with Figure 5.13 (in the main text), the spectra reveal the formation of radical anion $[\mathbf{1}]^{\bullet-}$ (↑), showing the characteristic bifurcated π^*-π^* intra-ligand absorption of $[dmbipy]^{\bullet-}$ around 500 nm, and 6-coordinate anion $[\mathbf{1}\text{-PrCN}]^-$ (*) (Scheme 5.1).

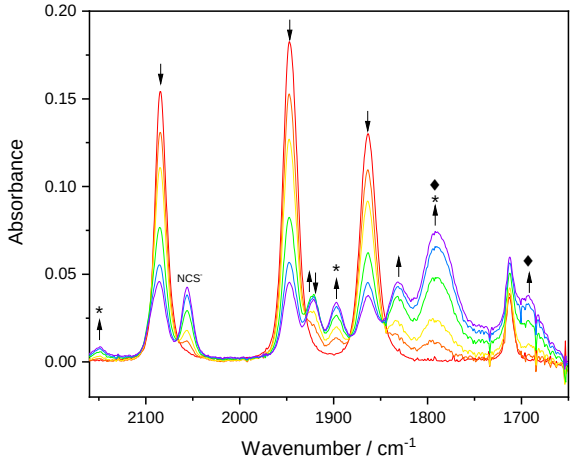

Figure 5A.25: IR SEC monitoring of the reduction of [Mo(η^3-allyl)(5,5′-dmbipy)$(CO)_2$(NCS)] (**2**) (↓) in PrCN/Bu_4NPF_6 at 223 K, producing radical anion $[\mathbf{2}]^{\bullet-}$ (↑↓), and $2e^-$ reduced 6-coordinate [**2**-PrCN]– (*) coexisting in an equilibrium with $2e^-$ reduced 5-coordinate $[\mathbf{2}\text{-A}]^-$ (♦). The electrolysis was completed within a cryostatted OTTLE cell.

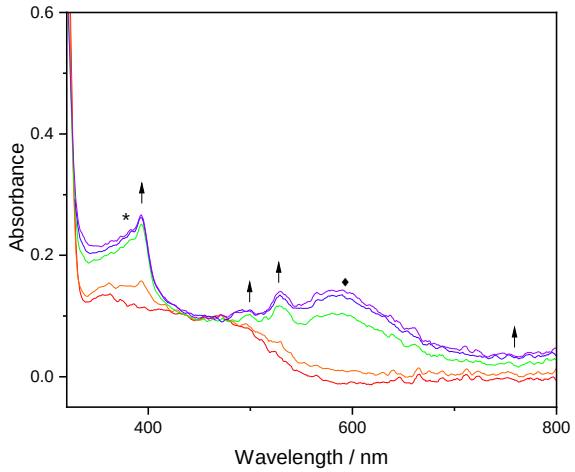

Figure 5A.26: UV-Vis spectroelectrochemistry of [Mo(η^3-allyl)(5,5′-dmbipy)$(CO)_2$(NCS)] (**2**), red line, in PrCN/Bu_4NPF_6 at 223 K, showing its reduction to intermediate $[2]^{\bullet -}$ (↑) that transforms concomitantly to two $2e^-$ reduced species in an equilibrium, viz. 6-coordinate [**2**-PrCN]$^-$ (*) and 5-coordinate [**2**-A]$^-$ (♦). The electrolysis was conducted in a cryostatted OTTLE cell.

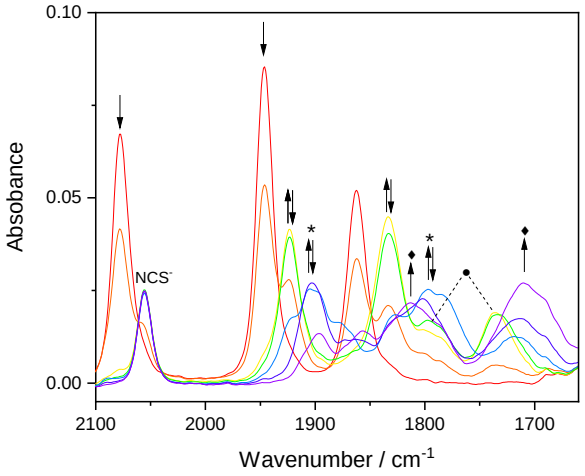

Figure 5A.27: IR spectroelectrochemistry of complex [Mo(η^3-allyl)(6,6′-dmbipy)$(CO)_2$(NCS)] (**3**) (↓) in PrCN/Bu_4NPF_6 at 298 K, showing the reduction at R1 to give radical [**3**-PrCN] (↑↓) as well as as a contact species (•) resulting from the interaction with $2e^-$ reduced 5-coordinate [**3**-A]$^-$, and the concomitant cathodic step converting [**3**-PrCN] (↓) to [**3**-PrCN]$^-$ (*) that further transforms to the true [**3**-A]$^-$ (♦).

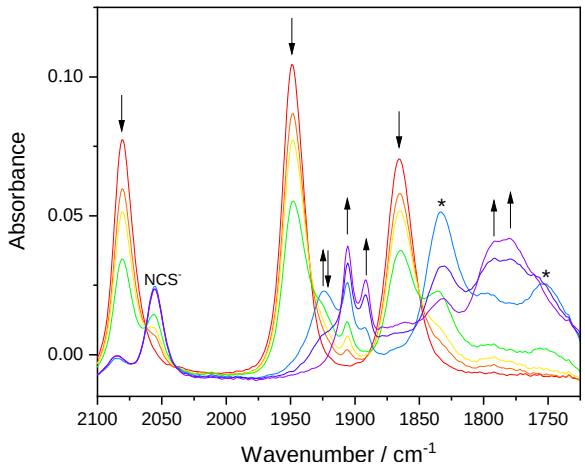

Figure 5A.28: IR SEC monitoring of the reduction of [Mo(η^3-allyl)(4,4′-dmbipy)$(CO)_2$(NCS)] (**1**) (↓) in PrCN/Bu_4NPF_6 at 298 K to radical [**1**-PrCN] (↑↓) and $2e^-$ reduced [**1**-A]$^-$(*) as a weak adduct with PrCN, converting ultimately to [Mo(η^3-allyl)(4,4′-dmbipy)$(CO)_2]_2$-related dimer [**1**-D′] (↑).

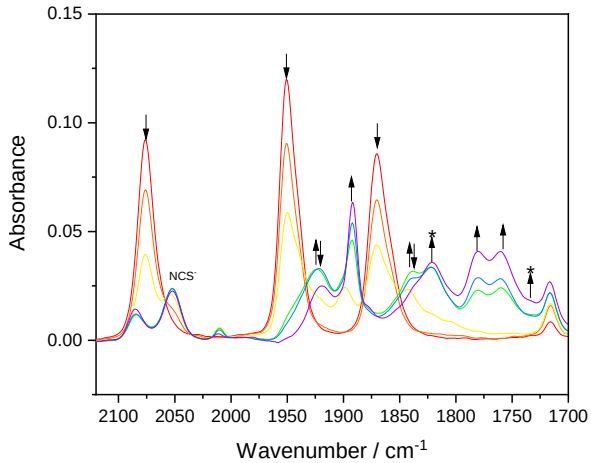

Figure 5A.29: IR SEC monitoring of the initial reduction of [Mo(η^3-allyl)(5,5′-dmbipy)$(CO)_2$(NCS)] (**2**) (↓) at R1 in THF/Bu_4NPF_6 at 298 K to intermediate $[\mathbf{2}]^{\bullet-}$ (↑↓), further converting to both $2e^-$ reduced [**2**-A]$^-$ (*) and dominant [Mo(η^3-allyl)(5,5′-dmbipy)$(CO)_2]_2$-related dimer [**2**-D′] (↑).

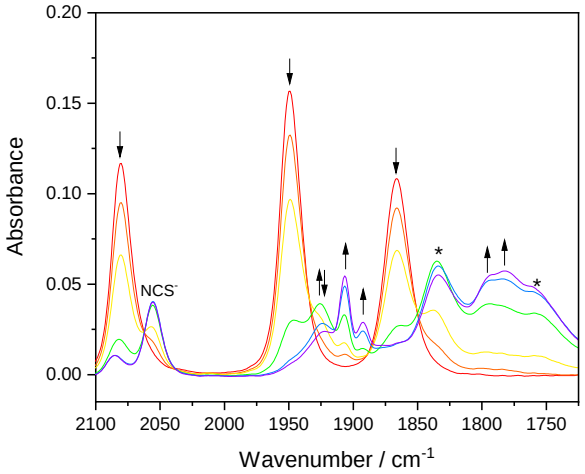

Figure 5A.30: IR SEC monitoring of the reduction of [Mo(η^3-allyl)(5,5′-dmbipy)$(CO)_2$(NCS)] (**2**) (↓) in PrCN/Bu_4NPF_6 at 298 K to radical [**2**-PrCN] (↑↓) and 2e$^-$ reduced [**2**-A]$^-$ (*) as a weak adduct with PrCN, in a mixture with [Mo(η^3-allyl)(5,5′-dmbipy)$(CO)_2$]$_2$-related dimer [**2**-D′] (↑).

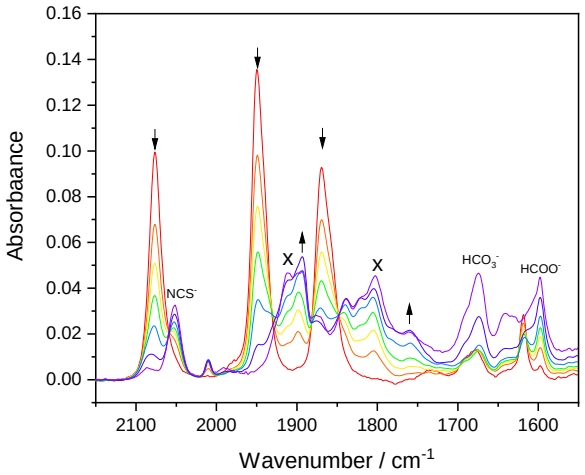

Figure 5A.31: IR spectroelectrochemistry of [Mo(η^3-allyl)(4,4′-dmbipy)$(CO)_2$(NCS)] (**1**) in CO_2-saturated THF/Bu_4NPF_6, showing the conversion of the parent complex (↓) at R1 to [**1**-CO_2]$^-$ (×), and inactive dimer [**1**-D′] (↑).

References

[1] N. Oceanic and A. Adminstration, *Monthly Average Mauna Loa CO_2*, 2018, `https://www.esrl.noaa.gov/gmd/ccgg/trends/index.html`, (Last Accessed: 08-01-2020).

[2] G. Centi and S. Perathoner, *Catal. Today*, 2009, **148**, 191–205.

[3] F. Marken and D. Fermin, *Electrochemical Reduction of Carbon Dioxide: Overcoming the Limitations of Photosynthesis*, The Royal Society of Chemistry, 2018, pp. 1–271.

[4] J. Qiao, Y. Liu, F. Hong and J. Zhang, *Chem. Soc. Rev.*, 2014, **43**, 631–675.

[5] R. Angamuthu, P. Byers, M. Lutz, A. L. Spek and E. Bouwman, *Science*, 2010, **327**, 313–315.

[6] C. D. Windle and R. N. Perutz, *Coord. Chem. Rev.*, 2012, **256**, 2562–2570.

[7] J. Hawecker, J. M. Lehn and R. Ziessel, *J. Chem. Soc., Chem. Commun.*, 1984, **984**, 328–330.

[8] C. W. Machan, S. A. Chabolla, J. Yin, M. K. Gilson, F. A. Tezcan and C. P. Kubiak, *J. Am. Chem. Soc.*, 2014, **136**, 14598–14607.

[9] H. Y. V. Ching, X. Wang, M. He, N. Perujo Holland, R. Guillot, C. Slim, S. Griveau, H. C. Bertrand, C. Policar, F. Bedioui and M. Fontecave, *Inorg. Chem.*, 2017, **56**, 2966–2976.

[10] A. Wilting, T. Stolper, R. A. Mata and I. Siewert, *Inorg. Chem.*, 2017, **56**, 4176–4185.

[11] C. J. Stanton, C. W. Machan, J. E. Vandezande, T. Jin, G. F. Majetich, H. F. Schaefer, C. P. Kubiak, G. Li and J. Agarwal, *Inorg. Chem.*, 2016, **55**, 3136–3144.

[12] A. Maurin, C. O. Ng, L. Chen, T. C. Lau, M. Robert and C. C. Ko, *Dalton Trans.*, 2016, **45**, 14524–14529.

[13] H. Hadadzadeh, H. Farrokhpour, J. Simpson, J. Shakeri, M. Daryanavard and M. Shokrollahi, *New J. Chem.*, 2016, **40**, 6347–6357.

[14] Z. Chen, C. Chen, D. R. Weinberg, P. Kang, J. J. Concepcion, D. P. Harrison, M. S. Brookhart and T. J. Meyer, *Chem. Commun.*, 2011, **47**, 12607–12609.

[15] M. Daryanavard, H. Hadadzadeh, M. Weil and H. Farrokhpour, *J. CO_2 Util.*, 2017, **17**, 80–89.

[16] A. Szymaszek and F. Pruchnik, *J. Organomet. Chem.*, 1989, **376**, 133–140.

[17] S. T. Ahn, E. A. Bielinski, E. M. Lane, Y. Chen, W. H. Bernskoetter, N. Hazari and G. T. R. Palmore, *Chem. Commun.*, 2015, **51**, 5947–5950.

[18] F. D. Sypaseuth, C. Matlachowski, M. Weber, M. Schwalbe and C. C. Tzschucke, *Chem. Eur. J.*, 2015, **21**, 6564–6571.

[19] S. Roy, B. Sharma, J. Pécaut, P. Simon, M. Fontecave, P. D. Tran, E. Derat and V. Artero, *J. Am. Chem. Soc.*, 2017, **139**, 3685–3696.

[20] G. Neri, J. J. Walsh, C. Wilson, A. Reynal, J. Y. C. Lim, X. Li, A. J. P. White, N. J. Long, J. R. Durrant and A. J. Cowan, *Phys. Chem. Chem. Phys.*, 2015, **17**, 1562–1566.

[21] J. Song, E. L. Klein, F. Neese and S. Ye, *Inorg. Chem.*, 2014, **53**, 7500–7507.

[22] M. Bourrez, F. Molton, S. Chardon-Noblat and A. Deronzier, *Angew. Chem. Int. Ed.*, 2011, **50**, 9903–9906.

[23] S. J. Spall, T. Keane, J. Tory, D. C. Cocker, H. Adams, H. Fowler, A. J. Meijer, F. Hartl and J. A. Weinstein, *Inorg. Chem.*, 2016, **55**, 12568–12582.

[24] M. D. Sampson, A. D. Nguyen, K. A. Grice, C. E. Moore, A. L. Rheingold and C. P. Kubiak, *J. Am. Chem. Soc.*, 2014, **136**, 5460–5471.

[25] M. D. Sampson and C. P. Kubiak, *J. Am. Chem. Soc.*, 2016, **138**, 1386–1393.

[26] J. M. Smieja, M. D. Sampson, K. A. Grice, E. E. Benson, J. D. Froehlich and C. P. Kubiak, *Inorg. Chem.*, 2013, **52**, 2484–2491.

[27] F. Franco, C. Cometto, L. Nencini, C. Barolo, F. Sordello, C. Minero, J. Fiedler, M. Robert, R. Gobetto and C. Nervi, *Chem. Eur. J.*, 2017, **23**, 4782–4793.

[28] D. C. Grills, M. Z. Ertem, M. McKinnon, K. T. Ngo and J. Rochford, *Coord. Chem. Rev.*, 2018, **374**, 173–217.

[29] I. Azcarate, C. Costentin, M. Robert and J.-M. Savéant, *J. Am. Chem. Soc.*, 2016, **138**, 16639–16644.

[30] C. Costentin, M. Robert and J. M. Savéant, *Acc. Chem. Res.*, 2015, **48**, 2996–3006.

[31] E. A. Mohamed, Z. N. Zahran and Y. Naruta, *Chem. Commun.*, 2015, **51**, 16900–16903.

[32] N. Elgrishi, M. B. Chambers, X. Wang and M. Fontecave, *Chem. Soc. Rev.*, 2017, **46**, 761–796.

[33] R. Francke, B. Schille and M. Roemelt, *Chem. Rev.*, 2018, **118**, 4631–4701.

[34] K. A. Grice, *Coord. Chem. Rev.*, 2017, **336**, 78–95.

[35] K. A. Grice and C. Saucedo, *Inorg. Chem.*, 2016, **55**, 6240–6246.

[36] M. L. Clark, K. A. Grice, C. E. Moore, A. L. Rheingold and C. P. Kubiak, *Chem. Sci.*, 2014, **5**, 1894–1900.

[37] J. Tory, B. Setterfield-Price, R. A. W. Dryfe and F. Hartl, *ChemElectroChem*, 2015, **2**, 213–217.

[38] F. Franco, C. Cometto, F. Sordello, C. Minero, L. Nencini, J. Fiedler, R. Gobetto and C. Nervi, *ChemElectroChem*, 2015, **2**, 1372–1379.

[39] J. O. Taylor, R. D. Leavey and F. Hartl, *ChemElectroChem*, 2018, **5**, 3155–3161.

[40] D. Sieh, D. C. Lacy, J. C. Peters and C. P. Kubiak, *Chem. Eur. J.*, 2015, **21**, 8497–8503.

[41] K. T. Ngo, M. McKinnon, B. Mahanti, R. Narayanan, D. C. Grills, M. Z. Ertem and J. Rochford, *J. Am. Chem. Soc.*, 2017, **139**, 2604–2618.

[42] G. Neri, P. M. Donaldson and A. J. Cowan, *J. Am. Chem. Soc.*, 2017, **139**, 13791–13797.

[43] G. Neri, J. J. Walsh, G. Teobaldi, P. M. Donaldson and A. J. Cowan, *Nat. Catal.*, 2018, **1**, 952–959.

[44] L. Rotundo, C. Garino, R. Gobetto and C. Nervi, *Inorg. Chim. Acta*, 2018, **470**, 373–378.

[45] D. E. Ryan, D. J. Cardin and F. Hartl, *Coord. Chem. Rev.*, 2017, **335**, 103–149.

[46] J. Tory, G. Gobaille-Shaw, A. M. Chippindale and F. Hartl, *J. Organomet. Chem.*, 2014, **760**, 30–41.

[47] J. W. Goodyear, C. W. Hemingway, R. W. Harrington, M. R. Wisemann and B. J. Brisdon, *J. Organomet. Chem.*, 2002, **664**, 176–181.

[48] A. Technologies, *Agilent CrysAlis PRO*, 2014.

[49] L. Palatinus and G. Chapuis, *J. Appl. Crystallogr.*, 2007, **40**, 786–790.

[50] P. W. Betteridge, J. R. Carruthers, R. I. Cooper, K. Prout and D. J. Watkin, *J. Appl. Crystallogr.*, 2003, **36**, 1487–1487.

[51] P. Van Der Sluis and A. L. Spek, *Acta Crystallogr. Sec. A*, 1990, **46**, 194–201.

[52] M. Krejčik, M. Daněk and F. Hartl, *J. Electroanal. Chem. Interfacial Electrochem.*, 1991, **317**, 179–187.

[53] T. Mahabiersing, H. Luytenn, R. Nieuwendam and F. Hartl, *Collect. Czech. Chem. Commun.*, 2003, **68**, 1687–1709.

[54] R. G. Parr and W. Yang, *Density-functional theory of atoms and molecules*, Oxford University Press, 1989.

[55] G. Te Velde, F. M. Bickelhaupt, E. J. Baerends, C. Fonseca Guerra, S. J. A. van Gisbergen, J. G. Snijders and T. Ziegler, *J. Comput. Chem.*, 2001, **22**, 931–967.

[56] C. Fonseca Guerra, J. G. Snijders, G. Te Velde and E. J. Baerends, *Theor. Chem. Acc.*, 1998, **99**, 391–403.

[57] V. U. Amsterdam, *Theoretical Chemistry, ADF2013 SCM*.

[58] S. H. Vosko, L. Wilk and M. Nusair, *Can. J. Phys.*, 1980, **58**, 1200–1211.

[59] A. D. Becke, *J. Chem. Phys.*, 1998, **109**, 2092–2098.

[60] J. P. Perdew, *Phys. Rev. B.*, 1986, **33**, 8822–8824.

[61] J. P. Perdew, *Phys. Rev. B*, 1986, **34**, 7406–7406.

[62] E. van Lenthe, A. Ehlers and E.-J. Baerends, *J. Chem. Phys.*, 1999, **110**, 8943–8953.

[63] S. J. A. van Gisbergen, A. Rosa, G. Ricciardi and E. J. Baerends, *J. Chem. Phys.*, 1999, **111**, 2499–2506.

[64] A. Rosa, E. J. Baerends, S. J. A. van Gisbergen, E. van Lenthe, J. A. Groeneveld and J. G. Snijders, *J. Am. Chem. Soc.*, 1999, **121**, 10356–10365.

[65] S. J. A. van Gisbergen, J. A. Groeneveld, A. Rosa, J. G. Snijders and E. J. Baerends, *J. Phys. Chem. A*, 1999, **103**, 6835–6844.

[66] F. Wang and T. Ziegler, *J. Chem. Phys.*, 2005, **123**, 154102.

[67] T. Ziegler and A. Rauk, *Inorg. Chem.*, 1979, **18**, 1755–1759.

[68] T. Ziegler and A. Rauk, *Theor. Chim. Acta*, 1977, **46**, 1–10.

[69] *Chemcraft Program*, 2018, `http://www.chemcraftprog.com/index.html`.

[70] A. J. Graham and R. H. Fenn, *J. Organomet. Chem.*, 1969, **17**, 405–422.

[71] F. C. Liu, P. S. Yang, C. Y. Chen, G. H. Lee and S. M. Peng, *J. Organomet. Chem.*, 2008, **693**, 537–545.

[72] J. R. Ascenso, C. G. De Azevedo, M. J. Calhorda, M. A. De, P. Costa, A. R. Dias,

M. G. Drew, V. Félix, A. M. Galvão and C. C. Romão, *J. Organomet. Chem.*, 2001, **632**, 197–208.

[73] J. W. Faller, D. A. Haitko, R. D. Adams and D. F. Chodosh, *J. Am. Chem. Soc.*, 1979, **101**, 865–876.

[74] J. C. Alonso, P. Neves, M. J. P. Da Silva, S. Quintal, P. D. Vaz, C. Silva, A. A. Valente, P. Ferreira, M. J. Calhorda, V. Félix and M. G. Drew, *Organometallics*, 2007, **26**, 5548–5556.

[75] S. A. Chabolla, E. A. Dellamary, C. W. Machan, F. A. Tezcan and C. P. Kubiak, *Inorg. Chim. Acta*, 2014, **422**, 109–113.

[76] J. Vichova, F. Hartl and A. Vlcek, *J. Am. Chem. Soc.*, 1992, **114**, 10903–10910.

[77] F. Hartl, P. Rosa, L. Ricard, P. Le Floch and S. Záliš, *Coord. Chem. Rev.*, 2007, **251**, 557–576.

[78] J. W. van Outersterp, F. Hartl and D. J. Stufkens, *Organometallics*, 1995, **14**, 3303–3310.

[79] G. J. Stor, F. Hartl, J. W. Van Outersterp and D. J. Stufkens, *Organometallics*, 1995, **14**, 1115–1131.

[80] F. Hartl, M. P. Aarnts, H. A. Nieuwenhuis and J. Van Slageren, *Coord. Chem. Rev.*, 2002, **230**, 107–125.

[81] Q. Zeng, J. Tory and F. Hartl, *Organometallics*, 2014, **33**, 5002–5008.

Chapter 6

Impact of the 2-R-Allyl Substituent on the Cathodic Paths of [Mo(η^3-2-R-allyl)(α-diimine)$(CO)_2$Cl] (R = H, CH_3; α-diimine = 6,6′-dimethyl-2,2′-bipyridine or bis(p-tolylimino)-acenaphthene)

The content of this chapter will be published in: **J. O. Taylor**, R. Culpeck, A. M. Chippindale, M. J. Calhorda, F. Hartl, *Organometallics*, Manuscript in Preparation.

6.1 Abstract

A new series of formally Mo(II) complexes, [Mo(η^3-2-R-allyl)(6,6′-dmbipy)$(CO)_2$Cl] (dmbipy = 6,6′-dimethyl-2,2′-bipyridine; 2-R-allyl = allyl for R = H, methallyl for R = CH_3) and [Mo(η^3-2-methallyl)(pTol-bian)$(CO)_2$Cl] (pTol-bian = bis(p-tolylimino)acenaphthene) have been synthesised and their redox properties and cathodic reactivity characterised with cyclic voltammetry (CV) and variable-temperature IR spectroelectrochemistry (IR SEC) in tetrahydrofuran (THF) and butyronitrile (PrCN) at a Pt working electrode. The experimental results significantly contribute to our understanding of the cathodic pathways of the family of complexes [Mo(η^3-allyl)(x,x′-dmbipy)$(CO)_2$(NCS)], which have recently been identified as precursors to 5-coordinate anions that are catalytically active toward the reduction of CO_2 (see Chapter 5). With this new series, the roles of the X and allyl ligand in the reduction-induced reactivity are explored, and it is shown that both ligands may play a stronger role than previously imagined, at all stages of the reduction path. Differently from previous studies, which found [Mo(η^3-allyl)(6,6′-dmbipy)$(CO)_2]^-$, derived from the corresponding NCS^- complex, to be stable toward dimerization, the alternative Cl^- ligand promotes the dimerization, by weakening the parent complex to attack by the $2e^-$ reduced species. On the other hand, replacement of the allyl ligand with 2-methylallyl (methallyl) has a similar effect, which leads to an irreversible (ECE) initial reduction and also dimerization at room temperature on a longer timescale. It is also shown that the new ligand core reduces the stability of radical anions derived from the strongly π-accepting R-bian ligands. Preliminary CV and IR SEC studies under CO_2 reveal that [Mo(η^3-allyl)(6,6′-dmbipy)$(CO)_2]^-$ retains its catalytic ability at the R2 wave. Under the same conditions [Mo(η^3-methallyl)(6,6′-dmbipy)$(CO)_2]^-$ appeared to be moderately active toward CO_2 already at the first wave; fully consistent with absent dimerization under argon on this timescale. In the thin electrolyte layer, the electrocatalytic generation of CO and formate is hampered by the competing formation of inactive dimer.

6.2 Introduction

There is a strong interest in the electrocatalytic reduction of CO_2, which offers a sustainable avenue to a variety of valuable chemical feedstocks for organic synthesis or chemical fuel. Transition metal complexes have been identified as highly effective catalysts for the $2e^-$ reduction of CO_2, allowing one to take advantage of energy-saving proton-coupled pathways.[1,2] The original reports mostly focused on complexes based on rare-Earth metals such as [Re(bipy)$(CO)_3$Cl], where the active catalyst is the $2e^-$ reduced 5-coordinate anion, [Re(bipy)$(CO)_3]^-$.[3–7] Although the expenses associated with such materials mean that current efforts are directed more toward the Earth-abundant metals such as Mn in [Mn(bipy)$(CO)_3]^-$, which has only recently been identified as a catalyst in the presence of small amounts of Brønsted acids.[8–11] Although catalysts based on many Earth-abundant first-row transition metals such as Fe, Co, Ni, with impressive catalytic abilities are now widely known[12], much less attention in this regard has been paid to the Group-6 metals (Cr, Mo, W).

Currently the limited literature, which regards the Group-6 metals, has been based largely on two families of complexes, viz. [Mo(α-diimine)$(CO)_4$][13–19] and [Mo(η^3-allyl)(α-diimine)$(CO)_2$X] X = halide or pseudohalide.[20,21] First, however, it is worth mentioning that the hexacarbonyl complex, [Mo$(CO)_6$], is also active toward the electrocatalytic reduction of CO_2, differently from the equivalent Group-7 complexes [M$(CO)_5]_2$ or [M$(CO)_5$X].[22] The complexes [Mo(α-diimine)$(CO)_4$] (α-diimine = 2,2′-bipyridine or x,x′-dimethyl-bipyridine (x = 4-6)) undergo reversible reduction to [Mo(α-diimine)$(CO)_4]^{\bullet-}$ and subsequent reduction to 6-coordinate [Mo(α-diimine)$(CO)_4]^{2-}$, producing the 5-coordinate catalyst [Mo(α-diimine)$(CO)_3]^{2-}$, resulting from a concomitant loss of a CO ligand. At an Au cathodic surface the onset of the catalytic wave may be shifted to less negative potentials, due to the enhanced equilibrium between [Mo(α-diimine)$(CO)_4]^{\bullet-}$ and [Mo(α-diimine)$(CO)_3]^{\bullet-}$, facilitating CO dissociation from the usually stable radical anion, producing the 5-coordinate radical which is reducible to the active catalyst at ca. 500 mV less negative potentials. Smart

choices of solvent and electrode materials coupled with ligand effects make the class more comparable with other Earth-abundant catalysts.[21] (see also Chapter 3 + 4)

The second class of complexes [Mo(η^3-allyl)(α-diimine)$(CO)_2$X] (α-diimine = 2,2′-bipyridine or x,x′-dimethyl-bipyridine (x = 4-6), X = halide, psuedohalide) have been identified as precursors to the catalytically active 5-coordinate anion [Mo(η^3-allyl)(α-diimine)$(CO)_2]^-$.[20,21] Differently from the Group-6 tetracarbonyls introduced above, the originator of the family, [Mo(η^3-allyl)(bipy)$(CO)_2$(NCS)] reduces irreversibly to the unstable radical anion, triggering contaminant loss of the NCS^- ligand and concomitant reduction of the 5-coordinate radical to 5-coordinate anion. A dimer formed, [Mo(η^3-allyl)(bipy)$(CO)_2]_2$ (ECEC), following zero-electron reaction of the $2e^-$ reduced 5-coordinate anion with the parent complex, very similarly to the reduction path of [Mn(bipy)$(CO)_3$Br].[8,23–25] However, differently from this reference Mn-based system , the Mo-allyl based dimer is not reduced to the corresponding 5-coordinate anion but is reactive and appears to exist also in its $1e^-$ reduced form.[20] The subsequent study, which regarded [Mo(η^3-allyl)(x,x′-dmbipy)$(CO)_2$(NCS)] (x = 4-6), revealed what factors control the perseverance of the 5-coordinate anion (see also Chapter 5).[21] In particular it revealed that the complexes are quite susceptible to electronic and steric changes in the ligand coordination sphere. For instance only for, [Mo(η^3-allyl)(6,6′-dmbipy)$(CO)_2$(NCS)], was the radical anion stable at room temperature on the CV timescale, radically altering the reduction pathway from ECEC, to EEC (resembling more the reduction path of [Mo(bipy)$(CO)_4$]). This allowed for the first time to characterize the active 5-coordinate catalyst by IR spectroelectrochemistry.

This current work is a comparative study meant to complement the valuable insight into these complexes gathered already from the [Mo(η^3-allyl)(x,x′-dmbipy)$(CO)_2$(NCS)] (x = 4-6) series.[21] The first complex in this new series, [Mo(η^3-allyl)(6,6′-dimethyl-2,2′-bipyridine)$(CO)_2$Cl], probes the effect of changing the anionic X^- ligand. The previous cases utilize the NCS^- ligand, a weaker π-donor; its ability to function as such is also decreasing in the reduced state, as the ligand tends more toward the Mo−C≡N−S resonance form. In this work, it is replaced with Cl^-, acting as both a stronger σ- and π-donor.

This can already be expected to have an effect on the stability of both the parent and reduced species. The second complex under study, [Mo(η^3-methallyl)(6,6′-dimethyl-2,2′-bipyridine)$(CO)_2$Cl] helps to investigate the impact of allylic methyl-substitution at the *meso*-C atom. Going from 2,2′-bipyridine to 6,6′-dimethyl-bipyridine a significant stabilization of the 1e$^-$ reduced radical anionic intermediate was observed. An opposite effect may be expected, but not automatically, from the replacement of the allyl ligand with methallyl. Finally, the third complex, [Mo(η^3-methallyl)(pTol-bian)$(CO)_2$Cl] with an extended conjugated bian π-system, was expected to act a reference compound featuring a strong π-acceptor ligand in contrast to donor dmbipy counterpart.

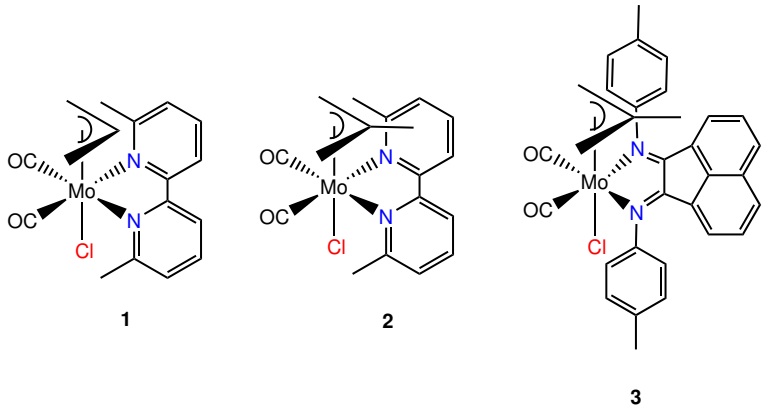

Chart 6.1: Molecular structures of the studied complexes, [Mo(η^3-allyl)(6,6′-dmbipy)$(CO)_2$Cl], **1**, [Mo(η^3-methallyl)(6,6′-dmbipy)$(CO)_2$Cl], **2**, and [Mo(η^3-methallyl)(pTol-bian)$(CO)_2$Cl], **3**.

Thus, the ultimate goals of the study are to probe, (i) the effect of the alternative Cl$^-$ ligand on the structures and reactivity of the reduced complexes, (ii) the steric and electronic consequences of allylic methyl substitution and (iii) the effect of the alternative coordination sphere also with a π-accepting ligand.

6.3 Experimental

Materials and Methods

All synthetic and electrochemical operations were carried out under an atmosphere of dry argon, using standard Schlenk techniques. Solvents were freshly distilled under nitrogen gas

from Na/benzophenone (ketyl) radicals (tetrahydrofuran, THF and CaH_2 (butyronitrile, PrCN). The supporting electrolyte, Bu_4NPF_6 (Acros-Organics), was recrystallized twice from ethanol, and dried under vacuum at 373 K for 5 h. Just prior to the experiment, the electrolyte was dried again overnight at 373 K. The precursor complexes, [Mo(η^3-2-R-allyl)$(MeCN)_2(CO)_2Cl$] (R = H, CH_3) were prepared in good yields by slight modification of the literature procedures.[26] The ligand bis(p-tolylimino)acenaphthene (pTol-bian), was prepared according to a literature procedure involving the condensation reaction of acenaphthenequinone and 2,6-dimethylaniline.[27] All other compounds were purchased from Sigma Aldrich and used without further purification. The final complexes were prepared by facile thermal substitution of the labile MeCN ligands in the precursor complexes. Purity and identity confirmed by infrared, NMR spectroscopy and single-crystal X-ray diffraction. ^{1}H NMR spectra were recorded on a 400 MHz Bruker NanoBay spectrometer.

General Synthesis of [Mo(η^3-2-R-allyl)(α-diimine)$(CO)_2Cl$] (R = H, CH_3)

A solution of [Mo(η^3-2-R-allyl)$(MeCN)_2(CO)_2Cl$] (0.62 mmol, 0.2 g) in dry DCM (10 mL) was mixed under argon with a solution of the appropriate α-diimine ligand in dry DCM (10 mL). The mixture was stirred for 4 h and then the volume was reduced by half. The crude product was precipitated by slow addition of hexane (10 x 5 mL). Roughly 100 mg of the precipitate was recovered by inert filtration and washed with cold hexane (2 x 10 mL). Spectroscopically pure samples were prepared by column chromatography on silica, using DCM:hexane (9:1, v/v) or DCM:diethyl ether (9:1, v/v) as the eluent, where necessary. Following the purification, yields ranged between 15-50%. Crystals for X-ray analysis were grown by slow evaporation of DCM-d_2.

[Mo(η^3-allyl)(6,6′-dimethyl-2,2′-bipyridine)$(CO)_2Cl$] (1)

The precursor [Mo(η^3-allyl)$(MeCN)_2(CO)_2Cl$] (0.62 mmol, 0.2 g) was reacted together with 6,6′-dimethyl-2,2′-bipyridine (0.54 mmol, 0.0997 g) to afford complex **1**. The crude product was purified on silica column, using DCM:hexane (9:1, v/v) as the eluent. Yield: (30 mg,

15%) ^{1}H NMR (400 MHz, DCM-d_2) δ 7.83 (2H, d, J = 8 Hz), 7.75 (2H, t, J = 8 Hz), 7.32 (2H, d, J = 8 Hz), 2.95 (6H, s), 2.66 (1H, m), 2.49 (2H, d, J = 8 Hz), 1.05 (2H, d, J = 8 Hz). IR (ν(CO), THF) 1945, 1861 cm^{-1}.

[Mo(η^3-methallyl)(6,6′-dimethyl-2,2′-bipyridine)(CO)$_2$Cl] (2)

The precursor [Mo(η^3-methallyl)(MeCN)$_2$(CO)$_2$Cl] (0.62 mmol, 0.2 g) was reacted together with 6,6′-dimethyl-2,2′-bipyridine (0.54 mmol, 0.0997 g), to afford complex **2**. The crude product was filtered and washed with cold hexane (2 x 10 mL). Yield: (97 mg, 42%) ^{1}H NMR (400 MHz, DCM-d_2) δ 7.87 (2H, d, J = 8 Hz), 7.75 (2H, t, J = 8 Hz), 7.34 (2H, d, J = 8 Hz), 2.95 (6H, s), 2.34 (2H, s), 1.18 (2H, s), 0.98 (3H, s). IR (ν(CO), THF) 1944, 1861 cm^{-1}.

[Mo(η^3-allyl)(bis(p-tolylimino)acenaphthene)(CO)$_2$Cl] (3)

The precursor [Mo(η^3-methallyl)(MeCN)$_2$(CO)$_2$Cl] (0.62 mmol, 0.2 g) was reacted together with bis(p-tolylimino)acenaphthene (0.54 mmol, 0.195 g) to afford complex **3**. The crude product was purified on silica column, using DCM:diethyl ether (9:1, v/v) as the eluent. Yield: (45 mg, 15%) ^{1}H NMR (400 MHz, DCM-d_2) δ 7.87 (2H, d, J = 8 Hz), 7.58 (2H, d, J = 8 Hz), 7.32 (6H, m), 7.01 (2H, d, J = 8 Hz), 6.78 (2H, d, J = 8 Hz) 2.63 (2H, s), 2.03 (3H, s), 1.18 (2H, s). IR (ν(CO), THF) 1956, 1886 cm^{-1}.

X-ray Structure Determination

Crystals were mounted under Paratone-N oil and flash-cooled to either 100 K (**1** and **3**) or 200 K for **2** in a stream of nitrogen in an Oxford Cryostream 800 cooler. Single-crystal X-ray intensity data were collected using a Rigaku XtaLAB Synergy diffractometer (Cu Kα radiation (λ = 1.54184 Å)). The data were reduced within the CrysAlis PRO software.[28] The structure was solved using the program Superflip,[29] and all non-hydrogen atoms were located. Least-square refinements were performed using the CRYSTALS suite of programs.[30] The non-hydrogen atoms were refined anisotropically. Each hydrogen atom of the ligands

was placed geometrically at a C−H distance of 0.95 Å and a U_{iso} of 1.2-1.5 times the value of U_{iso} of the parent C atom. The positions of the hydrogen atoms were then refined with riding constraints.

Cyclic Voltammetry

Cyclic voltammograms of complexes **1-3** were recorded on a Metrohm Autolab PGSTAT302N potentiostat operated with the NOVA 1.9 Software. The air-tight single-compartment electrochemical cell housed a Pt microdisc working electrode (active area of 0.4 mm^2) polished with 0.25-μm diamond paste (Kemet), a coiled Pt wire counter electrode and a coiled Ag wire pseudo-reference electrode. All values are reported vs the ferrocene/ferrocenium (Fc/Fc^+) redox couple serving as the internal standard for most measurements, added just before the final potential sweep. Where necessary, decamethylferrocence (Fc^*/Fc^{*+}) served this purpose in order to avoid overlap with the nearby Mo(II)/Mo(III) oxidation. In THF, the value $E_{1/2}$ (Fc^*/Fc^{*+}) = -0.48 V vs Fc/Fc^+ has been determined for this work.

IR Spectroelectrochemistry

IR spectroelectrochemical experiments were performed using a Bruker Vertex 70v FT-IR spectrometer equipped with a DLaTGS detector (for T = 298 K) or linked to an external Bio-RAD FTS 60 MCT dectector (for T = 223 K). The in-situ electrolyses at ambient temperature were conducted using an air-tight OTTLE cell.[31] The cell was equipped with Pt minigrid (32 wires per cm) working and auxiliary electrodes, an Ag-microwire pseudo-reference electrode, and optically transparent CaF_2 windows. The course of the spectroelectrochemical experiment was monitored by thin-layer cyclic voltammetry. The potentiostat control during the thin-layer CV was achieved using a PalmSens EmStat3 potentiostat, operated with the PSTrace5 software. Low temperature spectroelectrochemical measurements were carried out with a cryostatted OTTLE cell of a similar design.[32] Solutions contained 3 x 10^{-1} M Bu_4NPF_6 and 3 x 10^{-3} M analyte.

Computational Studies

Density functional theory (DFT) calculations[33] were performed, using the Amsterdam Density Functional (ADF) program.[34–36] Geometries were optimized with gradient correction, without symmetry constraints, using the Local Density Approximation (LDA) of the correlation energy (Vosko-Wilk-Nusair)[37] and the Generalized Gradient Approximation (Becke's[38] exchange and Perdew's[39,40] correlation functionals). Unrestricted calculations were performed for open-shell complexes. Solvent was considered in all geometry optimizations and single-point calculations, in accordance with the COSMO approach implemented in ADF. For modelling, tetrahydrofuran (THF) was always chosen as the solvent. Relativistic effects were treated with the ZORA approximation.[41] Triple-ζ Slater-type orbitals (STOs) were used to describe all the valence electrons of H, O, C, N, S, and Mo. A set of two polarization functions was added to H (single-ζ 2s, 2p), O, C, N, S (single-ζ, 3d, 4f), and Mo (5d, 4f). Frequency calculations were performed to obtain the vibrational spectra and to check that intermediates were minima in the potential energy surface.

6.4 Results and Discussion

6.4.1 Characterization and Crystal Structure Analysis

In THF, the IR spectra of complexes **1-3** exhibit two ν(CO) bands. For complexes **1** and **2** these absorption bands are almost identical, both in terms of intensity, pattern and wavenumbers, viz. 1945, 1861 cm^{-1}. Compared to the reference, [Mo(η^3-allyl)(6,6′-dmbipy)(CO)$_2$(NCS)] (1948, 1866 cm^{-1}) the absorption bands are slightly shifted to smaller wavenumbers, which reflects the increased π-back-donation experienced by the CO ligands, upon replacement of the weaker π-donor, NCS$^-$, with the stronger π-donor, Cl$^-$. Finally, in complex **3** the ν(CO) bands are observed at 1956, 1886 cm^{-1}, reflecting the reduced π-back-donation from the pTol-bian ligand compared with 6,6′-dmbipy.

The crystal structures of **1-3** are presented in Figure 6.1. Crystallographic data and selected bond lengths are summarized in Tables 6A.1 and 6A.2 (Appendix). All three com-

plexes adopt the type A pseudo-octahedral (equatorial) structure, much like the previously studied series. To reiterate, this structure is characterized by both L∩L donor atoms appearing in the trans position to both CO ligands. It is worth noting that this is quite unusual for the large and strongly π-accepting bian ligand, which in the past was usually only observed in the less symmetrical type B (axial) structure.[20,42–46] As is quite common, in all three cases the open face of the allyl ligand lies over the CO ligands (i.e., the *endo* isomer is preferred).

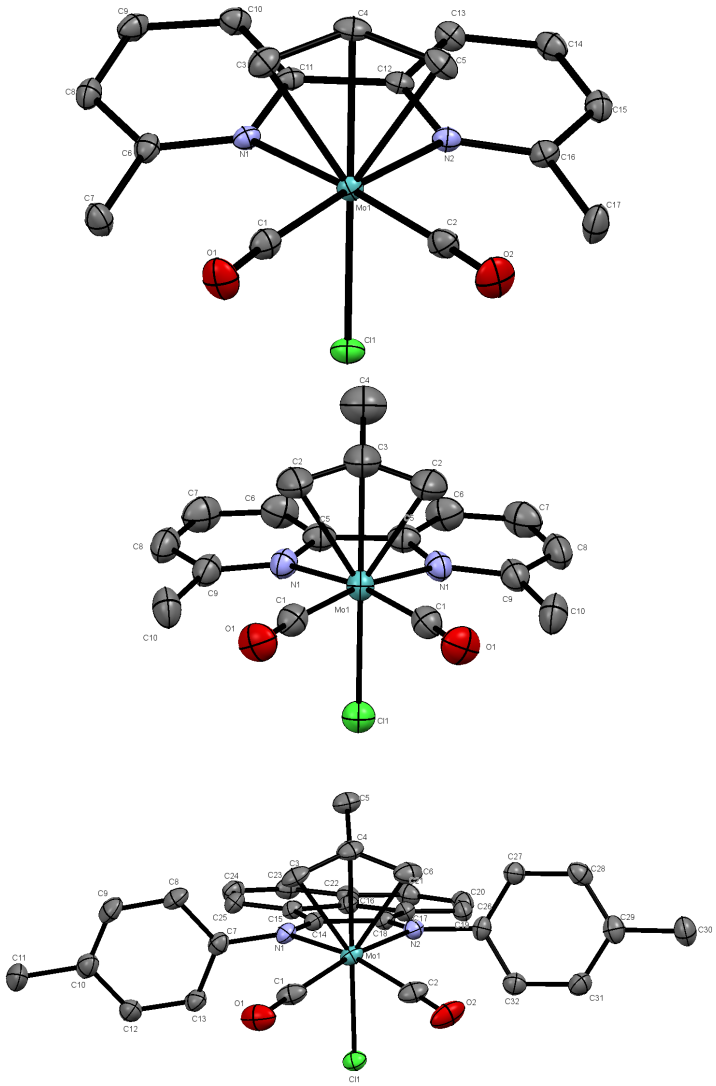

Figure 6.1: An ORTEP view (50% thermal probability) of the molecular structures of [Mo(η^3-allyl))(6,6′-dmbipy)$(CO)_2$Cl] (**1**, top), [Mo(η^3-methallyl)(6,6′-dmbipy)$(CO)_2$Cl] (**2**, middle) and [Mo(η^3-methallyl)(pTol-bian)$(CO)_2$Cl] (**3**, bottom) determined by single-crystal X-ray analysis. Hydrogen atoms have been omitted for clarity.

The length of the Mo−Cl bond varies in the order **2** (2.515(15) Å) > **1** (2.491(8) Å) > **3** (2.487(3) Å). As the length is often, although not always, indicative of the strength of the bond, these values may tentatively provide an indication of the relative stability of the parent complexes and their radical anions. It must be stressed, however, that the relative differences are quite small and these data only reflect a trend. On the other hand, these differences may already play a supportive role in the formulation of the conclusions drawn mainly from the (spectro)-electrochemistry and DFT (see following sections). The corresponding bond lengths, Mo−NCS, from previous cases[20,21] ranged around 2.15 Å, being somewhat shorter than the Mo−Cl recorded here, probably because of the Mo=N=C=S resonance. In all three complexes, the central allyl atom (*meso*-C) is closer to the metal center than the terminal C atoms. For instance in **1**, the central atom has a distance of 2.210(3) Å from Mo, and the two terminal C atoms have distances of 2.325(3) Å and 2.338(3) Å. The average bond lengths of C≡O in **1** and **2** are almost identical (1.152(6) Å), while that in **3** is somewhat shorter, 1.139(4) Å; conversely M−C is shorter in **1**-**2** (1.95 Å), and slightly longer in **3** (1.98 Å), which reflects the observations from the IR spectra regarding the degree of π-back-donation in these complexes. The phenyl rings in **2** are co-planar, with the dihedral angle around the NCCN moiety of 0°, while in **1** the phenyl rings appear to have a larger degree of freedom, and in this case a dihedral angle of -5.21° is observed. This observation of course proves that the methylallyl group has a stronger steric influence than the allyl group on the rest of the complex, as one might expect. Finally, the bond angle between the equatorial N∩N donor atoms (N_1−Mo−N_2) remains nearly the same throughout the series. On the other hand, the bond angle defined by the equatorial CO ligands (C_1−Mo−C_2) does change, being smallest (compressed) for **2** (74°) and largest for **3** (80°), with **1** being an intermediate case (76°).

DFT calculations[33], using the ADF program[34–36], were conducted on the parent (**1**-**3**) structures and they reveal that the equatorial (type A) isomer is indeed always preferred over the axial (type B) isomer. The energy difference (kcal mol^{-1}) is increasing on going from **1** (5.92) to **2** (7.92), reflecting the influence of the extra methyl group (Table

6A.3, Appendix). A comparable energy difference is seen for the axial/equatorial isomers of [Mo(η^3-allyl)(6,6′-dmbipy)$(CO)_2$(NCS)].[21] While for **3**, the energy difference between the two isomers is somewhat smaller at only 1.72 kcal mol^{-1}, highlighting the differences in bonding within the three complexes. The structural parameters (Table 6A.4, Appendix) are well reproduced by DFT calculations.

6.4.2 Cyclic Voltammetry

Table 6.1: Redox potentials of complexes **1**-**3** and their reduction products (see Scheme 6.1) from cyclic voltammetry at a Pt microdisc electrode at 298 K.

	Redox Potentials [V vs Fc/Fc^+]				
Solvent	$Mo^{II/III}$ ($E_{1/2}$)	R1 ($E_{1/2}$)	R2 ($E_{p,c}$)	R2′ ($E_{1/2}$)	O1′ ($E_{p,a}$)
[Mo(η^3-allyl)(6,6′-dmbipy)$(CO)_2$(NCS)][a]					
THF	0.26	-2.02	-2.57	-2.94[b]	-1.84
THF[c]	0.28	-1.98	-2.60	-2.82	-1.66
PrCN	0.32	-1.93	-2.45	-	-1.73
PrCN[c]	0.28	-1.94	-2.56	-	-1.54
[Mo(η^3-allyl)(6,6′-dmbipy)$(CO)_2$Cl] (1)					
THF	0.16	-2.04	-2.61	-2.82[b]	-1.74
THF[c]	0.19	-2.01	-2.59	-2.78	-1.63
PrCN	0.16	-2.03	-2.60	-2.79[b]	-1.74
PrCN[c]	0.20	-1.99	-2.63	-2.83	-1.55
[Mo(η^3-methallyl)(6,6′-dmbipy)$(CO)_2$Cl] (2)					
THF	0.06	-2.25[b]	-	-2.98[b]	-1.83
THF[c]	0.10	-2.02	-2.60	-2.82	-1.64
PrCN	0.07	-2.14[b]	-	-2.89[b]	-1.71
PrCN[c]	0.10	-2.07	-2.66	-2.90	-1.61
[Mo(η^3-methallyl)(pTol-bian)$(CO)_2$Cl] (3)					
THF	0.05	-1.34	-1.91	-2.80[b]	-
THF[c]	0.11	-1.29	-2.03	-2.64	-0.99
PrCN	0.04	-1.32	-1.93	-2.81[b]	-1.05
PrCN[c]	0.11	-1.28	-1.91	-2.72	-1.03

[a] Reference complex measured at an Au microdisc electrode.[21] [b] $E_{p,c}$ value (anodic counter wave not observed). [c] Measured at 195 K. [d] Not reported.

Cyclic voltammetry of **1**-**3** was conducted in argon-saturated THF/Bu_4NPF_6 (Figures 6.2 and 6.3) and $PrCN/Bu_4NPF_6$ (Figures 6A.1 to 6A.3, Appendix) at variable temperature (298 or 195 K) on a Pt electrode. The redox potentials obtained for **1**-**3** are summarized in Table 6.1.

At the CV level, the redox behavior of **1** closely resembles that of the already reported [Mo(η^3-allyl(6,6′-dmbipy)(CO)$_2$(NCS)].[21] In the anodic region, **1** undergoes a reversible largely metal-based 1e$^-$ oxidation to [Mo(η^3-allyl)(6,6′-dmbipy)(CO)$_2$Cl]$^+$ at $E_{1/2}$ = 0.16 V vs Fc/Fc$^+$. While in the cathodic region the complex undergoes a reversible bipy-based reduction (R1) at $E_{1/2}$ = -2.04 V (THF) or -2.03 V (PrCN) producing the radical anion, [Mo(η^3-allyl)(6,6′-dmbipy)(CO)$_2$Cl]$^{\bullet-}$ ([**1**]$^{\bullet-}$). Much like the NCS$^-$ progenitor, there is no evidence for the formation of the 5-coordinate anion, [Mo(η^3-allyl)(6,6′-dmbipy)(CO)$_2$]$^-$ ([**1**-A]$^-$) until the second, irreversible (R2) wave is passed at $E_{p,c}$ = -2.61 V (THF) or -2.60 V (PrCN). The oxidation of [**1**-A]$^-$ is then seen on the reverse anodic scan as a new anodic wave O1′ at $E_{p,a}$ = -1.74 V. The final detectable cathodic process in the THF electrolyte, R2′ at $E_{p,c}$ = -2.82 V (THF) or -2.79 V (PrCN), corresponds to the partly reversible reduction of the 5-coordinate anion to the 5-coordinate dianion, ([**1**-A]$^{2-}$). At low-temperature (195 K), the behavior is almost unchanged relative to the room temperature CV, although the R2′ wave becomes fully reversible and shifts slightly, appearing now at $E_{1/2}$ = -2.78 V (THF) or -2.83 V (PrCN).

In the anodic region, **2** also undergoes a reversible metal-based oxidation, to [**2**]$^+$ at $E_{1/2}$ = 0.06 V. The cathodic behavior of **2** strongly differs from that of **1**, as the initial reduction in THF is a totally irreversible, 2e$^-$ (ECE) process occurring at $E_{p,c}$ = -2.25 V (THF) or -2.14 V (PrCN). Compared to **1** in THF, this corresponds to a ca. 200 mV negative shift in the initial reduction potential, resulting from the increased electron density in the complex upon replacement of allyl with methallyl. A similar shift was observed following the replacement of bipy with dmbipy[21,47] (see also Chapter 5). The anodic wave O1′ assigned to the oxidation of the 5-coordinate anion [**2**-A]$^-$ is observed at $E_{p,a}$ = -1.83 V (THF) or -1.71 V (PrCN) on the reverse scan started directly beyond R1. There is only one other detectable cathodic wave, R2′, which is also shifted to the more negative potential of $E_{p,c}$ = -2.98 V (THF) or -2.89 V (PrCN) and corresponds to 1e$^-$ reduction of [**2**-A]$^-$ formed at R2. This behavior resembles that of [Mo(η^3-allyl)(CO)$_2$(4,4′-dmbipy)(NCS)][21]; however, in this case there is no follow-up reduction of the dimer species [**2**-D] on the (sub)second CV

timescale (i.e., no R(D) wave is detected). This either means that the dimer is reduced at the same cathodic potential of the parent complex (R1), cf. [Mn(iPr-dab)$(CO)_3$Br][23]; or that the ultimate dimerization reaction (ECEC) is inhibited or to slow on the CV timescale to be observed. The first option seems unlikely given the large (almost 500 mV) separation between R1 and R(D) determined from the closely related complexes with the 4,4′ and 5,5′-dmbipy ligands.[21] At T = 195 K, the initial R1 wave of **2** becomes fully reversible, with $E_{1/2}$ = -2.02 V (THF) or -2.07 V (PrCN). The subsequent wave, R2, is detected at $E_{p,c}$ = -2.60 V (THF) and -2.66 V (PrCN), corresponds to the irreversible reduction of stable $[\mathbf{2}]^{\bullet-}$ yielding the 5-coordinate anion, [**2**-A]$^-$. The latter reduces again to the corresponding 5-coordinate dianion at R2′, lying at $E_{1/2}$ = -2.82 V (THF) and -2.90 V (PrCN).

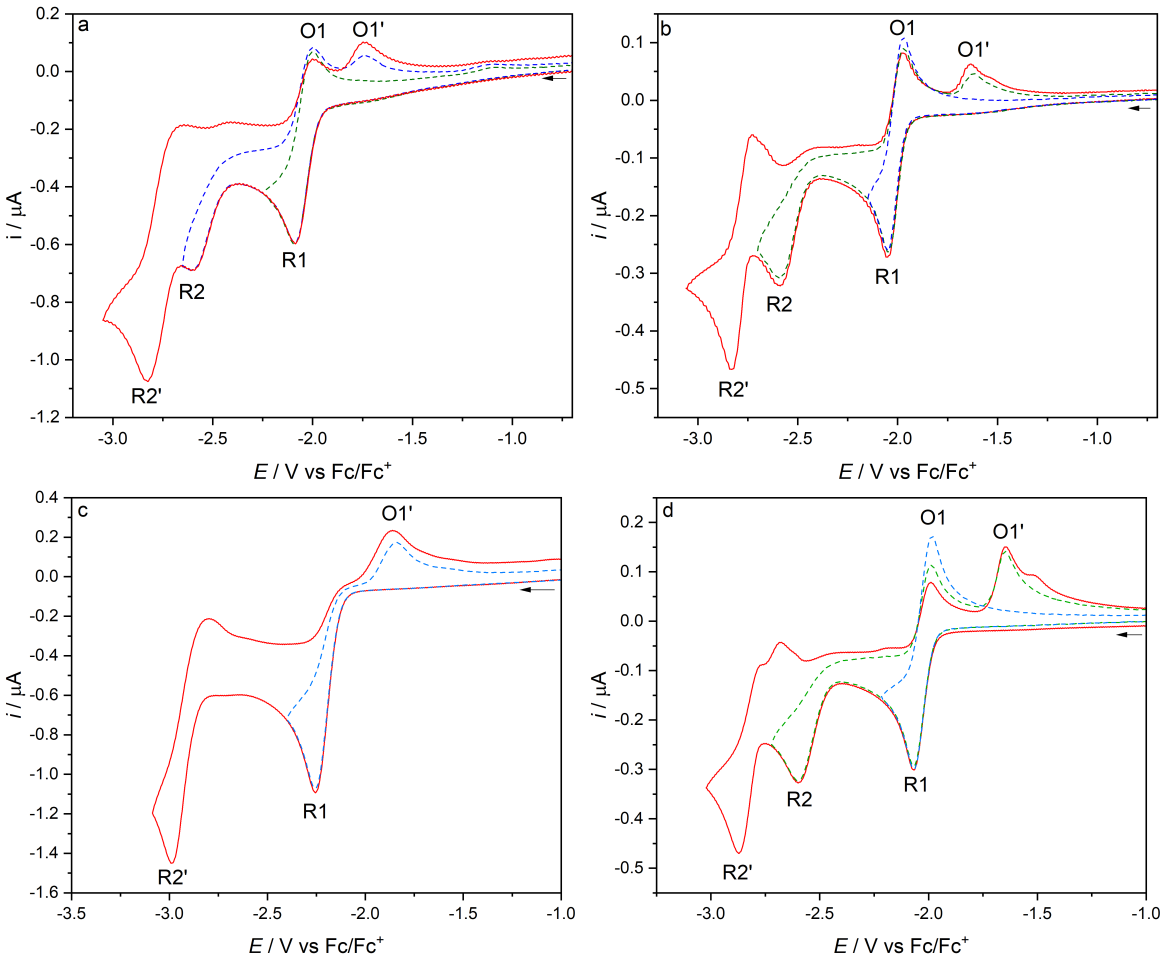

Figure 6.2: Cyclic voltammograms of complex **1** at 298 K (a) or 195 K (b) and complex **2** at 298 K (c) or 195 K (d) in THF/Bu_4NPF_6. The arrow indicates the initial scan direction. Conditions: Pt microdisc electrode, υ = 100 mV s^{-1}.

Finally, also complex **3** undergoes a reversible metal-centered oxidation to $[\mathbf{3}]^+$ at $E_{1/2}$ = 0.05 V vs Fc/Fc^+ testifying to the donor power of the methallyl and Cl^- ligands, capable of stabilizing the Mo(III) oxidation state, despite significantly increased π-acceptor capacity of the pTol-bian ligand (an electron sponge), compared to 6,6′-dmbipy. This anodic behavior is quite remarkable when compared with closely related reference systems[20] such as [Mo(η^3-allyl)(2,6-bis(xylyl)-bian)$(CO)_2$(NCS)] that becomes irreversibly oxidised at ca. 0.6 V vs Fc/Fc^+, a positive shift of more than 500 mV.[20] In the cathodic region, **3** is reversibly reduced to $[\mathbf{3}]^{\bullet-}$ at much less negative potentials than either **1** or **2**, viz. $E_{1/2}$ = -1.34 V (THF) and -1.32 V (PrCN). This marked stabilization of the LUMO of **3** is fully

consistent with the increased π-accepting capacity of the pTol-bian ligand. However, this cathodic potential is still more negative than determined for the above reference Mo-allyl-bian system that is reversibly reduced already at $E_{1/2}$ = -1.16 V (THF). The radical anion $[\mathbf{3}]^{\bullet-}$ is further reduced at R2, which at room temperature is at $E_{p,c}$ = -1.91 V (THF) and is only poorly seen in PrCN at -1.93 V, likely converting to the 6-coordinate solvento anion, [Mo(η^3-methallyl)(pTol-bian)$(CO)_2$(Sv)] (Sv = THF, PrCN), [**3**-Sv]$^-$.[20] This assignment is supported by the larger potential separation between R2′ and R2, compared to either complex **1** or **2**. Another piece of evidence is the absent anodic wave O1′ due to oxidation of the 5-coordinate anion [**3**-A]$^-$ on the reverse anodic scan at 298 K (Figure 6.3). The subsequent cathodic wave R2′ at $E_{p,c}$ = -2.80 V (THF) or -2.81 V (PrCN) is followed by another one at $E_{p,c}$ = -3.01 V (THF) or -2.97 V (PrCN) likely correspond to reduction of the 5-coordinate [**3**-A]$^-$ and 6-coordinate [**3**-Sv]$^-$. This assignment without the IR SEC support is, however, speculative.

At T = 195 K, the cathodic CV of **3** closely resembles the course recorded for **1** and **2**. Several changes are apparent in comparison with the CV at room temperature. First, R1 adopts a totally reversible shape comparable with the internal ferrocene standard. Second, the irreversible wave R2 due to $[\mathbf{3}]^{\bullet-}$ shifts slightly negatively to -2.03 V (THF) or -1.91 V (PrCN) and becomes more pronounced. This cathodic step generates true 5-coordinate anion, [**3**-A]$^-$ that indeed oxidises on the reverse anodic scan at O1′, $E_{p,a}$ = -0.99 V (THF) or -1.03 V (PrCN); this wave was not seen at 298 K. It appears that the 5-coordinate anion [**3**-A]$^-$ is more stable at low temperature on the relatively short timescale of CV. If the reactivity of [**3**-A]$^-$ at ambient conditions is ascribed to the coordination of a donor-solvent molecule and transformation to 6-coordinate [**3**-Sv]$^-$, then this behavior is highly unusual because the solvento anions are generally more stable at low temperature. This implies that the reason for the diminished cathodic wave R2 for the reduction of $[\mathbf{3}]^{\bullet-}$ at 298 K may be different from ordinary coordination of the donor solvent to [**3**-A]$^-$ formed at R2 from highly reactive $[\mathbf{3}]^{2-}$ generated initially.

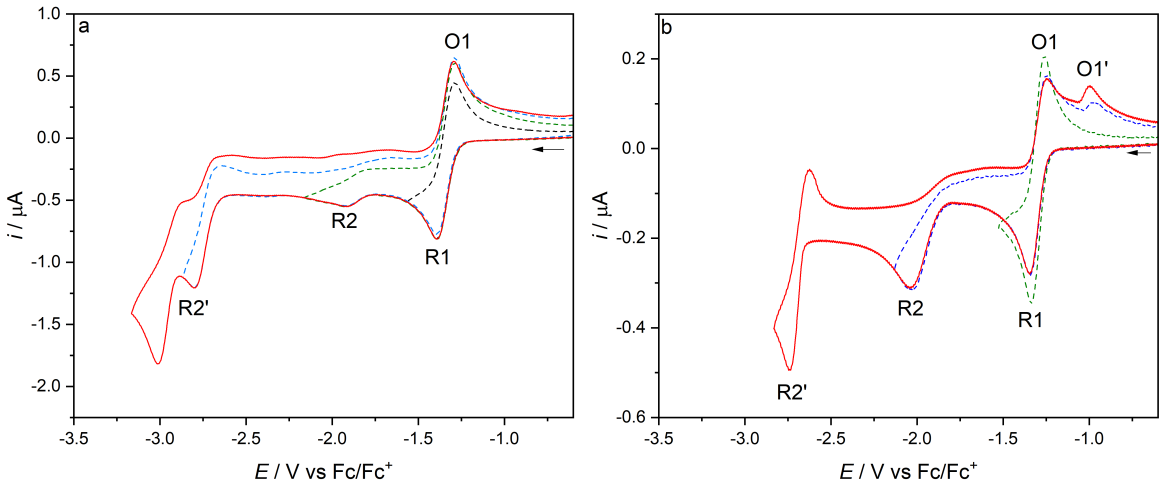

Figure 6.3: Cyclic voltammograms of complex **3** at 298 K (a) or 195 K (b) in THF/Bu_4NPF_6. The arrow indicates the initial scan direction. Conditions: Pt microdisc electrode, $\upsilon = 100$ mV s^{-1}.

6.4.3 Computational Studies

In addition to CV in the preceding section and IR SEC in the following section, **1**-**3** and their reduced forms have also been characterized with quantum chemical calculations. The initial $1e^-$ reduction (Scheme 6.1) leads to the corresponding radical anions, from the preceding CV studies, only $[\mathbf{1}]^{\bullet-}$ and $[\mathbf{3}]^{\bullet-}$ are stable under ambient conditions. The geometry-optimized structures (Table 6A.3, depicted in Figure 6.4 for **2** and in Figures 6A.4 and 6A.5 in the Appendix for **1** and **3**) reveal that, at the radical anionic level, all three complexes retain their preference for the less-strained equatorial isomer by 5.83 (**1**), 9.00 (**2**) and 2.39 kcal mol^{-1} (**3**). The dominant localization of the initial reduction at the α-diimine ligand is visualized predominantly by the shortening of the dmbipy C1 − C1′ bond (for example, from 1.481 to 1.433 Å in $[\mathbf{1}]^{\bullet-}$ and $[\mathbf{2}]^{\bullet-}$ and from 1.481 to 1.442 Å in $[\mathbf{3}]^{\bullet-}$).

As depicted in Figure 6.5 for **2** and Figures 6A.6-6A.7 (Appendix) for **1** and **3**, the HOMO of **1**-**3** is bonding between the metal, (meth)allyl and the π-acceptor carbonyls, but π-antibonding between the Mo center and the axial chloride ligand. Hence, the oxidation reaction described above transforms formally Mo(II) to Mo(III). Conversely, the LUMO and LUMO+1 are dominated by the electronic contribution from the dmbipy ligand (**1**-**2**) or the pTol-bian ligand (**3**), providing further evidence for the localization of the initial reduction.

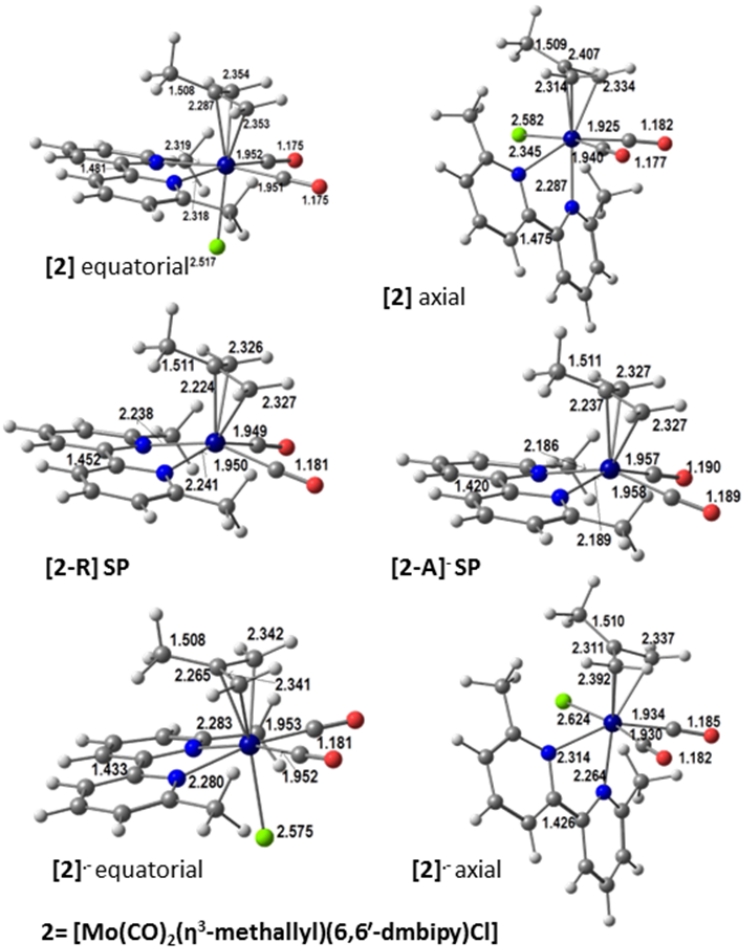

Figure 6.4: DFT-optimized structures of the parent complex [Mo(η^3-methallyl)(6,6′-dmbipy)$(CO)_2$Cl] (**2**) (the equatorial isomer (top left) and the axial isomer (top right)), $1e^-$ reduced radical anion $[\mathbf{2}]^{\bullet -}$ (bottom left, equatorial isomer, bottom right, axial isomer), 5-coordinate radical [**2**-R] (the SP isomer (center left), the TBP isomer (center right)) and $2e^-$ reduced 5-coordinate anion $[\mathbf{2}\text{-A}]^-$ (center right), with the relevant bond lengths (Å).

For **1** and **2** the calculated ν(CO) wavenumbers are practically identical (Table 6A.5). The absorption maxima of the IR ν(CO) symmetric modes for **1** and **2** reside at 1878 and 1879 cm^{-1}, respectively, while the absorption maxima for the antisymmetric modes fall at 1797 cm^{-1} in both cases. For **3** the calculated wavenumbers are somewhat higher, with the symmetric mode appearing at 1891 cm^{-1} and the antisymmetric one at 1821 cm^{-1}. The higher wavenumbers are reflecting the increased π-acceptor character of pTol-bian. A scaling factor of 0.97 must be applied in order to reproduce the experimental values. For **1**, the experimental wavenumbers are 1945 and 1861 cm^{-1}: application of the 0.97 scaling

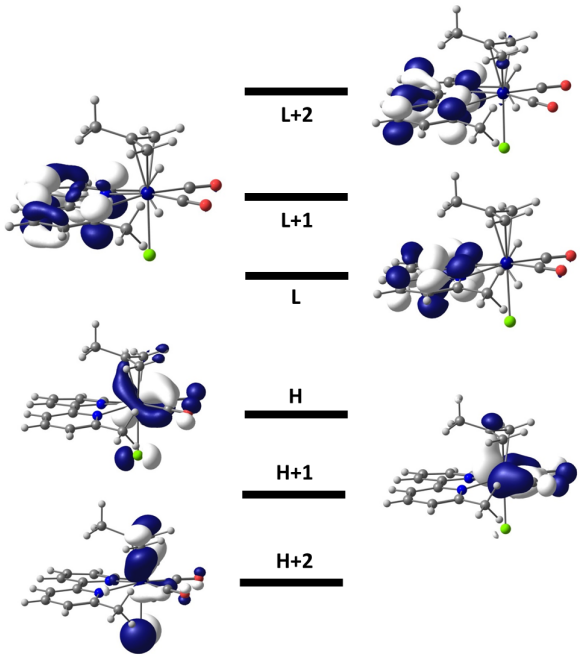

Figure 6.5: DFT-calculated frontier orbitals of the parent complex [Mo(η^3-methallyl)(6,6′-dmbipy)$(CO)_2$Cl] (**2**). The HOMO-LUMO (H-L) gap is 1.629 eV.

factor converts these to 1886 and 1805 cm^{-1} - in good agreement with the calculated values.

Loss of the chloride ligand from the initial 6-coordinate radical anion affords a 5-coordinate radical [**X**-R], which in principle may adopt either a square planar (SP) or trigonal bipyramid (TBP) geometry.[21] In these cases, however, the SP geometry is enforced by the more sterically demanding substituents. For least strained [**1**-R], the SP geometry is preferred by 1.56 kcal mol^{-1}. In comparison, after the optimization using TBP geometry, for [**2**-R] and [**3**-R], the structure either converged to a SP geometry (for [**2**-R]) or would not converge at all (for [**3**-R]). The somewhat longer C−C′ inter-ring bonds and somewhat shorter Mo−C(allyl) bonds in [**X**-R] compared to $[\mathbf{X}]^{\bullet-}$ are the result of a higher degree of π-delocalization over the complex upon the loss of the chloride ligand.

Direct reduction of the 5-coordinate radicals affords the perceived active $2e^-$ catalysts for these systems, the 5-coordinate anions, $[\mathbf{X}\text{-A}]^-$. These may exist in either a closed-shell singlet (diamagnetic) or an open-shell triplet (paramagnetic) state. As in the previous cases,[21] the former state is more stable by a high margin, 16.48 (**1**), 19.17 (**2**) and 11.77

kcal mol^{-1} (**3**). All the 5-coordinate anions modelled in this study adopt a SP geometry.

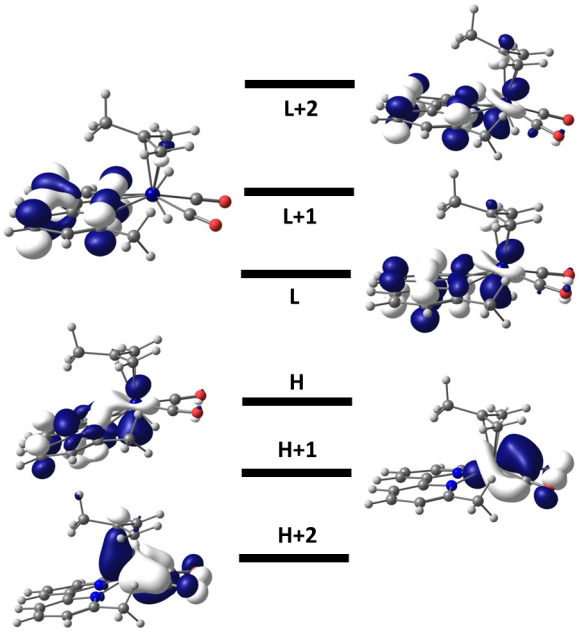

Figure 6.6: DFT-calculated, strongly Mo-dmbipy π-delocalized frontier orbitals of the 5-coordinate anion [Mo(η^3-methallyl)(6,6′-dmbipy)(CO)$_2$]$^-$ (**2**). The HOMO-LUMO (H-L) gap is 1.265 eV.

Upon reaching the 1e$^-$ reduction that forms the radical anions [**X**]$^{\bullet-}$, the calculated IR ν(CO) wavenumbers for the symmetric mode shift by 26-33 cm^{-1}, while for the shifts for the antisymmetric mode are some what larger, ranging from 36 to 63 cm^{-1}. For the 6,6′-dmbipy complexes **1** and **2**, the loss of the chloride ligand from the radical anions, forming the 5-coordinate radicals [**X**-R], has an almost negligible impact on the calculated wavenumbers; the origin of this phenomenon has already been discussed in Chapter 5. A more dramatic effect is calculated on proceeding from [**X**-R] to the 2e$^-$ reduced 5-coordinate anions, [**1**-A]$^-$ and [**2**-A]$^-$, with a red shift exceeding 55 cm^{-1}. The strong impact of the second added electron is, consistent with the highly π-delocalized nature of the Mo-bipy bonding in these 5-coordinate anions. The calculated frontier orbitals are depicted in Figure 6.6 for [**2**-A]$^-$ and Figures 6A.8 (Appendix) for [**1**-A]$^-$. For both electron-rich, formally 16 VE compounds they reproduce the characteristic bonding situation in this this family; intense π-delocalization over the complex, in particular the dicarbonyl Mo-dmbipy unit for both the HOMO and LUMO, consistent with the dramatic red shift observed for both the calculated

and experimental IR ν(CO) wavenumbers.

The bonding situation in 5-coordinate anion [**3**-A]$^-$ is notably different in comparison to π-delocalized [**2**-A]$^-$, as shown in Figure 6A.9 (Appendix). The LUMO of [**3**-A]$^-$ is almost exclusively (92 %) localized on the pTol-bian ligand. Surprisingly, this also applies for the HOMO of [**3**-A]$^-$ where the MO center contributes less (19 %) than determined for the HOMO of [**2**-A]$^-$ (29 %). The theoretical data actually reveals that the added two electrons reside more on the pTol-bian ligand than the Mo center. This explains the smaller ν(CO) red shift of ca. 41 and 47 cm^{-1} on going from [**3**-R] to [**3**-A]$^-$ than the 47/57 cm^{-1} calculated for the corresponding 6,6′-dmbipy complexes (Table 6A.5). It is therefore not surprising that the electron-deficient MO center in 16 VE [**3**-A]$^-$ tends to bind a donor solvent molecule, converting to 6-coordinate [**3**-Sv]$^-$ characterised by much larger ν(CO) wavenumbers (Table 6.2), as revealed by the IR SEC experiments presented in the next section and previously reported[20] for the 2e$^-$ cathodic path of the closely related complex [Mo(η^3-allyl)(2,6-bis(xylyl)-bian)(CO)$_2$(NCS)]. The HOMO-LUMO electronic transition in 5-coordinate [**3**-A]$^-$ exhibits an unusual ILET/MLCT character, remarkably different from the strongly delocalized π-π^* (Mo-dmbipy) character in [**2**-A]$^-$.

6.4.4 IR Spectroelectrochemistry at Variable Temperature

IR spectroelectrochemistry has proven an invaluable tool for unravelling the mechanistic details of different cathodic paths. The data presented in this section is applied again to support the major insights gained from the cyclic voltammograms in Section 6.4.2. The IR ν(CO) absorption data recorded for parent **1**-**3**, their reduction products and key reference compounds are summarised in Table 6.2.

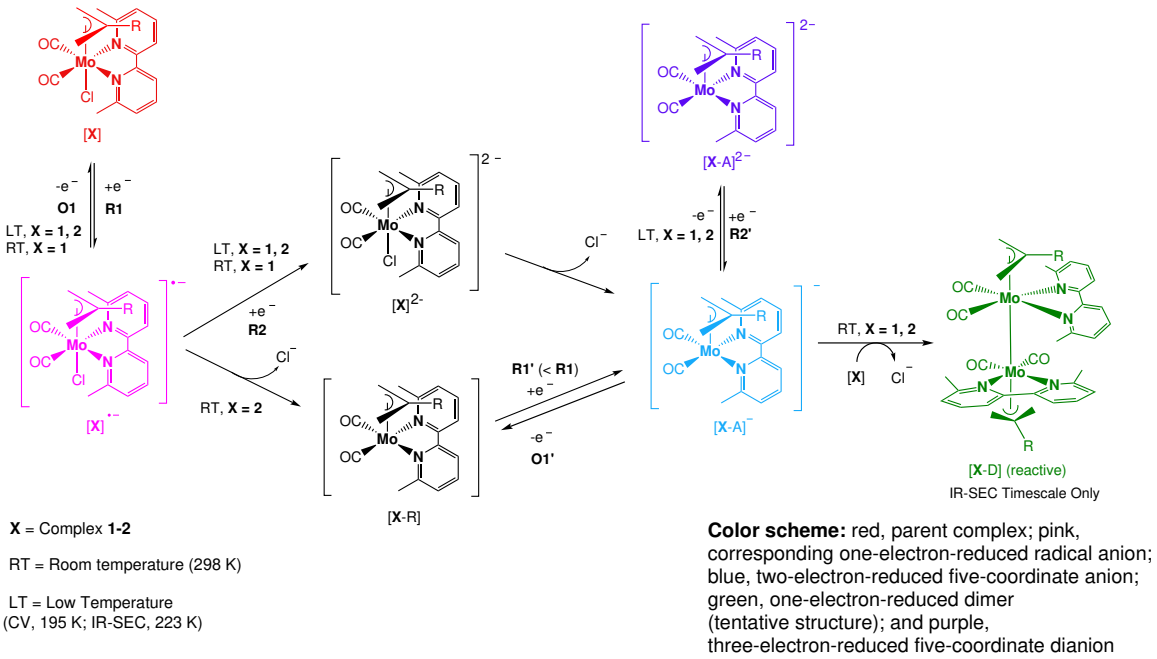

Scheme 6.1: General cathodic pathways of the studied complexes, [Mo(η^3-allyl)(6,6′-dmbipy)(CO)$_2$Cl], **1**, and [Mo(η^3-methallyl)(6,6′-dmbipy)(CO)$_2$Cl], **2**, based on the evidence from cyclic voltammetry (CV) and IR spectroelectrochemistry (IR SEC).

It is useful to begin the discussion with the cathodic paths of **1**-**3** determined at low temperature, as these results are the most straightforward to consider. Reducing **1** (ν(CO): 1940, 1854 cm^{-1}) at a potential coinciding with R1 in PrCN at 223 K (Figure 6.7), results in the conversion of the parent complex to a mixture of two products absorbing in the ν(CO) region. Based on comparison with reference complexes, these are assigned as the (partly stabilized) primary radical anion, [**1**]$^{\bullet-}$ (ν(CO): 1916, 1821 cm^{-1}) and the 2e$^-$ reduced 5-coordinate anion (ECE), [**1**-A]$^-$ (ν(CO): 1797, 1700 cm^{-1}). The former 1e$^-$ dmbipy-reduced complex is assigned based on the characteristic red shift of ν(CO) by ca. 30 cm^{-1} from the parent stretching frequencies. The wavenumber values of the latter are consistent with the characteristic electron-rich, M-diimine π-delocalized structures of many 5-coordinate anions, such as [Re(bipy)(CO)$_3$]$^-$[4,48] and are also identical with those recorded for the 5-coordinate anion derived from the corresponding parent complex bearing the NCS$^-$ axial ligand[21], see Table 5.2 (Chapter 5). Differently from [Mo(η^3-allyl)(6,6′-dmbipy)(CO)$_2$(NCS)]$^{\bullet-}$, the radical anion [**1**]$^{\bullet-}$ is not stable on the SEC timescale even at the reduced temperature, despite

the fully reversible R1 wave in the cyclic voltammogram, no doubt as a consequence of the increased π-donation from the Cl^- ligand that is less tunable than NCS^- in Mo=N=C=S.

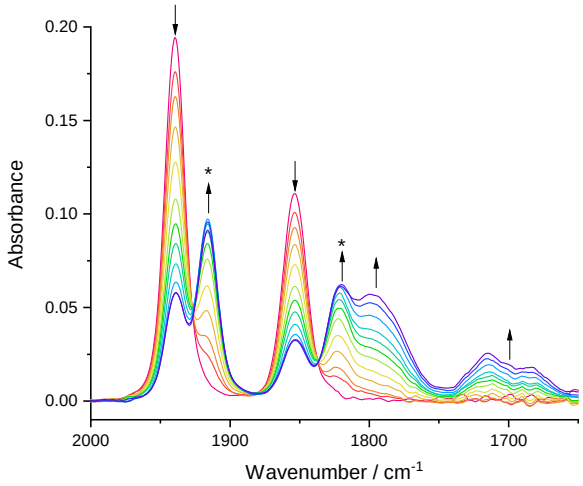

Figure 6.7: IR SEC monitoring of the reduction of [Mo(η^3-allyl)(6,6′-dmbipy)$(CO)_2$Cl], **1** (↓) at R1 to yield $[\mathbf{1}]^{\bullet-}$ (*), and 5-coordinate [**1**-A]$^-$ as the ultimate secondary product. (↑). Conditions: a cryostatted OTTLE cell, PrCN/Bu_4NPF_6, T = 223 K.

In contrast, reducing **2** at the cathodic wave R1 under the same low-temperature conditions (Figure 6.8) results in the conversion of the parent complex to just a single species, the 5-coordinate anion, [Mo(η^3-methallyl)(6,6′-dmbipy)$(CO)_2]^-$ [**2**-A]$^-$ with slightly smaller ν(CO) wavenumbers of 1782, 1683 cm^{-1}, compared with those of [**1**-A]$^-$, which reflects the increased electron density due to the *meso*-C methyl substituent at the methallyl ligand. This factor certainly impacts the CO ligands more strongly in [**2**-A]$^-$ than the parent complex due to the strongly delocalized nature of the π-bonding in the 5-coordinate anion (see the preceding section). These two IR SEC results comply with the CV behavior presented in Section 6.4.2, clearly confirming that the substitution on the allyl group significantly destabilizes the $1e^-$ reduced intermediate; at low temperature this results in the rapid formation of the stable 5-coordinate anion [**2**-A]$^-$ via [**2**-R] already at R1. The situation in the thin-solution layer of the OTTLE cell at ambient temperature, however, is not that simple, as will be shown in the next section.

Table 6.2: IR ν(CO) absorption data for complexes **1**-**3**, and their reduction products (cf. Scheme 6.1). Key reference compounds are included as well.

	ν(CO)/ cm^{-1}		ν(CN)/ cm^{-1}	
Complex	Exp	DFT	Exp	DFT
[Mo(η^3-allyl)(6,6′-dmbipy)(CO)$_2$(NCS)][a,b,c]	1944, 1860	-	2082	-
[Mo(η^3-allyl)(6,6′-dmbipy)(CO)$_2$(NCS)][c,d]	1948, 1866	1881, 1800	2074	2054
[Mo(η^3-allyl)(6,6′-dmbipy)(CO)$_2$Cl][d]	1945, 1861	1878, 1797	-	-
[Mo(η^3-allyl)(6,6′-dmbipy)(CO)$_2$Cl][a,b]	1940, 1854	-	-	-
[Mo(η^3-methallyl)(6,6′-dmbipy)(CO)$_2$Cl][d]	1944, 1861	1879, 1797	-	-
[Mo(η^3-methallyl)(6,6′-dmbipy)(CO)$_2$Cl][d,e]	1943, 1859	-	-	-
[Mo(η^3-methallyl)(6,6′-dmbipy)(CO)$_2$Cl][a,b]	1940, 1853	-	-	-
[Mo(η^3-methallyl)(pTol-bian)(CO)$_2$Cl][d]	1956, 1886	1891, 1821	-	-
[Mo(η^3-methallyl)(pTol-bian)(CO)$_2$Cl][a,b]	1948, 1866	-	-	-
[Mo(η^3-allyl)(6,6′-dmbipy)(CO)$_2$Cl]$^{+}$[d]	2053, 2000	-	-	-
[Mo(η^3-methallyl)(6,6′-dmbipy)(CO)$_2$Cl]$^{+}$[d]	2053, 2000	-	-	-
[Mo(η^3-methallyl)(pTol-bian)(CO)$_2$Cl]$^{+}$[d]	2061, 2009	-	-	-
[Mo(η^3-allyl)(6,6′-dmbipy)(CO)$_2$(NCS)]$^{\bullet-}$[a,b,c]	1920, 1829	1855, 1764	2089	2069
[Mo(η^3-allyl)(6,6′-dmbipy)(CO)$_2$Cl]$^{\bullet-}$[a,b]	1916, 1821	1852, 1759	-	-
[Mo(η^3-methallyl)(pTol-bian)(CO)$_2$Cl]$^{\bullet-}$[a,b]	1928, 1836	1858, 1758	-	-
[Mo(η^3-allyl)(4,4′-dmbipy)(CO)$_2$]$_2$[d]	1891, 1766, 1759	1775, 1787, 1844, 1858	-	-
[Mo(η^3-allyl)(6,6′-dmbipy)(CO)$_2$]$_2$[d]	1887, 1763, 1742	1855, 1847, 1782, 1778	-	-
[Mo(η^3-methallyl)(6,6′-dmbipy)(CO)$_2$]$_2$[d]	1887, 1766, 1744	1855, 1847, 1782, 1778	-	-
[Mo(η^3-allyl)(6,6′-dmbipy)(CO)$_2$]$^{-}$[a,b]	1797, 1700[f]	1803, 1702[g]	-	-
[Mo(η^3-allyl)(6,6′-dmbipy)(CO)$_2$]$^{-}$[d]	1795, 1720	-	-	-
[Mo(η^3-methallyl)(6,6′-dmbipy)(CO)$_2$]$^{-}$[a,b]	1782, 1683[f]	-	-	-
[Mo(η^3-methallyl)(6,6′-dmbipy)(CO)$_2$]$^{-}$[d,e]	1784, 1683	1801, 1704	-	-
[Mo(η^3-methallyl)(6,6′-dmbipy)(CO)$_2$]$^{-}$[d]	1792, 1714	-	-	-
[Mo(η^3-allyl)(4,4′-dmbipy)(CO)$_2$(PrCN)]$^{-}$[c]	1896, 1797	1797, 1705	-	-
[Mo(η^3-methallyl)(pTol-bian)(CO)$_2$(PrCN)]$^{-}$[a,b]	1890, 1793	-	-	-
[Mo(η^3-methallyl)(pTol-bian)(CO)$_2$(THF)]$^{-}$[d]	1897, 1800	1827, 1734[h]	-	-

[a] Measured in PrCN. [b] Measured at 223 K. [c] Reproduced from ref[21].[d] Measured in THF.[e] Measured at 268 K. [f] Broad absorption bands. [g] Derived from the equatorial isomer. [h] Calculated with DFT as a pure 5-coordinate structure, which explains the much smaller wavenumbers compared to the experimental IR SEC data.

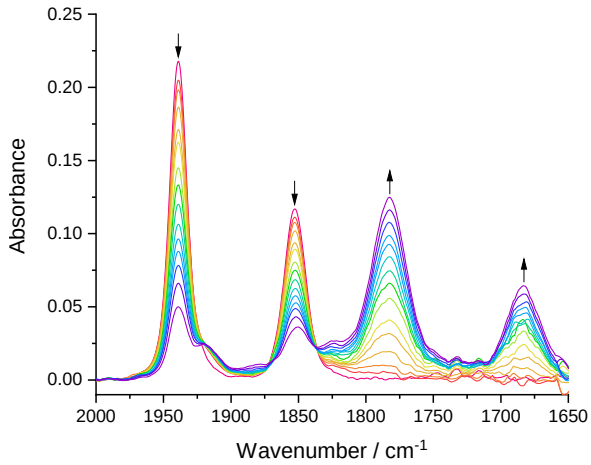

Figure 6.8: IR SEC monitoring of the overall $2e^-$ reduction of [Mo(η^3-methallyl)(6,6′-dmbipy)$(CO)_2$Cl], **2** (↓) at R1 to the 5-coordinate anion, [**2**-A]$^-$ (↑). Conditions: a cryostatted OTTLE cell, PrCN/Bu_4NPF_6, T = 223 K.

Perhaps most surprising in the series is the cathodic behavior of **3** (ν(CO): 1951, 1876 cm^{-1}) under the same low-temperature conditions (Figure 6.9). One would expect, based on CV results and the choice of a strongly π-accepting bian ligand, that the corresponding radical anion, [**3**]$^{\bullet-}$ persists in the electrolyte at low temperature. However, the initial reduction at R1 generated a mixture of two species absorbing in the ν(CO) region, akin to **1**. Compared with the reference complexes (Table 6.2) they can be assigned as the remaining radical anion (ν(CO): 1925, 1836 cm^{-1}) and the secondary product, the 6-coordinate solvent anion, [**3**-PrCN]$^-$ (ν(CO): 1890, 1793 cm^{-1}). On the longer SEC timescale, the low temperature set in the cryostatted OTTLE cell is apparently insufficient to stabilize the radical anion completely. The reason for this behavior most likely stems from the cooperative donor effect of the alternative Cl$^-$ ligand, and the already documented, cf. **1** vs **2**, destabilizing influence of the additional, allylic, methyl group. Considering that [Mo(η^3-allyl)(2,6-bis(xylyl)-bian)$(CO)_2$(NCS)] showed perfectly stable radical anion already at room temperature[20], it is quite surprising that this radical anion is not stable even at low temperature. Obviously, the strong coordinating capacity of the PrCN solvent must not be forgotten. On the other hand, the cyclic voltammetric study of **3** documented that the reduction of [**3**]$^{\bullet-}$ at R2 generates the 5-coordinate anion [**3**-A]$^-$. At R1 the solvento anion [**3**-PrCN]$^-$ is most

likely formed from the equilibrium between $[\mathbf{3}]^{\bullet-}$ and $[\mathbf{3}\text{-PrCN}]^{\bullet}$, the latter being reducible at R1 to $[\mathbf{3}\text{-PrCN}]^{-}$. Such cathodic behavior is known for example for $[Re(bipy)(CO)_3Cl]$ in PrCN.[4]

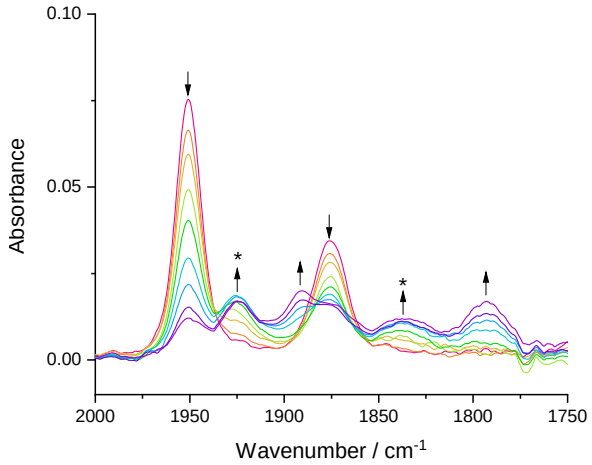

Figure 6.9: IR SEC monitoring of the reduction of 2 mM [Mo(η^3-methallyl)(pTol-bian)$(CO)_2$Cl], **3** (↓) at R1, resulting in a mixture of $[\mathbf{3}]^{\bullet-}$ (*) and 6-coordinate anion, $[\mathbf{3}\text{-PrCN}]^{-}$ (↑). Conditions: a cryostatted OTTLE cell, PrCN/Bu_4NPF_6, T = 223 K.

6.4.5 IR Spectroelectrochemistry at Ambient Temperature

In line with the ordinary reversible anodic cyclic voltammetric scans (Section 6.4.2), Mo-methallyl complexes, **2** (Figure 6A.10b, Appendix) and **3** (Figure 6.10) are both oxidised on the longer SEC timescale to corresponding, stable, formally Mo(III) cationic products. On the other hand, $[\mathbf{1}]^{+}$ is unstable at room temperature (Figure 6A.10a, Appendix) and slowly decomposes (decarbonylates) during the electrolysis. The accompanying shifts of the ν(CO) bands (summarized in Table 6.2) to larger wavenumbers are significant. They comply with the depopulation of the largely Cl-Mo-based HOMO of the parent complexes (Figure 6.5 and Figures 6A.6-6A.7, Appendix), having the expected large impact on the degree of CO π-back-donation, that becomes strongly reduced in the formally Mo(III) products. It is truly remarkable, that even complex **3** is reversibly oxidised on the SEC timescale. Apparently the axial Cl^{-} and meth(allyl) ligands play the key role, in determining the stability, sufficiently compensating the replacement of donor 6,6′-dmbipy in **2** with acceptor pTol-bian in **3**. It is however the dominant effect of the methallyl ligand that decides, as revealed by the marked

difference in the stability of $[\mathbf{1}]^+$ and $[\mathbf{2}]^+$ compared to equatorial α-diimine ligand in the energy of the HOMO.

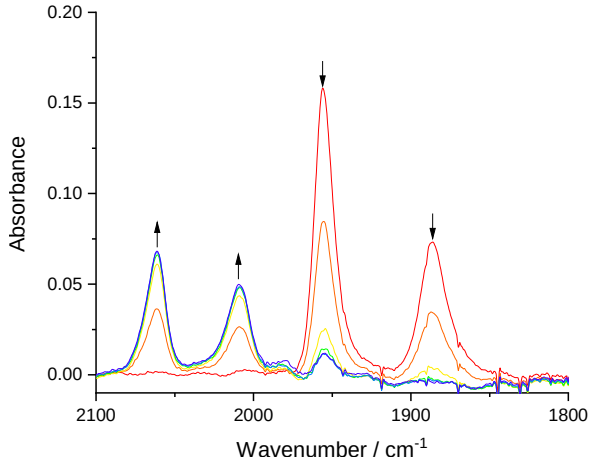

Figure 6.10: IR SEC monitoring of the 1e$^-$ oxidation of [Mo(η^3-methallyl)(pTol-bian)$(CO)_2$Cl], **3** (↓) at to the stable cationic complex, [Mo(η^3-methallyl)(pTol-bian)$(CO)_2$Cl]$^+$ $[\mathbf{3}]^+$ (↑). Conditions: an OTTLE cell, THF/Bu_4NPF_6, $T = 298$ K.

Conducting IR SEC in the cathodic region at ambient temperature in THF/Bu_4NPF_6 reveals additional complexity in the cathodic path of **1** and **2** compared to the straightforward cathodic behavior seen at 223 K (see preceding section). The reduction of **1** at R1 (Figure 6.11) leads to a mixture of products, a very minor component of which is radical anion $[\mathbf{1}]^{\bullet-}$. Initially the mixture contains two major products that can be identified from their ν(CO) stretching wavenumbers. The first reduced compound displays more than 2 ν(CO) bands and, based on the comparison with relevant reference systems[21] it can only be assigned as the dimer: [Mo(η^3-allyl)(6,6′-dmbipy)$(CO)_2]_2$, [**1**-D] (ν(CO): 1887, 1760, 1738 cm^{-1}). Further, the DFT-calculated wavenumbers for [**1**-D] are in good agreement with the experimental data (Table 6.2). The second detectable reduced species is assigned as the 5-coordinate anion, $[\mathbf{1}\text{-A}]^-$ (ν(CO): 1795, 1720). The wavenumbers of the asymmetric stretch is slightly larger than reported in the chilled PrCN electrolyte (Table 6.2), indicating that $[\mathbf{1}\text{-A}]^-$ forms a weak adduct with THF. The dimer is reactive[21] (see also Chapter 5), and is further reduced in the course of the SEC experiment but not to the 5-coordinate anion, as is the case for other metal-metal bound dimers such as $[Mn(bipy)(CO)_3]_2$ resulting from a similar ECEC cathodic route.[8] Instead, the follow up cathodic step converts [**1**-D] to its

1e$^-$ reduced form. Evidence for this assignment is embodied in the preserved ν(CO) pattern of [**1**-D]$^-$ (ν(CO): 1844, 1710, 1700 cm^{-1}). The exact structure of the dimer remains to be resolved, presenting a challenge for preparative electrochemistry. Although we can reasonably assume that [**1**-D] closely resembles other (α-diimine)M-M(α-diimine) bound dimers, it is worth noting that also other structures are known for dimers derived from these types of complexes.[49]

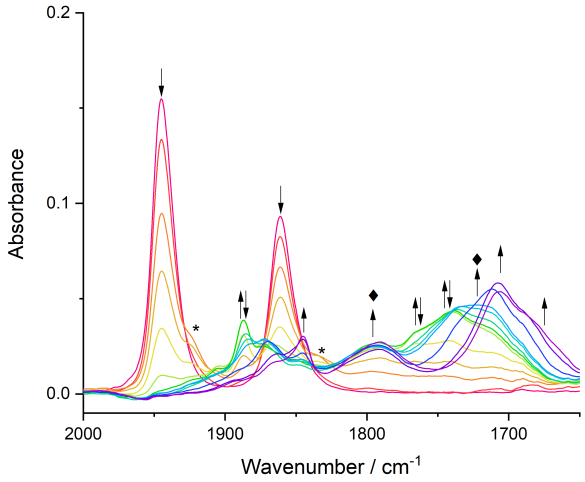

Figure 6.11: IR SEC monitoring of the reduction of [Mo(η^3-allyl)(6,6′-dmbipy)(CO)$_2$Cl], **1** (↓) at R1 generating a mixture of [Mo(η^3-allyl)(6,6′-dmbipy)(CO)$_2$]$_2$ [**1**-D] (↑↓) and [Mo(η^3-allyl)(6,6′-dmbipy)(CO)$_2$]$^-$ (♦). The subsequent 1e$^-$ reduction of [**1**-D] to [**1**-D]$^-$ (↑) is also shown. The asterix* indicates the absorption of [**1**]$^{\bullet-}$ present as a minor intermediate product. Conditions: an OTTLE cell, THF/Bu$_4$NPF$_6$, T = 298 K.

The reduction of **2** (Figure 6.12) under these conditions (THF, under argon, room temperature) proceeds in a very similar fashion as described above for **1**. The cathodic step R1 (Table 6.1) is irreversible, leading to a mixture of products again. Importantly, the ν(CO) absorption belonging to the radical anion, [**2**]$^{\bullet-}$ does not appear, proving the increased reactivity of the primary reduction product. The dominant component of the mixture is dimer [**2**-D] (ν(CO): 1887, 1766, 1743) and its 1e$^-$ reduced form [**2**-D]$^-$ (ν(CO): 1845, 1706, 1681), but 5-coordinate anion [**2**-A]$^-$ (ν(CO): 1793, 1720; again, as a weak adduct with THF) is also detected in higher concentration than [**1**-A]$^-$, reflecting the sluggish dimerization reaction, consistent with the absent R(D) wave in the conventional CV of **2** (see Figure 6.2c and accompanying discussion). The cathodic paths of **1** and **2** are very

similar to that followed by related [Mo(η^3-allyl)(CO)$_2$(5,5′-dmbipy)(NCS)], where such a mixture of products was also observed.[21] Conducting the reduction of **2** again in chilled (T = 255 K) THF electrolyte (Figure 6A.11, Appendix) is sufficient to once again observe the [**2**-A]$^-$ as the dominant cathodic product.

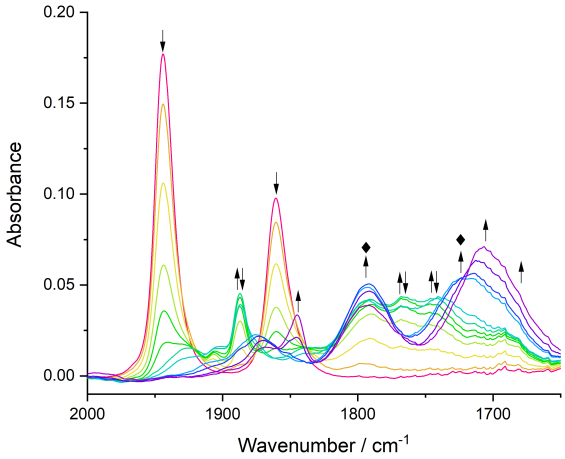

Figure 6.12: IR SEC monitoring of the reduction of [Mo(η^3-methallyl)(6,6′-dmbipy)(CO)$_2$Cl], **2** (↓) at R1 to [Mo(η^3-methallyl)(6,6′-dmbipy)(CO)$_2$]$_2$ [**2**-D] (↑↓) and the 5-coordinate anion, [**2**-A]$^-$ as a weak adduct with THF (♦). The subsequent reduction of [**2**-D] to [**2**-D]$^-$ (↑) is also seen. Conditions: an OTTLE cell, THF/Bu_4NPF_6, T = 298 K.

Conveniently, the reduction of **3** in THF at ambient temperature, depicted in Figure 6.13, exhibits similar cathodic behavior as encountered for this complex in PrCN at low temperature. The initial reduction at R1 produces once more unstable radical anion [**3**]$^{\bullet -}$, transforming to the solvated 6-coordinate anion, [**3**-THF]$^-$ (ν(CO): 1897, 1800 cm^{-1}). No dimer [**3**-D] was observed on the SEC timescale. This can be a result of the steric hindrance from the bulky pTol-bian ligand destabilizing the dimer conformation. Another alternative is the concerted transformation of [**3**]$^{\bullet -}$ to solvent radical [**3**-THF] reducible at R1 to [**3**-THF]$^-$, thereby preventing the dimerization step.

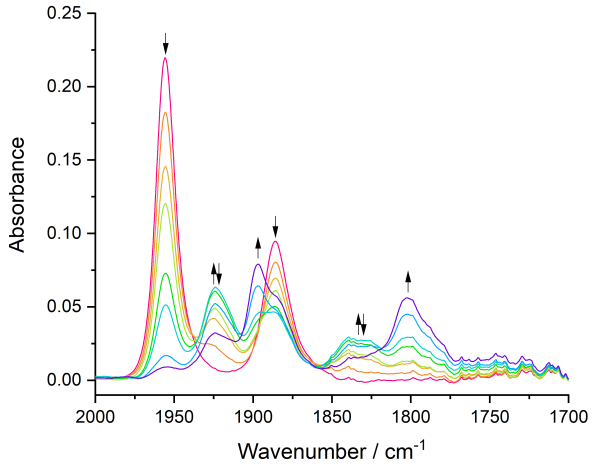

Figure 6.13: IR SEC monitoring of the reduction of [Mo(η^3-methallyl)(pTol-bian)$(CO)_2$Cl], **3** (↓) at R1 to $[\mathbf{3}]^{\bullet-}$ (↑↓) and 6-coordinate anion, $[\mathbf{3}\text{-THF}]^-$ in a redox equilibrium (↑). Conditions: a OTTLE cell, THF/Bu_4NPF_6, T = 298 K.

The appearance of dimer for [**1**-D] might be considered highly surprising, as results (CV, DFT, SEC) from the previous series [Mo(η^3-allyl)(x,x′-dmbipy)$(CO)_2$(NCS)] (x,x′ = 4-6), indicated that the most sterically demanding 6,6′-dmbipy ligand stabilized the 5-coordinate anion toward dimerization. From the results in this Chapter however, it is clear that the true story is more complicated. We expect the dimer must form as a result of a zero-electron coupling reaction between the 5-coordinate anion and the parent complex. Thus, the proclivity of the dimer formation is dependent on a number of factors. The first of which is the stability of the parent complex itself. If in the parent complex the Mo−X (X = Cl, NCS) bond is weaker, then it is simply more susceptible to this form of attack on the appropriate timescale, and the dimer therefore has a higher chance to form. We may reasonably conclude then that the Mo−Cl bond in **1** and **2** is weaker than the Mo−N(CS) bond in the reference structure, [Mo(η^3-allyl)(6,6′-dmbipy)$(CO)_2$(NCS)]. Secondly, the stability of the $1e^-$ reduced intermediate, i.e., the radical anions, $[\mathbf{1}]^{\bullet-}$ and $[\mathbf{2}]^{\bullet-}$, also plays a role. The more reactive Mo−Cl bond facilitates a larger amount of the 5-coordinate anions being available to react with the parent during the initial cathodic step, driving the reduction mechanism more along the pathway involving the dimer. This conclusion again underlines the need to determine the molecular structure of [**X**-D] and the exact mechanism of its formation. The cathodic pathways described in this study impact strongly the results uncovered during

cathodic experiments under the CO_2 atmosphere, presented in the next section.

6.4.6 Cyclic Voltammetry and IR Spectroelectrochemistry under a CO_2 Atmosphere

The CV studies of **1**-**3** in THF were repeated under the atmosphere of CO_2 (Figure 6.14) in order to probe for any catalytic activity of the detected 5-coordinate anions [**X**-A]$^-$ (**X** = **1** and **2**) toward the catalytic conversion of CO_2 to CO. For complex **1** the 1e$^-$ cathodic wave R1 (cf. Figure 6.2) remains unchanged, producing [**1**]$^{\bullet-}$ that remains stable on the CV timescale. However, a catalytic enhancement of the current is observed at the R2 wave, where the 5-coordinate anion is produced via the subsequent reduction of the radical anion. On the reverse anodic scan the wave O1′, which corresponds to the 5-coordinate anion reoxidation, is absent, confirming the rapid interaction of [**1**-A]$^-$ with CO_2. For complex **2**, the situation is different. Interestingly, a modest increase in the cathodic current is observed already at R1, which most likely corresponds to the catalytic reduction of CO_2 by [**2**-A]$^-$, that has already been identified as the dominant product at this wave on the CV timescale (Figure 6.2c). Correspondingly, the anodic counter wave O1′ is absent. However, the bulk of the catalytic current enhancement is not seen until slightly more negative potentials are reached, where a new quasi-reversible wave is detected, which may correspond to reduction of an unreactive intermediate such as a bicarbonate complex, encountered for instance for [Mn(mesityl-bipy)$(CO)_3$]$^-$ and [Mn(iPr-dab)$(CO)_3$]$^-$ catalysts.[24,50] Under the same conditions, **3** was not catalytically active toward the CO_2 substrate along the cathodic CV scan, which is consistent with previous observations on the poor catalytic performance of another Mo-bian complex.[20] Indeed, IR spectroelectrochemistry in the preceding section did not provide any evidence for the cathodic generation of 5-coordinate [**3**-A]$^-$

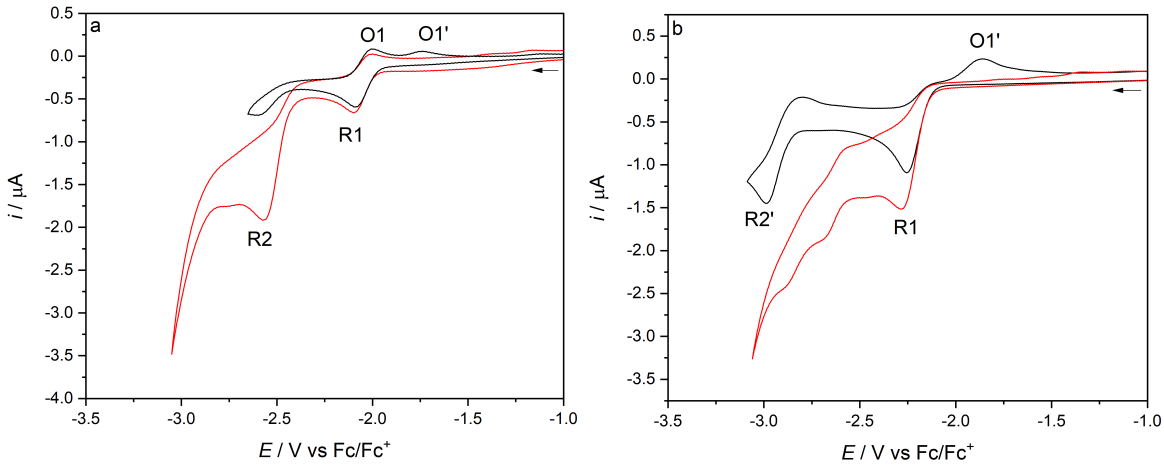

Figure 6.14: Cyclic voltammograms of complexes **1** (a) and 2 (b) in CO_2-saturated THF/Bu_4NPF_6. Conditions: Pt microdisc electrode, $\upsilon = 100$ mV s^{-1}, $T = 298$ K.

IR spectroelectrochemistry was conducted with **1** and **2** to analyse the reduction products in CO_2-saturated THF/Bu_4NPF_6. For both complexes the initial reduction at R1 triggers conversion to the inactive dimer (ν(CO): 1891, 1764, 1746), and some 5-coordinate anion interacting with CO_2 to give, 6-coordinate $[\mathbf{X}\text{-}CO_2]^-$ (ν(CO): 1810, 1720).[21] As the cathodic potential is swept more negatively, $[\mathbf{X}\text{-}CO_2]^-$ converts more toward the inactive dimer, which represents a deactivation route for these catalysts. A moderate catalytic conversion of CO_2 within the OTTLE cell is revealed during the cathodic scan, both by the decreasing reference $^{13}CO_2$ peak at 2275 cm^{-1} and the generation of free CO (supported by the accompanying absorption of subordinate bicarbonate at 1674 and 1649 cm^{-1}) and formate (1607 cm^{-1}).[51] It is hardly possible to claim from these spectroelectrochemical experiments whether there is any difference between **1** or **2** in terms of the catalytic ability. However, it is interesting to note the different behavior at the CV level, which complies with the differences in the cathodic paths of the complexes.

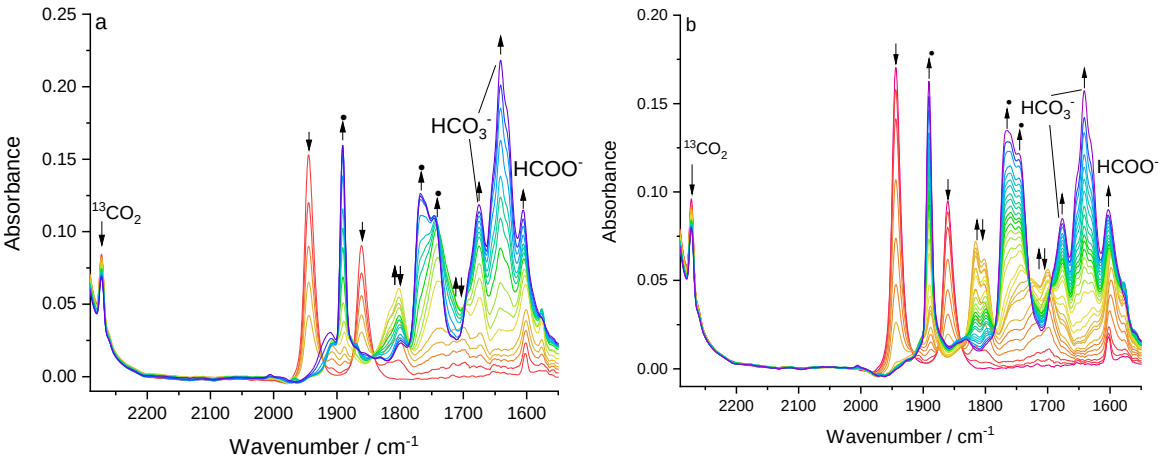

Figure 6.15: IR spectroelectrochemistry of **1** (a) and **2** (b) in CO_2-saturated THF/Bu_4NPF_6, showing the conversion of parent (↓) to 6-coordinate $[\mathbf{X}\text{-}CO_2]^-$ (↑↓) and its concomitant reduction to inactive dimer (•). Conditions: Pt microdisc electrode, $T = 298$ K.

6.5 Conclusions

The work presented in Chapter 6 strongly supports our ongoing efforts to characterize the fascinating redox reactivity of these Mo-allyl complexes. The study has resulted in several important discoveries. First of all, the interplay of steric and electronic effects between the various ligands is more complex than originally anticipated; it is also important to consider effects of different timescales, in order to fully appreciate the whole situation. For instance, the replacement of the NCS^- ligand with Cl^-, initially (when analysing the CV scans) did not seem to impact strongly the cathodic path. On the other hand, IR SEC has revealed that there is actually a strong impact on the room temperature stability of the $1e^-$ reduced radical anions the reactivity of the $2e^-$ reduced 5-coordinate anions toward the parent complexes, resulting in the detection of ultimate dimeric products. Differently from the dimethyl-bipy substitution in the 6,6′ position, the substitution at the *meso*-carbon of the allyl ligand results in strongly decreased stability of the primary reduced species towards the cleavage of the Mo−Cl bond. On the CV timescale, the substitution at the allyl ligand also hinders the formation of the inactive dimer (for 4,4′-dmbipy). Intended future studies may probe this effect more deeply, perhaps by increasing the steric demand of the axial allylic functionality (e.g., 1,1-dimethyl-allyl, which may, however, be to reactive) and also the α-diimine ligand

(i.e., bearing *t*Bu or Mes substituents). The new ligands studied in this work, Cl^- and methylallyl also effect the usually stabilizing influence of the R-bian ligand on the reduced species, resulting not only in a different parent molecular structure (A-type) compared to a majority of Mo-bian complexes, but also in an unstable radical anion (even at low temperature). In the near future, these observations will allow us to make some generalizations specifically for the Group-6 metals (mainly Mo, but also W) about the types of ligands that should be selected in order to promote the formation of the 5-coordinate catalyst. For **2** we obtained some indication that the catalysis may occur already at the R1 cathodic wave, which gives a good hope for tuning the properties of the complexes the right way, although the catalysis in the thin layer electrolyte is far from efficient (if nothing else than accumulating CO at the cathode). Now that we have a larger library of compounds to work from it remains a challenge in a follow-up study to characterize fully the issues surrounding the catalytic activity. In particular, the impact of added Brønsted or Lewis acids on the catalysis has yet to be investigated, and it also remains a challenge to chemically produce and characterize the intermediate or ultimate reduced species. Our efforts to explore the Group-6 catalysts are supported by ongoing investigations into the related $[Mo(CO)_4(\alpha\text{-diimine})]$ (α-diimine = R-substituted 2,2′-bipyridine, 1,4-di-R-1,4-diazabuta-1,3-diene) family, which shows quite unique and promising photo-electrocatalytic behavior.

6.6 Appendix to Chapter 6

Table 6A.1: Crystallographic data for **1**-**3**.

Complex	**1**	**2**	**3**
Formula	C17H17ClMoN2O2 [+CH2Cl2]	C18H19ClMoN2O2	C32H27ClMoN2O2
M_r	412.73[a]	426.75	602.97
Crystal System	monoclinic	monoclinic	triclinic
Space Group	$P2_1/n$	$P2_1/m$	*P-1*
Z	4	2	2
a/Å	10.562150(13)	8.035419(13)	9.82412(2)
b/Å	10.536079(13)	11.431569(18)	12.11344(2)
c/Å	17.448809(16)	9.600330(15)	12.88898(2)
α/°	90	90	74.449(3)
β/°	90	93.890(3)	70.667(3)
γ/°	90	90	68.437(4)
V/Å^3	1941.75	879.830(4)	1327.19(4)
ρ_{calc}/g cm^{-1}	1.702[a]	1.611	1.509
Radiation	Cu Kα	Cu Kα	Cu Kα
T/K	100	200	100
Crystal habit	Red Plate	Yellow plate	Orange Plate
Crystal dimensions/mm	0.05×0.096×0.161	0.034×0.106×0.186	0.050×0.086×0.142
μ/mm^{-1}	9.456[a]	7.598	5.227
R(F), R_w(F)	0.0463, 0.0374	0.0437, 0.0595	0.0349, 0.0532
CCDC code	1989618	1989622	1989623

[a] Excludes the solvent.

Table 6A.2: Selected bond lengths (Å) and angles (°) for **1**-**3**.

Complex	**1** with 6,6′-dmbipy	**2** with 6,6′-dmbipy	**3** with pTol-bian
Mo(1)−Cl(1)	2.491(8)	2.515(15)	2.487(3)
Mo(1)−N(1)	2.300(3)	2.283(4)	2.261(2)
Mo(1)−N(2)	2.292(3)	2.283(4)	2.333(2)
Mo(1)−C(1)	1.957(3)	1.958(5)	1.984(3)
Mo(1)−C(2)	1.956(3)	1.958(5)	1.972(3)
Mo(1)−C(3)	2.325(3)	2.324(5)	2.318(3)
Mo(1)−C(4)	2.210(3)	2.221(8)	2.258(3)
Mo(1)−C(5)	2.338(3)	2.324(5)	2.334(3)
C(2)−O(1)	1.156(4)	1.152(6)	1.139(4)
C(3)−O(2)	1.155(3)	1.152(6)	1.144(4)
N(1)−Mo(1)−N(2)	72.31(10)	73.31(19)	73.67(8)
C(1)−Mo(1)−C(2)	76.07(14)	74.36(3)	80.66(14)

Table 6A.3: DFT-calculated energies (kcal mol^{-1}) for **1**, **2**, and **3** (= **X**), their radical anions [**X**]$^{\bullet-}$ and derived 5-coordinate radicals [**X**-R], 5-coordinate anions [**X**-A]$^{-}$ (obtained by the loss of chloride), and dimers [**X**-D] (for the molecular structures see Scheme 6.1).

Complex	**1** / kcal mol^{-1}	**2** / kcal mol^{-1}	**3** / kcal mol^{-1}	Others
X eq	-5912.02	-6286.30	-9800.54	
X ax	-5906.79	-6278.38	-9798.82	
[**X**]$^{\bullet-}$ eq	-5975.47	-6348.98	-9877.25	
[**X**]$^{\bullet-}$ ax	-5969.64	-6339.98	-9874.86	
[**X**−R] SP	-5814.16	-6190.84	-9717.81	
[**X**-R] TBP	-5812.60	also SP	-[a]	
[**X**-A]$^{-}$ diamag.	-5883.55	-6259.58	-9798.24	
[**X**-A]$^{-}$ paramag.	-5871.71	-6240.76	-9777.82	
[**X**-D]	-11632.00	-12383.32	-[a]	

[a] Not converged.

Table 6A.4: Relevant DFT-calculated distances (Å) in **1**, **2**, and **3** (= **X**), as well as their radical anions $[\mathbf{X}]^{\bullet-}$ and derived 5-coordinate radicals [**X**-R] and reduced $[\mathbf{X}\text{-A}]^{-}$ (obtained by the loss of chloride).

Complex		**X**		$[\mathbf{X}]^{\bullet-}$		[**X**-R]	$[\mathbf{X}\text{-A}]^{-}$
	Exp(eq)	equat	axial	equat	axial	SP	from ax
Complex **1**							
Mo−C_1	2.325	2.356	2.359	2.346	2.353	2.325	2.326
Mo−C_2	2.210	2.237	2.234	2.225	2.235	2.200	2.211
Mo−C_3	2.338	2.354	2.341	2.45	2.339	2.326	2.329
Mo−C(O)	1.957	1.953	1.943	1.955	1.948	1.954	1.961
Mo−C(O)	1.956	1.952	1.944	1.954	1.936	1.954	1.961
Mo−N (trans CO)	2.300	2.328	2.371	2.290	2.325	2.235	2.185
Mo−N	2.292	2.324	2.281	2.286	2.256	2.236	2.187
C−C (inter-ring bipy)	1.482	1.481	1.478	1.433	1.428	1.454	1.421
Mo−Cl	2.491	2.510	2.177	2.560	2.256	-	-
Complex **2**							
Mo−C_1	2.324	2.354	2.407	2.342	2.337	2.326	2.327
Mo−C_2	2.221	2.287	2.314	2.265	2.311	2.224	2.327
Mo−C_3	2.324	2.353	2.334	2.341	2.392	2.327	2.327
Mo−C(O)	1.958	1.952	1.925	1.953	1.934	1.949	1.957
Mo−C(O)	1.958	1.952	1.940	1.952	1.930	1.950	1.958
Mo−N (trans CO)	2.283	2.319	2.345	2.283	2.314	2.238	2.186
Mo−N	2.283	2.318	2.287	2.281	2.264	2.241	2.189
C−C (inter-ring bipy)	1.488	1.481	1.475	1.433	1.431	1.452	1.420
C−C (methallyl)	1.539	1.508	1.509	1.508	1.510	1.511	1.511
Mo−Cl	2.515	2.517	2.582	2.143	2.624	-	-
Complex **3**							
Mo−C_1	2.318	2.354	2.356	2.334	2.357	2.327	2.332
Mo−C_2	2.258	2.303	2.285	2.254	2.274	2.198	2.211
Mo−C_3	2.334	2.353	2.353	2.333	2.349	2.325	2.330
Mo−C(O)	1.984	1.973	1.952	1.956	1.935	1.943	1.954
Mo−C(O)	1.972	1.972	1.967	1.955	1.950	1.945	1.954
Mo−N (trans CO)	2.261	2.259	2.309	2.276	2.320	2.201	2.160
Mo−N	2.333	2.253	2.220	2.270	2.214	2.220	2.153
C−C (inter-ring bipy)	1.498	1.481	1.476	1.442	1.436	1.447	1.403
C−C (methallyl)	1.507	1.507	1.507	1.508	1.509	1.512	1.513
Mo−Cl	2.487	2.510	2.579	2.572	2.652	-	-

Table 6A.5: DFT (ADF)-calculated frequencies of the symmetric and antisymmetric CO-stretching modes in **1**-**3** (= **X**) and their reduction products (see Scheme 6.1).

Complex	**X**	$[\mathbf{X}]^{\bullet-}$		[**X**-R]		$[\mathbf{X}\text{-A}]^{-}$		[**X**-D]
	Equat	Equat	Axial	SP	TBP	TBP	SP	
1								
ν_s(C≡O)	1878	1852	1847	1851	1830	-	1804	1855, 1847
ν_a(C≡O)	1797	1759	1752	1759	1743	-	1702	1782, 1778[a]
2								
ν_s(C≡O)	1879	1851	1844	1857	-	-	1802	1855, 1847
ν_a(C≡O)	1797	1760	1750	1759	-	-	1701	1782, 1778[a]
3								
ν_s(C≡O)	1891	1858	1856	1868	-	-	1827	-
ν_a(C≡O)	1821	1758	1769	1781	-	-	1734	-

[a] Four calculated ν(CO) modes of the dimer.

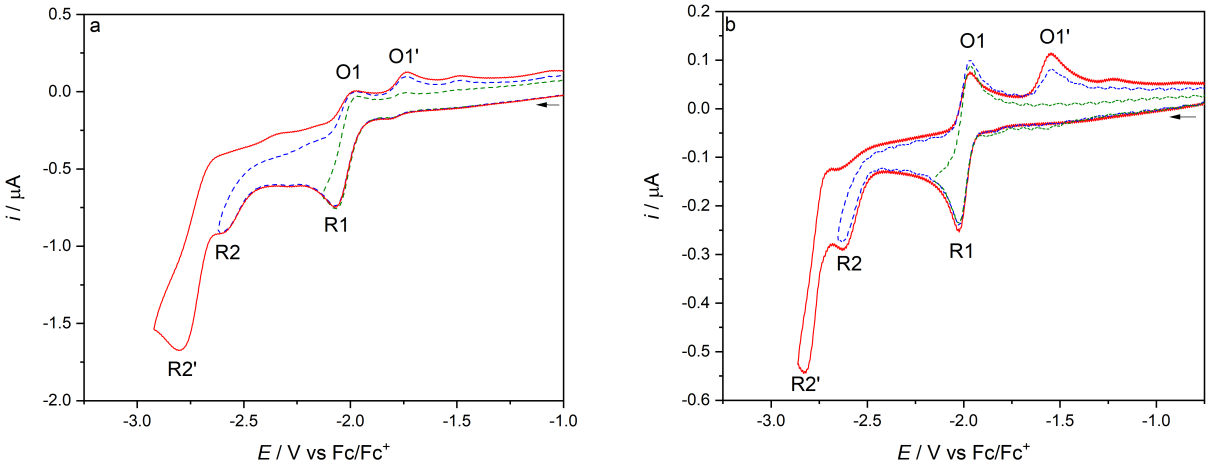

Figure 6A.1: Cyclic voltammograms of complex **1** at T = 298 K (a) and 195 K (b) in PrCN/Bu_4NPF_6. The arrow indicates the initial scan direction. Conditions: Pt microdisc electrode, υ = 100 mV s^{-1}.

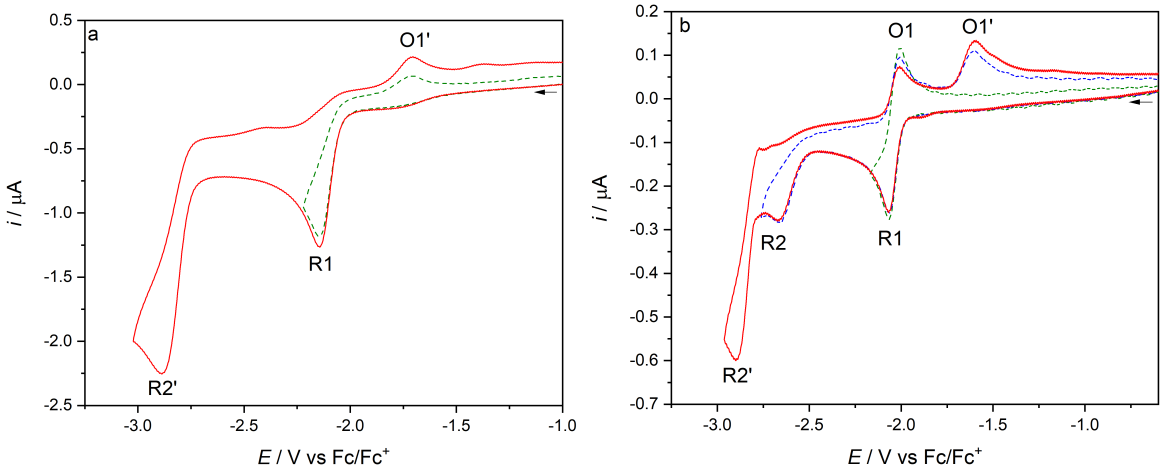

Figure 6A.2: Cyclic voltammograms of complex **2** at T = 298 K (a) and 195 K (b) in PrCN/Bu_4NPF_6. The arrow indicates the initial scan direction. Conditions: Pt microdisc electrode, υ = 100 mV s^{-1}.

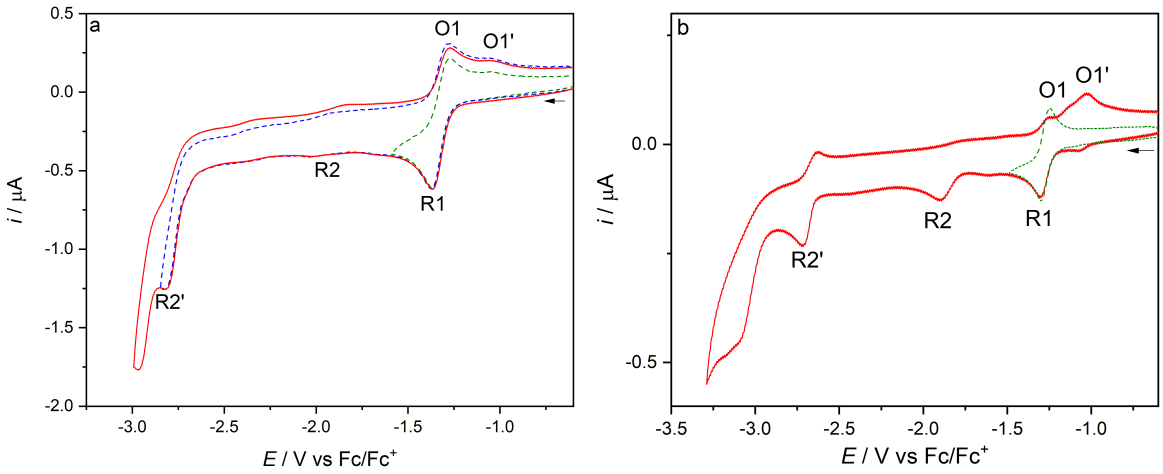

Figure 6A.3: Cyclic voltammograms of complex **3** at T = 298 K (a) and 195 K (b) in PrCN/Bu_4NPF_6. The arrow indicates the initial scan direction. Conditions: Pt microdisc electrode, υ = 100 mV s^{-1}.

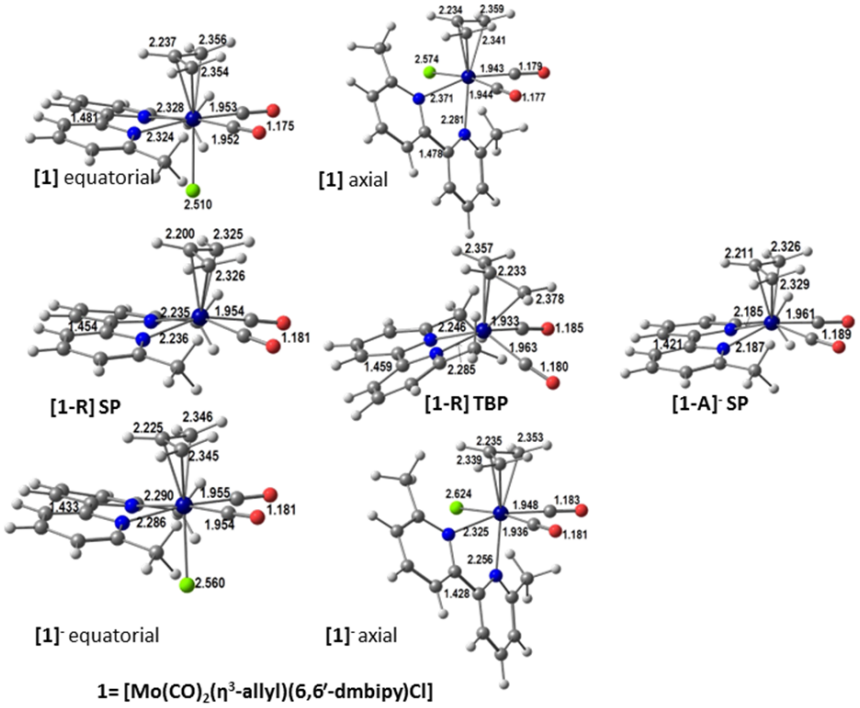

Figure 6A.4: DFT-optimized structures of the parent complex [Mo(η^3-methallyl)(6,6′-dmbipy)$(CO)_2$Cl] (**1**) (the equatorial isomer (top left) and the axial isomer (top right)), $1e^-$ reduced radical anion $[\mathbf{1}]^{\bullet -}$ (bottom left, equatorial isomer, bottom right, axial isomer), 5-coordinate radical [**1**-R] (the SP isomer (center left)) and $2e^-$ reduced 5-coordinate anion $[\mathbf{1}\text{-A}]^-$ (center right), with the relevant bond lengths (Å).

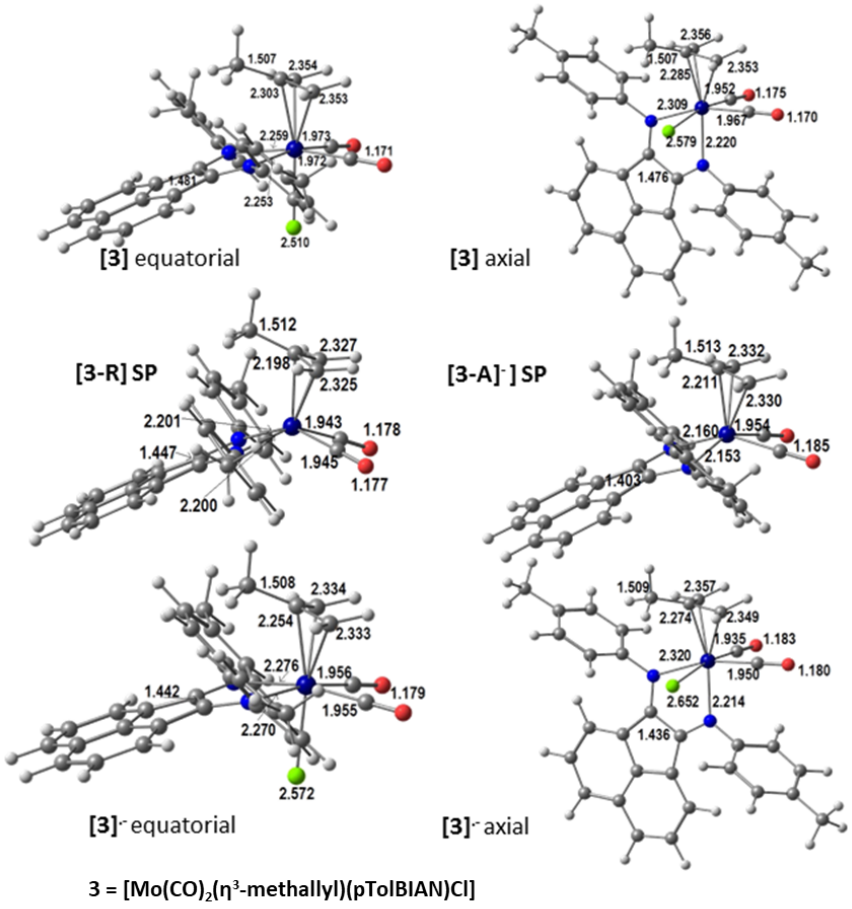

Figure 6A.5: DFT-optimized structures of the parent complex [Mo(η^3-methallyl)(pTolbian)$(CO)_2$Cl] (**3**) (the equatorial isomer (top left) and the axial isomer (top right)), $1e^-$ reduced radical anion $[\mathbf{3}]^{\bullet -}$ (bottom left, equatorial isomer, bottom right, axial isomer), 5-coordinate radical [**3**-R] (the SP isomer (center left)) and $2e^-$ reduced 5-coordinate anion [**3**-A]$^-$ (center right), with the relevant bond lengths (Å).

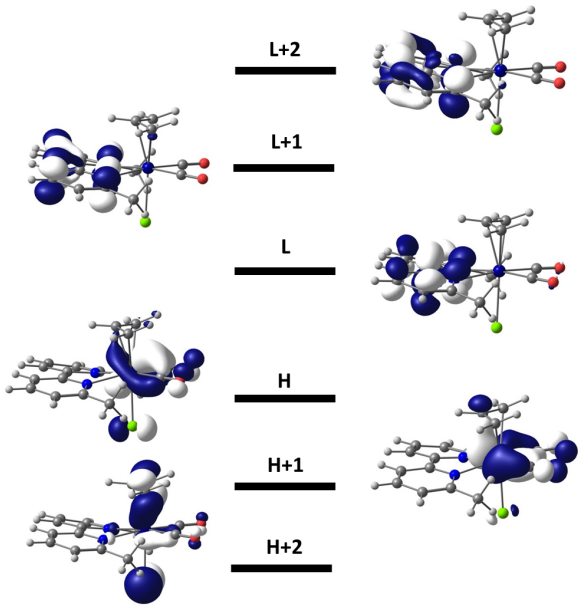

Figure 6A.6: DFT-calculated frontier orbitals of the parent complex [Mo(η^3-allyl)(6,6′-dmbipy)$(CO)_2$Cl] (**1**). The HOMO-LUMO (H-L) gap is 1.651 eV.

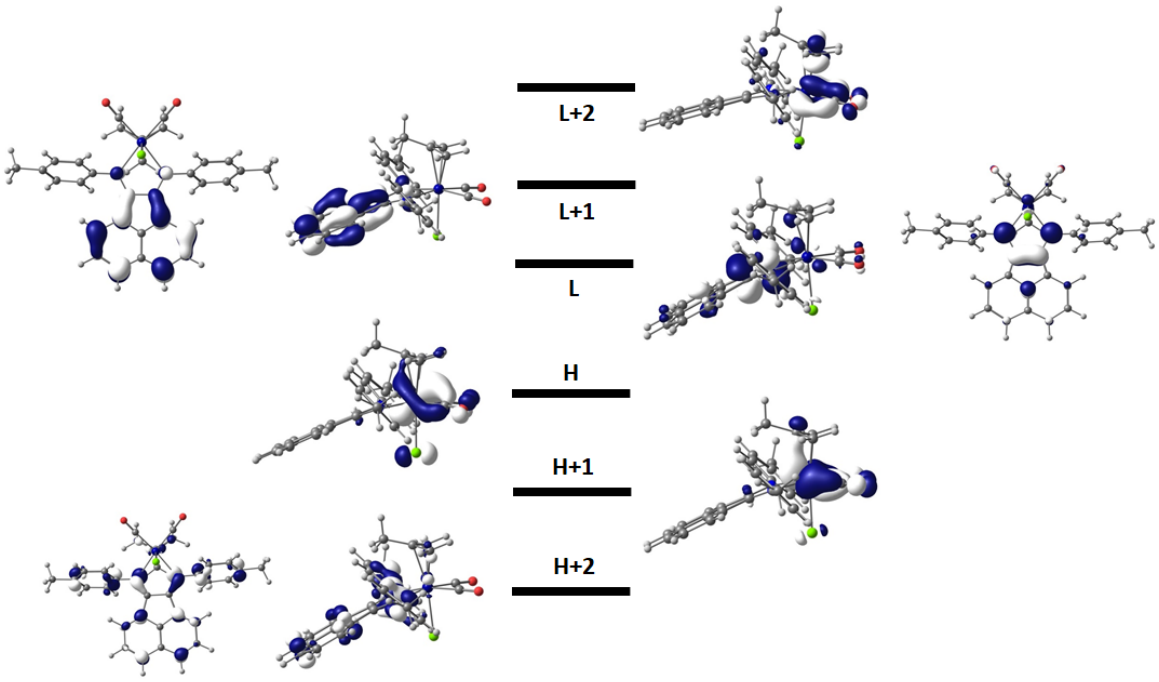

Figure 6A.7: DFT-calculated frontier orbitals of the parent complex [Mo(η^3-methallyl)(pTolbian)$(CO)_2$Cl] (**3**). The HOMO-LUMO (H-L) gap is 1.054 eV.

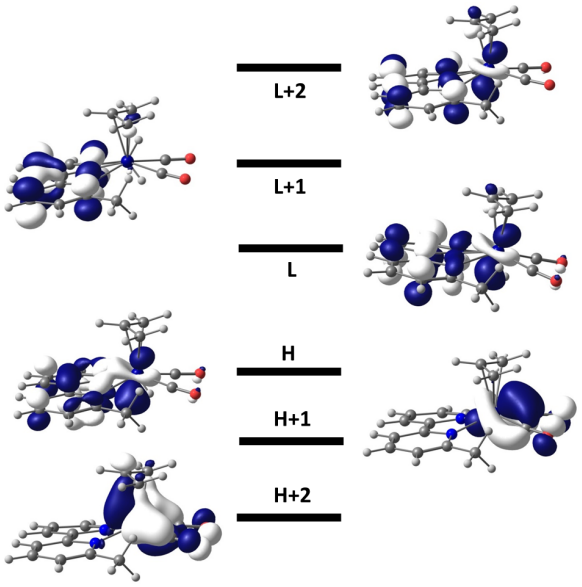

Figure 6A.8: DFT-calculated frontier orbitals of the 5-coordinate anion [Mo(η^3-allyl)(6,6′-dmbipy)$(CO)_2]^-$ (**1**). The HOMO-LUMO (H-L) gap is 1.265 eV.

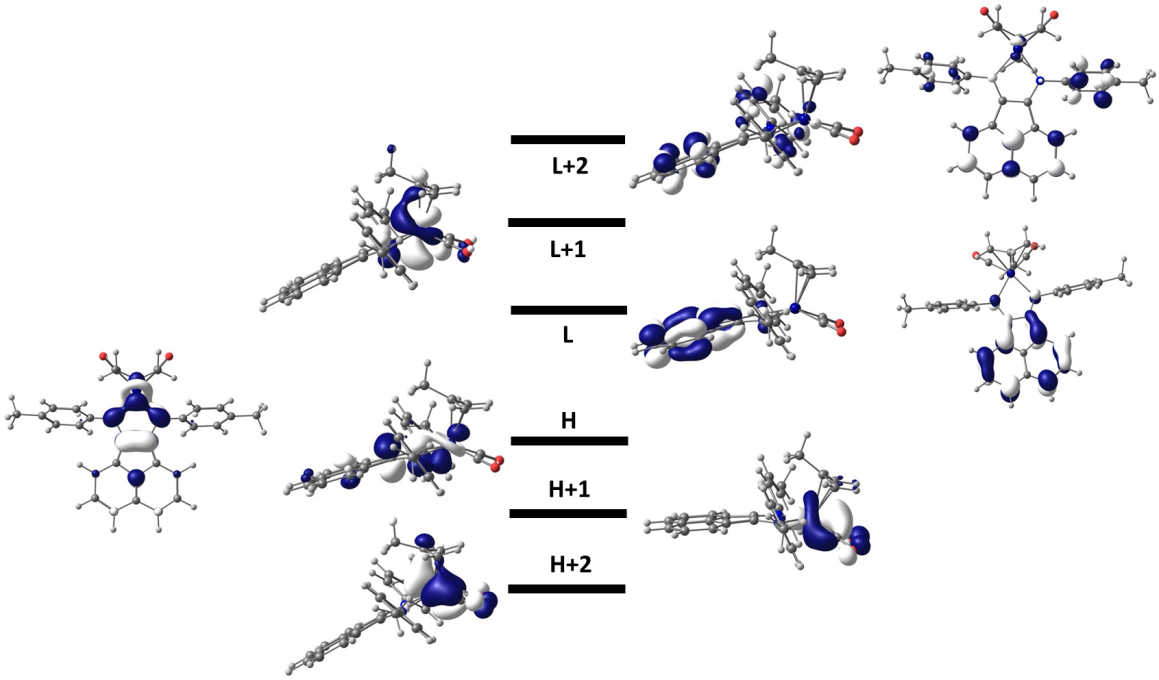

Figure 6A.9: DFT-calculated frontier orbitals of the 5-coordinate anion [Mo(η^3-methallyl)(pTolbian)$(CO)_2$]$^-$ (**3**). The HOMO-LUMO (H-L) gap is 1.127 eV.

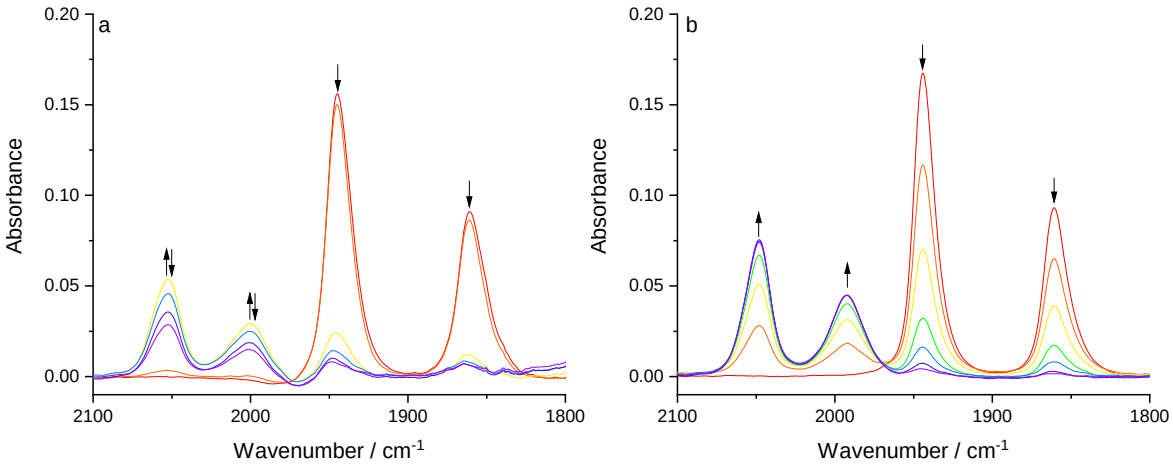

Figure 6A.10: IR SEC monitoring of the 1e$^-$ oxidation of (a) [Mo(η^3-allyl)(6,6′-dmbipy)(CO)$_2$Cl], **1** (↓) to slowly decomposing cation [**1**]$^+$ (↑) and (b) oxidation of **2** (↓) to stable [**2**]$^+$ (↑) Conditions: an OTTLE cell, THF/Bu$_4$NPF$_6$, T = 298 K.

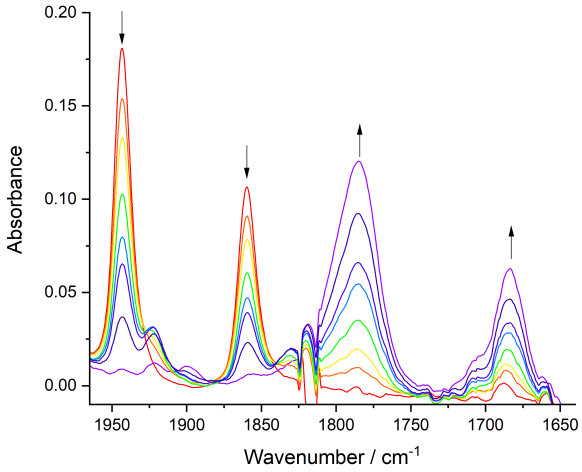

Figure 6A.11: IR SEC monitoring of the overall 2e$^-$ reduction of [Mo(η^3-methallyl)(6,6′-dmbipy)(CO)$_2$Cl], **2** (↓) at R1 to the 5-coordinate anion, [**2**-A]$^-$ (↑). Conditions: a cryostatted OTTLE cell, THF/Bu$_4$NPF$_6$, T = 255 K.

References

[1] N. Elgrishi, M. B. Chambers, X. Wang and M. Fontecave, *Chem. Soc. Rev.*, 2017, **46**, 761–796.

[2] R. Francke, B. Schille and M. Roemelt, *Chem. Rev.*, 2018, **118**, 4631–4701.

[3] J. Hawecker, J. M. Lehn and R. Ziessel, *J. Chem. Soc., Chem. Commun.*, 1984, **984**, 328–330.

[4] F. P. Johnson, M. W. George, F. Hartl and J. J. Turner, *Organometallics*, 1996, **15**, 3374–3387.

[5] C. W. Machan, S. A. Chabolla, J. Yin, M. K. Gilson, F. A. Tezcan and C. P. Kubiak, *J. Am. Chem. Soc.*, 2014, **136**, 14598–14607.

[6] M. L. Clark, P. L. Cheung, M. Lessio, E. A. Carter and C. P. Kubiak, *ACS Catal.*, 2018, **8**, 2021–2029.

[7] C. Riplinger, M. D. Sampson, A. M. Ritzmann, C. P. Kubiak and E. A. Carter, *J. Am. Chem. Soc.*, 2014, **136**, 16285–16298.

[8] M. Bourrez, F. Molton, S. Chardon-Noblat and A. Deronzier, *Angew. Chem. Int. Ed.*, 2011, **50**, 9903–9906.

[9] S. J. Spall, T. Keane, J. Tory, D. C. Cocker, H. Adams, H. Fowler, A. J. Meijer, F. Hartl and J. A. Weinstein, *Inorg. Chem.*, 2016, **55**, 12568–12582.

[10] J. M. Smieja, M. D. Sampson, K. A. Grice, E. E. Benson, J. D. Froehlich and C. P. Kubiak, *Inorg. Chem.*, 2013, **52**, 2484–2491.

[11] D. C. Grills, M. Z. Ertem, M. McKinnon, K. T. Ngo and J. Rochford, *Coord. Chem. Rev.*, 2018, **374**, 173–217.

[12] K. E. Dalle, J. Warnan, J. J. Leung, B. Reuillard, I. S. Karmel and E. Reisner, *Chem. Rev.*, 2019, **119**, 2752–2875.

[13] M. L. Clark, K. A. Grice, C. E. Moore, A. L. Rheingold and C. P. Kubiak, *Chem. Sci.*, 2014, **5**, 1894–1900.

[14] F. Franco, C. Cometto, F. Sordello, C. Minero, L. Nencini, J. Fiedler, R. Gobetto and C. Nervi, *ChemElectroChem*, 2015, **2**, 1372–1379.

[15] J. Tory, B. Setterfield-Price, R. A. W. Dryfe and F. Hartl, *ChemElectroChem*, 2015, **2**, 213–217.

[16] J. O. Taylor, R. D. Leavey and F. Hartl, *ChemElectroChem*, 2018, **5**, 3155–3161.

[17] D. Sieh, D. C. Lacy, J. C. Peters and C. P. Kubiak, *Chem. Eur. J.*, 2015, **21**, 8497–8503.

[18] G. Neri, P. M. Donaldson and A. J. Cowan, *J. Am. Chem. Soc.*, 2017, **139**, 13791–13797.

[19] L. Rotundo, C. Garino, R. Gobetto and C. Nervi, *Inorg. Chim. Acta*, 2018, **470**, 373–378.

[20] J. Tory, G. Gobaille-Shaw, A. M. Chippindale and F. Hartl, *J. Organomet. Chem.*, 2014, **760**, 30–41.

[21] J. O. Taylor, F. L. Veenstra, A. M. Chippindale, M. J. Calhorda and F. Hartl, *Organometallics*, 2019, **38**, 1372–1390.

[22] K. A. Grice and C. Saucedo, *Inorg. Chem.*, 2016, **55**, 6240–6246.

[23] B. D. Rossenaar, F. Hartl, D. J. Stufkens, C. Amatore, E. Maisonhaute and J. N. Verpeaux, *Organometallics*, 1997, **16**, 4675–4685.

[24] Q. Zeng, J. Tory and F. Hartl, *Organometallics*, 2014, **33**, 5002–5008.

[25] G. J. Stor, F. Hartl, J. W. Van Outersterp and D. J. Stufkens, *Organometallics*, 1995, **14**, 1115–1131.

[26] J. W. Goodyear, C. W. Hemingway, R. W. Harrington, M. R. Wisemann and B. J. Brisdon, *J. Organomet. Chem.*, 2002, **664**, 176–181.

[27] C. D. Nunes, P. D. Vaz, V. Félix, L. F. Veiros, T. Moniz, M. Rangel, S. Realista, A. C. Mourato and M. J. Calhorda, *Dalton Trans.*, 2015, **44**, 5125–5138.

[28] R. O. Diffraction, *Agilent CrysAlis PRO*, 2019.

[29] L. Palatinus and G. Chapuis, *J. Appl. Crystallogr.*, 2007, **40**, 786–790.

[30] P. W. Betteridge, J. R. Carruthers, R. I. Cooper, K. Prout and D. J. Watkin, *J. Appl. Crystallogr.*, 2003, **36**, 1487–1487.

[31] M. Krejčik, M. Daněk and F. Hartl, *J. Electroanal. Chem. Interfacial Electrochem.*, 1991, **317**, 179–187.

[32] F. Hartl, *Inorg. Chim. Acta*, 1995, **232**, 99–108.

[33] R. G. Parr and W. Yang, *Density-functional theory of atoms and molecules*, Oxford University Press, 1989.

[34] G. Te Velde, F. M. Bickelhaupt, E. J. Baerends, C. Fonseca Guerra, S. J. A. van Gisbergen, J. G. Snijders and T. Ziegler, *J. Comput. Chem.*, 2001, **22**, 931–967.

[35] C. Fonseca Guerra, J. G. Snijders, G. Te Velde and E. J. Baerends, *Theor. Chem. Acc.*, 1998, **99**, 391–403.

[36] V. U. Amsterdam, *Theoretical Chemistry, ADF2013 SCM*.

[37] S. H. Vosko, L. Wilk and M. Nusair, *Can. J. Phys.*, 1980, **58**, 1200–1211.

[38] A. D. Becke, *J. Chem. Phys.*, 1998, **109**, 2092–2098.

[39] J. P. Perdew, *Phys. Rev. B.*, 1986, **33**, 8822–8824.

[40] J. P. Perdew, *Phys. Rev. B*, 1986, **34**, 7406–7406.

[41] E. van Lenthe, A. Ehlers and E.-J. Baerends, *J. Chem. Phys.*, 1999, **110**, 8943–8953.

[42] F. C. Liu, P. S. Yang, C. Y. Chen, G. H. Lee and S. M. Peng, *J. Organomet. Chem.*, 2008, **693**, 537–545.

[43] J. R. Ascenso, C. G. De Azevedo, M. J. Calhorda, M. A. De, P. Costa, A. R. Dias, M. G. Drew, V. Félix, A. M. Galvão and C. C. Romão, *J. Organomet. Chem.*, 2001, **632**, 197–208.

[44] J. C. Alonso, P. Neves, M. J. P. Da Silva, S. Quintal, P. D. Vaz, C. Silva, A. A.

Valente, P. Ferreira, M. J. Calhorda, V. Félix and M. G. Drew, *Organometallics*, 2007, **26**, 5548–5556.

[45] S. Quintal, M. J. Pires da Silva, S. R. M. Martins, R. Sales, V. Félix, M. G. B. Drew, M. Meireles, A. C. Mourato, C. D. Nunes, M. S. Saraiva, M. Machuqueiro and M. J. Calhorda, *Dalton Trans.*, 2019, **48**, 8449–8463.

[46] M. J. Calhorda and P. J. Costa, *Coord. Chem. Rev.*, 2017, **344**, 83 – 100.

[47] S. A. Chabolla, E. A. Dellamary, C. W. Machan, F. A. Tezcan and C. P. Kubiak, *Inorg. Chim. Acta*, 2014, **422**, 109–113.

[48] F. Hartl, P. Rosa, L. Ricard, P. Le Floch and S. Záliš, *Coord. Chem. Rev.*, 2007, **251**, 557–576.

[49] D. E. Ryan, D. J. Cardin and F. Hartl, *Coord. Chem. Rev.*, 2017, **335**, 103–149.

[50] M. D. Sampson, A. D. Nguyen, K. A. Grice, C. E. Moore, A. L. Rheingold and C. P. Kubiak, *J. Am. Chem. Soc.*, 2014, **136**, 5460–5471.

[51] S. C. Cheng, C. A. Blaine, M. G. Hill and K. R. Mann, *Inorg. Chem.*, 1996, **35**, 7704–7708.

Chapter 7

Strong Impact of Intramolecular Hydrogen Bonding on the Reduction Path of [Re(3,3′-dihydroxy-2,2′-bipyridine)$(CO)_3$Cl] and the Catalytic Reduction of Carbon Dioxide

The content of this chapter was published in: **J. O. Taylor**, G. Neri, L. Banerji, A. Cowan, F. Hartl, *Inorganic Chemistry*, Manuscript Accepted, DOI: 10.1021/acs.inorgchem.0c00263.

7.1 Abstract

Herein, we present the cathodic paths of the Group 7 metal complex [Re(3,3′-dhbipy)$(CO)_3$Cl] (3,3′-dhbipy = 3,3′-dihydroxy-2,2′-bipyridine) producing a moderately active catalyst of the electrochemical reduction of CO_2 to CO. Combined techniques of cyclic voltammetry and IR/UV-Vis spectroelectrochemistry have revealed significant differences in the chemistry of the electrochemically reduced parent complex compared to the previously published Re/4,4′-dhbipy congener. The initial, irreversible cathodic step in weakly coordinating THF is shifted toward much less negative electrode potentials, reflecting facile reductive deprotonation of one hydroxyl group and strong intramolecular hydrogen bonding, O-H...O^-. The latter process occurs spontaneously in basic dimethylformamide where Re/4,4′-dhbipy remains stable. The subsequent reduction of singly deprotonated [Re(3,3′-dhbipy-H^+)$(CO)_3$Cl] at ambient conditions occurs at a cathodic potential close to that of the Re/4,4′-dhbipy-H^+ derivative. However, for the stabilized 3,3′-dhbipy-H^+ ligand the latter process at the second cathodic wave is more complex and involves an overall transfer of three electrons. Rapid potential-step electrolysis induces $1e^-$ reductive cleavage of the second O–H bond, triggering dissociation of the Cl^- ligand from [Re(3,3′-dhbipy-$2H^+$)$(CO)_3$Cl]$^{2-}$. The ultimate product of the second cathodic step in THF was identified as 5-coordinate [Re(3,3′-dhbipy-$2H^+$)$(CO)_3$]$^{3-}$, the equivalent of classical $2e^-$ reduced [Re(bipy)$(CO)_3$]$^-$. Each reductive deprotonation of the dhbipy ligand results in a red shift of the IR ν(CO) absorption of the tricarbonyl complexes by ca. 10 cm^{-1}, facilitating the product assignment based on comparison with the literature data for corresponding Re/bipy complexes. The Cl^- dissociation from [Re(3,3′-dhbipy-$2H^+$)$(CO)_3$Cl]$^{2-}$ was proven in strongly coordinating butyronitrile. The latter dianion is stable at 223 K, converting at 258 K to 6-coordinate [Re(3,3′-dhbipy-$2H^+$)$(CO)_3$(PrCN)]$^{3-}$. Useful reference data were obtained with substituted parent [Re(3,3′-dhbipy)$(CO)_3$(PrCN)]$^+$ that also smoothly deprotonates by the initial reduction to [Re(3,3′-dhbipy-H^+)$(CO)_3$(PrCN)]. The latter complex ultimately converts at the second cathodic wave to [Re(3,3′-dhbipy-$2H^+$)$(CO)_3$(PrCN)]$^{3-}$ via a counterintuitive ETC step

generating the $1e^-$ radical of the parent complex, viz. [Re(3,3′-dhbipy)$(CO)_3$(PrCN)]. The same alternative reduction path is also followed by [Re(3,3′-dhbipy-H^+)$(CO)_3$Cl]$^-$ at the onset of the second cathodic wave, where an ETC step results in the intermediate [Re(3,3′-dhbipy)$(CO)_3$Cl]$^{\bullet-}$ which is further reducible to [Re(3,3′-dhbipy-$2H^+$)$(CO)_3$]$^{3-}$ as the CO_2 catalyst.

7.2 Introduction

The environmental impact of anthropogenic CO_2 emissions has become one of the biggest concerns of modern science. Solar fuels, produced efficiently from either electrocatalytic or photocatalytic CO_2 reduction, offer a tantalizing route toward sustainable energy production.[1–3] Many transition metal complexes have been studied as possible precursors to catalytically active species. The goal is to accomplish multiple electron-proton transfers required to transform CO_2 not only to CO and formic acid ($2e^-$) but also to highly desirable high-density fuels such as acetone ($4e^-$) or methanol ($6e^-$).[4–14] One of the classical complexes, [Re(bipy)$(CO)_3$Cl] (bipy = 2,2′-bipyridine) and the family of its plentiful derivatives have been well established in the literature as the subject of numerous studies over the past few decades.[15–24] However, the scarcity of noble metals such as rhenium have led to a refocusing of efforts toward complexes of the more Earth-abundant metals. In Group 7, manganese is the most promising candidate and the analogous Mn-bipy complexes have recently been shown to be also active toward CO_2 in the presence of Brønsted or Lewis acids.[25–27] Since then the wealth of literature regarding the catalyst family of manganese α-diimine complexes has grown considerably.[28–38] Despite the clear move in the literature toward these Earth-abundant metals, rhenium complexes still play a critical role as model or reference systems - especially as other avenues of research are pioneered, including the study of so-called proton-responsive ligands acting as local sources of the protons consumed along the catalytic CO_2 reduction path.[39–44]

The idea of introducing an intramolecular source of protons proximal to the site of CO_2 coordination and concomitant reduction to improve turnover rates, has received a great deal

of attention. In 2012, iron tetraphenylporphyrin (FeTPP) was modified by placing phenolic groups in all ortho/ortho′-positions, which led to a significant increase in the observed catalytic activity, attributed to the local proton sources now present.[39] Another efficient iron-based catalyst for selective reduction of CO_2 to formate in aqueous solution is the reduced hydride cluster $[HFe_4\text{-}N(CO)_{12}]^-$.[45] Recently, a dinuclear rhenium complex, $[Re(CO)_3Cl_2(\mu\text{-}L)]$ (L = 4-tert-butyl-2,6-bis(6-(1H-imidazol-2-yl)-pyridin-2-yl)phenol) has been reported by Siewert and co-workers to show an increased catalytic activity for the CO production in DMF/H_2O relative to the activity of $[Re(bipy)(CO)_3Cl]$ in $MeCN/H_2O$.[40] In the absence of CO_2, the dinuclear complex undergoes two $2e^-$ cathodic steps. The first $2e^-$ reduction is L-based, triggering homolytic N-H bond cleavage at the imidazole site and reductive liberation of H_2. The reductive deprotonation of imidazole (ImH) to imidazolate (Im^-) has also been demonstrated by Hartl and co-workers in the related complexes *fac*-$[Re(bipy)(CO)_3(ImH)]^+$ and *fac*-$[Re(phen)(CO)_3(ImH)]^+$ (phen = 1,10-phenanthroline).[41,42] The second $2e^-$ reduction of the dinuclear Re complex triggers O–H bond cleavage at the phenol group and is accompanied by the loss of the Cl^- ligand and concomitant metal-centered reduction. It is the latter step where a catalytic response is observed in the presence of CO_2.

In addition to this, the complex *fac*-$[Mn(pdbipy)(CO)_3Br]$ (pdbipy = 4-phenyl-6-(phenyl-2,6-diol)-2,2′-bipyridine) shows extreme sensitivity toward added-acid strength as well an atypical reduction pathway for tricarbonyl Mn-bipy complexes, presenting with suppressed dimer formation in acetonitrile.[43] Interestingly, alternative positions of the phenolic groups from ortho in the latter complex to meta/para in related *fac*-$[Mn(ptbipy)(CO)_3Br]$ (ptbipy = 4-phenyl-6-(phenyl-3,4,5-triol)-2,2′-bipyridine) resulted in a different cathodic path under Ar (dimerization, absent reductive deprotonation of the phenolic groups), as well as a reduced catalytic reactivity toward CO_2.[43] Recently, the study has been extended to the corresponding Re complexes showing a higher selectivity for formate.[44]

Fujita and co-workers studied the cathodic behavior of two proton-responsive complexes *fac*-$[Re(x,x'\text{-}dhbipy)(CO)_3Cl]$ (x = 4 and 6, dhbipy = dihydroxy-2,2′-bipyridine).[46] In the case of Re/4,4′-dhbipy, an enhanced catalytic activity relative to reference Re/bipy was

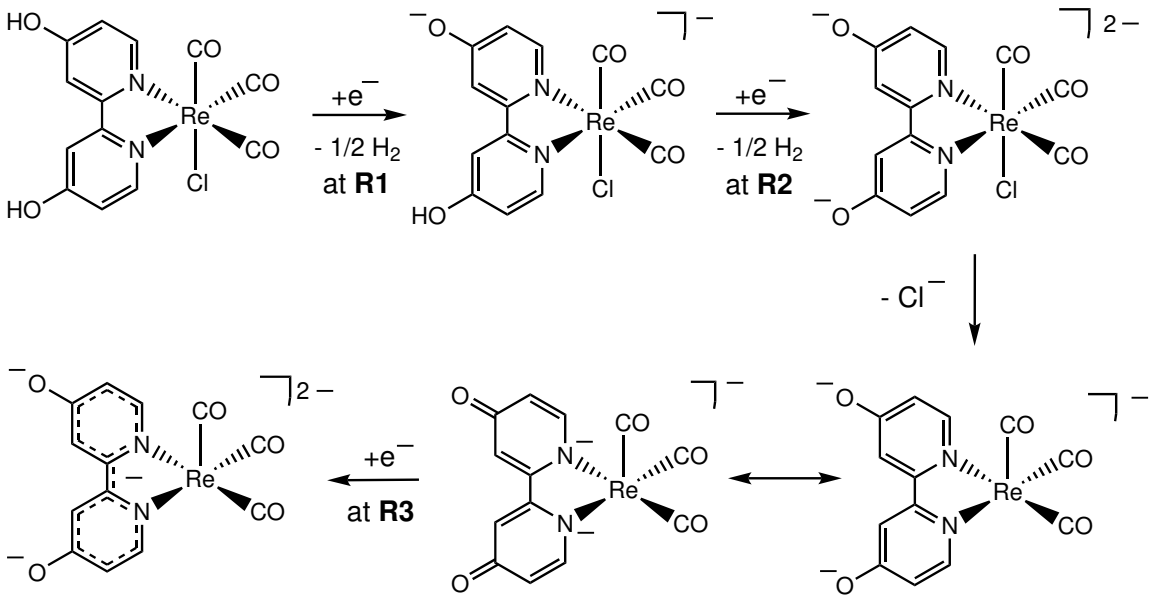

Scheme 7.1: Reduction path of [Re(4,4′-dhbipy)$(CO)_3$Cl], involving two successive 1e$^-$ reductive deprotonation steps R1 and R2.

reported, while Re/6,6′-dhbipy proved to be inactive toward CO_2 reduction. Both Re/x,x′-dhbipy complexes undergo two closely spaced, 1e$^-$ reductive deprotonations, R1 at $E_{p,c}$ = -1.56 V and R2 at $E_{p,c}$ = -1.76 V vs Ag/AgCl for x = 4 (Scheme 7.1). The intimate mechanism has been suggested to involve initial protonation of the singly reduced 4,4′-dhbipy ligand followed by H_2 and proton dissociation to give [Re(4,4′-dhbipy-H^+)$(CO)_3$Cl]$^-$. The three separate ν(CO) absorption bands corresponding to the parent Cs facial geometry, become red-shifted by about 10 cm^{-1} per 1e$^-$ reduction. This value indicates that the Re-bipy metallacycle and, therefore, also the π-back-donation to the carbonyl ligands are barely affected by lowering the oxidation state. The moderate ν(CO) shift is explained by the formation of the reductively deprotonated 4,4′-dhbipy ligand acting as a stronger σ-donor. Dissociation of the axial Cl$^-$ ligand was proposed to accompany the second reductive-deprotonation step R2, yielding a 5-coordinate complex, Re(4,4′-dhbipy-2H^+)$(CO)_3]^-$ (Scheme 7.1). However, the split ν(CO) band pattern is not in favor of such assignment, as fluxional 5-coordinate tricarbonyls generally show two (A1 + E) absorption bands. Electrocatalytic reduction of CO_2 with Re/4,4′-dhbipy becomes triggered by the cathodic step R3 at $E_{p,c}$ = -2.03 V vs Ag/AgCl rather than preceding R2 (see Figure 6 in ref.[46]), selectively transforming

CO_2 to CO with a faradaic efficiency of 95% ± 2% in dry DMF. Fujita and co-workers assigned [Re(4,4′-dhbipy-$2H^+$)$(CO)_3]^-$ as the catalyst but did not monitor the electron transfer process R3 and underlying structural transformation by IR spectroelectrochemistry; the molecular and electronic structure of the catalytically active species at R3 has therefore remained uncertain. Scheme 7.1 presents it as the five-coordinate dianion, [Re(4,4′-dhbipy-$2H^+$)$(CO)_3]^{2-}$, an equivalent of the radical [Re(4,4′-di-*t*Bu-bipy)$(CO)_3$], but it also could be the corresponding trianion, [Re(4,4′-dhbipy-$2H^+$)$(CO)_3]^{3-}$, an equivalent of [Re(4,4′-di-*t*Bu-bipy)$(CO)_3]^-$ the well-established catalyst with two added electrons delocalized over the π-system of the Re–N∩N(bipy) metallacycle.[47]

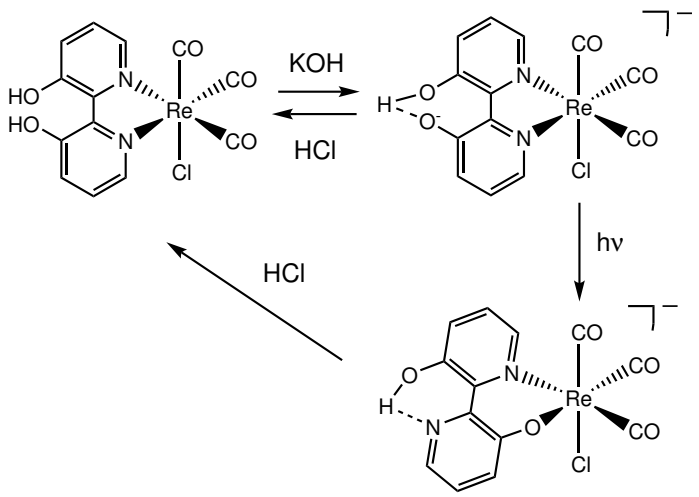

Scheme 7.2: The reaction pathway of [Re(3,3′-dhbipy)$(CO)_3$Cl] involving facile chemical deprotonation of one hydroxyl group at 3,3′-dhbipy by addition of excess KOH to yield [Re(3,3′-dhbipy-H^+)$(CO)_3$Cl]$^-$ stabilized by intra-ligand hydrogen bonding. Exposure to the light of $\lambda > 400$ nm triggers the "roll-over" isomerization, resulting in the Re–N∩O^- metallacycle. Addition of HCl at any stage will reverse the process.

This study will address the cathodic activation of a related double-deprotonated precatalyst. Notably, Fujita and co-workers[46] did not involve in their study the close complex with the 3,3′-dihydroxy-2,2′-bipyridine (3,3′-dhbipy) ligand. The photophysical properties of this complex and interesting photochemistry of its deprotonated anionic form were reported in the literature by Vogler and co-workers.[48,49] The parent Re/3,3′-dhbipy complex was shown to undergo single deprotonation with excess KOH or in dimethylformamide (DMF). Interestingly, the deprotonated anionic product, [Re(3,3′-dhbipy-H^+)$(CO)_3$Cl]$^-$, with the

Re–N∩N metallacycle strongly absorbing at 416 nm, converts on exposure to light of $\lambda >$ 400 nm to a linkage isomer with Re–N∩O$^-$ coordination (Scheme 7.2). Although rarely encountered for Re tricarbonyl complexes, this photoisomerization behavior bears some similarity with the so-called "roll-over" pathway common to several rhodium[50,51] and platinum[52] based C–H functionalization catalysts. In the original reports[48,49] it remains unclear whether the chelating Re–N∩O$^-$ coordination induces dissociation of the axial Cl$^-$ ligand (not shown in Scheme 7.2). This concomitant step cannot be excluded, as documented by another complex with a bidentate N∩O$^-$ ligand at the $Re(CO)_3^+$ core, which binds pyridine in the axial position instead of Cl$^-$.[53]

The objective of this comparative study was to ascertain whether the metallacycle isomerization could also be induced electrochemically, on further reduction of [Re(3,3′-dhbipy-H$^+$)$(CO)_3$Cl]$^-$. Otherwise, the goal was to unravel the impact of the initial deprotonation step on the cathodic behavior of the complex and a potential of the identified reduction products to trigger catalytic reduction of carbon dioxide.

7.3 Experimental

Materials and Methods

Organic solvents were freshly distilled prior to use under an inert atmosphere of nitrogen from an appropriate drying agent: Na/benzophenone for tetrahydrofuran (THF) and CaH_2 for butyronitrile (PrCN). The supporting electrolyte, Bu_4NPF_6 (Acros-Organics), was recrystallized twice from absolute ethanol. It was dried under vacuum at 373 K for 5 h, and an additional 20 min just prior to electrochemical measurements carried out under an atmosphere of dry argon. Standard Schlenk techniques were applied to all procedures. ^{1}H NMR spectra were recorded on a Bruker Nanobay spectrometer (400 MHz). For the electrocatalytic studies (CV/IR SEC), the electrolyte was saturated with CO_2 by bubbling it on a frit at atmospheric pressure for ca. 10 min. Chemical deprotonation of [Re(3,3′-dhbipy)$(CO)_3$Cl] was carried out using solid sodium bis(trimethylsilyl)amide (NaHMDS,

95%, Sigma-Aldrich).

Synthesis of [Re(3,3′-dhbipy)(CO)$_3$Cl]

A sample of [Re(3,3′-dhbipy)(CO)$_3$Cl] was prepared according to the literature procedures.[21] The product identity and purity were confirmed by molecular absorption spectroscopies. IR (THF): ν(CO) at 2018, 1914 and 1893 cm^{-1}. UV-vis (THF): λ_{max} = 350 nm. ^{1}H NMR (400 MHz, CD$_3$CN) δ 8.75 (2H, d, J = 5.2 Hz), 7.72 (2H, d, J = 8.8 Hz), 7.53 (2H, dd, J = 13.6 Hz, 3.2 Hz). For comparison, the ^{1}H NMR spectrum of [Re(4,4′-dhbipy)(CO)$_3$Cl] shows similar resonances at δ 8.66 (d), 7.69 (d) and 7.03 (dd). The broad signal of the phenolic protons at $\delta > 9$ (ref.[46]) was not observed due to some moisture in acetonitrile-d$_3$.

Synthesis of [Re(3,3′-dhbipy)(CO)$_3$(OTf)] (OTf = CF$_3$SO$_3^-$) and reactivity towards PrCN

[Re(3,3′-dhbipy)(CO)$_3$Cl] (100 mg, 0.20 mol) and AgOTf (64 mg, 0.25 mol) were dissolved under an inert atmosphere in the dark in freshly distilled anhydrous THF (10 mL). The solution was stirred for 2 h at room temperature. The white precipitate of AgCl was then filtered off and the solution collected in a Schlenk vessel purged with argon. Hexane (4 x 10 mL) was added slowly to precipitate a yellow solid. The solvent was evaporated to dryness to collect a dry but extremely hydroscopic yellow powder in a moderate yield (33.6 %). IR (THF): ν(CO) at 2032, 1928, 1910 cm^{-1}. Rapid thermal conversion of [Re(3,3′-dhbipy)(CO)$_3$(OTf)] to [Re(3,3′-dhbipy)(CO)$_3$(PrCN)]$^+$ takes place in PrCN. IR (PrCN): ν(CO) at 2039, 1933br cm^{-1}. ^{1}H NMR (400 MHz, CD$_3$CN) δ 8.78 (2H, d, J = 5.2 Hz), 7.85 (2H, d, J = 8.8 Hz), 7.65 (2H, dd, J = 13.6 Hz, 3.2 Hz). This facile ligand exchange was utilized to prepare in situ electrochemical samples with the latter cationic complex.

Cyclic Voltammetry

Cyclic voltammograms were recorded with a Metrohm Autolab PGSTAT 302N potentiostat operated with the Nova 1.9 software. The air-tight single-compartment electrochemical cell

housed a 0.42 mm^2 platinum microdisc working electrode (polished between scans with a 0.25-μm diamond paste (Kemet International Ltd.)), a coiled platinum wire counter electrode, and a silver-wire pseudo-reference electrode. The ferrocene/ferrocenium (Fc/Fc^+) redox couple served as an internal standard for voltammetric measurements. Solutions contained 10^{-1} M Bu_4NPF_6 and 10^{-3} M analyte. The cell was chilled to 195 K by submersion in an acetone/dry ice slurry.

IR and UV-Vis Spectroelectrochemistry

IR spectroelectrochemical experiments were performed using a Bruker Vertex 70v FT-IR spectrometer equipped with a DLaTGS detector or linked to an external Bio-Rad FTS 60 MCT detector (with the sample compartment adapted for low-temperature spectroelectrochemistry). UV-Vis spectroelectrochemical experiments were conducted with a Scinco S-3100 diode-array spectrophotometer (200-1100 nm). The in situ electrolyses were carried out using an air-tight OTTLE cell.[54] The cell was equipped with platinum minigrid (32 wires per cm) working and auxiliary electrodes, a Ag-microwire pseudo-reference electrode, and optically transparent CaF_2 windows. The course of the spectroelectrochemical experiment was monitored by thin-layer cyclic voltammetry controlled with a PalmSens EmStat3 potentiostat operated with the PSTrace5 software. Low-temperature spectroelectrochemical measurements were carried out with a cryostatted OTTLE cell.[55] Solutions contained 3 $\times$ 10^{-1} M Bu_4NPF_6 and 3 $\times$ 10^{-3} M analyte.

Coulometry

To quantify electrocatalytic reactions reported in this work, controlled potential electrolysis was conducted under Ar and CO_2 in two electrochemical cells. The first one, controlled by a PalmSens3 potentiostat, was a pear-shaped cell, equipped with a Pt-microdisc (2 mm, diameter) working electrode, a Pt-wire counter electrode separated from the bulk solution by a Vycor tip, and an Ag-wire pseudo-reference electrode. The second one, controlled by a Bio-Logic SP-200 potentiostat, was an H-shaped cell with three compartments separated at

the bottom by dense glass frits and housing the Pt-foil working and counter electrodes with the geometric surface areas of 2×0.96 cm^2 and 2×0.5 cm^2, respectively, and a coiled Ag-wire pseudo-reference electrode. In both cases, the working and reference electrodes were immersed in a CO_2-saturated THF solution containing 3 mM [Re(3,3′-dhbipy)$(CO)_3$Cl], 0.5 M Bu_4NPF_6 and 3 mM ferrocene (as a CV potential reference). To prevent anodic THF polymerisation, the solution surrounding the counter electrode was 0.5 M Bu_4NPF_6 in CO_2-saturated acetonitrile. The solutions were stirred continuously during the measurements. The turnover numbers and faradaic efficiencies were quantified by GC-headspace analysis. On the timescale of the experiments, only the pear-shaped cell was suitable for recording accurate faradaic efficiency values, while the H-shaped cell, due to diffusion of CO between the compartments and not into the headspace, was only used to determine accurate turnover numbers. Combined, the data gives a more accurate view of the overall picture. The gas chromatography was conducted on an Agilent 6890N instrument equipped with a 5 Å molecular sieve column (ValcoPLOT, 30 m length, 0.53 mm ID) and a pulsed discharge detector (D-3-I-HP, Valco Vici), with helium as the carrier gas. H_2 and CO were quantified by using a custom made calibrant gas (500 ppm of H_2, 200 ppm CH_4 and 200 ppm CO in CO_2 as the balance gas).

7.4 Results and Discussion

7.4.1 Cyclic Voltammetry

Cyclic Voltammetry of [Re(3,3′-dhbipy)$(CO)_3$Cl] in THF at Variable Temperature

The cathodic behavior of [Re(3,3′-dhbipy)$(CO)_3$Cl] differs significantly from that of its congener with the 4,4′-dhbipy ligand. In THF the title complex exhibits two irreversible cathodic waves (Figure 7.1). The first wave, R1, at $E_{p,c}$ = -1.01 V vs Fc/Fc^+ is very broad, indicating an irreversible, slow electron transfer process. Notably, the initial reduction of [Re(4,4′-dhbipy)$(CO)_3$Cl] is shifted significantly more negatively, by ca. 1 V (Table 7.1). This

Table 7.1: Cyclic voltammetry of [Re(3,3′-dhbipy)$(CO)_3$Cl] and related dhbipy complexes.

Complex	Solvent	Cathodic Wave	$E_{p,c}$ / V vs Fc/Fc^+
[Re(3,3′-dhbipy)$(CO)_3$Cl]	THF	R1	-1.01
			-1.40[a]
[Re(3,3′-dhbipy)$(CO)_3$Cl]		R1*	-1.90[a,b]
[Re(3,3′-dhbipy)$(CO)_3$Cl]$^{\bullet-}$		R2	-2.38
[Re(3,3′-dhbipy-H^+)$(CO)_3$Cl]$^-$		R2′	-2.38
			-2.30[a]
[Re(3,3′-dhbipy-H^+)$(CO)_3$Cl]$^-$		R2*	-2.16
[Re(3,3′-dhbipy)$(CO)_3$Cl]	PrCN	R1	-0.84
			-1.22[a]
[Re(3,3′-dhbipy-H^+)$(CO)_3$Cl]$^-$		R2′	-2.30
			-2.25[a]
[Re(3,3′-dhbipy)$(CO)_3$(PrCN)]$^+$	PrCN	R1	-0.93
[Re(3,3′-dhbipy-H^+)$(CO)_3$(PrCN)]		R2′	-2.07
[Re(4,4′-dhbipy)$(CO)_3$Cl]	DMF	R1	-1.98
[Re(4,4′-dhbipy-H^+)$(CO)_3$Cl]$^-$		R2	-2.18
[Re(4,4′-dhbipy-$2H^+$)$(CO)_3$]$^-$		R3	-2.45

[a] Measured at 195 K. [b] No concomitant reductive deprotonation of the 3,3′-dhbipy ligand taking place. $E_{1/2}$ = -1.87 V. [c] Prepared by chemical deprotonation of [Re(3,3′-dhbipy)$(CO)_3$Cl] with 1 equiv. NaHMDS. [d] Measured by Fujita and coworkers.[46] [e] No deprotonation of the parent complex in DMF was reported.

extraordinary difference can be ascribed to a strong stabilizing effect of the single reductive deprotonation resulting in a hydrogen bond between the bipy oxo-anion substituents (Scheme 7.2).[56] The following cathodic step, R2′, appears as a quasi-reversible cathodic wave at a much more negative potential of $E_{p,c}$ = -2.38 V vs Fc/Fc^+. The large potential gap, reaching nearly 1.4 V, is in stark contrast to the CVs recorded for the 4,4′-dhbipy and 6,6′-dhbipy derivatives and their singly (selectively) deprotonated forms, where the separation between first and second cathodic waves is merely 200 mV. At room temperature, R1 is totally irreversible with any counter wave absent even at scan rates in excess of 1 V s^{-1} (Figure 7A.1, Appendix). Additionally, turning the scan positively beyond R2′ does not generate a well-defined counterwave O2′ (Figure 7.1a) but reveals a new anodic wave, O(A), at $E_{p,a}$ = -2.01 V vs Fc/Fc^+, which becomes better perceptible at higher scan rates (Figure 7A.2, Appendix). The origin of both phenomena will be analyzed in the following

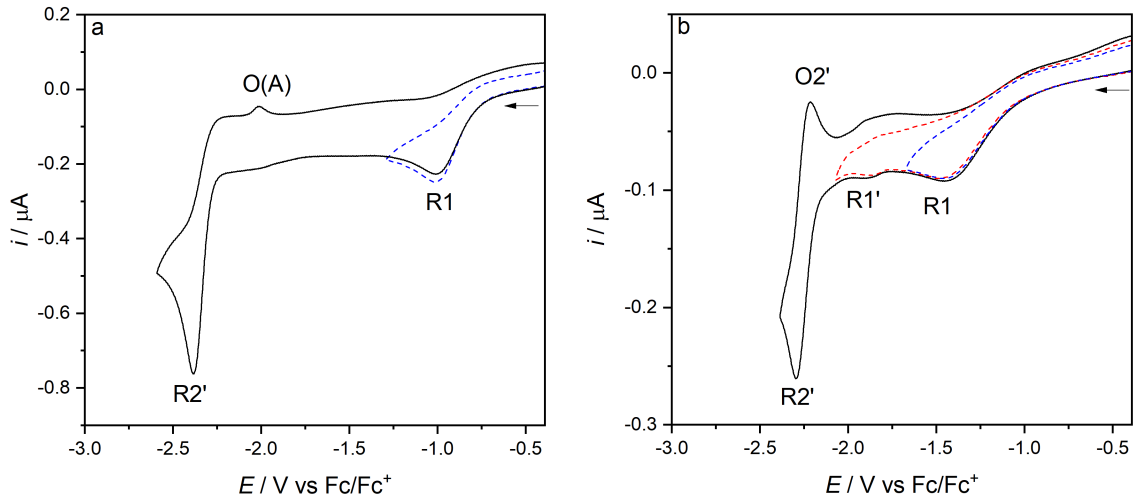

Figure 7.1: Cyclic voltammograms of [Re(3,3′-dhbipy)$(CO)_3$Cl] in THF/Bu_4NPF_6. Experimental conditions: Pt microdisc, T = 298 K (a) and 195 K (b), υ = 100 mV s^{-1}.

IR spectroelectrochemical section.

On cooling to 195 K, the cathodic CV of [Re(3,3′-dhbipy)$(CO)_3$Cl] in THF changes notably (Figure 7.1b). First, R1 is shifted negatively by ca. 400 mV ($E_{p,c}$ = -1.45 V vs Fc/Fc^+) and significantly broadened. A new, minor cathodic wave R1* appears at $E_{p,c}$ = -1.90 V vs Fc/Fc^+. At higher scan rates, R1* grows relative to R1 and becomes reversible (Figures 7A.3 and 7A.4, Appendix) at υ < 500 mV s^{-1}. The reversible nature of the process on the subsecond timescale suggests that R1* corresponds to the reduction of parent [Re(3,3′-dhbipy)$(CO)_3$Cl] to the corresponding non-deprotonated radical anion. It will be shown in the spectroelectrochemical section that this process contributes to the overall cathodic path of the title complex even at ambient temperature. Sweeping the electrode potential toward R2′ at 195 K located this wave at $E_{p,c}$ = -2.30 V vs Fc/Fc^+ (Figure 7.1b and Figure 7A.3 in Appendix). Its shape and overall reversibility (indicated by the anodic counterwave O2′ and the unity peak/current ratio) points to a diffusion-controlled $1e^-$ cathodic process on the (sub)second CV timescale that does not trigger any significant chemical transformation of [Re(3,3′-dhbipy-H^+)$(CO)_3Cl]^-$ generated at R1 (see the IR spectroelectrochemical section). This temperature-controlled behavior reveals the increased stability of [Re(3,3′-dhbipy-H^+)$(CO)_3Cl]^{2-}$ (both O–H and Re–Cl bonds, in contrast to the

Re/4,4′-dhbipy congener) ascribed to the strong hydrogen bonding in the ligand redox couple [3,3′-dhbipy-H^+]$^-$/[3,3′-dhbipy$^{\bullet-}$-H^+]$^{2-}$ that hinders the second reductive proton elimination to give [3,3′-dhbipy-$2H^+$]$^{2-}$.

Cyclic Voltammetry of [Re(3,3′-dhbipy)(CO)$_3$Cl] and [Re(3,3′-dhbipy)(CO)$_3$(PrCN)]$^+$ in PrCN at Variable Temperature

The cathodic behavior of [Re(3,3′-dhbipy)(CO)$_3$Cl] was investigated by cyclic voltammetry also in butyronitrile, PrCN (Figure 7.2). At room temperature, the totally irreversible wave R1 is shifted less negatively to $E_{p,c}$ = -0.84 vs Fc/Fc$^+$ in this electrolyte compared to THF (Table 7.1). The second cathodic wave R2′ is shifted by merely 80 mV, which reveals the stability of [Re(3,3′-dhbipy-H^+)(CO)$_3$Cl]$^-$ in the potentially coordinating solvent. Apart from the moderate potential shifts, the CV response does not deviate significantly from that recorded in THF. This also applies for the CV scan at 195 K (Figure 7.2b), where only R1* is absent.

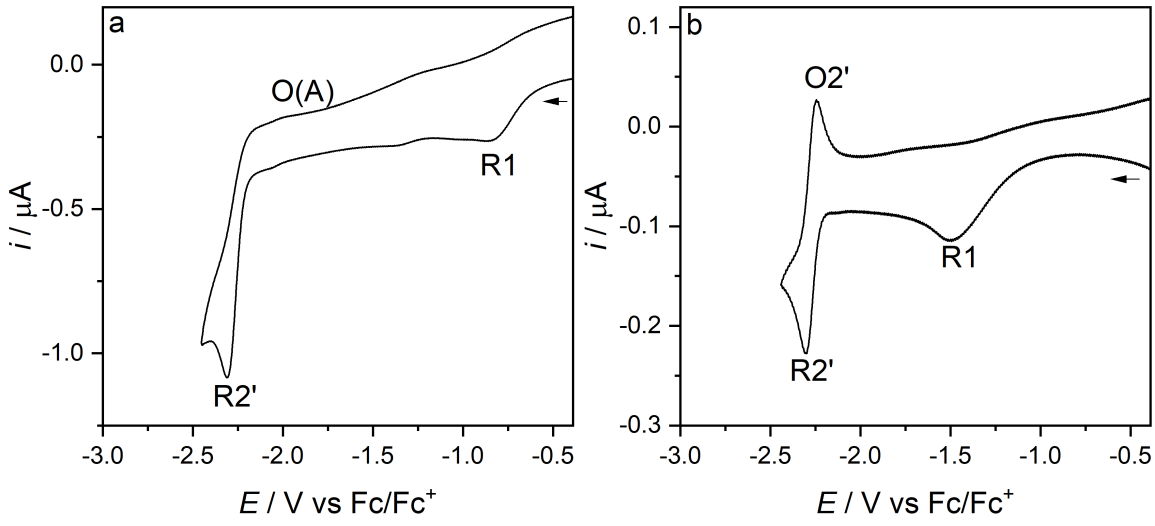

Figure 7.2: Cyclic voltammograms of [Re(3,3′-dhbipy)(CO)$_3$Cl] in PrCN/Bu_4NPF_6. Experimental conditions: Pt microdisc, T = 298 K (a) and 195 K (b), υ = 100 mV s^{-1}.

Compared to [Re(4,4′-dhbipy)(CO)$_3$Cl] in DMF (Table 7.1) the cathodic wave R3 is absent or unresolved in the CV responses of [Re(3,3′-dhbipy)(CO)$_3$Cl] both in THF (see above) and PrCN. This is understandable at 195 K where the Re–Cl bond remains stable upon the

$1e^-$ reduction generating intact $[Re(3,3'\text{-dhbipy}^{\bullet-}\text{-}H^+)(CO)_3Cl]^{2-}$ (Figures 7.1 and 7.2). The double-deprotonated complex $[Re(3,3'\text{-dhbipy-}2H^+)(CO)_3Cl]^{2-}$, which is supposed to reduce further at an R3 potential, is not formed on the short timescale of the CV experiment due to the strong intramolecular hydrogen bonding in the single-deprotonated precursor.[56] At ambient temperature the irreversible cathodic wave R2′ in fact encompasses several secondary EC processes resulting from the instability of $[Re(3,3'\text{-dhbipy-}2H^+)(CO)_3Cl]^{2-}$. These deductions have been corroborated by IR spectroelectrochemical experiments described in the following section. Direct comparisons of the two Re/x,x′-dhbipy (x = 3, 4) complexes in DMF are not possible as $[Re(3,3'\text{-dhbipy})(CO)_3Cl]$ instantly deprotonates in this basic solvent.

Separate substitution of the axial chloride ligand in $[Re(3,3'\text{-dhbipy})(CO)_3Cl]$ with PrCN to form the corresponding cationic complex impacts strongly the cathodic process at R2′, causing its positive shift by 230 mV. The less negative electrode potential agrees with the reduction of less basic $[Re(3,3'\text{-dhbipy-}H^+)(CO)_3(PrCN)]$ formed at R1 from singly reduced $[Re(3,3'\text{-dhbipy})(CO)_3(PrCN)]^+$ (Figure 7.3, Table 7.1). This observation supports the stability of $[Re(3,3'\text{-dhbipy-}H^+)(CO)_3Cl]^-$ in PrCN when formed from parent $[Re(3,3'\text{-dhbipy})(CO)_3Cl]$ at R1 (Figure 7.2a).

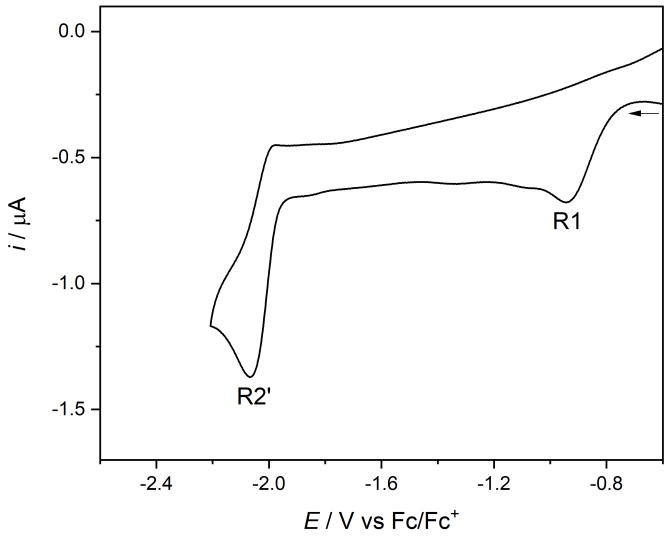

Figure 7.3: Cyclic voltammogram of $[Re(3,3'\text{-dhbipy})(CO)_3(PrCN]^+$ in $PrCN/Bu_4NPF_6$. Experimental conditions: Pt microdisc, T = 298 K, υ = 100 mV s^{-1}.

Cyclic Voltammetry of [Re(3,3′-dhbipy-H$^+$)(CO)$_3$Cl]$^-$ in THF at Ambient Temperature

The cyclic voltammogram of [Re(3,3′-dhbipy-H$^+$)(CO)$_3$Cl]$^-$ prepared in situ in THF by chemical deprotonation of [Re(3,3′-dhbipy)(CO)$_3$Cl] with NaHMDS is highly revealing (Figure 7.4). The cathodic wave R1 of the neutral parent complex is absent, as expected. However, instead of the single cathodic wave R2′ assigned deliberately to the deprotonated anionic complex formed electrochemically at R1 (Figure 7.1a), there are two close-lying waves, the first one at $E_{p,c}$ = -2.16 V denoted as R2*, followed by R2 at $E_{p,c}$ = -2.38 V which coincides with R2′ and is also allied to the anodic wave O(A) recorded on the reverse potential scan. This cathodic behavior is echoed in the corresponding IR spectroelectrochemical experiment presented and thoroughly discussed in the following section, where [Re(3,3′-dhbipy-H$^+$)(CO)$_3$Cl]$^-$ is fully transformed already at R2* but not to the anticipated double-deprotonated product. Instead, the IR monitoring revealed the formation of [Re(3,3′-dhbipy)(CO)$_3$Cl]$^{\bullet -}$, similar to the reversible reduction of parent [Re(3,3′-dhbipy)(CO)$_3$Cl] at R1* (Table 7.1) at 195 K. This surprising transformation corresponds to a net zero-electron, electron-transfer catalytic (ETC) process, which agrees with the rather low peak-current at R2*. The cathodic wave R2 in Figure 7.4 can be then ascribed to the collective subsequent reduction of [Re(3,3′-dhbipy)(CO)$_3$Cl]$^{\bullet -}$ and [Re(3,3′-dhbipy-H$^+$)(CO)$_3$Cl]$^-$ diffusing from the bulk solution. The ETC process is reminiscent, for example, of the 1e$^-$ reduction of [Re(DBSQ)(CO)$_3$(PPh$_3$)] (DBSQ = 3,5-di-*t*Bu-1,2-benzosemiquinone anion) which produces isoelectronic [Re(DBSQ)(CO)$_2$(PPh$_3$)$_2$] instead of [Re(DBCat)(CO)$_3$(PPh$_3$)]$^-$ (DBCat = 3,5-di-*t*Bu-1,2-catecholate dianion).[57]

7.4.2 IR Spectroelectrochemistry

Reduction of [Re(3,3′-dhbipy)(CO)$_3$Cl] in THF at Ambient Temperature

At cathodic potentials coinciding with R1, [Re(3,3′-dhbipy)(CO)$_3$Cl] in the thin-solution layer of the OTTLE cell undergoes O–H bond cleavage (reductive deprotonation) yielding

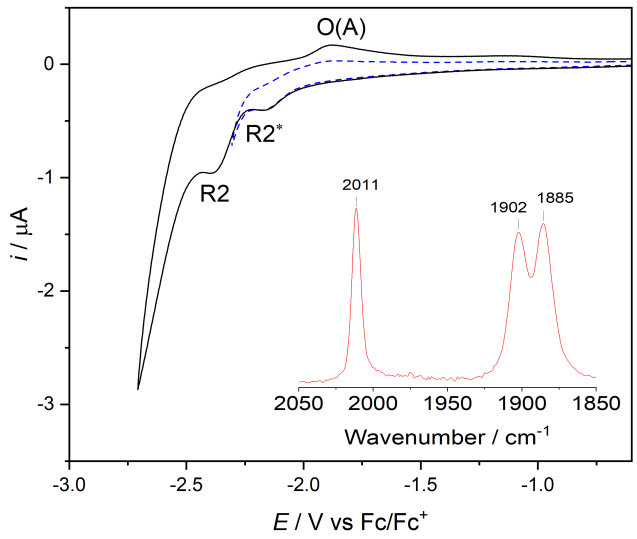

Figure 7.4: Cyclic voltammograms of $[Re(3,3'\text{-dhbipy-H}^+)(CO)_3Cl]^-$ in THF/Bu_4NPF_6. Experimental conditions: Pt microdisc, $T = 298$ K, $\upsilon = 100$ mV s^{-1}.

$[Re(3,3'\text{-dhbipy-H}^+)(CO)_3Cl]^-$ (Figure 7.5a,b and Scheme 7.3). The UV-Vis spectral changes (Figure 7.5b) reveal the characteristic replacement of the Re-to-bipy MLCT band at 351 nm with a new, likely intra-ligand (dhbipy-H^+) absorption band at 425 nm, as reported by Vogler and co-workers[49] for the chemical reaction of $[Re(3,3'\text{-dhbipy})(CO)_3Cl]$ with solid KOH in wet acetonitrile (Scheme 7.2). In the infrared CO-stretching region (Figure 7.5a), a small but perceptible red shift of the three ν(CO) absorption bands ($2A' + A''$; Cs geometry) by ca. 10 cm^{-1} from the parent complex is observed. The reference wavenumber values for $[Re(4,4'\text{-dhbipy-H}^+)(CO)_3Cl]^-$ are indeed very close (Table 7.2). The data confirms that the added electron does not enter the π^*(bipy) LUMO as in the archetypal case of the $1e^-$ reduction of $[Re(bipy)(CO)_3Cl]$.[24,58,59] The assignment of the reduction product at R1 as $[Re(3,3'\text{-dhbipy-H}^+)(CO)_3Cl]^-$ is strongly supported by the independent chemical deprotonation of the parent complex by the added base, NaHMDS, (Figure 7.4 and Figure 7A.5, Appendix). It is noteworthy that instant single deprotonation was also encountered[49] in DMF (Table 7.2) where the neutral congener $[Re(4,4'\text{-dhbipy})(CO)_3Cl]$ remains stable. The close proximity of the hydroxyl substituents in $[Re(3,3'\text{-dhbipy-H}^+)(CO)_3Cl]^-$ enables strong hydrogen bonding[48,49], providing a significant thermodynamic driving force to form readily a stable deprotonated complex, as also reflected in the much lower R1 overpotential

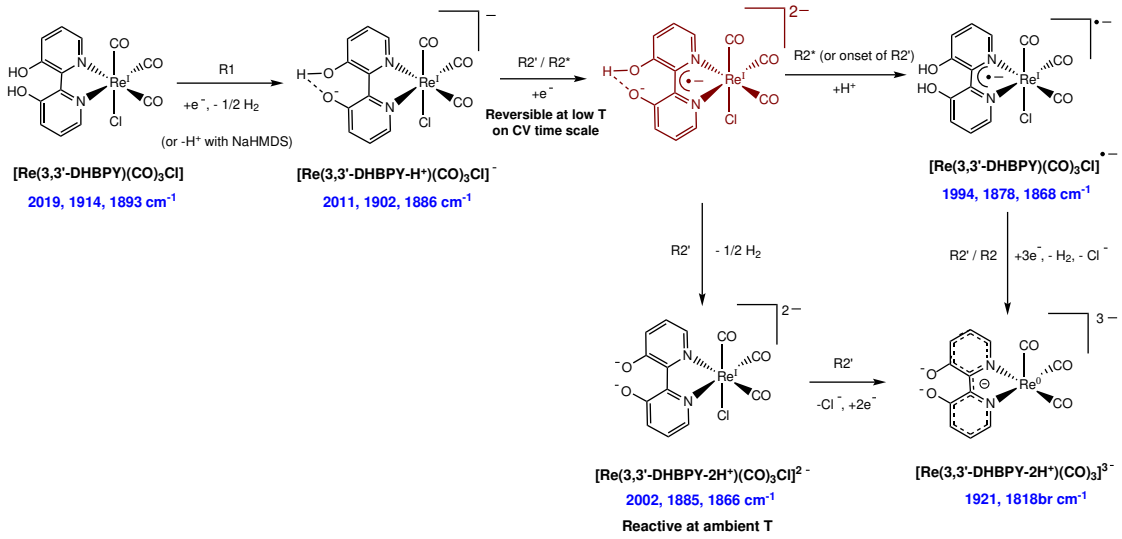

Scheme 7.3: Cathodic pathways of [Re(3,3′-dhbipy)$(CO)_3$Cl] in THF. First 1e$^-$ reductive deprotonation at R1 followed by rapid second 1e$^-$ reductive deprotonation at R2′, concomitant chloride dissociation and 2e$^-$ reduction of the 5-coordinate transient complex delocalized over the bipy–Re$(CO)_3$ π-system. The alternative (potential-controlled) ETC pathway (at R2*, or the onset of R2′) produces the corresponding radical anion of the parent complex.

compared to the initial reduction of [Re(4,4′-dhbipy)$(CO)_3$Cl].

The subsequent reduction of electrochemically generated [Re(3,3′-dhbipy-H$^+$)$(CO)_3$Cl]$^-$ occurs at the cathodic wave R2′ (Figure 7.1a), proceeding via two alternative paths (Scheme 7.3) controlled by the mode of tuning the cathodic potential on the spectroelectrochemical timescale: either a rapid potential step (a) beyond R2′ and (b) at R2′, or (c) slow potential sweep through R2′. This cathodic course is remarkably more complex than indicated by the reversible CV response in THF/Bu_4NPF_6 at 195 K (Figure 7.1b). The intramolecular hydrogen bond in [Re(3,3′-dhbipy-H$^+$)$(CO)_3$Cl]$^-$ is strong enough to extend the lifetime of the bipy-reduced species compared to the Re/4,4′-dhbipy congener but the second reductive elimination of hydrogen triggers structural changes monitored by IR spectroscopy, using information from selected reference systems.

In the first instance, the results from the potential-step experiment (a) at 200 mV beyond R2′ are presented. The cathodic electrolysis at the overpotential produces in just a few seconds a single detectable species with IR ν(CO) bands markedly shifted to 1921

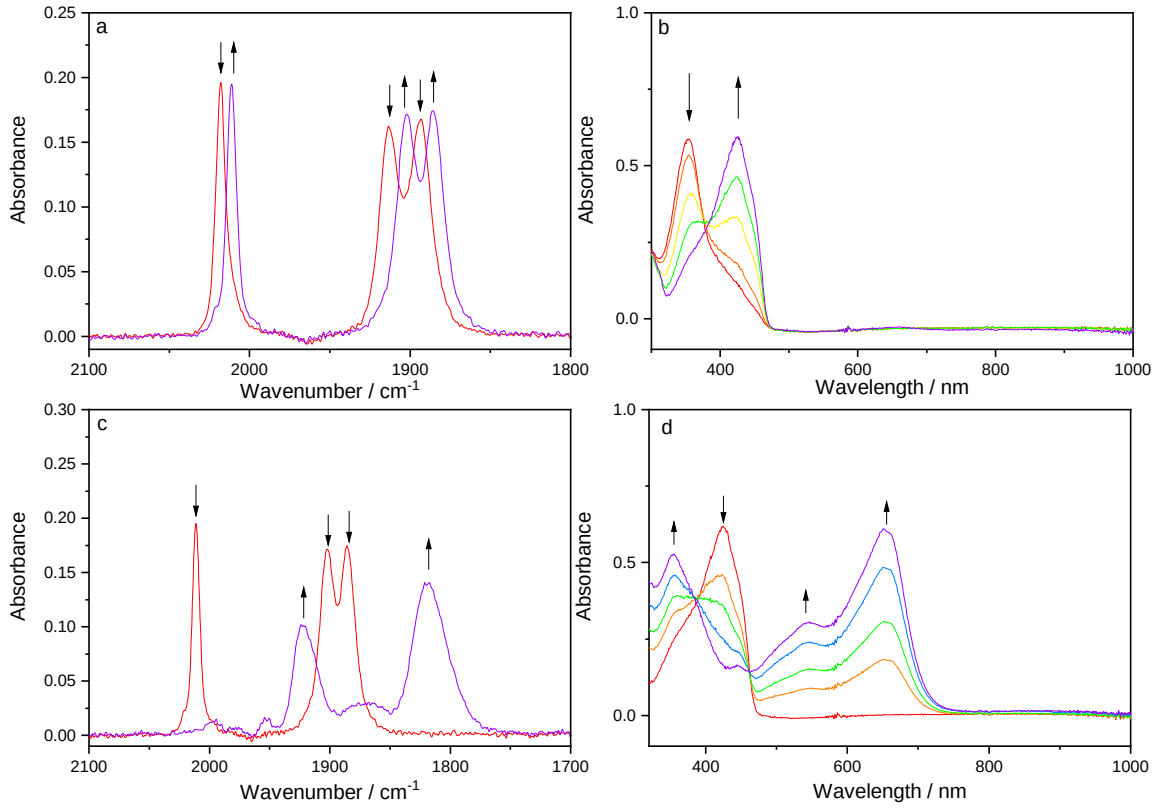

Figure 7.5: Cathodic IR (a, c) and UV-Vis (b, d) spectroelectrochemistry: (a, b) 1e$^-$ reductive deprotonation of [Re(3,3′-dhbipy)(CO)$_3$Cl] (↓) to [Re(3,3′-dhbipy-H$^+$)(CO)$_3$Cl]$^-$ (↑) at R1; (c,d) rapid potential-step conversion of [Re(3,3′-dhbipy-H$^+$)(CO)$_3$Cl]$^-$ (↓) to 5-coordinate [Re(3,3′-dhbipy-2H$^+$)(CO)$_3$]$^{3-}$ (↑) in an unresolved 3e$^-$ process at 200 mV beyond the onset of R2′. Conditions: an OTTLE cell, THF/Bu$_4$NPF$_6$, T = 298 K.

and 1818br cm^{-1}, which strongly absorbs in the visible spectral region (Figures 5c and 5d, respectively, and Table 7.2). This product is assigned as a formally Re^0-bipy$^-$ 5-coordinate complex [Re(3,3′-dhbipy-2H$^+$)(CO)$_3$]$^{3-}$. The ν(CO) intensity pattern and the large red shift correspond with the properties of the well-known[58] fluxional complex [Re(bipy)(CO)$_3$] absorbing in THF at 1947 and 1843 cm^{-1}. The additional $>$ 20 cm^{-1} downward shift seen for [Re(3,3′-dhbipy-2H$^+$)(CO)$_3$]$^{3-}$ complies with the preceding double reductive deprotonation of dhbipy, increasing the π-back-donation to the carbonyl ligands. The identification of this 5-coordinate structure also offers an explanation as to the origin of the O(A) counterwave seen in the CV on the reverse anodic scan (Figure 7.1a). This may be considered now as the re-oxidation of this 5-coordinate complex. While encountered for isoelectronic 5-coordinate

tricarbonyl complexes, such as $[Mn(bipy)(CO)_3]^-$ or $[W(bipy)(CO)_3]^{2-}$,[26,60] the O(A) signature has never been reported[16,24], for either $[Re(t\text{Bu-bipy})(CO)_3]^-$ or $[Re(bipy)(CO)_3]^-$ but it is our strong expectation that if such a wave were detected it would also occur in this region.

Table 7.2: Infrared and UV-Vis Absorption Data for [Re(3,3′-dhbipy)$(CO)_3$Cl] and [Re(3,3′-dhbipy)$(CO)_3$(PrCN)]$^+$, and their reduction products.

Complex	Solvent	ν(CO) / cm^{-1}	λ_{max} / nm
[Re(bipy)$(CO)_3$Cl]	THF[a]	2019, 1917, 1895	
[Re(3,3′-dhbipy)$(CO)_3$Cl]	THF	2018, 1914, 1893	351
	PrCN	2020, 1915, 1897	353
[Re(4,4′-di-*t*Bu-bipy)$(CO)_3$Cl]	DMF[b]	2018, 1913, 1890	
[Re(3,3′-dhbipy-H$^+$)$(CO)_3$Cl]$^-$	THF	2011, 1902, 1886	425
	PrCN	2012, 1903, 1885	426
	THF[c]	2011, 1902, 1885	
	DMF[d]	2011, 1902, 1882	425
[Re(bipy)$(CO)_3$Cl]$^{\bullet-}$	THF	1996, 1883, 1868[a]	
		1996, 1882, 1867[f]	361, 486sh, 511[f]
[Re(3,3′-dhbipy)$(CO)_3$Cl]$^{\bullet-}$	THF	1994, 1878, 1866	480[h]
[Re(4,4′-di-*t*Bu-bipy)$(CO)_3$Cl]$^{\bullet-}$	DMF[b]	1992, 1878 and 1860	
[Re(3,3′-dhbipy-2H$^+$)$(CO)_3$Cl]$^{2-}$	THF[e]	2002, 1883, 1873	
	PrCN[g]	2002, 1885, 1867	
[Re(3,3′-dhbipy-2H$^+$)$(CO)_3$]$^{3-}$	THF	1921, 1818br	354, 553, 654
[Re(3,3′-dhbipy)$(CO)_3$(OTf)]	THF	2032, 1928, 1910	
[Re(3,3′-dhbipy)$(CO)_3$(PrCN)]$^+$	PrCN	2039, 1933br	
[Re(bipy)$(CO)_3$(PrCN)]$^+$	PrCN[a]	2041, 1937br	
[Re(3,3′-dhbipy)$(CO)_3$(PrCN)]	PrCN	2004, 1890br	
[Re(bipy)$(CO)_3$(PrCN)]	PrCN[a]	2010, 1895br	
[Re(3,3′-dhbipy-H$^+$)$(CO)_3$(PrCN)]	PrCN	2031, 1928br	
[Re(3,3′-dhbipy-2H$^+$)$(CO)_3$(PrCN)]$^-$	PrCN[g]	2023, unresolved	
[Re(3,3′-dhbipy-2H$^+$)$(CO)_3$(PrCN)]$^{2-}$	PrCN	1986, 1874br	
[Re(3,3′-dhbipy-2H$^+$)$(CO)_3$(PrCN)]$^{3-}$	PrCN	1967, 1849, 1835	
[Re(4,4′-dhbipy)$(CO)_3$Cl][b]	DMF	2019, 1911, 1893	
[Re(4,4′-dhbipy-H$^+$)$(CO)_3$Cl]$^{-}$[b]	DMF	2012, 1900, 1881	
[Re(4,4′-dhbipy-2H$^+$)$(CO)_3$Cl]$^{2-}$[b]	DMF	2002, 1886, 1865	

[a] Reproduced from[24] [b] Reported by Fujita and co-workers[46]. [c] Prepared by single deprotonation of the parent complex with NaHMDS. [d] Formed by the instatneous deprotonation of the parent complex in DMF. [e] Observed only as a transient in THF during a potential step experiment. [f] T = 253 K. Reproduced from reference[59]. [g] T = 223 K. [h] Only partly resolved due to an overlapping absorbance.

In case (b), where the course of the thin-layer spectroelectrochemical experiment is not stepped but rapidly scanned through R2′ to the maximum faradaic current (Figure 7.6), an intermediate species is detected in consort with the ultimate 5-coordinate complex. On comparison with the Re/4,4′-dhbipy congener (Table 7.2), this transient is assigned as the double-deprotonated species $[Re(3,3'\text{-dhbipy-}2H^+)(CO)_3Cl]^{2-}$ (ν(CO) at 2002, 1885 and 1868 cm^{-1}). Differently from Re/4,4′-dhbipy, the double-deprotonated species is unstable at room temperature, decaying via concerted Cl^- dissociation and electron transfer to $[Re(3,3'\text{-dhbipy-}2H^+)(CO)_3]^{3-}$. It will be shown later that $[Re(3,3'\text{-dhbipy-}2H^+)(CO)_3Cl]^{2-}$ can be stabilized at low temperature in coordinating butyronitrile, which supports the intact Re–Cl still present in this intermediate 6-coordinate complex, in line with the well-resolved 2A′ + A″ ν(CO) band pattern.

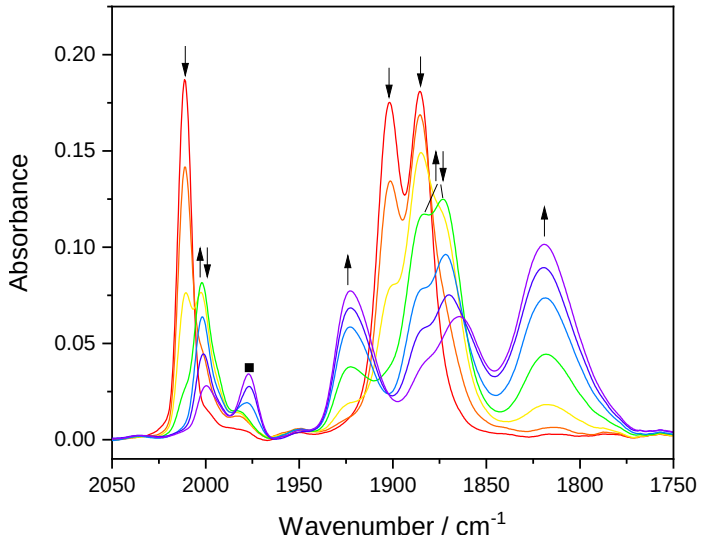

Figure 7.6: Cathodic IR spectroelectrochemistry at R2′ as $[Re(3,3'\text{-dhbipy-}H^+)(CO)_3Cl]^-$ (↓), undergoes $1e^-$ reductive deprotonation to transient $[Re(3,3'\text{-dhbipy-}2H^+)(CO)_3Cl]^{2-}$ (↑↓), and its concomitant decay to $[Re(3,3'\text{-dhbipy-}2H^+)(CO)_3]^{3-}$ (↑). Conditions: an OTTLE cell, THF/Bu_4NPF_6, T = 298 K. The label ■ corresponds to an unassigned side product.

In the slow potential-sweep experiment (c), the R2′ wave due to the reduction of $[Re(3,3'\text{-dhbipy-}H^+)(CO)_3Cl]^-$ is gradually scanned through, adding additional complexity to the overall mechanistic description. The strength of the internal hydrogen bond is of key importance to the single-deprotonated anion and the activation energy for the second deprotonation is therefore quite high. In a very limited potential range this allows

for a situation, where the primary bipy-reduced species, [Re(3,3′-dhbipy$^{\bullet-}$-H$^+$)(CO)$_3$Cl]$^{2-}$ does not undergo the second reductive deprotonation to [Re(3,3′-dhbipy-2H$^+$)(CO)$_3$Cl]$^{2-}$ (experiment (b)) but converts to a more stable product absorbing in the ν(CO) region at 1994, 1878 and 1866 cm^{-1} (Figure 7.7). These wavenumbers can be assigned to the non-deprotonated radical anion of the title complex, [Re(3,3′-dhbipy)(CO)$_3$Cl]$^{\bullet-}$. The revealing evidence for this rather surprising assignment comes from the comparison with the equivalent complexes [Re(bipy)(CO)$_3$Cl]$^{\bullet-}$ (ν(CO) at 1998, 1885 and 1867 cm^{-1})[24] or [Re(4,4′-di-*t*Bu-bipy)(CO)$_3$Cl]$^{\bullet-}$ (ν(CO) at 1992, 1878 and 1860 cm^{-1})[46], taking into account the relative donor power of the bipy substituents (H, OH and *t*Bu). While [Re(3,3′-dhbipy)(CO)$_3$Cl]$^{\bullet-}$ is highly unstable at R1, where the facile single reductive deprotonation takes place (see above), it persists in the limited potential interval between the onset of R2′ and its own reduction coinciding with the R2′ maximum, which converts it ultimately to [Re(3,3′-dhbipy-2H$^+$)(CO)$_3$]$^{3-}$ (Figure 7.7). The transformation of [Re(3,3′-dhbipy-H$^+$)(CO)$_3$Cl]$^-$ to [Re(3,3′-dhbipy)(CO)$_3$Cl]$^{\bullet-}$ is a zero-electron, ETC reaction that kinetically dominates over the double reductive deprotonation of the 3,3′-dhbipy ligand. The latter process is triggered only by the subsequent electrochemical reduction of [Re(3,3′-dhbipy)(CO)$_3$Cl]$^{\bullet-}$, monitored accurately by the thin-layer cyclovoltammetric response. Thus, differently from the Re/4,4′-dhbipy congener, double-deprotonated [Re(3,3′-dhbipy-2H$^+$)(CO)$_3$Cl]$^{2-}$ can only be observed at ambient temperature at potentials more negative than the reduction potential of [Re(3,3′-dhbipy)(CO)$_3$Cl]$^{\bullet-}$ (experiment (b) in this section). The partly resolved electronic absorption of [Re(3,3′-dhbipy)(CO)$_3$Cl]$^{\bullet-}$ in the visible spectral region (around 480 nm) is shown in Figure 7A.6 (Appendix).

Summarizing the striking results in this section, the cathodic behavior of [Re(3,3′-dhbipy-H$^+$)(CO)$_3$Cl]$^-$ in THF at R2′ comprises a range of different processes. The initial 1e$^-$ reduction gives [Re(3,3′-dhbipy$^{\bullet-}$-H$^+$)(CO)$_3$Cl]$^{2-}$ stable at low temperature on the CV timescale, which converts by an ETC step at low overpotentials (the onset of R2′) to [Re(3,3′-dhbipy)(CO)$_3$Cl]$^{\bullet-}$ or undergoes the second dhbipy deprotonation at higher overpotentials to generate reactive [Re(3,3′-dhbipy-2H$^+$)(CO)$_3$Cl]$^{2-}$. In both cases, the ultimate reduction

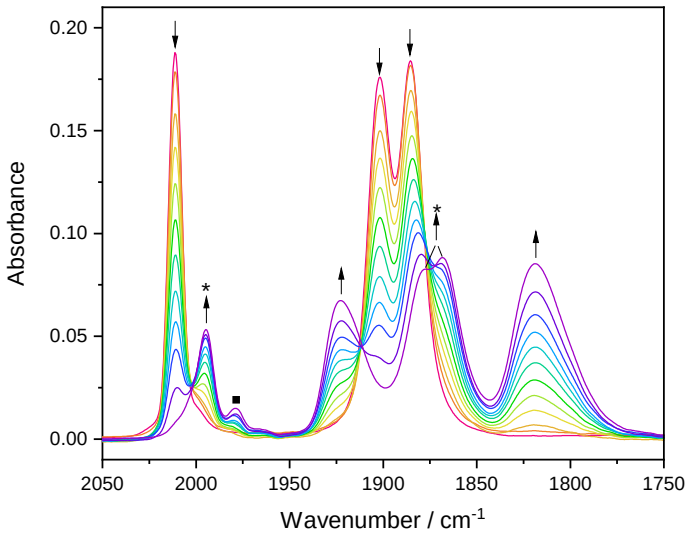

Figure 7.7: Cathodic potential-sweep IR spectroelectrochemistry at R2′ where starting $[Re(3,3'\text{-dhbipy-H}^+)(CO)_3Cl]^-$ (↓), undergoes $1e^-$ reduction and ETC conversion to $[Re(3,3'\text{-dhbipy})(CO)_3Cl]^{\bullet-}$ (*), and its subsequent reduction to $[Re(3,3'\text{-dhbipy-2H}^+)(CO)_3]^{3-}$ (↑). Conditions: an OTTLE cell, THF/Bu_4NPF_6, T = 298 K. The label ■ corresponds to an unassigned side product.

product at R2′ is the 5-coordinate π-delocalized complex $[Re(3,3'\text{-dhbipy-2H}^+)(CO)_3]^{3-}$, the double-deprotonated equivalent of $2e^-$-reduced $[Re(bipy)(CO)_3]^-$.

The following sections present cathodic IR SEC experiments with $[Re(3,3'\text{-dhbipy})(CO)_3Cl]$ conducted in THF following chemical deprotonation, and at low temperature in PrCN, to collect more supporting evidence for the intriguing cathodic path in Scheme 7.3.

Reduction of $[Re(3,3'\text{-dhbipy-H}^+)(CO)_3Cl]^-$ in THF at Ambient Temperature

The electrochemical reduction of chemically single-deprotonated $[Re(3,3'\text{-dhbipy-H}^+)(CO)_3Cl]^-$ (Figure 7.8) resembles strongly the potential-sweep IR spectroelectrochemical experiment at R2′ described in the preceding section. Notably, as visualized in the corresponding cyclic voltammogram (Figure 4), the separation of the initial cathodic wave (R2*) is more distinct, allowing the ETC-product $[Re(3,3'\text{-dhbipy})(CO)_3Cl]^{\bullet-}$ to be generated separately (Figure 7.8a), prior to its conversion to $[Re(3,3'\text{-dhbipy-2H}^+)(CO)_3]^{3-}$ at R2 (Figure 7.8b). The parallel UV-Vis monitoring of these two steps is presented in Figure 7A.6.

Given the facile deprotonation of the title complex at R1 to [Re(3,3′-dhbipy-H^+)$(CO)_3Cl]^-$, the formation of [Re(3,3′-dhbipy)$(CO)_3Cl]^{\bullet-}$ with 'restored' 3,3′-dhbipy in the radical anionic state may be considered as surprising. The initial formation of [Re(3,3′-dhbipy$^{\bullet-}$-H^+)$(CO)_3Cl]^{2-}$ at R2* (or the onset of R2′) was expected to trigger the second reductive deprotonation generating $\frac{1}{2}\,H_2$ and [Re(3,3′-dhbipy-$2H^+$)$(CO)_3Cl]^{2-}$. However, this process is apparently unfavorable for the clashing two phenoxide groups in the 3,3′-positions and there is a limited chance to delocalize the negative charges onto the ring nitrogens, differently from the Re/4,4′-dhbipy congener (Scheme 7.1). The singly reduced complex [Re(3,3′-dhbipy)$(CO)_3Cl]^{\bullet-}$ can be generated at R1* (Figure 7A.4, Appendix) but the formation of the strong intramolecular hydrogen bond in [Re(3,3′-dhbipy-H^+)$(CO)_3Cl]^-$ is favored and the radical anion of the title complex is then only restored at R2* where the hydrogen bond gets disrupted by the reduction localized at the π^*(bipy) LUMO. Obviously, this thermodynamic advantage is lost by the subsequent reduction of [Re(3,3′-dhbipy)$(CO)_3Cl]^{\bullet-}$ at more negative R2 (Figure 7.4), which leads directly to double-deprotonated [Re(3,3′-dhbipy-$2H^+$)$(CO)_3]^{3-}$ and no [Re(3,3′-dhbipy-$2H^+$)$(CO)_3Cl]^{2-}$ is detectable at ambient temperature during the potential sweep.

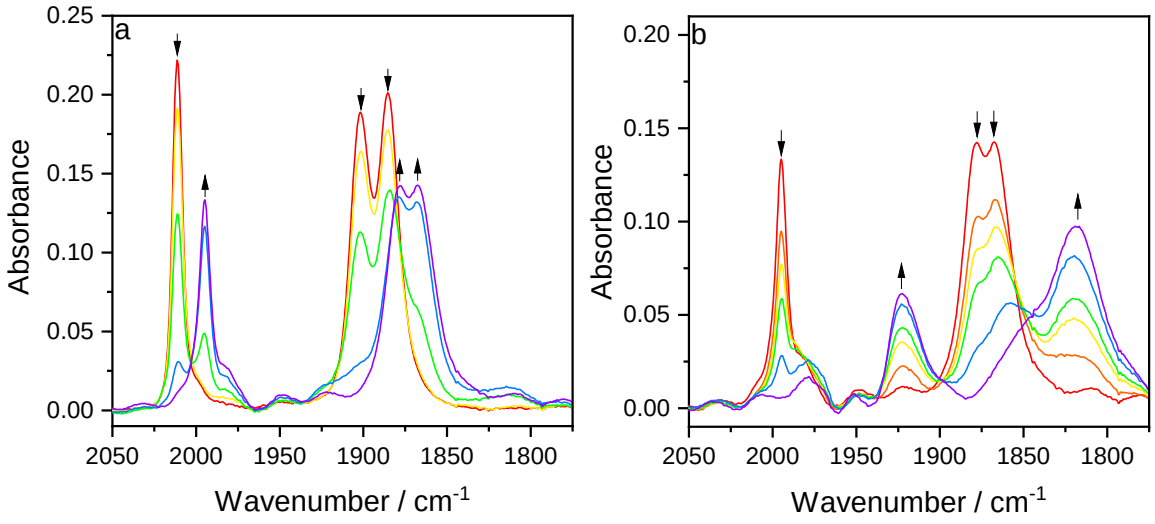

Figure 7.8: Cathodic IR spectroelectrochemistry showing (a) ETC conversion of [Re(3,3′-dhbipy-H^+)$(CO)_3Cl]^-$ (↓) at R2* (cf. Figure 7.4) to [Re(3,3′-dhbipy)$(CO)_3Cl]^{\bullet-}$ (↑), and (b) its subsequent reduction to [Re(3,3′-dhbipy-$2H^+$)$(CO)_3]^{3-}$ (↑) at R2. Conditions: an OTTLE cell, THF/Bu_4NPF_6, T = 298 K.

Reduction of [Re(3,3′-dhbipy)(CO)$_3$Cl] in PrCN at Variable Temperature

IR SEC experiments with [Re(3,3′-dhbipy)(CO)$_3$Cl] in PrCN at 223 K (Figure 7.9) and 258 K (Figure 7.10) complement the description of the tangled cathodic path in THF at ambient temperature (Figures 7.1 and 7.6-7.8). The first cathodic step at R1 results also in PrCN in the instant formation of [Re(3,3′-dhbipy-H$^+$)(CO)$_3$Cl]$^-$ independently of the temperature. Only the reduction process at R2′ (Figure 2) depends strongly on the electrolyte temperature. At 223 K, the Re–Cl bond remains sufficiently stable in the reduced state to allow the direct observation of the double-deprotonated complex, [Re(3,3′-dhbipy-2H$^+$)(CO)$_3$Cl]$^{2-}$, with ν(CO) absorption bands at 2002, 1885 and 1866 cm^{-1} (Figure 7.9). Notably, for Re/4,4′-dhbipy the corresponding dianionic complex is stable already at room temperature[46], exhibiting comparable ν(CO) wavenumbers (Table 7.2 – considered in this work still as 6-coordinate, with the Re–Cl bond intact). As the IR SEC experiment at 223 K progresses there is evidence for the formation of a small amount of a secondary product absorbing at 1967, 1849 and 1835 cm^{-1} (Figure 7.9). The latter compound becomes the dominant observable product already during the reduction of [Re(3,3′-dhbipy-H$^+$)(CO)$_3$Cl]$^-$ at R2′ when the electrolyte temperature is elevated to 258 K; its precursor [Re(3,3′-dhbipy-2H$^+$)(CO)$_3$Cl]$^{2-}$ is almost not perceptible during the IR spectral monitoring at this temperature (Figure 7.10). This development is consistent with the cleavage of the Re–Cl bond in [Re(3,3′-dhbipy-2H$^+$)(CO)$_3$Cl]$^{2-}$ and coordination of a PrCN solvent molecule in the vacated position. Indeed, the above ν(CO) wavenumbers can be ascribed to the 6-coordinate (solvento) analogue of 5-coordinate [Re(3,3′-dhbipy-2H$^+$)(CO)$_3$]$^{3-}$ seen at room temperature in weakly coordinating THF (Figures 7.5-7.7), that is, [Re(3,3′-dhbipy-2H$^+$)(CO)$_3$(PrCN)]$^{3-}$ (Table 7.2). The reference complex [Re(bipy)(CO)$_3$(PrCN)], lacking the two donor phenoxide groups, absorbs in the IR ν(CO) region consistently at higher wavenumbers, viz. 1980, 1861 and 1851 cm^{-1}; the stability of the PrCN-coordinated Re center increases by lowering the temperature.[24]

At room temperature, [Re(3,3′-dhbipy-H$^+$)(CO)$_3$Cl]$^-$ formed at R1 (Figures 7A.7a and 7A.7b, Appendix) becomes further reduced at R2′ to give a mixture of products (Fig-

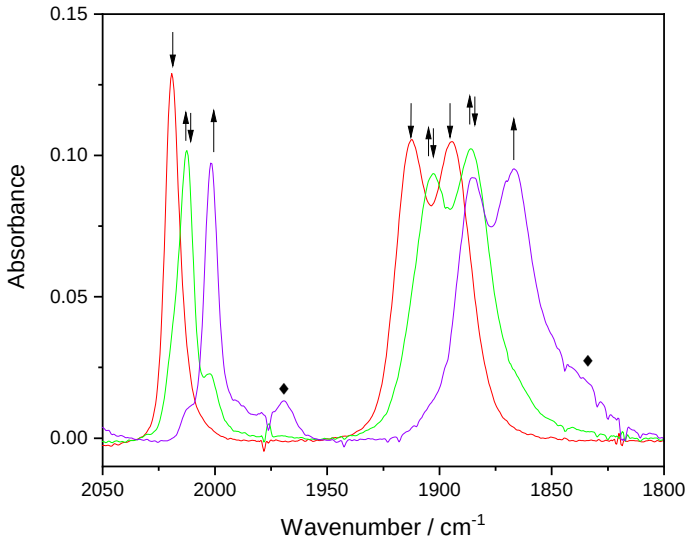

Figure 7.9: Cathodic IR spectroelectrochemistry of [Re(3,3′-dhbipy)$(CO)_3$Cl] (↓) in PrCN/Bu_4NPF_6 at 223 K. The parent complex undergoes two successive reductive deprotonations yielding [Re(3,3′-dhbipy-H^+)$(CO)_3$Cl]$^-$ (↑↓) at R1, and [Re(3,3′-dhbipy-$2H^+$)$(CO)_3$Cl]$^{2-}$ (↑) at R2′. The label ♦ indicates the presence of a small amount of [Re(3,3′-dhbipy-$2H^+$)$(CO)_3$(PrCN)]$^{3-}$ as a secondary product resulting from the dissociation of the Re–Cl bond in the double-deprotonated precursor complex.

ure 7A.7c, Appendix), starting with the radical anion of the parent complex, [Re(3,3′-dhbipy)$(CO)_3$Cl]$^{\bullet-}$ detectable also in THF along the ETC path (see above). Importantly, no [Re(3,3′-dhbipy-$2H^+$)$(CO)_3$Cl]$^{2-}$ seems to be formed in this case (cf. Figure 7.8b). The subsequent 6-coordinate, double-deprotonated reduction product, [Re(3,3′-dhbipy-$2H^+$)$(CO)_3$(PrCN)]$^{3-}$, which replaces the 5-coordinate analogue [Re(3,3′-dhbipy-$2H^+$)$(CO)_3$]$^{3-}$ in the PrCN electrolyte, appears to co-exist initially with its $1e^-$ oxidized form, [Re(3,3′-dhbipy-$2H^+$)$(CO)_3$(PrCN)]$^{2-}$ (ν(CO) at 1986 and 1874br cm^{-1}). For comparison, the reference radical [Re(bipy)$(CO)_3$(PrCN)] with less donating bipy$^{\bullet-}$ absorbs in the ν(CO) region at 2010 and 1895br cm^{-1}.[24] At the $1e^-$ bipy-reduced level, the additional double deprotonation of the 3,3′-dhbipy ligand in [Re(3,3′-dhbipy-$2H^+$)$(CO)_3$(PrCN)]$^{2-}$ shifts the ν(CO) bands to smaller wavenumbers again by ca. 20 cm^{-1}. The PrCN coordination can be distinguished by the local C_{3v} symmetry at the Re center and the two ν(CO) absorption bands belonging to the A1 + E modes. Toward the end of the cathodic step at R2′, the radical species [Re(3,3′-dhbipy-$2H^+$)$(CO)_3$(PrCN)]$^{2-}$ was further reduced to the 6-coordinate

trianion. Differently from the situation at 258 K, $[Re(3,3'\text{-dhbipy-}2H^+)(CO)_3(PrCN)]^{3-}$ formed in an equilibrium with 5-coordinate $[Re(3,3'\text{-dhbipy-}2H^+)(CO)_3]^{3-}$ (Figure 7A.7d, Appendix).

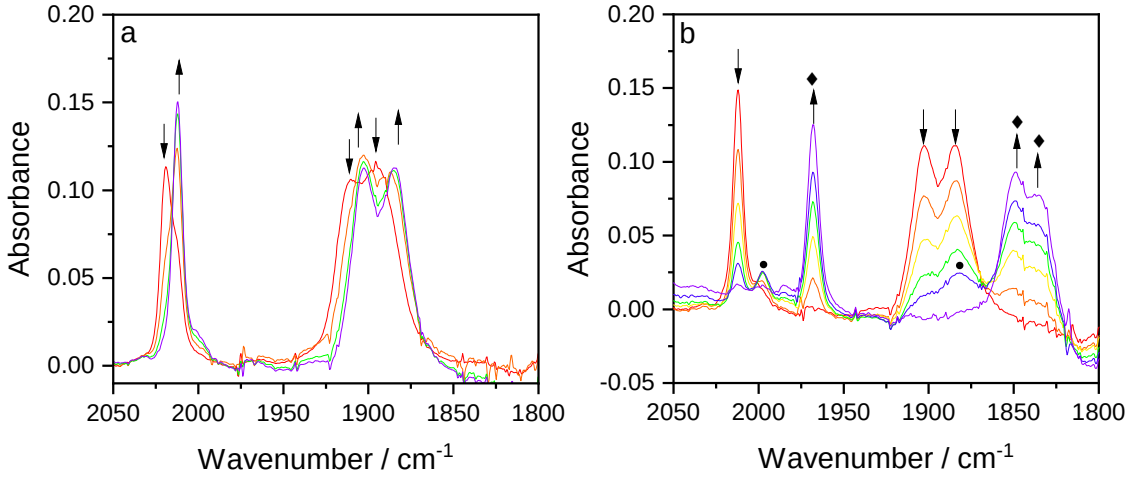

Figure 7.10: Cathodic IR spectroelectrochemistry of $[Re(3,3'\text{-dhbipy})(CO)_3Cl]$ (↓) in PrCN/Bu_4NPF_6 at 258 K. (a) Conversion of the parent complex to $[Re(3,3'\text{-dhbipy-}H^+)(CO)_3Cl]^-$ (↑) at R1. (b) Reductive transformation of $[Re(3,3'\text{-dhbipy-}H^+)(CO)_3Cl]^-$ (↓) at R2′ to transient $[Re(3,3'\text{-dhbipy-}2H^+)(CO)_3Cl]^{2-}$ denoted by •, and dominant $[Re(3,3'\text{-dhbipy-}2H^+)(CO)_3(PrCN)]^{3-}$ (♦).

Reduction of $[Re(3,3'\text{-dhbipy})(CO)_3(PrCN)]^+$ in PrCN at Variable Temperature

The reductive deprotonation of the 3,3′-dhbipy ligand was also investigated at the more electron-deficient Re center in the complex $[Re(3,3'\text{-dhbipy})(CO)_3(PrCN)]^+$ (ν(CO) at 2039, 1933br cm^{-1}) prepared instantly in the PrCN electrolyte from the precursor $[Re(3,3'\text{-dhbipy})(CO)_3(OTf)]$ (absorbing in THF at ν(CO) 2032, 1928, 1910 cm^{-1}). The cationic complex undergoes smooth reductive deprotonation at R1 (Figure 7.3) producing $[Re(3,3'\text{-dhbipy-}H^+)(CO)_3(PrCN)]$, as testified by the characteristic < 10 cm^{-1} shift to smaller ν(CO) wavenumbers (Figure 7.11a, Table 7.2). Based on this observation, the facile reductive deprotonation of 3,3′-dhbipy hardly depends on the axial ligand. It also proves that after the first reduction at R1, singly deprotonated 3,3′-dhbipy-H^+ remains chelated in the N,N′-coordination mode (the local C_{3v} symmetry), for the ν(CO) A1 + E pattern of the precursor is preserved.

The subsequent reduction of $[Re(3,3'\text{-dhbipy-}H^+)(CO)_3(PrCN)]$ at R2′ is again decid-

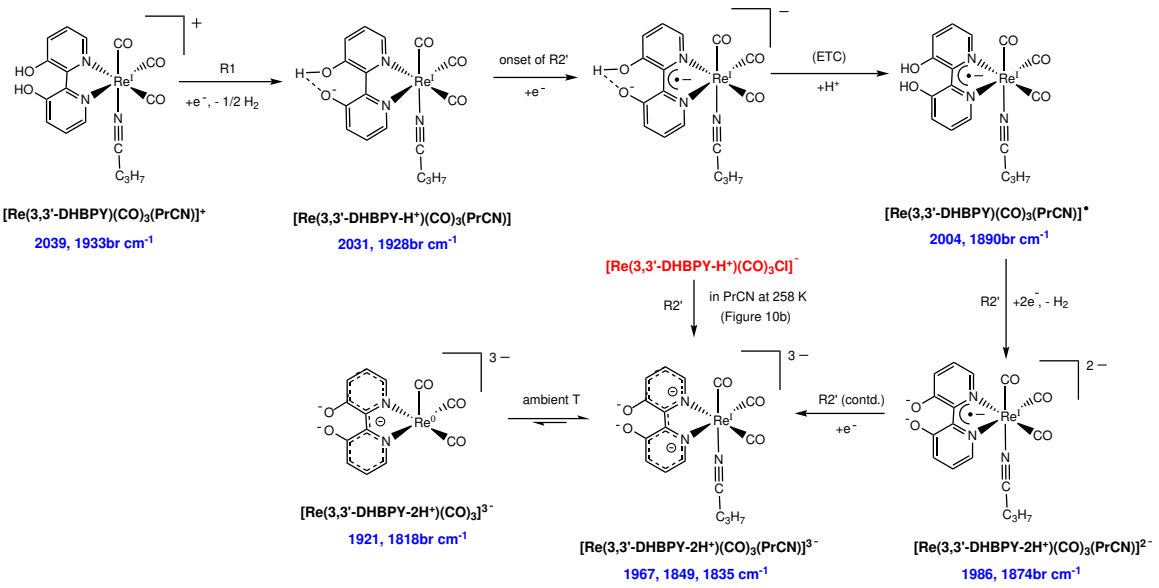

Scheme 7.4: Cathodic pathway of $[Re(3,3'\text{-dhbipy})(CO)_3(PrCN)]^+$ in PrCN. First $1e^-$ reductive deprotonation at R1 followed by the ETC pathway at the onset of R2′ that produces the corresponding radical of the parent complex, $[Re(3,3'\text{-dhbipy})(CO)_3(PrCN)]^\bullet$. The ultimate $2e^-$ reductive double deprotonation at R2′ is triggered by the concomitant reduction of the ETC product, resulting in 6-coordinate $[Re(3,3'\text{-dhbipy-}2H^+)(CO)_3(PrCN)]^{2-}$ and its reduced trianionic form isoelectronic with $[Re(bipy)(CO)_3(PrCN)]^-$.

edly more complex, generating initially a new species absorbing in the IR ν(CO) region at 2004, 1890br cm^{-1} (Figure 7.11b). These wavenumbers are too small to correspond to the reductively double-deprotonated complex $[Re(3,3'\text{-dhbipy-}2H^+)(CO)_3(PrCN)]^-$ (Table 7.2). In analogy with the above ETC path of $[Re(3,3'\text{-dhbipy-}H^+)(CO)_3Cl]^-$ at R2′ producing $[Re(3,3'\text{-dhbipy})(CO)_3Cl]^{\bullet-}$ (Scheme 7.3), we assign the intermediate as the non-deprotonated radical $[Re(3,3'\text{-dhbipy})(CO)_3(PrCN)]$ existing in the limited cathodic potential range between the onset and the maximum of R2′ where it reduces further (Scheme 7.4). In support of this assignment, $[Re(bipy)(CO)_3(PrCN)]$ with the weaker bipy donor absorbs at slightly larger wavenumbers, viz. 2010 and 1895br cm^{-1}.[59] The ultimate cathodic step encompassed in the potential scan at R2′ is the conversion of $[Re(3,3'\text{-dhbipy})(CO)_3(PrCN)]$ into the double-deprotonated complex with the $2e^-$ reduced aromatic bipy system, viz. $[Re(3,3'\text{-dhbipy-}2H^+)(CO)_3(PrCN)]^{3-}$, and its $1e^-$ oxidized form (Figure 7.11b), reflecting the redox equilibrium observed already at the terminal stage of the cathodic path of $[Re(3,3'\text{-dhbipy})(CO)_3Cl]$ in PrCN (Figure 7A.7c-d, Appendix). The electrochemical reduction of

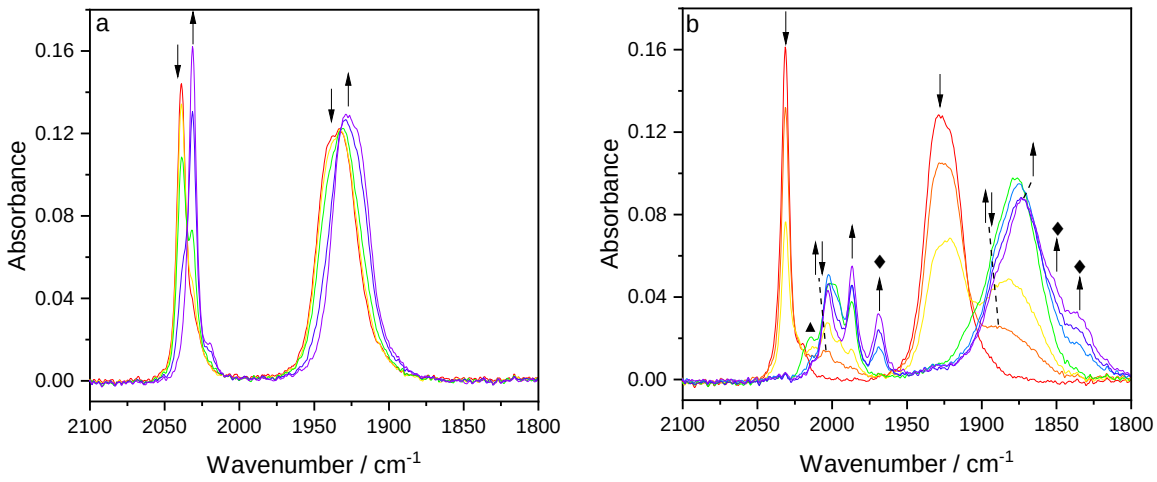

Figure 7.11: Cathodic IR spectroelectrochemistry of $[Re(3,3'\text{-dhbipy})(CO)_3PrCN]^+$ in PrCN/Bu_4NPF_6 at 298 K. (a) $1e^-$ reduction of the parent complex (↓) at R1 producing deprotonated $[Re(3,3'\text{-dhbipy-H}^+)(CO)_3(PrCN)]$ (↑). (b) Subsequent reduction of $[Re(3,3'\text{-dhbipy-H}^+)(CO)_3(PrCN)]$ (↓) at R2′ to give initially the $1e^-$ reduced ETC-species $[Re(3,3'\text{-dhbipy})(CO)_3(PrCN)]$ (↑↓), which further converts cathodically to the double-deprotonated and $2e^-$ reduced 6-coordinate species, $[Re(3,3'\text{-dhbipy-2H}^+)(CO)_3(PrCN)]^{3-}$ (♦), in redox equilibrium with its $1e^-$ oxidized radical form, $[Re(3,3'\text{-dhbipy-2H}^+)(CO)_3(PrCN)]^{2-}$ (↑). The label ▲ denotes an unassigned reduced intermediate.

$[Re(3,3'\text{-dhbipy})(CO)_3(PrCN)]^+$ in PrCN at 223 K (Figure 7A.8, Appendix) follows the same path as described above at ambient temperature (Scheme 7.4).

The only notable difference is the appearance of the reductively double-deprotonated complex $[Re(3,3'\text{-dhbipy-2H}^+)(CO)_3(PrCN)]^-$, although only as a minor intermediate when reducing $[Re(3,3'\text{-dhbipy-H}^+)(CO)3(PrCN)]$ at R2′ (Figure 7A.8b, Appendix). It is important to reiterate that analogous $[Re(3,3'\text{-dhbipy-2H}^+)(CO)_3Cl]^{2-}$ was stable under the same conditions (Figure 7.9).

7.4.3 Cyclic Voltammetry and IR Spectroelectrochemistry in CO_2-Saturated THF

The cathodic wave R1 of $[Re(3,3'\text{-dhbipy})(CO)_3Cl]$, slightly shifted to $E_{p,c}$ = -1.09 V vs Fc/Fc^+ and further broadened in the THF electrolyte saturated with CO_2, was passed without any significant increase in the peak current compared to the CV scan under argon (Figure 7.12). On the other hand, the second wave R2′ near -2.40 V vs Fc/Fc^+ led to a high

current increase, indicative of catalytic CO_2 reduction. This behavior coincides with the generation of the $2e^-$ reduced 5-coordinate complex $[Re(3,3'\text{-dhbipy-}2H^+)(CO)_3]^{3-}$ (Scheme 7.3, Figures 7.5c,d), the double-deprotonated equivalent of $[Re(bipy)(CO)_3]^-$ as one of the iconic catalysts for the CO_2 conversion to CO.[59] We cannot confirm an active role of the transient 5-coordinate species $[Re(3,3'\text{-dhbipy-}2H^+)(CO)_3]^-$ in the catalytic mechanism, as proposed by Fujita and co-workers for $[Re(4,4'\text{-dhbipy-}2H^+)(CO)_3]^-$ (see Scheme 7.1).[46] According to the ν(CO) pattern (Figures 7.6 and 7.9), the detectable double-deprotonated complex is still 6-coordinate, viz. $[Re(3,3'\text{-dhbipy-}2H^+)(CO)_3Cl]^{2-}$. The Cl^- dissociation at elevated temperature results in weakly coordinating THF to ultimate cathodic generation of $[Re(3,3'\text{-dhbipy-}2H^+)(CO)_3]^{3-}$ which is isoelectronic with $[Re(bipy)(CO)_3]^-$, each phenoxide group lowering the ν(CO) wavenumbers by ca. 10 cm^{-1} compared to the unsubstituted bipy ligand.

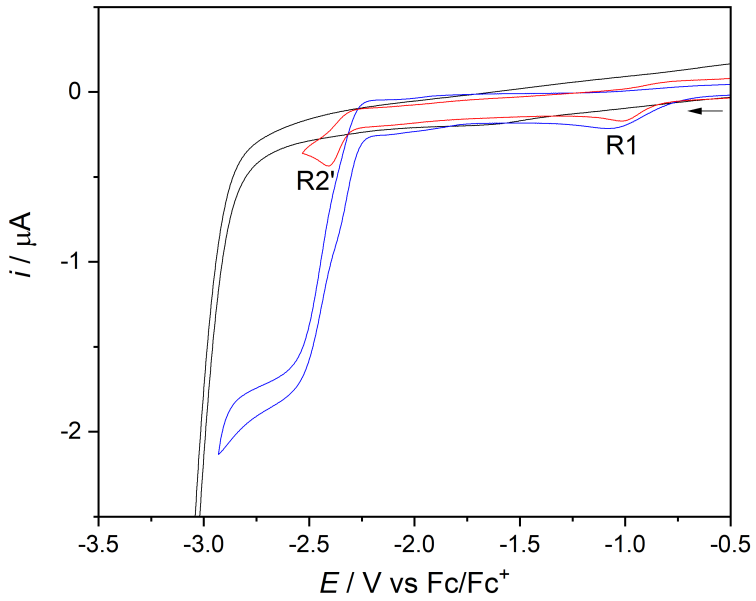

Figure 7.12: Cyclic voltammograms of $[Re(3,3'\text{-dhbipy})(CO)_3Cl]$ in THF/Bu_4NPF_6 saturated with argon (red curve) and CO_2 (blue curve). The black curve represents the background CV of CO_2 dissolved in the electrolyte. Experimental conditions: Pt microdisc, T = 298 K, υ = 100 mV s^{-1}.

Cathodic IR spectroelectrochemistry of $[Re(3,3'\text{-dhbipy})(CO)_3Cl]$ in the THF electrolyte saturated with CO_2 was conducted to probe the catalytic process triggered at the ca-

thodic wave R2′ (Figure 13). Passing the initial cathodic wave R1 reveals again the smooth transformation of the parent complex to [Re(3,3′-dhbipy-H$^+$)(CO)$_3$Cl]$^-$ while the $^{13}CO_2$ satellite absorption remains intact (Figure 13a). The situation changes at R2′ where the $^{13}CO_2$ band rapidly drops and the absorption of free CO at 2135 cm^{-1} is clearly detectable together with that of free HCO_3^- at 1675 and 1641 cm^{-1} (Figure 13b).[61] At the same time, the ν(CO) bands of [Re(3,3′-dhbipy-H$^+$)(CO)$_3$Cl]$^-$ have only slightly decreased, reflecting the efficient catalytic transformation of CO_2 to CO. As expected, the catalyst of the latter process, viz. [Re(3,3′-dhbipy-2H$^+$)(CO)$_3$]$^{3-}$ generated at R2′ (Figure 7.7), is not observable in the presence of CO_2 dissolved in the electrolyte. The strong catalytic performance triggered by the reduction of [Re(3,3′-dhbipy-H$^+$)(CO)$_3$Cl]$^-$ resembles [Re(bipy)(CO)$_3$Cl] in acetonitrile, where 2e$^-$ reduced [Re(bipy)(CO)$_3$]$^-$ is formed already at the cathodic wave of the parent complex.[24]

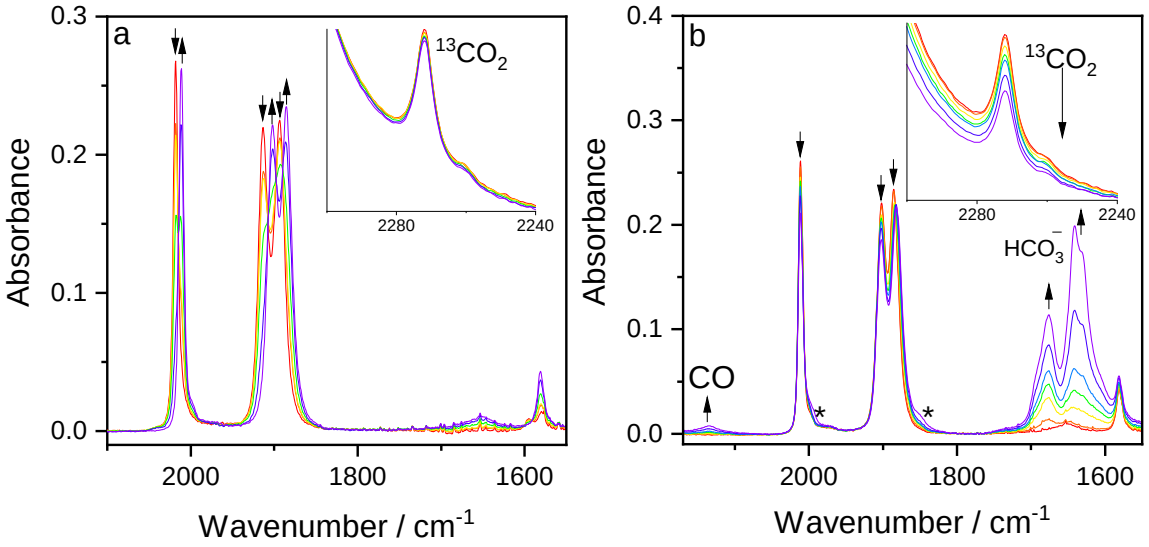

Figure 7.13: IR spectroelectrochemistry of [Re(3,3′-dhbipy)(CO)$_3$Cl] in CO_2-saturated THF/Bu_4NPF_6. (a) Reduction at R1 - reductive deprotonation forming [Re(3,3′-dhbipy-H$^+$)(CO)$_3$Cl]$^-$ (↑). (b) Reduction at R2′ - efficient electrocatalytic conversion of CO_2 to CO, with a minor appearance of free bicarbonate. Inset: the reference $^{13}CO_2$ satellite band. Asterisk indicates a minor amount of [Re(3,3′-dhbipy)(CO)$_3$Cl]$^{\bullet-}$ (cf. Figure 7.7).

7.4.4 Coulometry of [Re(3,3′-dhbipy)(CO)$_3$Cl] in CO$_2$-saturated THF

In order to verify the catalytic activity revealed by cyclic voltammetry and IR spectroelectrochemistry, bulk electrolysis measurements (Figures 7A.9 and 7A.10, Appendix) were carried out under CO_2 at the catalytic potential of -2.6 V vs Fc/Fc^+, using foil and microdisc Pt working electrodes for the 3 mM catalyst precursor in THF/0.5 M $TBAPF_6$. Two different cells were used to accurately determine the faradic efficiency (at the small Pt microdisc) and turnover numbers (at the larger Pt foil). The results have revealed that the current enhancement under CO_2 is due to its catalytic conversion to CO, consistent with the reductive disproportionation mechanism: $2\,CO_2 + 2\,e^- \longrightarrow CO + CO_3^{2-}$.[15,33] By headspace gas chromatography, an excellent selectivity for CO_2 reduction was observed. After 1 h, the total faradaic efficiency was 83% (82% for CO and 1% for H_2), with a turnover number of 2.3 (increasing to 3.8 after 3 h). At the smaller microdisc electrode, roughly 0.31 Coulombs passed in 1 h (Figure 7A.9, Appendix); at the same time, the charge passed at the larger foil electrode was roughly 11 Coulombs (Figure 7A.10, Appendix). The corresponding control experiment under argon, using the foil electrode, produced only trace amounts of CO detected by GC, and only 0.43 Coulombs passed (Figure 7A.11, Appendix).

7.5 Conclusions

Much like the earlier reported[46] complex [Re(4,4′-dhbipy)(CO)$_3$Cl], [Re(3,3′-dhbipy)(CO)$_3$Cl] also undergoes facile reductive deprotonation generating [Re(3,3′-dhbipy-H^+)(CO)$_3$Cl]$^-$. The stabilizing strong intraligand hydrogen bonding in 3,3′-dhbipy-H^+ is the most likely reason for the unusually large positive shift of the reduction potential, $E_{p,c}$,(R1), and the instantaneous deprotonation in basic DMF compared to the other two isomers. The Cl^- ligand in [Re(3,3′-dhbipy-H^+)(CO)$_3$Cl]$^-$ can be replaced with PrCN; however, this substitution reaction does not occur along the cathodic path and [Re(3,3′-dhbipy-H^+)(CO)$_3$Cl]$^-$ remains stable in PrCN under ambient conditions. On the other hand, the second reductive deprotonation at $E_{p,c}$ (R2′) produces [Re(3,3′-dhbipy-$2H^+$)(CO)$_3$Cl]$^{2-}$ that is only stable at

sufficiently low temperature (223 K in PrCN). The 6-coordinate geometry and the preserved Re–Cl bond in the latter dianion are strongly supported by the 2A′ + A″ ν(CO) band pattern (Cs geometry).

The ν(CO) wavenumbers in the [Re(x,x′-dhbipy-2H$^+$)(CO)$_3$Cl]$^{2-}$ (x = 3 and 4) series are very similar. For x = 4 the reductively double-deprotonated species was formulated[46] as a (stable) 5-coordinate complex [Re(4,4′-dhbipy-2H$^+$)(CO)$_3$]$^-$; however, this does not correspond with the fluxionality of the Re(CO)$_3$ moiety and the modest low-energy shift of the ν(CO) wavenumbers, ca. 10 cm^{-1} per each deprotonating step. No evidence for [Re(3,3′-dhbipy-2H$^+$)(CO)$_3$]$^-$ has also been obtained at room temperature in weakly coordinating THF. Instead, the cleavage of the Re–Cl bond at the cathodic wave R2′ induces a concomitant transfer of two extra electrons placed in the aromatic bipy system of the 3,3′-dhbipy-2H$^+$ ligand. The ultimate reduction product, 5-coordinate [Re(3,3′-dhbipy-2H$^+$)(CO)$_3$]$^{3-}$, reveals a high degree of π-delocalization of the added electron pair over the Re tricarbonyl unit, similar to the bonding situation in reference[24,58] Re(bipy)(CO)$_3$]$^-$. The alternative cathodic transformation of [Re(3,3′-dhbipy-H$^+$)(CO)$_3$Cl]$^-$ to [Re(3,3′-dhbipy-2H$^+$)(CO)$_3$]$^{3-}$ at R2′ begins with an ETC process at the onset of the wave, which counterintuitively produces the radical anion of the parent complex, [Re(3,3′-dhbipy)(CO)$_3$Cl]$^{\bullet -}$. A similar cathodic path is followed by the cationic derivative [Re(3,3′-dhbipy)(CO)$_3$(PrCN)]$^+$ that smoothly reductively deprotonates at R1 to [Re(3,3′-dhbipy-H$^+$)(CO)$_3$(PrCN)], followed by the ETC step at R2′ generating the radical [Re(3,3′-dhbipy)(CO)$_3$(PrCN)]. In the ultimate reduction step encompassed by the R2′ sequence in PrCN, 6-coordinate [Re(3,3′-dhbipy-2H$^+$)(CO)$_3$(PrCN)]$^{3-}$ replaces the 5-coordinate trianion seen in weakly coordinating THF. This also applies for the cathodic path of [Re(3,3′-dhbipy)(CO)$_3$Cl] in PrCN at low temperature. Finally, [Re(3,3′-dhbipy-2H$^+$)(CO)$_3$]$^{3-}$ was found in THF to catalyze 2e$^-$ reductive disproportionation of CO$_2$ to CO with 82% current efficiency, as revealed by IR spectroelectrochemistry and coulometry combined with gas chromatography. The modest catalytic performance places the precursor [Re(3,3′-dhbipy)(CO)$_3$Cl] between more efficient Re/4,4′-dhbipy and poorly performing Re/6,6′-dhbipy congeners.[46] This difference can be ascribed

to higher nucleophilicity of the nitrogen atoms in chelated $[4,4'\text{-dhbipy-}2H^+]^{2-}$ (see the resonance structure in Scheme 7.1) compared to $[3,3'\text{-dhbipy-}2H^+]^{2-}$.

7.6 Appendix to Chapter 7

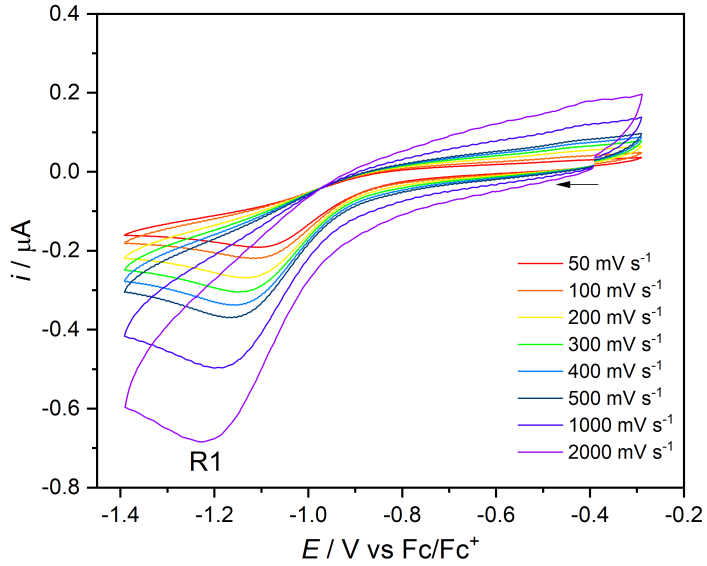

Figure 7A.1: Cyclic voltammograms of $[Re(3,3'\text{-dhbipy})(CO)_3Cl]$ in THF/Bu_4NPF_6 in the region of R1. Experimental conditions: Pt microdisc, $T = 298$ K, scan rates $\upsilon = 50$ - 2000 mV s^{-1}. Arrow indicates the initial scan direction.

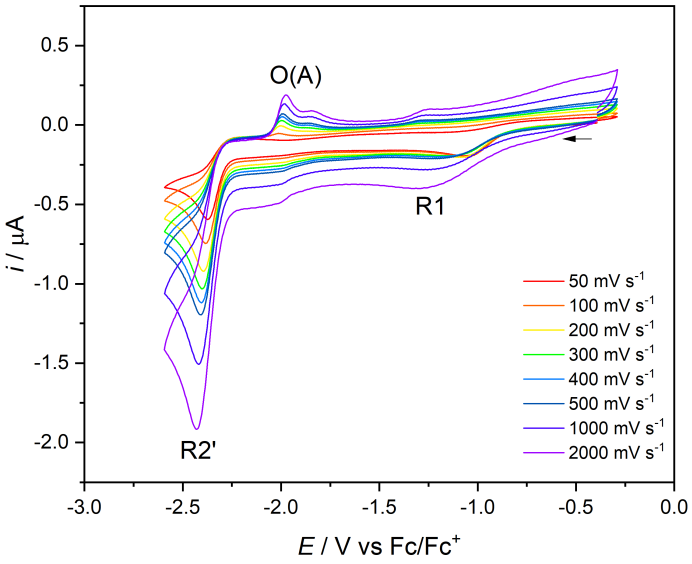

Figure 7A.2: Cyclic voltammograms of [Re(3,3′-dhbipy)$(CO)_3$Cl] in THF/Bu_4NPF_6 across the full cathodic region. Experimental conditions: Pt microdisc, T = 298 K, scan rates υ = 50 - 2000 mV s^{-1}. Arrow indicates the initial scan direction.

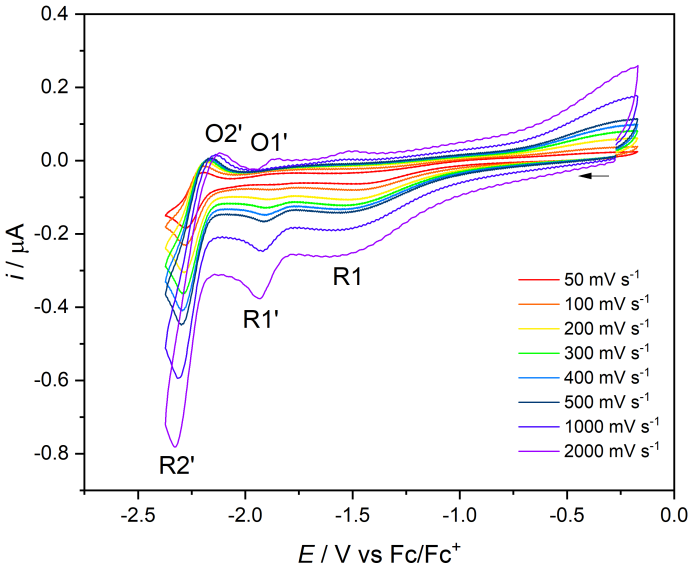

Figure 7A.3: Cyclic voltammograms of [Re(3,3′-dhbipy)$(CO)_3$Cl] in THF/Bu_4NPF_6 across the full cathodic region. Experimental conditions: Pt microdisc, T = 195 K, scan rates υ = 50 - 2000 mV s^{-1}. Arrow indicates the initial scan direction.

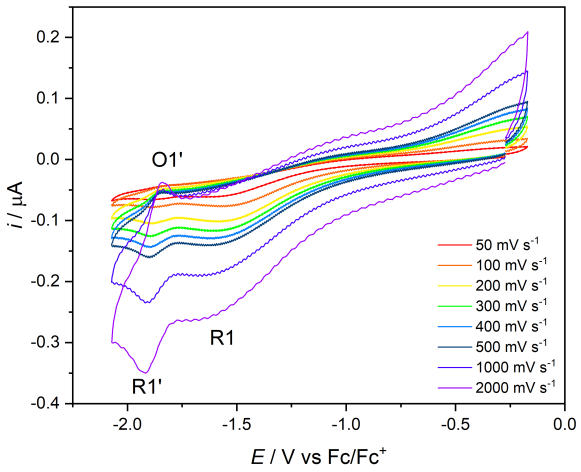

Figure 7A.4: Cyclic voltammograms of [Re(3,3′-dhbipy)$(CO)_3$Cl] in THF/Bu_4NPF_6 up to R1*. Experimental conditions: Pt microdisc, T = 195 K, scan rates υ = 50 - 2000 mV s^{-1}. Arrow indicates the initial scan direction.

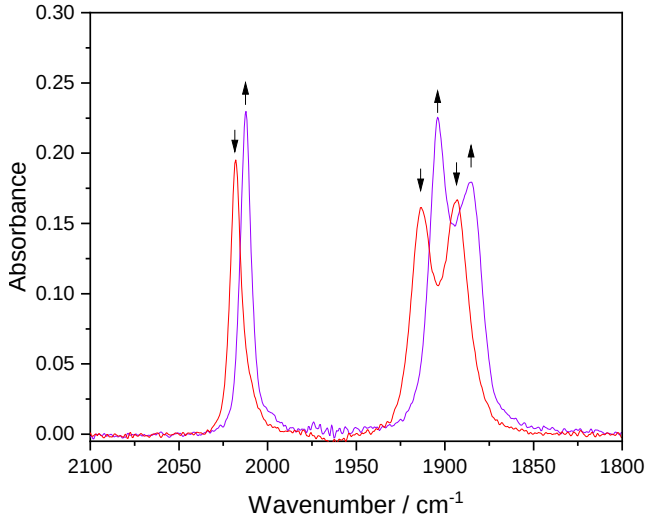

Figure 7A.5: Chemical deprotonation of [Re(3,3′-dhbipy)$(CO)_3$Cl] to [Re(3,3′-dhbipy-H^+)$(CO)_3$Cl]$^-$ in THF caused by the addition of 1 equiv. NaHMDS.

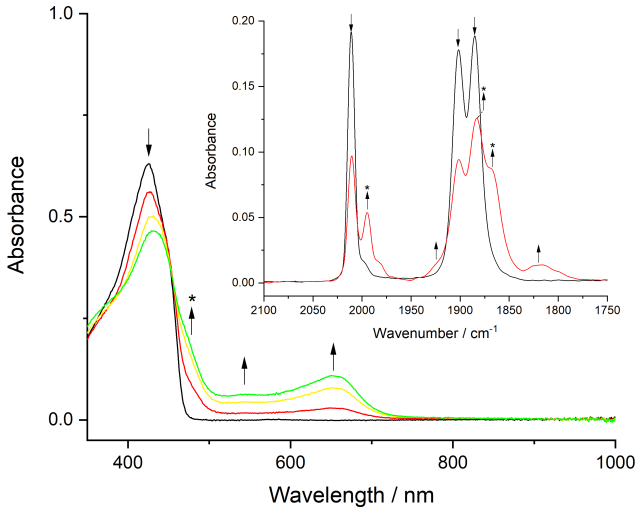

Figure 7A.6: Cathodic potential-sweep UV-Vis spectroelectrochemistry with parallel IR monitoring (inset) at R2* (cf. Figure 7.4) where parent single-deprotonated $[Re(3,3'\text{-dhbipy-H}^+)(CO)_3Cl]^-$ (↓) undergoes $1e^-$ reduction and ETC conversion to $[Re(3,3'\text{-dhbipy})(CO)_3Cl]^{\bullet -}$ (*) and the subsequent reduction of the latter intermediate at close-lying R2 to $[Re(3,3'\text{-dhbipy-2H}^+)(CO)_3]^{3-}$ (↑). Conditions: an OTTLE cell, THF/Bu_4NPF_6, $T = 298$ K.

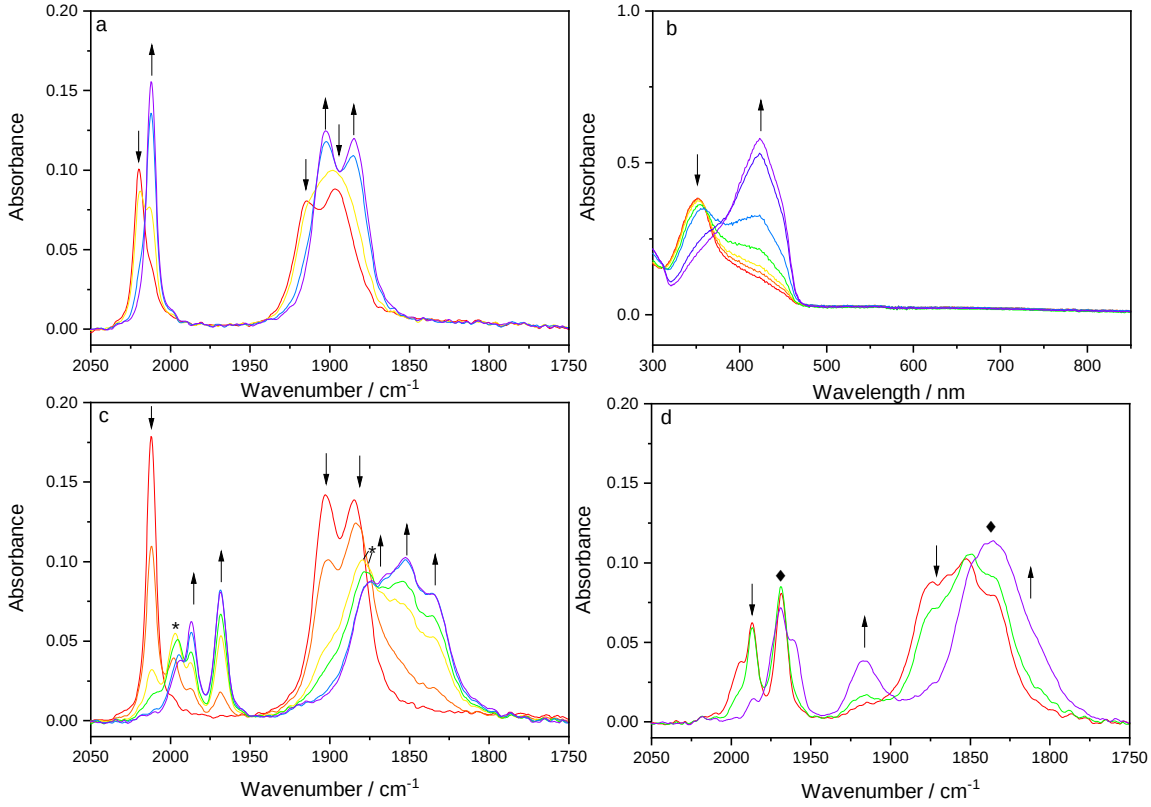

Figure 7A.7: (a) IR and (b) UV-Vis spectroelectrochemistry of [Re(3,3′-dhbipy)$(CO)_3$Cl] (↓) in PrCN/Bu_4NPF_6 at 298 K as it is converted by reductive deprotonation at R1 to [Re(3,3′-dhbipy-H^+)$(CO)_3$Cl]$^-$ (↑) in an OTTLE cell. (c) IR spectroelectrochemistry of [Re(3,3′-dhbipy-H^+)$(CO)_3$Cl]$^-$ (↓) as it undergoes, 1e$^-$ reduction at the onset of R2′ and ETC conversion to [Re(3,3′-dhbipy)$(CO)_3$Cl]$^{\bullet-}$ (*). The latter radical anion is further reduced on scanning through R2′, forming the 6-coordinate redox couple [Re(3,3′-dhbipy-2H^+)$(CO)_3$(PrCN)]$^{n-}$ (n = 2, 3) (↑) existing in redox equilibrium (cf. Figure 11). (d) [Re(3,3′-dhbipy-2H^+)$(CO)_3$(PrCN)]$^{2-}$ (↓) continues to reduce by a small negative potential shift, generating mainly 5-coordinate [Re(3,3′-dhbipy-2H^+)$(CO)_3$]$^{3-}$ (↑) in equilibrium with 6-coordinate [Re(3,3′-dhbipy-2H^+)$(CO)_3$(PrCN)]$^{3-}$ (⧫).

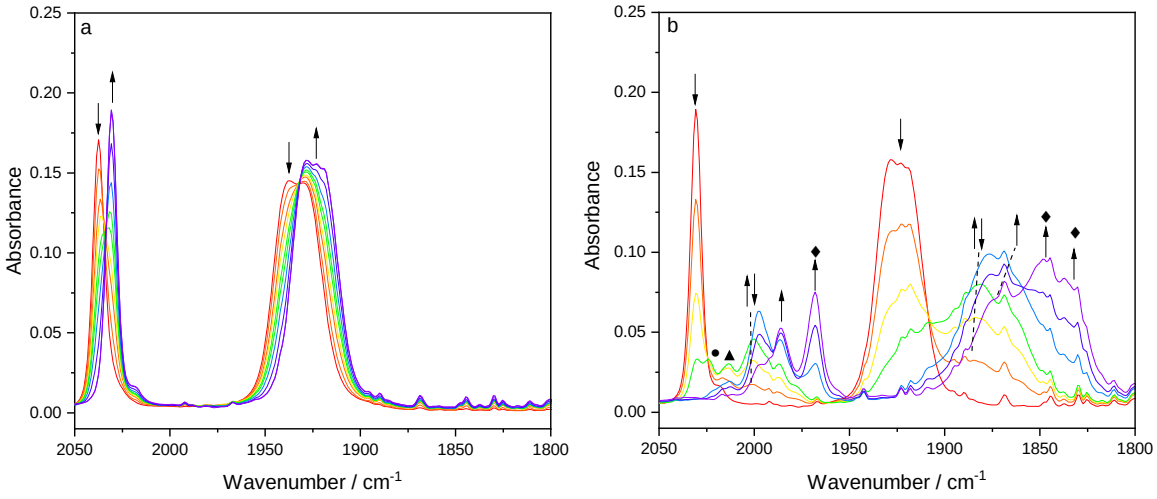

Figure 7A.8: Cathodic IR spectroelectrochemistry of $[Re(3,3'\text{-dhbipy})(CO)_3(PrCN)]^+$ in $PrCN/Bu_4NPF_6$ at 223 K. (a) $1e^-$ reduction of the parent complex (↓) at R1 producing deprotonated $[Re(3,3'\text{-dhbipy-H}^+)(CO)_3(PrCN)]$ (↑). (b) Subsequent reduction of $[Re(3,3'\text{-dhbipy-H}^+)(CO)_3(PrCN)]$ (↓) at R2′ to give a mixture of products with dominating $[Re(3,3'\text{-dhbipy})(CO)_3(PrCN)]$ (↑↓) formed in an ETC step. The small band labelled with • may belong to marginal reductively double-deprotonated $[Re(3,3'\text{-dhbipy-2H}^+)(CO)_3(PrCN)]^-$. It's $1e^-$ and $2e^-$ reduced forms, $[Re(3,3'\text{-dhbipy}^{\bullet-}\text{-2H}^+)(CO)_3(PrCN)]^{2-}$ (↑) and $[Re(3,3'\text{-dhbipy-2H}^+)(CO)_3(PrCN)]^{3-}$ (⧫), terminate the cathodic path. The label ▲ denotes an unassigned reduced intermediate (see also Figure 7.11b).

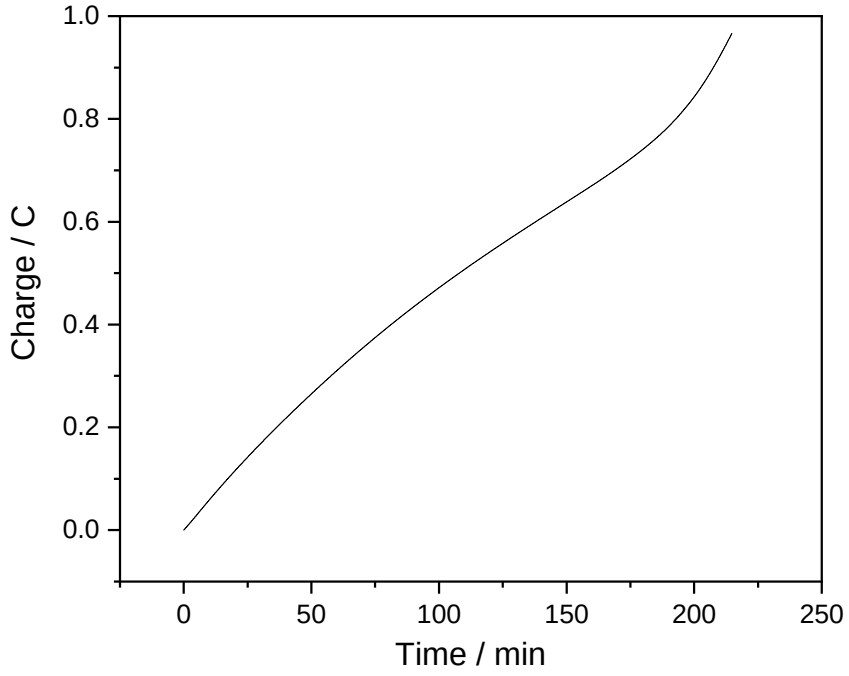

Figure 7A.9: Charge vs time plot following the CPE of 3 mM $[Re(3,3'\text{-dhbipy})(CO)_3Cl]$ in CO_2-saturated 0.5 M THF/Bu_4NPF_6. The catalytic electrode potential was held at -2.6 V vs Fc/Fc^+ for 3 h, using a Pt microdisc electrode (diameter of 2 mm).

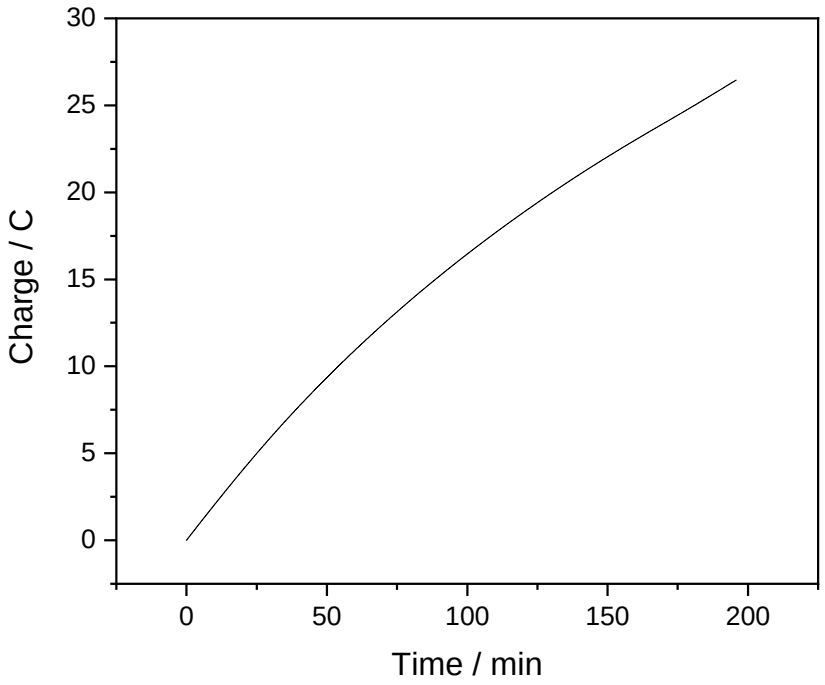

Figure 7A.10: Charge vs time plot following the CPE of 3 mM [Re(3,3′-dhbipy)$(CO)_3$Cl] in CO_2-saturated 0.5 M THF/Bu_4NPF_6. The catalytic electrode potential was held at -2.6 V vs Fc/Fc^+ for 3 h, using a Pt foil electrode (surface area of 2×0.96 cm^2).

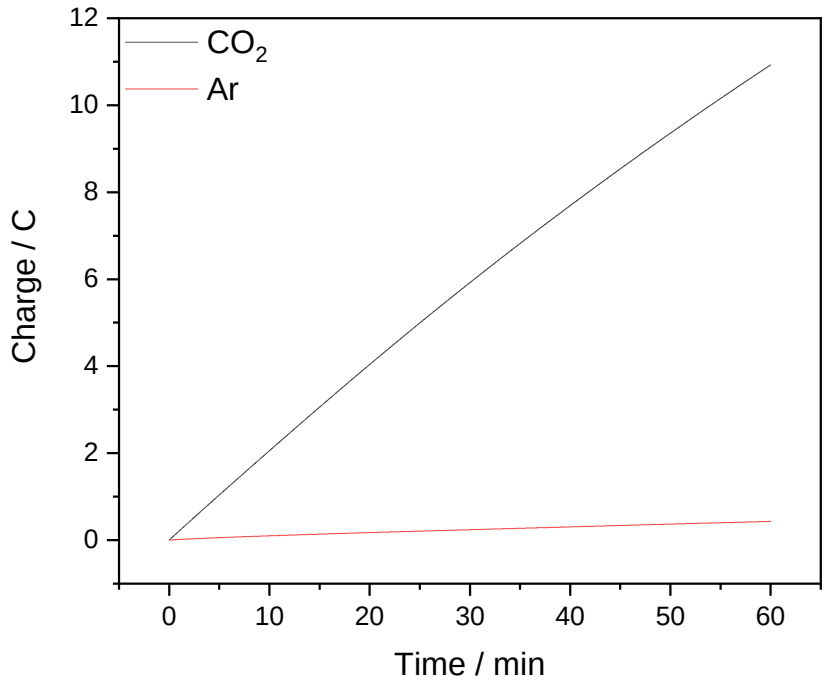

Figure 7A.11: Charge vs time plot following the CPE of 3 mM [Re(3,3′-dhbipy)$(CO)_3$Cl] in CO_2-saturated (black) and Ar-saturated (red) 0.5 M THF/Bu_4NPF_6. The catalytic electrode potential was held at -2.6 V vs Fc/Fc^+ for 1 h, using a Pt foil electrode (surface area of 2×0.96 cm^2).

References

[1] A. J. Morris, G. J. Meyer and E. Fujita, *Acc. Chem. Res.*, 2009, **42**, 1983–1994.

[2] D. Gust, T. A. Moore and A. L. Moore, *Acc. Chem. Res.*, 2009, **42**, 1890–1898.

[3] N. Armaroli and V. Balzani, *Chem. Eur. J.*, 2016, **22**, 32–57.

[4] E. E. Benson, C. P. Kubiak, A. J. Sathrum and J. M. Smieja, *Chem. Soc. Rev.*, 2009, **38**, 89–99.

[5] J.-M. Savéant, *Chem. Rev.*, 2008, **108**, 2348–2378.

[6] C. D. Windle and R. N. Perutz, *Coord. Chem. Rev.*, 2012, **256**, 2562–2570.

[7] N. Elgrishi, M. B. Chambers, X. Wang and M. Fontecave, *Chem. Soc. Rev.*, 2017, **46**, 761–796.

[8] K. A. Grice, *Coord. Chem. Rev.*, 2017, **336**, 78–95.

[9] K. E. Dalle, J. Warnan, J. J. Leung, B. Reuillard, I. S. Karmel and E. Reisner, *Chem. Rev.*, 2019, **119**, 2752–2875.

[10] C. Jiang, A. W. Nichols and C. W. Machan, *Dalton Trans.*, 2019, **48**, 9454–9468.

[11] R. Francke, B. Schille and M. Roemelt, *Chem. Rev.*, 2018, **118**, 4631–4701.

[12] T. Mizukawa, K. Tsuge, H. Nakajima and K. Tanaka, *Angew. Chem. Int. Ed.*, 1999, **38**, 362–363.

[13] K. Tanaka, *Chem. Rec.*, 2009, **9**, 169–186.

[14] K. Kobayashi and K. Tanaka, *Phys. Chem. Chem. Phys.*, 2014, **16**, 2240–2250.

[15] C. W. Machan, S. A. Chabolla and C. P. Kubiak, *Organometallics*, 2015, **34**, 4678–4683.

[16] J. M. Smieja and C. P. Kubiak, *Inorg. Chem.*, 2010, **49**, 9283–9289.

[17] C. J. Stanton, C. W. Machan, J. E. Vandezande, T. Jin, G. F. Majetich, H. F. Schaefer, C. P. Kubiak, G. Li and J. Agarwal, *Inorg. Chem.*, 2016, **55**, 3136–3144.

[18] J. Hawecker, J. M. Lehn and R. Ziessel, *J. Chem. Soc., Chem. Commun.*, 1984, **984**, 328–330.

[19] B. P. Sullivan, C. M. Bolinger, D. Conrad, W. J. Vining and T. J. Meyer, *J. Chem. Soc., Chem. Commun.*, 1985, **985**, 1414–1416.

[20] J. A. Keith, K. A. Grice, C. P. Kubiak and E. A. Carter, *J. Am. Chem. Soc.*, 2013, **135**, 15823–15829.

[21] M. V. Vollmer, C. W. Machan, M. L. Clark, W. E. Antholine, J. Agarwal, H. F. Schaefer, C. P. Kubiak and J. R. Walensky, *Organometallics*, 2015, **34**, 3–12.

[22] M. R. Crawley, K. J. Kadassery, A. N. Oldacre, A. E. Friedman, D. C. Lacy and T. R. Cook, *Organometallics*, 2019, **38**, 1664–1676.

[23] S. A. Chabolla, C. W. MacHan, J. Yin, E. A. Dellamary, S. Sahu, N. C. Gianneschi, M. K. Gilson, F. A. Tezcan and C. P. Kubiak, *Faraday Discuss.*, 2017, **198**, 279–300.

[24] F. P. Johnson, M. W. George, F. Hartl and J. J. Turner, *Organometallics*, 1996, **15**, 3374–3387.

[25] J. M. Smieja, M. D. Sampson, K. A. Grice, E. E. Benson, J. D. Froehlich and C. P. Kubiak, *Inorg. Chem.*, 2013, **52**, 2484–2491.

[26] M. Bourrez, F. Molton, S. Chardon-Noblat and A. Deronzier, *Angew. Chem. Int. Ed.*, 2011, **50**, 9903–9906.

[27] D. C. Grills, M. Z. Ertem, M. McKinnon, K. T. Ngo and J. Rochford, *Coord. Chem. Rev.*, 2018, **374**, 173–217.

[28] J. Agarwal, T. W. Shaw, C. J. Stanton, G. F. Majetich, A. B. Bocarsly and H. F. Schaefer, *Angew. Chem. Int. Ed.*, 2014, **53**, 5152–5155.

[29] Y. C. Lam, R. J. Nielsen, H. B. Gray and W. A. Goddard, *ACS Catal.*, 2015, **5**, 2521–2528.

[30] M. Stanbury, J.-D. Compain and S. Chardon-Noblat, *Coord. Chem. Rev.*, 2018, **361**, 120–137.

[31] M. D. Sampson, A. D. Nguyen, K. A. Grice, C. E. Moore, A. L. Rheingold and C. P. Kubiak, *J. Am. Chem. Soc.*, 2014, **136**, 5460–5471.

[32] C. W. Machan, C. J. Stanton, J. E. Vandezande, G. F. Majetich, H. F. Schaefer, C. P. Kubiak and J. Agarwal, *Inorg. Chem.*, 2015, **54**, 8849–8856.

[33] M. D. Sampson and C. P. Kubiak, *J. Am. Chem. Soc.*, 2016, **138**, 1386–1393.

[34] S. J. Spall, T. Keane, J. Tory, D. C. Cocker, H. Adams, H. Fowler, A. J. Meijer, F. Hartl and J. A. Weinstein, *Inorg. Chem.*, 2016, **55**, 12568–12582.

[35] G. Neri, J. J. Walsh, G. Teobaldi, P. M. Donaldson and A. J. Cowan, *Nat. Catal.*, 2018, **1**, 952–959.

[36] M. L. Clark, A. Ge, P. E. Videla, B. Rudshteyn, C. J. Miller, J. Song, V. S. Batista, T. Lian and C. P. Kubiak, *J. Am. Chem. Soc.*, 2018, **140**, 17643–17655.

[37] A. Sinopoli, N. T. La Porte, J. F. Martinez, M. R. Wasielewski and M. Sohail, *Coord. Chem. Rev.*, 2018, **365**, 60–74.

[38] C. Riplinger and E. A. Carter, *ACS Catal.*, 2015, **5**, 900–908.

[39] C. Costentin, S. Drouet, M. Robert and J. M. Savéant, *Science*, 2012, **338**, 90–94.

[40] A. Wilting, T. Stolper, R. A. Mata and I. Siewert, *Inorg. Chem.*, 2017, **56**, 4176–4185.

[41] Q. Zeng, M. Messaoudani, A. Vlček and F. Hartl, *Electrochim. Acta*, 2013, **110**, 702–708.

[42] Q. Zeng, M. Messaoudani, A. Vlček and F. Hartl, *Eur. J. Inorg. Chem.*, 2012, **2012**, 471–474.

[43] F. Franco, C. Cometto, L. Nencini, C. Barolo, F. Sordello, C. Minero, J. Fiedler, M. Robert, R. Gobetto and C. Nervi, *Chem. Eur. J.*, 2017, **23**, 4782–4793.

[44] L. Rotundo, C. Garino, E. Priola, D. Sassone, H. Rao, B. Ma, M. Robert, J. Fiedler, R. Gobetto and C. Nervi, *Organometallics*, 2019, **38**, 1351–1360.

[45] A. Taheri, E. J. Thompson, J. C. Fettinger and L. A. Berben, *ACS Catal.*, 2015, **5**, 7140–7151.

[46] G. F. Manbeck, J. T. Muckerman, D. J. Szalda, Y. Himeda and E. Fujita, *J. Phys. Chem. B*, 2015, **119**, 7457–7466.

[47] M. L. Clark, P. L. Cheung, M. Lessio, E. A. Carter and C. P. Kubiak, *ACS Catal.*, 2018, **8**, 2021–2029.

[48] H. Kunkely and A. Vogler, *Inorg. Chim. Acta*, 2003, **343**, 357–360.

[49] A. Vogler and I. G. Shenderovich, *Inorg. Chim. Acta*, 2014, **421**, 496–499.

[50] D. Ghorai, C. Dutta and J. Choudhury, *ACS Catal.*, 2016, **6**, 709–713.

[51] S. Y. Hong, J. Kwak and S. Chang, *Chem. Commun.*, 2016, **52**, 3159–3162.

[52] L. Maidich, G. Dettori, S. Stoccoro, M. A. Cinellu, J. P. Rourke and A. Zucca, *Organometallics*, 2015, **34**, 817–828.

[53] R. Czerwieniec, A. Kapturkiewicz, R. Anulewicz-Ostrowska and J. Nowacki, *J. Chem. Soc., Dalton Trans.*, 2002, 3434–3441.

[54] M. Krejčik, M. Daněk and F. Hartl, *J. Electroanal. Chem. Interfacial Electrochem.*, 1991, **317**, 179–187.

[55] F. Hartl, *Inorg. Chim. Acta*, 1995, **232**, 99–108.

[56] Y. Himeda, N. Onozawa-Komatsuzaki, H. Sugihara, H. Arakawa and K. Kasuga, *Organometallics*, 2004, **23**, 1480–1483.

[57] F. Hartl and A. Vlček, *Inorg. Chem.*, 1992, **31**, 2869–2876.

[58] G. J. Stor, F. Hartl, J. W. Van Outersterp and D. J. Stufkens, *Organometallics*, 1995, **14**, 1115–1131.

[59] S. Záliš, C. Consani, A. E. Nahhas, A. Cannizzo, M. Chergui, F. Hartl and A. Vlček, *Inorg. Chim. Acta*, 2011, **374**, 578–585.

[60] J. Tory, B. Setterfield-Price, R. A. W. Dryfe and F. Hartl, *ChemElectroChem*, 2015, **2**, 213–217.

[61] S. C. Cheng, C. A. Blaine, M. G. Hill and K. R. Mann, *Inorg. Chem.*, 1996, **35**, 7704–7708.

Chapter 8

Final Discussion and Summary

The work presented here has contributed significantly to the understanding of Group-6 and -7 metal carbonyl electrocatalysts. Investigations into the redox chemistry of a wide variety of electrocatalysts have been conducted. We have applied a combined approach of cyclic voltammetry, mechanistic IR and UV-Vis spectroelectrochemistry alongside supporting computational techniques, which has proven highly effective in determining the intimate details of the various cathodic pathways. This has ultimately allowed for a more thorough assessment of the potential for catalytic CO_2 reduction with Group-6 metal complexes.

Our initial forays into complex electrochemistry of the Group-6 electrocatalysts began with the work in Chapter 3, where the contribution of solvent and cathodic material to the catalysis are investigated in appreciable detail. Inspired by the previous work, we have been able to show that there is also a strong impact from the redox non-innocent ligand, as well as confirm the activity of the low-energy pathway for other derivatives of the title $[Mo(CO)_4(bipy)]$ complex. Our work with the $[Mo(CO)_4(x,x'\text{-dmbipy})]$ (x = 4-6) systems reminded us of their equally rich photochemistry. It became clear that there was significant similarity between the low-energy pathway that had been characterized in Chapter 3 and the chemical behaviour following MLCT excitation in the UV region of the parent complex, both involving CO dissociation from a 6-coordinate structure. Chapter 4 has then addressed the similarities between these routes, and answer whether photochemistry could be exploited in a similar manner with regard to reducing the catalytic overpotential. For a comparison, the assisting photochemistry was also applied to the well known $[Mn(bipy)(CO)_3Br]$ catalyst precursor, where the photoexcitation triggers Mn−Mn bond cleavage in the nearly inert dimer, yielding the active catalyst already at the parent reduction potential. The data have successfully revealed that photochemical irradiation can be an effective alternative for the second, significantly more negative reduction step, which perhaps opens a new way to optimise the cathodic paths of these catalysts.

Chapter 5, described an in-depth mechanistic study with the same ligand series as in Chapter 3, but with an alternative coordination sphere: $[Mo(\eta^3\text{-allyl})(CO)_2(x,x'\text{-dmbipy})(NCS)]$ (x = 4-6). The series proved suitable for diagnostic probing of the cathodic

paths, and has revealed many interesting facets about the complexities of the Mo-allyl system. In particular the striking similarities to the [Mn(bipy)$(CO)_3$Br] system and as well the strong substituent control over the reduction path, make the possibility of further optimization quite promising. This finally became part of the following Chapter 6. Systematic alterations to the appended ligands allowed for further characterization of the redox behaviour. In particular, assessing the impact of the clearly non-innocent allyl and (pseudo)-halide ligands takes the focus and thus building a more accurate picture of the various effects which control the reactivity of these Group-6 allyl complexes.

In the final Chapter 7, the work presented adds to the literature on the proton-responsive ligands. In general these ligands have proven to be very effective at improving the catalytic efficiency. In this case though, the positioning of the hydroxyl groups adds additional complexity, and reveal the importance of careful ligand design. The proton responsive ligand 3,3′-dhbipy was studied with the well known Group-7 catalyst scaffold: [Re(α-diimine)$(CO)_3$Cl]. In principle however the same design principles learnt here may be applied also to the Group-6 scaffolds from preceding chapters.

More generally, the work in the Thesis has covered a wide range of research: (i) a deep characterization of the cathodic paths of close to a dozen new Group-6 α-diimine complexes using cyclic voltammetry and spectroelectrochemistry, (ii) a preliminary assessment of each new complex's reactivity under CO_2, (iii) the discovery of a new photo-assisted route to reduced catalytic overpotentials, and (iv) an investigation of an unusually complicated proton responsive ligand.

Longer term continuation of the project may resolve around expanding study of the two families, [M(η^3-allyl)$(CO)_2$(α-diimine)X] and [M$(CO)_4$(α-diimine)] (M = Cr, Mo, W). Of the two the latter is perhaps more promising for catalytic CO_2 reduction, owing to its relatively simple, but highly optimizable cathodic behaviour. In the immediate future, work is already underway to investigate systems which contain non-aromatic ligands such as [M$(CO)_4$(tBu-dab)] (M = Mo, W; dab = 1,4-diazabuta-1,3-diene) and also [Mo(η^3-

allyl)$(CO)_2(R_2$-(Me)-dab)X] (X = Br^-, NCS^- and MeCN, R_2-(Me)-dab = (2,3-dimethyl)-1,4-diazabuta-1,3-diene, R = phenyl and 2,6-dimethylphenyl). Studies involving the role of external and internal proton sources in Group-6 catalysts may also be a route forward. However, a particular focus should be payed to opportunities which exploit the novel photo-assisted route described in Chapter 4, and preliminary results on the $[M(CO)_4(t$Bu-dab)] series are very encouraging in this regard. Besides this, there are other exciting chances for advancing the fundamental role of mechanistic spectroelectrochemistry in this field. The most promising involve coupling to laser spectroscopy - with ps/ns time-resolved IR (TRIR) spectroelectrochemistry being of particular interest.

Several other projects were conducted within the scope of the PhD project however, these are not included within this Thesis for reasons of coherence and conciseness. These studies include the spectroelectrochemical study of a new series of complexes with the structure $[Ru(bipy)_n(CN\text{-}Me\text{-}bipy)_{3-n}](PF_6)_2$ (n = 0, 1, 2). Upon $1e^-$ reduction the intensity of the CN band in CN-Me-bipy ligand increases rapidly, reaching a maximum intensity many times that of the parent band. In the future this effect has the potential to play a key role in the design of new spectroscopic labels for the in-situ study of proteins. Finally, the development and application of several new spectroelectrochemical techniques, such as 2D-IR, far-IR and IR SEC in room temperature ionic liquids (RTIL) has begun.